THE UNIVERSITY *of* EDINBURGH

An exploration of novel correlated electronic states in 5d transition metal oxides

Emily Hunter

Doctor of Philosophy
The University of Edinburgh
June 2015

Abstract

The crystal growth conditions of compounds of the series $Sr_{n+1}Ir_nO_{3n+1}$ (n=1, 2 and ∞) are investigated. It was found that the ratio of IrO_2:$SrCO_3$ in the starting mixture is the most important variable in determining the phase formed. Good quality samples of $Sr_3Ir_2O_7$ were found to have a sharp change in gradient at the Néel temperature of 287.5 K and no secondary T* transition between 230 K and 260 K. All crystals of $Sr_3Ir_2O_7$ grown were found to be heavily oxygen deficient by EPMA regardless of the crystal growth conditions used with an average stoichiometry of $Sr_{2.87}Ir_2O_{6.27}$. Adding more electrons via replacing strontium with lanthanum causes $(Sr_{(1-x)}La_x)_3Ir_2O_7$ to become metallic by x=0.072, which also fully quenches the long-range antiferromagnetic order. Heat capacity and resistivity measurements show that metallic $(Sr_{(1-x)}La_x)_3Ir_2O_7$ is a weakly correlated Fermi-liquid metal. Given that there are only subtle changes to the structure upon lanthanum doping, the metal-insulator transition is a result of electron doping rather than structural distortions. No structural phase transitions were found up to a temperature of 800°C and no additional evidence was found to support the B*bcb* space group model of the structure of $Sr_3Ir_2O_7$. Using crystals five times better in quality than those reported in the literature, $SrIrO_3$ was found to be a Fermi-liquid metal, rather than a non-Fermi liquid metal as previously reported, and no superconductivity was found down to temperatures of 20 mK.

A known Pt(III) compound, $CaPt_2O_4$, was found to be a weakly correlated metal down to 2 K and a novel Pt(III) based compound, $K_2CaPt_{3-\delta}O_6$ ($\delta \approx 0.4$), was discovered. $K_2CaPt_{3-\delta}O_6$ has a structure consisting of monolayers of edge-sharing PtO_6 octahedra separated by layers of ordered K^+ and Ca^{2+} ions in a 2:1 ratio. The structure of $K_2CaPt_{3-\delta}O_6$ was found to be flexible to doping with copper, causing the magnetic properties to change from temperature independent to paramagnetic.

Lay Summary

The crystal growth and properties of two families of 5d transition metal oxides are explored in this thesis. The first is a series of three different compounds of strontium iridate that are thought to have unusual ground states. We investigated the crystal growth conditions needed to grow the three different phases of strontium iridate and whether the properties of the $Sr_3Ir_2O_7$ crystals are dependent on the conditions under which they were grown. We find that the properties of $Sr_3Ir_2O_7$ change from insulating to metallic and that the magnetic properties are destroyed if around 7% of the strontium in the structure is replaced with lanthanum. We also discover that the structure of $Sr_3Ir_2O_7$ remains unchanged up to 800°C. Another strontium iridate compound, $SrIrO_3$, was found to be a normal metal and did not show any low temperature superconductivity in contrast to previous predictions.

In the second half of the thesis we search for new electronic and magnetic properties in platinate compounds. In metal oxides platinum normally has an oxidation state of either +2 or +4, resulting in the material being an insulator. To obtain a platinate compound with more exotic properties, new compounds need to be made that contain platinum in an unusual oxidation state such as +1 or +3. We use molten potassium hydroxide to grow crystals of a new platinate compound of formula $K_2CaPt_{3-\delta}O_6$ ($\delta \approx 0.4$) that has a platinum oxidation state close to +3 and a crystal structure that is similar to that of battery materials. The magnetic properties of $K_2CaPt_{3-\delta}O_6$ can be altered by replacing some platinum in the structure with copper. The properties of another Pt(III) compound, $CaPt_2O_4$ were measured down to temperatures of -275°C for the first time, confirming that $CaPt_2O_4$ is a metal and that the Pt(III) oxidation state is very stable in this compound.

Publications and Conferences attended

Publications in progress

- *A review of the crystal growth conditions of* $Sr_{n+1}Ir_nO_{3n+1}$ *(n=1, 2 and* ∞*)*
- *Formation of a weakly correlated Fermi-liquid metal on electron doping* $Sr_3Ir_2O_7$
- *Absence of superconductivity and Fermi-liquid behaviour in* $SrIrO_3$
- *Robustness of the Pt(III) ground state of* $CaPt_2O_4$
- *The crystal growth and structure of a novel* Pt^{3+} *based oxide,* $K_2CaPt_{(3-\delta)}O_6$

Conferences attended

Oral presentations

- *Tuning the electronic properties of* $Sr_3Ir_2O_7$*: The formation of a quasi-2D metal via electron doping*, Oxford Symposium on Quantum Materials, Somerville College, Oxford, May 2014
- *The evolution of the ground state of lanthanum doped* $Sr_3Ir_2O_7$, Mott Physics Beyond the Heisenberg Model, Oriel College, Oxford, Sept 2014

Poster presentations

- *The crystal growth and structure of a novel* Pt^{3+} *oxide,* $K_2CaPt_3O_6$, Gordon Research Conference on Solid State Chemistry, New London, U.S., July 2014

- *Correlating the structural evolution of $Sr_3Ir_2O_7$ upon lanthanum doping with the formation of a quasi-2D metal.*, Strongly Correlated Electron Systems, Grenoble, France, July 2014

- *Tuning the electronic properties of $Sr_3Ir_2O_7$: The formation of a quasi-2D metal via electron doping.*, RSC Solid State Group Christmas Meeting, University of Bath, Dec 2013 and Frontiers in Unconventional Superconductivity and Magnetism, University of Bristol, Jan 2014

- *Materials discovery via flux growth: Novel platinates*, RSC Solid State Group Christmas Meeting, University of St Andrews, Dec 2012

Declaration

I declare that this thesis was composed by myself, that the work contained herein is my own except where explicitly stated otherwise in the text, and that this work has not been submitted for any other degree or professional qualification except as specified.

The candidate confirms that the work submitted is his/her own, except where work which has formed part of jointly-authored publications has been included. The contribution of the candidate and the other authors to this work has been explicitly indicated below. The candidate confirms that appropriate credit has been given within the thesis where reference has been made to the work of others.

Sections 4.6.5 and Appendix D and F are based upon previously published work as referenced below. My contribution to the paper upon which section 4. 6.5 is based was providing the samples and information on the structural and bulk properties of the crystals, including the Sommerfeld coefficients published. The structural information provided formed the basis of the LDA + SO + U band structure calculations performed. My contribution to the paper upon which Appendix D is based was providing the samples and collecting the data. The results of the paper, for which I provided the samples, in Appendix F are summarised as it adds to the discussion of the ground state of Sr_2IrO_4 and $Sr_3Ir_2O_7$.

Parts of this work have been published in [132][92][41].

(*Emily Hunter, June 2015*)

Acknowledgements

Firstly I would like to thank Dr Robin Perry, my original principal supervisor at the University of Edinburgh and my day to day supervisor when I was based at the UCL crystal growth laboratory at ISIS, for giving me the opportunity to do this research, his advice and guidance and for his practical help in the laboratory. This includes putting contacts on the strontium iridate crystals for the resistivity measurements conducted in this thesis.

Secondly, I would like to thank Dr Chris Stock for agreeing to become my principal supervisor at the University of Edinburgh in the absence of Dr Robin Perry. I would also like to thank my second supervisor Prof Paul Attfield for his advice and guidance and for involving me in all of the activities of his research group. I would also like to thank members of his group - in particular Dr Angel Arevalo Lopez, Dr Alex Sinclair and Dr Lucy Clark for their help and for being my office buddies while I was based in Edinburgh. My thanks also goes to Prof Toby Perring for being my local sponsor whilst I was based at ISIS.

I would also like to thank Prof Des McMorrow at UCL for overseeing collaborative experiments on my samples and giving me the opportunity to attend some of these experiments, allowing me to engage in his group meetings and for useful discussions of my results. Furthermore I would like to thank James Vale, Dr Feng Zhuo, Christian Donnerer and Dr Stefano Boseggia for their help on these high pressure x-ray diffraction experiments. Thanks for making night shifts more enjoyable during these beamtimes.

Further thanks go to Prof Felix Baumberger and Alberto de la Torre, from the University of Geneva, for carrying out the ARPES experiments and analysing the resultant data on the La doped $Sr_3Ir_2O_7$ crystals. They have been a pleasure to work with.

This brings me onto thanking the beamline scientists who I have worked with on experiment. Firstly I would like to thank Dr Moritz Hoesch, our local contact for the I05 beamline, for helping to set up the ARPES experiments and for his enthusiasm. I would like to thank Dr Kevin Knight, the principle beamline scientist for HRPD, for running the powder neutron diffraction experiment on $K_2CaPt_{3-\delta}O_6$. For the high pressure x-ray diffraction experiments I would like to thank Dr Heribert Wilhelm, principle beamline scientist on I15 at Diamond,

and Dr Michael Hanfland, principle beamline scientist on ID09 for their help in setting up the experiments.

Thanks also go to Dr Malcolm McMahon from the University of Edinburgh for providing and setting up the pressure cells for one such experiment and for his help in solving the high pressure crystal structure of $Sr_3Ir_2O_7$. I would like to thank Dr Gary Nichol, from the School of Chemistry at the University of Edinburgh, for collecting the first set of single crystal x-ray diffraction data on $K_2CaPt_{3-\delta}O_6$ and Dr Jeppe Christensen, from the Research Complex at Harwell, for advising me on the best settings for collecting an additional set of single crystal data and noticing the superstructure reflections. I would also like to thank Dr Stephen Moggach for assisting me with the single crystal refinement of the original data set.

For setting up and teaching me how to use the EPMA instrument in the School of Geosciences at the University of Edinburgh I would like to thank Dr Chris Hayward and I would like to thank Dr Mike Hall for polishing the samples beforehand. For teaching me how to prepare samples for and to carry out EDX measurements in the Research Complex at Harwell I would like to thank Dr Jennifer Holter. I would also like to thank Dr Marek Jura and Dr Gavin Stenning for arranging time for me to carry out physical properties measurements on my samples in the Materials Characterisation Laboratory at ISIS and for showing me how to use the instruments. I would also like to thank Dr Ed Yelland and Dr Jack Barraclough for carrying out dilution fridge measurements on $SrIrO_3$ at the University of St Andrews.

I would also like to thank Jane Patterson for being so lovely and friendly in helping to sort out admin related matters at the University of Edinburgh.

Finally I would like to thank my family for their support and my partner, Terence, for his moral support on writing this thesis and for brightening up my days at RAL. I would also like to thank the other students I've met at the University of Edinburgh, UCL, RAL and on conferences for making my PhD more enjoyable.

Contents

List of Figures

List of Tables

Chapter 1

Introduction

Strongly correlated electronic behaviour is responsible for many of the interesting and often technologically useful properties of mixed-metal oxides including, but not limited to, superconductivity, long-range magnetic order and colossal magnetoresistance (CMR). Their behaviour diverges from that predicted by single electron theories such as density functional theory (DFT) and Hartree-Fock theory as the electrons cannot be assumed to be non-interacting. Particularly strong correlations have been found in the compounds of the first row transition metals due to their often partially filled d-orbitals and narrow energy bands. For example NiO, according to crystal field theory, has a half-filled e_g band, which should make it metallic but in reality it is a Mott insulator[13]. This is because a band gap is created between the two e_g orbitals in order to minimise the columbic repulsion between the electrons.

5d transition metal oxides (TMOs) are compounds that are composed of at least one 5d transition metal element (highlighted in the periodic table in figure 1.1), oxygen and any number of other elements. The 5d elements range from Lu to Hg, and do not include the lanthanide series from La to Yb, and are a couple of rows below the 3d transition series (also highlighted). The 5d electronic orbitals are much larger and more diffuse than the 3d orbitals, resulting in a greater bandwidth so 5d metal oxides were traditionally only expected to display weakly correlated electronic behaviour; i.e be mainly metallic with few examples of magnetic ordering. However, work on the iridates has revealed that certain compounds such as Sr_2IrO_4 and Ba_2IrO_4, which were predicted to be metallic, are actually antiferromagnetically ordered insulators[27][99]. These unexpected

properties are thought to be facilitated by a spin-orbit coupling induced $J_{eff} = 1/2$ Mott insulating ground state, the origin of which is described in section 2.4.

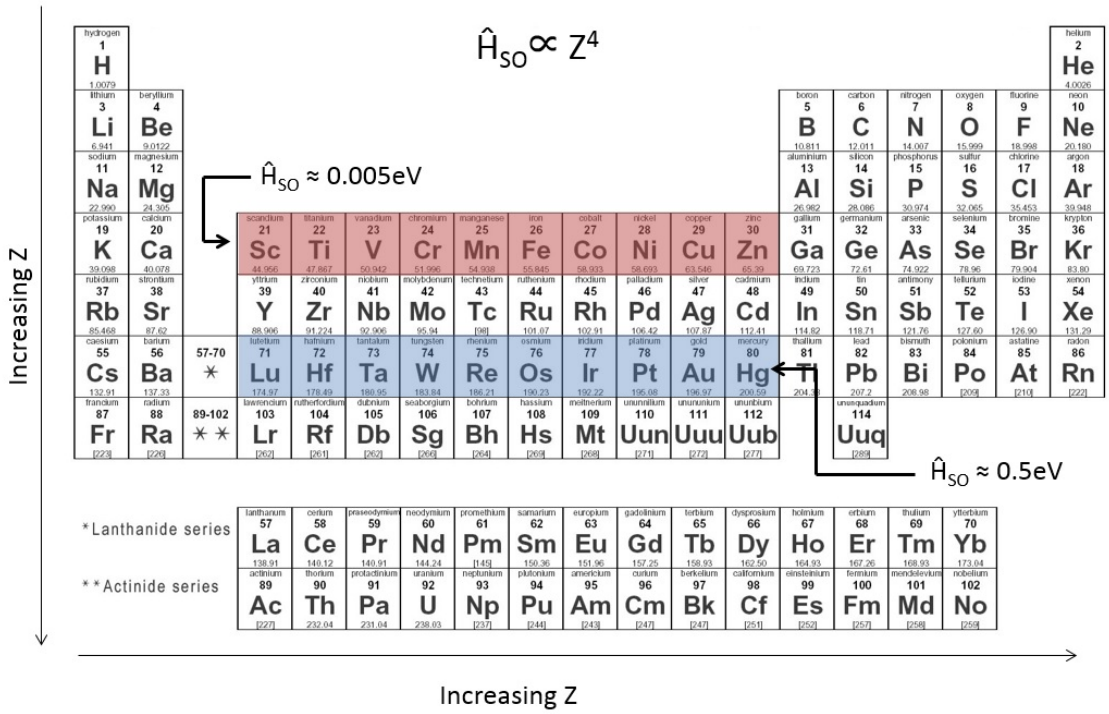

Figure 1.1 *Periodic table to show the location of the 3d and 5d transition metal series (highlighted in red and blue respectively). The effective nuclear charge, Z, of the elements increases down a group and across a period.*

Spin-orbit coupling,$\hat{H}_{SO}$, is a mixing of the L and S quantum numbers due to the coupling of an electrons intrinsic spin with its orbital angular momentum (see equation 1.1). In most 3d transition metal oxides this effect is too small to effect the electronic properties of the material but, as H_{SO} increases with effective nuclear charge, Z, by a factor of Z^4[9], for 5d elements spin-orbit coupling becomes comparable with other electronic properties that govern the electronic properties of a material such as crystal field strength.

$$H_{\mathrm{SO}} = \lambda L \cdot S \tag{1.1}$$

Little work has been done experimentally on 5d transition metal oxides partially due to the difficulty of making good quality single crystal samples. However, there has recently been much theoretical interest in these compounds and, as a result of the enhanced electron correlations induced by spin-orbit coupling,

they have been predicted to exhibit a range of, in some cases novel, phenomena such as topological insulating states, Majorana fermions, unconventional high temperature superconductivity, highly frustrated systems with spin-liquid ground states and thermally driven metal-insulator transitions. Some novel physics has already been discovered, for example, $Cd_2Os_2O_7$ shows a second order metal-insulator transition at 225K[86] and may be the first well documented example of a Slater transition[127] while the beta pyrochlore AOs_2O_6 (A=K, Rb, Cs) compounds exhibit exotic superconductivity thought to be induced by a low energy rattling mode of the respective alkali metal cation[131]. More experimental work is needed to explore the properties of these exciting new materials, with the promise of uncovering and confirming new and predicted physics.

1.1 Correlated electronic behaviour exhibited by 5d transition metal oxides

1.1.1 Magnetic ordering

In the case where there is a $J_{\text{eff}} = 1/2$ Mott insulating ground state magnetic order can occur. Most iridate compounds contain Ir^{4+}, which has an electronic configuration of $5d^6$ and the $J_{\text{eff}} = 1/2$ ground state is a result of the coupling of the S=1/2 and L=1 quantum numbers. These Ir^{4+} ions can couple to each other and magnetically order via superexchange pathways (see section 2.5.1). As mentioned previously Sr_2IrO_4 and Ba_2IrO_4 are classic examples of antiferromagnetically ordered insulators. However, long-range magnetic order is not limited to the iridates. Ba_2NaOsO_6 is a double perovskite with Os^{7+} in an octahedral coordination environment with an electronic configuration of $5d^1$. This leaves the t_{2g} band partially filled so metallic behaviour would be expected by crystal field theory, however it has been experimentally measured to be a ferromagnetically ordered insulator[45]. In this case the ground state is thought to arise from a $J_{\text{eff}} = 3/2$ quartet split into two Kramers doublets with the ferromagnetism arising from orbital ordering. Meanwhile the isostructural and isoelectronic Ba_2LiOsO_6 is an antiferromagnetic insulator [8] so the ground state is finely balanced.

Whether a 5d TMO magnetically orders is also dependent on its structure. Pyrochlore compounds are often geometrically frustrated magnets due to the

inability of spins to align antiparallel on its corner-shared tetrahedron structure. (see figure 1.2). This is also true for most iridate pyrochlore compounds with the exception of $Eu_2Ir_2O_7$, which exhibits long-range antiferromagnetic order below 120 K[146]. Other iridate compounds too are magnetically frustrated. Na_2IrO_3 was theoretically predicted to be a spin-liquid[33] and due to its honeycomb lattice and it was also a candidate for the Kitaev spin model. However, experimentally it was found to exhibit long-range antiferromagnetic order[81]. Although Na_2IrO_3 is highly unlikely to have a spin liquid ground state; it is still thought to follow a modified Kitaev-Heisenberg model, which takes interactions beyond nearest neighbour exchange into account[34]. $Na_4Ir_3O_8$, which has a highly frustrated hyper-kagome structure consisting of corner shared Ir^{4+} triangles, could be a 3D example of a spin liquid. To date magnetisation and magnetic specific heat show an absence of long-range magnetic order down to 2K, although single crystal samples are required for more accurate measurements[100].

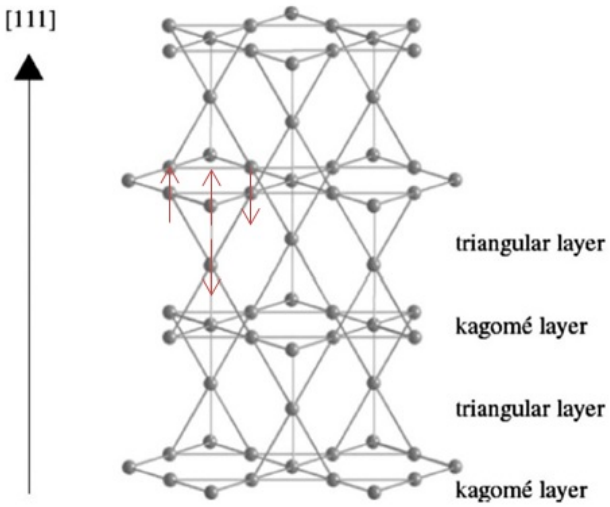

Figure 1.2 *Magnetic frustration arises on a pyrochlore lattice, which consitsts of corner sharing tetrahedra arranged in alternating triangular and kagome layers along the [111] direction, as the spins (shown in red) cannot be arranged to satify the condition of an antiferromagnet that all nearest neighbour spins need to arranged antiparallel to one another[48]*

Given that the ground state of an iridate compound is a delicate balance of the strength of the spin-orbit interaction, the strength of the crystal field and the magnitude of the Mott-Hubbard repulsion U, the Mott insulating state is not always observed, although, these compounds can exhibit other interesting properties. For example $Bi_2Ir_2O_7$ possesses strongly exchange enhanced Pauli paramagnetism with a molar magnetic susceptibility of 1.007×10^{-2} emu mol^{-1}.

$Bi_2Ir_2O_7$ also has a large Wilson ratio of 53.5 plus a temperature and field dependent Hall resistivity, which suggests that it may behave like a non-Fermi liquid[110]. Another Pauli paramagnetic metal, the perovskite $SrIrO_3$, also exhibits non-Fermi liquid behaviour in proximity to its quantum critical point and its paramagnetic moment also shows extremely strong exchange enhancement[31].

Another interesting magnetic phenomenon to arise from 5d mixed-metal oxides is weak ferromagnetism. It can be debatable whether weak ferromagnetism is an intrinsic property of the compound in question or whether it is down to the samples containing a ferromagnetic impurity but weak ferromagnetism has been found in multiple compounds and has been confirmed using a variety of tests. One such compound, $BaIrO_3$, undergoes a weak ferromagnetic transition at 175 K before returning to metallic behaviour at 80 K[29]. As well as magnetic susceptibility with temperature and hysteresis measurements the weak ferromagnetic transition is also evidenced by a drop in the resistivity at T_c and muon-spin resonance studies. The current view is that the low Iridium moment of 0.0 $3\mu_B$ is a result of small exchange splitting and d-p orbital hybridisation[77]. Low iridium moments have also been found for Sr_2IrO_4 (μ_B = 0.04 and T_c=250 K) and $CaIrO_3$ (χ=3.95 $\times$ 10^{-4} emu mol^{-1})[27]. Weak ferromagnetism and small moments are not exclusively seen for iridates. $Ba_{11}Os_4O_{24}$ has a weak ferromagnetic transition at 7.5 K with a corresponding γ type anomaly in its specific heat capacity at 6.8K[135] and the isostructural $Sr_{11}Re_4O_{24}$ has a weak ferrimagnetic transition at 11.94 K with a moment of 0.0734 μ_B per rhenium ion[21].

1.1.2 Thermally driven Metal-Insulator transitions

Structural, electronic and magnetic phase transitions are induced either by a change in temperature, a change in the applied field, a change in the sample stoichiometry (e.g. due to oxygen depletion), through chemical doping or induced by applying pressure. In the previous section the compounds underwent a transition from a paramagnetic state to a long-range magnetically ordered state at a specific transition temperature; however, often metallic compounds undergo a similar transition at a specific temperature to become an insulator and the insulating phase can exhibit long-range magnetic order. As mentioned previously, $Eu_2Ir_2O_7$ is an antiferromagnetic insulator below 120 K but above 120 K it is a pauli paramagnetic metal[146]. The long-range magnetic order is only possible

due to the localisation of the electrons onto individual ions in the insulating state rather than being itinerant in the band metal. $Nd_2Ir_2O_7$ and $Sm_2Ir_2O_7$ also undergo metal-insulator (or MI) transitions at 36 K and 117 K respectively[88]. What is unusual about the MI transitions in the iridate and osmate pyrochlores, particularly for $Cd_2Os_2O_7$, is that the metal-insulator transition is second-order rather than first-order. The majority of MI transitions are either structurally driven, of a Mott-Hubbard origin or from disorder in the sample. Structurally driven MITs include those that are from a Jahn-Teller distortion, a Peierls distortion, a charge density wave or to a different crystal structure. A Mott-Hubbard MIT occurs when the thermal energy is no longer sufficient to overcome the coloumbic repulsion that occurs as a result of inter-ion electron hopping. Most of these MITs result in a first-order phase transition, although there are second-order Jahn-Teller transitions in organic compounds. For $Cd_2Os_2O_7$, and potentially the other osmate and iridate pyrochlores, the second order MIT is due to the Slater mechanism, which was first proposed in 1951[127] but until now there have been no concrete examples. In Slater's model a second order MIT is caused by a doubling of the unit cell when long-range antiferromagnetic order occurs in a compound with a half-filled band. The exchange field causes the spins on the two sublattices to be aligned antiparallel to each other and for compounds where U/W is large (where W is the band width) an atomic scale antiferromagnetic insulator results and a band gap opens at the Fermi surface. $Cd_2Os_2O_7$ is thought to be an example of a Slater transition because it undergoes a second order MIT at 226 K without a change in crystal symmetry and with a minimal change in unit cell volume of less than 0.05% plus measurements show that it also orders antiferromagnetically at 226 K[86].

1.1.3 Other phenomena

Superconductivity

It was known that most of the 5d elements superconduct under ambient pressure at low enough temperatures, however, 5d pyrochlore compounds have only been found to superconduct fairly recently. For example the pyrochlore $Cd_2Re_2O_7$[54] has a T_c of 1K and the beta pyrochlores AOs_2O_6 (A = K, Rb, Cs) have T_cs of 9.6 K[144], 6.3 K[143] and 3.3 K[142] respectively. The superconductivity of the osmate beta pyrochlore compounds is thought to be unconventional and linked to a low energy rattling mode of the respective alkali metal cation[131]. On the other

hand Na_xWO_3 or sodium tungsten bronze has been known to superconduct since 1964 for certain values of x[112]. The highest critical temperature recorded was for $Na_{0.23}WO_3$, which has a T_c of 2.2K[103]. Further exploration of 5d transition metal oxides may unveil more superconducting compounds.

Topological Insulators

A topological insulator behaves as a band insulator in the bulk but has surface metallic states, which causes the Fermi level at the surface to be in the bulk band gap between the valence and conduction bands (Figure 1.3). The spin of the electrons on the surface are fixed at a right angle to their momentum in one particular spin-orientation, making topological insulators ideal for spintronic materials. Originally predicted to occur in quantum wells of mercury telluride sandwiched between cadmium telluride (and observed in 2007[74]) they have been found in three dimensional bulk solids of binary compounds involving bismuth such as bismuth antimony, bismuith selenide and antimony telluride. Several other materials are now thought to possess topological surface states including half-heusler compounds[139].

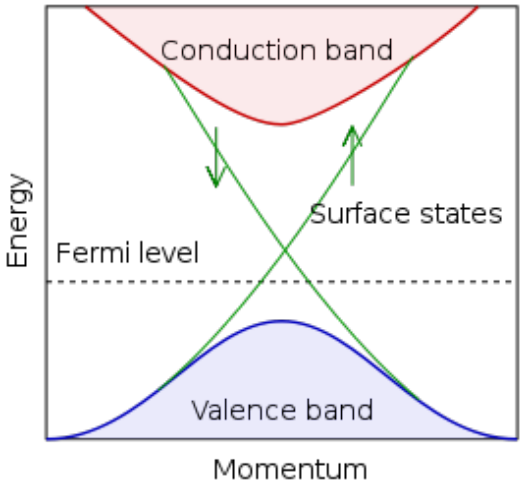

Figure 1.3 *The idealised band structure of a topological insulator.*

The two main criteria for a compound to be a topological insulator are that firstly it needs to be a bulk insulator and secondly that there is strong spin-orbit coupling present as this acts like a magnetic field to cause electrons to precess in a cyclotron orbit in a similar way to the integer quantum hall effect. 5d transition metal ions have large spin orbit coupling constants and Na_2IrO_3 has been suggested to be a candidate material for a topological insulator[70] as well

as potentially any non-magnetic pyrochlores with strong spin orbit coupling such as $Cd_2Os_2O_7$ and iridium based pyrochlores[52].

1.2 The $Sr_{n+1}Ir_nO_{3n+1}$ (n=1, 2, ∞) series

The fourth chapter of my thesis is focused on a series of iridate compounds of formula $Sr_{n+1}Ir_nO_{3n+1}$ for n=1,2 and ∞ with a main focus on the n=2 member, $Sr_3Ir_2O_7$. The n=1 and 2 members of the series are known as Ruddlesden-Popper phases, which are layered compounds with alternating rock salt and perovskite layers of the more general formula $(AO)_{(n)}(AMO_3)_n$. As shown in figure 1.4 the n=1 member, Sr_2IrO_4 has monolayers of corner-sharing IrO_6 octahedra in a perovskite structure separated by SrO rock-salt structure monolayers while $Sr_3Ir_3O_7$ has bilayers of IrO_6 octahedra. Conventionally the n=∞ member of a Ruddlesden-Popper series has fully perovskite structure without any rock-salt layers, however the structure of $SrIrO_3$ is actually a monoclinic distortion of the 6H hexagonal perovskite structure and high pressures are required for the perovskite structure to be adopted [83]. A more in-depth discussion of the Ir^{4+} environments in these compounds and the controversy over the actual structure of $Sr_3Ir_2O_7$ will be conducted in section 4.1.1.

The $Sr_{n+1}Ir_nO_{3n+1}$ series has been the subject of much interest. At the time of submission a search of the web of science database yielded 120 journal articles on strontium iridate compounds, 33 of which have been published within the last year. The interest is due to a variety of reasons. Firstly as n is increased there is a transition from insulating to metallic behaviour. Sr_2IrO_4 is a insulator with a relatively large band gap that antiferromagnetically orders below 240 K, $Sr_3Ir_2O_7$ is still an insulator but with a smaller band gap of 120 meV[137] and has an antiferromagnetic transition temperature of 287 K and both the ambient and high pressure forms of $SrIrO_3$ are Pauli paramagnetic metals. Therefore the bandwidth and strength of the electron correlations are tuneable by the thickness of the perovskite layers, which allows factors influencing the formation of the $J_{\text{eff}} = 1/2$ mott-insulating ground state to be studied in detail. The $J_{\text{eff}} = 1/2$ ground state is still a relatively new concept in condensed matter physics and its accuracy is still being determined. For example in the strontium iridates the local geometry around the iridium ion is not perfectly octahedral, which is one of the conditions for the $J_{\text{eff}} = 1/2$ state to form. Novel x-ray magnetic scattering techniques are being used to determine whether the ground state of

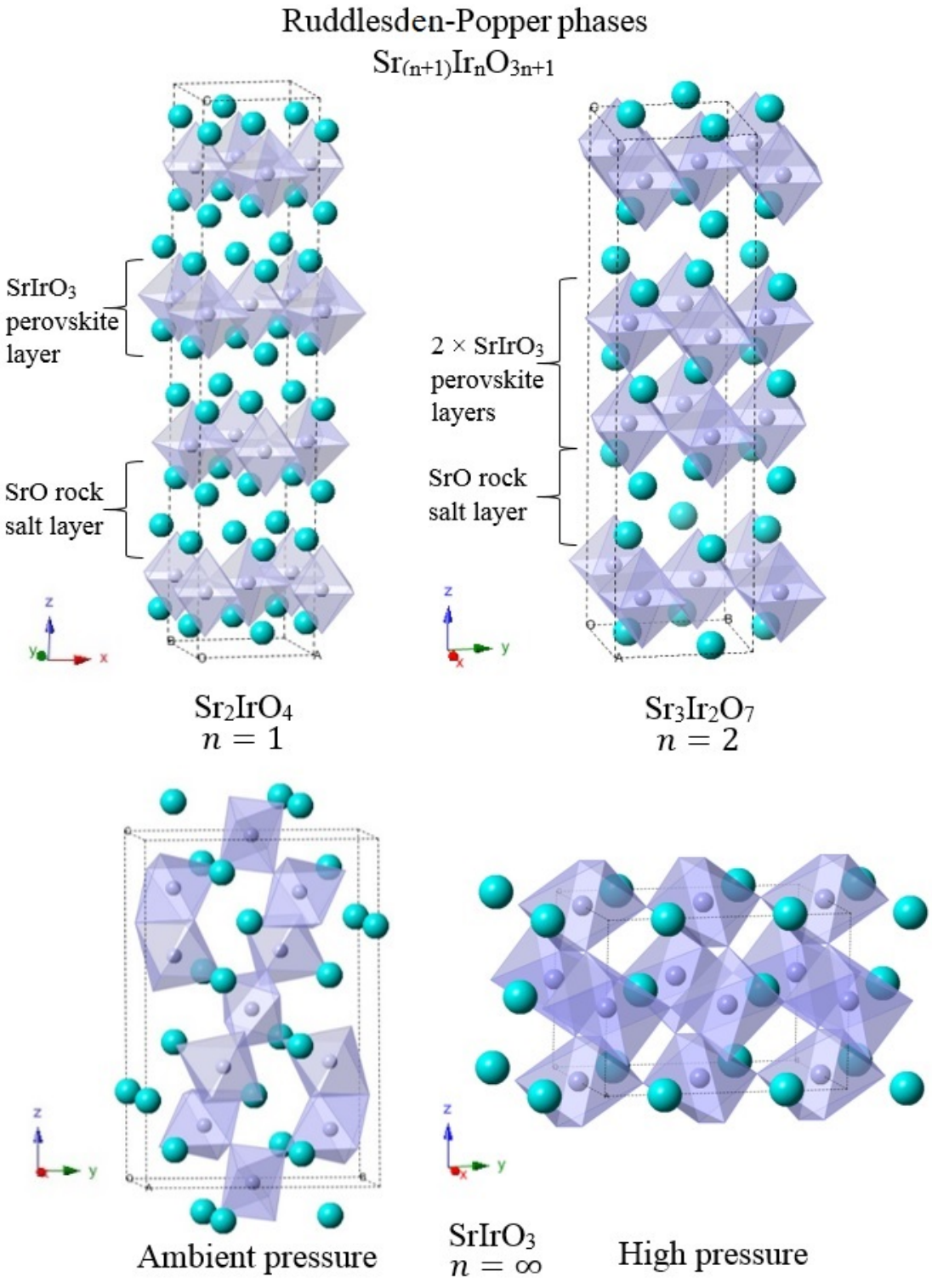

Figure 1.4 *The crystal structures of Sr_2IrO_4, $Sr_3Ir_2O_7$ and $SrIrO_3$. The IrO_6 octahedra are shown as purple polyhedra with the oxygen ions omitted for clarity and the strontium ions are shown as turquiose spheres.*

the strontium iridates can be described as purely $J_{\text{eff}} = 1/2$, even when there is a small tetragonal distortion. On another note the structure of the n=1 and 2 members of the series are analogous to the cuprates; the high temperature superconducting properties of which are still not fully understood. Thus studying the electronic correlations of the strontium iridates may help theorists improve their models for the cuprates. In section 4.6 $Sr_3Ir_2O_7$ is doped with lanthanum to create a system similar to that of the doped cuprates. As well as trying to turn the system metallic, one of the aims of the project was to investigate whether a novel superconductor could be created.

1.3 The platinates

The fifth chapter of my thesis is concerned with the search for novel correlated electronic states in the platinates. Of all the 5d TMOs the platinate (and aurate) compounds have the least number of ternary and quaternary compounds (see figure 1.5). This may be because the chemistry of synthesising platinum compounds is very challenging as platinum is a noble metal and so by nature is very unreactive. Furthermore, growing crystals of platinate compounds is even more challenging as platinum oxides tend to have low decomposition temperatures. The pioneering work on the platinates was conducted in the 1970s with the discovery of a multitude of alkali and alkali-earth platinate compounds such as $Na_xPt_3O_4$ [136] and Rb_2PtO_3 [133], although some new platinate compounds, most notably the APt_3O_6 (A= Cd, Mn, Co, Zn, Mg, Ni) series [108][118], have been discovered since then. From the literature it is noted that the most common oxidation states of platinum are +2 and +4. Pt^{4+} normally is found in an octahedral coordination environment while it is often energetically favourably for Pt^{2+} to adopt a square planar coordination environment. In fact there are a number of platinum (II) oxides that have structures that consist of chains of square planar Pt^{2+}. For both of these cases the total spin quantum number of the platinum ion is zero so the compounds are diamagnetic insulators. The challenge is to discover platinum compounds that possess platinum in an unusual oxidation state such as +1, +3 or even +5 so that the spin quantum number is non zero. This is the case in some of the examples cited above but the papers have largely only been concerned with structure determination and not with the physical properties of the compounds. Previous measurements, if published, have been of a poor quality and often not to low temperatures.

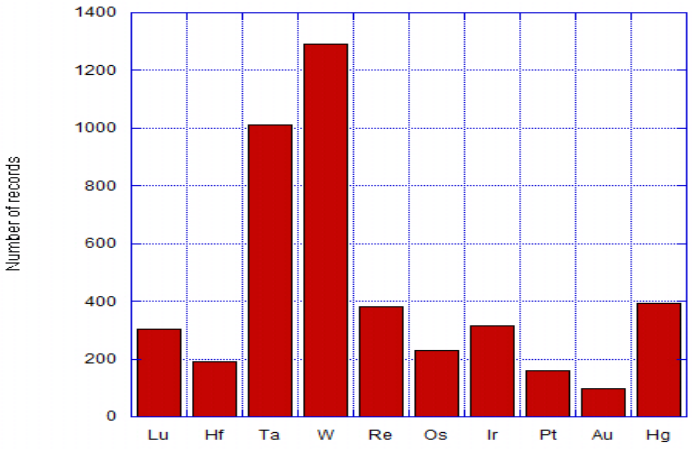

Figure 1.5 *The combined number of records of ternary and quaternary oxides in the Chemical Structure Database (CDS) of each 5d transition metal ion.*

One well researched example of a platinum oxide with Pt in the unusual +1 oxidation state is $CoPtO_2$. It is a highly anisotropic pauli paramagnetic metal [61] with low conductivity in the *ab* plane. It has a large thermopower and depending on its thermal conductivity it may be a candidate thermoelectric material [101]. In light of the exotic phenomena recently observed in 5d TMOs, especially as platinum has a larger Z and so potentially a larger spin-orbit coupling constant than iridium, it is vital to search for and characterise novel non spin zero platinate compounds and to ensure that pre-existing platinate compounds are properly characterised at low temperatures and high pressures using the latest x-ray and neutron techniques.

1.4 Aims of thesis: To explore and study novel correlated electronic behaviour in strong spin-orbit systems

This thesis is split into two parts. The first half explores the effect of crystal quality, temperature and electron-doping on the ground state of $Sr_3Ir_2O_7$. There are discrepancies in the literature with regards to the bulk properties of $Sr_3Ir_2O_7$ and little information about the crystal growth conditions for growing any of the strontium iridate compounds. Thus in section 4.2 the crystal growth conditions of all of the strontium iridate compounds are determined. The crystal quality of batches of $Sr_3Ir_2O_7$ grown under different conditions is assessed with the aim of determining whether varying crystal quality is responsible for the discrepancies in the reported bulk properties in the literature.

The crystal structure of $Sr_3Ir_2O_7$ is still under debate therefore the evolution of the crystal structure with temperature was studied so that any peak splitting could be tracked and used to determine the correct space group. As the structure of $Sr_3Ir_2O_7$ has not been previously studied above room temperature, a secondary aim of the study was to look for high temperature structural phase transitions.

Section 4.6 looks at the effect of electron doping on the ground state of $Sr_3Ir_2O_7$. This was done by substituting some strontium with lanthanum with the aim of turning the system metallic so that the ground state could be studied via Angle resolved photoelectron spectroscopy (ARPES). The ARPES study is included in this thesis and provides some important information about the ground state of $Sr_3Ir_2O_7$.

While exploring the crystal growth phase diagram of $Sr_3Ir_2O_7$, crystals of Sr_2IrO_4 and $SrIrO_3$ were also grown. This was taken advantage of by measuring the resistivity of $SrIrO_3$ down to 20 mK in a dilution fridge at St Andrews University in order to look for evidence of superconductivity that had been predicted in the literature[30]. Some crystals were also given to collaborators to explore the ground state of both Sr_2IrO_4 and $Sr_3Ir_2O_7$ and to look at the structure of $Sr_3Ir_2O_7$ under pressure, details of their findings are included in appendix D.

The second half of the thesis is concerned with the search for novel correlated electronic states in the platinates. This was approached in two ways. Firstly

in section 5.2 through experimenting with hydroxide fluxes to try and stabilise platinum compounds with unusual oxidation states a new platinum compound, $K_2CaPt_{3-\delta}O_6$, was discovered. This novel compound was doped with copper to try to introduce some magnetic properties. Secondly in section 5.4 the properties of an existing platinum compound, $CaPt_2O_4$, that is known to possess platinum in the unusual +3 oxidation state, are reinvestigated.

Chapter 2

Background Information

2.1 Classical atomic theory

The Hamiltonian of a hydrogen atom, H_0, can be described by a complete set of commuting observables (CSCOs) in terms of the operators H_0, L^2 and L_z. L^2 gives the magnitude of the orbital angular momentum and gives eigenvalues of l while L_z operates to give the direction of the orbital angular momentum, described by eigenvalues of m. Both L_z and L^2 arise from the angular part of the wave function of a hydrogen atom. H_0 arises from the radial part of the wave function of the hydrogen atom and gives energy eigenvalues, n. Thus, the combination of n, l and m can describe the shape and energy of any atomic orbital and are related as follows:

l = n-1, n-2, ...0 with n-1 possible states

m =l+l, l-1, l-2...-l with 2l+1 possible states

The shapes of the orbitals for particular combinations of l and m are shown in figure 2.1. The set of$l$=2 orbitals, known as d orbitals, will be particularly important in understanding the properties of 5d transition metal oxides. As a result of the Stern-Gerlach experiment, which found that an electron had an extra degree of freedom, termed spin, two additional operators, S^2 and S_z are required to give the spin eigenvalue m_s, which can be $\pm\frac{1}{2}$.

For a multi-electron atom additional terms such as the electron-electron repulsion need to be added to the ground state Hamiltonian. One such term is H_{SO}, which

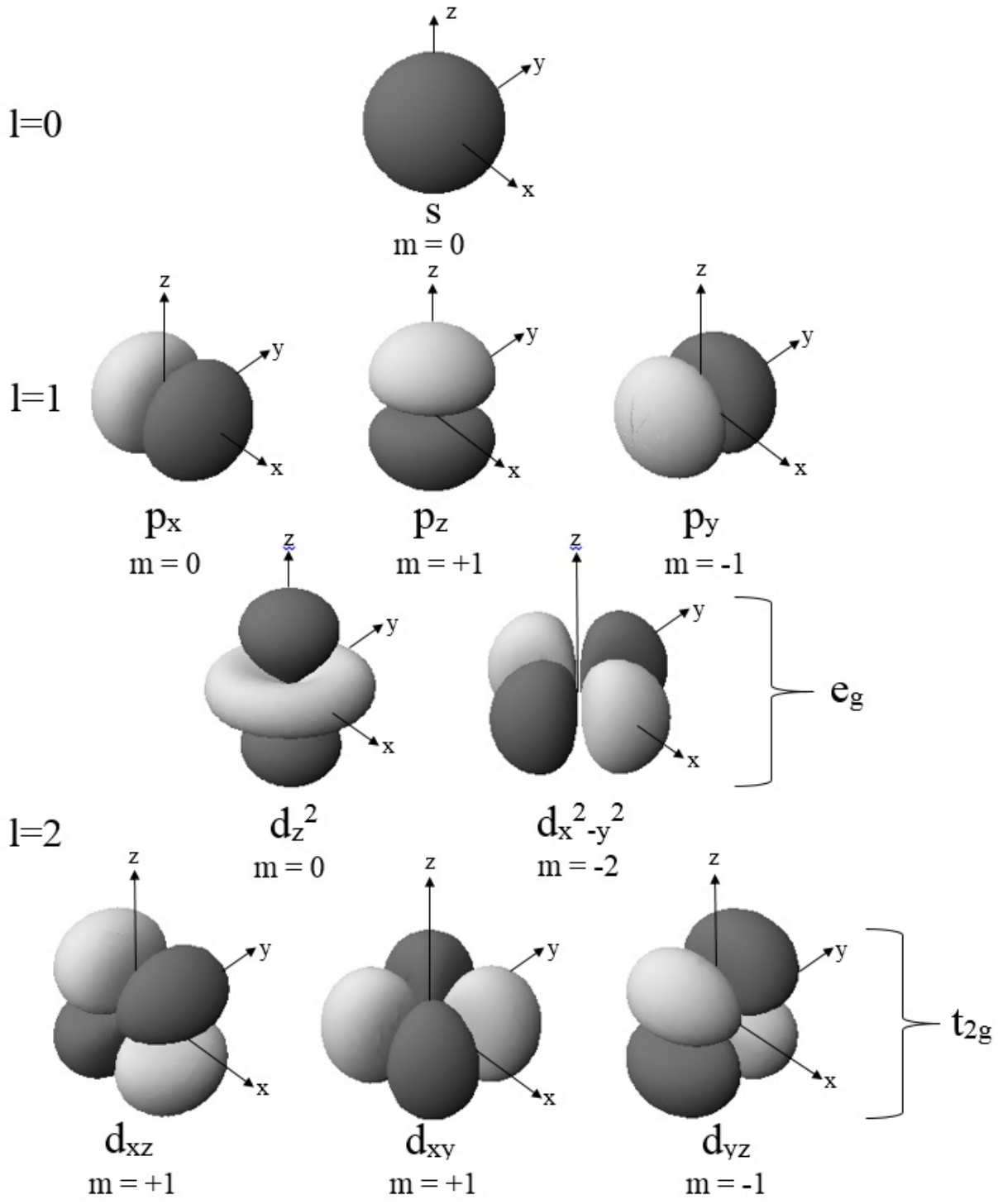

Figure 2.1 *The angular distribution of electrons in the s, p and d orbitals with the corresponding l and m quantum numbers. The d_{z^2} and $d_{x^2-y^2}$ orbitals form the e_g set and the d_{xy}, d_{xz} and d_{xy} orbitals form the t_{2g} set.*

is given by equation 2.1. H_{SO} is applicable to transition metal compounds and describes the effect of the spin of an electron coupling with the angular momentum of a particular orbital. In a hydrogen atom H_{SO} is not applicable as the occupied s orbital has no angular momentum. In equation 2.1 λ is the magnitude of the spin-orbit coupling, L is the total orbital angular momentum and S is the total spin of a multi-electron atom. λ scales to the fourth power of the effective nuclear charge[9], Z, $L = \sum_i l_i$ and $S = \sum_i m_{si}$. This spin-orbit coupling results in (2S+1) total angular momentum quantum terms, J, with $J = L + S, L + S - 1....L - S$.

$$H_{\mathrm{SO}} = \lambda L \cdot S \tag{2.1}$$

For 3d transition metal compounds $\mathrm{H_{SO}}$ is negligible compared to the crystal field so it is ignored, however, for 5d transition metal oxides λ has been measured to be up to 0.5eV, which is comparable to the strength of the crystal field and so must be taken into account. On the other hand H_{SO} is not larger than the crystal field splitting so the j-j coupling scheme that is applicable to lanthanide compounds cannot be used. To overcome this problem the L.S or Russell-Saunders coupling scheme, is applied to 5d transition metal ions where spin-orbit coupling is a perturbation on the ground state derived from crystal field effects. How this gives rise to the $J_{\mathrm{eff}} = \frac{1}{2}$ insulating ground state of the iridates will be discussed in section 2.4.

5d orbitals have a greater radial extension and are much more diffuse than their 3d counterparts. As the same number of electrons are distributed over a larger region of space, it is expected that the electronic correlations are weaker than those of elements where the valence electrons are in the 3d orbitals. Thus, depending on the electronic configuration of the 5d transition metal ion, 5d TMOs are expected to be either band insulators or band metals. The exotic properties that are observed in 5d-TMOs, as described in my introduction, are thought to arise from this special $J_{\mathrm{eff}} = \frac{1}{2}$ ground state.

2.2 Crystal field theory

Crystal field theory is used to determine the electronic ground state of an ion in the case where H_0 is significantly larger than H_{SO}. The crystal field is caused by the non-spherically symmetrical electric field and electronic coulomb repulsion produced within the ion's local environment. If the crystal field is weaker than the coulombic repulsion of electrons in the valence orbitals of the ion then Hund's rules are used in the intermediate crystal field approximation to calculate the ground state total orbital angular momentum and total spin.

If the crystal field is strong, as is normally the case with 5d TMOs, the ground state can be determined by considering the neighbouring orbitals from the anions as point charges. In an octahedral coordination environment, which is very common for a 5d TMO ion, the neighbouring anion p_x, p_y and p_z orbitals overlap with the 5d d_{z^2} and $d_{x^2-y^2}$ orbitals more than the d_{xy}, d_{xz} and d_{zy} orbitals causing the d_{z^2} and $d_{x^2-y^2}$ orbitals to form a degenerate doublet, known as the e_g set, that is higher in energy than the degenerate d_{xy}, d_{xz} and d_{zy} triplet or t_{2g} set (see figure 2.2). The energy difference between the t_{2g} and e_g set is known as Δ, which for 5d TMOs is larger than the colombic repulsion between electrons sharing an orbital. In this scenario Hund's rules are quenched to give a low spin electronic configuration where electrons fill the lower energy t_{2g} orbitals first rather than maximising the total spin by populating the e_g set before doubly occupying orbitals in the t_{2g} set (known as a high spin ion). This gives an Ir^{4+} ion in an octahedral crystal field an electronic ground state of ${t_{2g}}^5$.

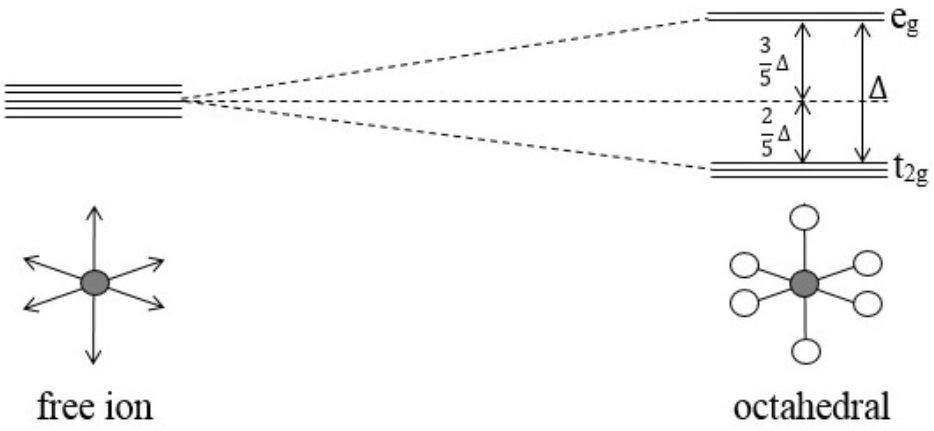

Figure 2.2 *The splitting of the initially degenerate d-orbitals in an octahedral crystal field.*

For a metal ion in an octahedral coordination environment a distortion of the octahedron can occur that can split the e_g and t_{2g} sets as shown in figure 2.3. This Jahn-Teller distortion is most common for high spin (H.S) d^4, d^7 and d^9 ions as the splitting of the e_g set, which overlap more with anion p_x, p_y and p_z orbitals, significantly lowers the electronic energy of the system. The Jahn-Teller distortion can also occur for ions with an electronic configuration of d^1, d^2, low spin (L.S) d^4, L.S d^5, H.S d^6 and H.S d^7 but the distortion is not as pronounced as the electronic energy stabilisation gained from the distortion is smaller and so more poorly offsets the additional elastic energy required to distort the octahedron in the first place. Ir^{4+} has a L.S d^5 configuration so a weak Jahn-Teller distortion can be seen in some compounds, which is often referred to in the literature as a tetragonal distortion.

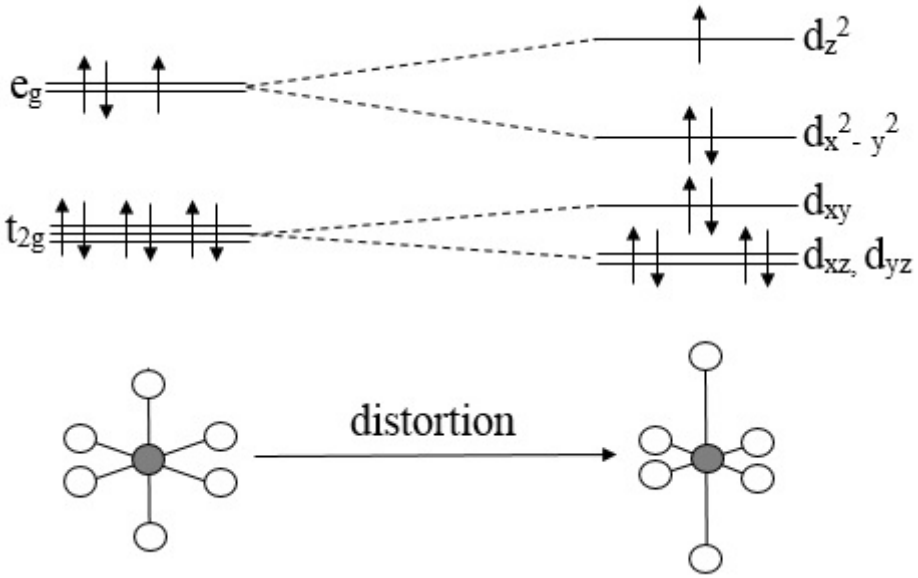

Figure 2.3 *The effect of the Jahn-Teller distortion on the ground state of a d^9 ion in an originally purely octahedral (or cubic) crystal field.*

Another important point worth noting is that while the 5d set of orbitals in the absence of a crystal field have a spin orbital angular momentum of two, in the presence of an octahedral crystal field the orbital angular momentum is quenched to one due to the loss of rotational invariance between the orbitals and for some electronic configurations such as d^5 and d^{10} the orbital angular momentum is fully quenched.

2.3 The Mott-Hubbard Model

$$H = -t \sum_{\langle i,j \rangle, s} \{c_{is}^{\dagger} c_{js} + c_{js}^{\dagger} c_{is}\} + U \sum_{i} n_{i\uparrow} n_{i\downarrow} \tag{2.2}$$

The Hubbard-model, which describes electron transfer in a system, is described by equation 2.2, where the first term describes electron hopping between nearest neighbours, i and j, and the second term describes the on-site repulsion between electrons. t is the bandwidth and U is the on-site coulomb repulsion. If the bandwidth is small and the coulomb repulsion is large then it is not energetically favourable for electrons to migrate from ion to ion and so they become localised. In this way a compound that has a half filled band can behave as an insulator rather than a metal. These compounds are known as Mott insulators. This t and U dependent metal-insulator transition is demonstrated in figure 2.4. The coulomb repulsion, or Hubbard U, opens up an energy gap to create a full band with an excited state that is not thermally accessible. 5d orbitals are large and diffuse so they have a large bandwidth and would be expected to be metallic rather than insulating if the bands were partially filled.

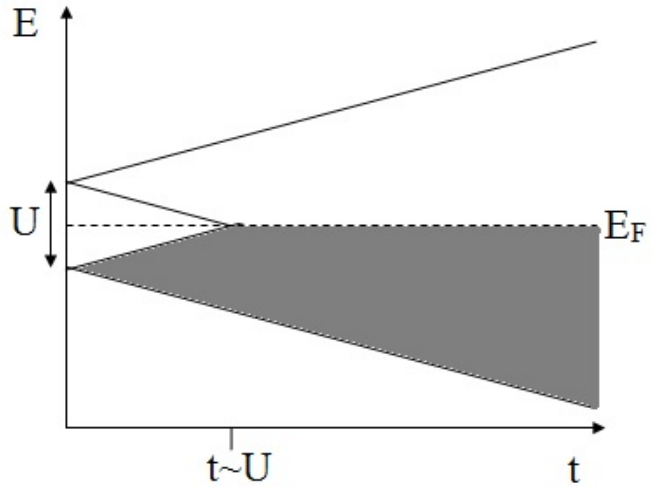

Figure 2.4 *The bandwidth,* t*, dependence of the Mott-Hubbard gap.*

2.4 The $J_{eff} = 1/2$ ground state model

If Ir^{4+} truly had a ground state electronic configuration of $t_{2g}{}^5$, due to the diffuse nature of the 5d orbitals, the properties of Ir(IV) oxides would be metallic as the t_{2g} band would only be partially filled. However, many Ir(IV) oxides are in fact insulators or undergo metal to insulator transitions as described in section 1.1. These properties can be explained by the presence of a special Mott-Hubbard $J_{eff} = 1/2$ ground state that arises from an interplay between crystal field and spin-orbit effects.

As shown in figure 2.5, in the presence of an octahedral crystal field the degenerate states of the free Ir^{4+} ion splits into an e_g and t_{2g} set. As Δ is larger than the coulombic repulsion for 5d TMOs the ground state electronic configuration is $t_{2g}{}^5$. This state has a total spin of $\frac{1}{2}$ and, due to orbital quenching, the total orbital angular momentum associated with t_{2g} set is one. As iridium has a relatively large Z, spin-orbit coupling needs to be considered unlike for an ion of a 3d TMO. For example Sr_2IrO_4 has a H_{SO} of 0.4eV[68] while 3d-ion compounds have a H_{SO} less than 10meV[111]. As section 2.1 states, $J = L + S, L + S - 1....L - S$, which means that for Ir^{4+} the t_{2g} band is split into a $J_{eff} = 1/2$ doublet and a $J_{eff} = 3/2$ quartet band. The $J_{eff} = 3/2$ band is fully occupied while the higher energy $J_{eff} = 1/2$ band is only half filled. With this ground state the system would still be metallic but because this $J_{eff} = 1/2$ band is much narrower than the t_{2g} set was the electronic correlations are stronger so only a relatively small U (U = Mott-Hubbard repulsion) is needed to open a Mott band gap, making some iridates $J_{eff} = 1/2$ Mott-Hubbard insulators[69].This lower Mott-Hubbard band is narrow enough to enhance the electron correlations enough for magnetic ordering to occur. This is the case for Sr_2IrO_4 that has a T_N of 240K resulting from canted antiferromagnet order[27], and Ba_2IrO_4 - a Mott insulating quasi-2D antiferromagnet[99].

For the $J_{eff} = 1/2$ Mott- insulating ground state to be realised in an iridate or any other 5d TMO compound several conditions need to be satisfied. Often the crystal field around the Ir^{4+} ion is not perfectly octahedral and there is a slight tetragonal (or Jahn-Teller) distortion that lifts the degeneracy of the t_{2g} manifold. This adds an extra term to H_{SO} so that it becomes:

$$H_{SO} = \lambda L.S - \Delta_t L_Z^2$$

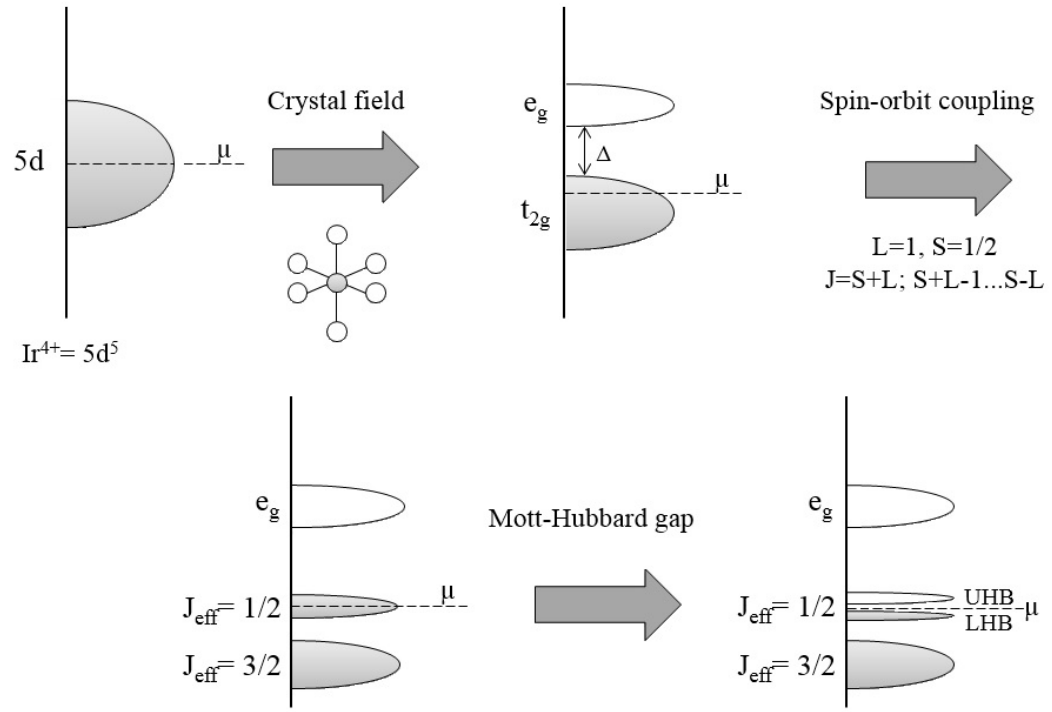

Figure 2.5 *The interplay of crystal field splitting, spin-orbit coupling and columbic repulsion to yield the $J_{eff} = 1/2$ ground state*

where Δ_t is the tetragonal crystal field. For the $J_{eff} = 1/2$ ground state to be realised Δ_t should technically be zero as a tetragonal field will further quench the orbital angular momentum. However, in practice the $J_{eff} = 1/2$ ground state can still be realised as long as Δ_t is much smaller than λ. Another condition is that e_g states must not mix with the ground state wave function. This requires the cubic crystal field, Δ to be much larger than λ. From LDA + SO + U calculations $CaIrO_3$ is thought to not have a pure $J_{eff} = 1/2$ ground state for this reason [128].

The $J_{eff} = 1/2$ ground state may be more stable under a tetragonal distortion than originally thought with x-ray resonant magnetic scattering (XRMS) providing experimental evidence for the robustness of the $J_{eff} = 1/2$ ground state in Ba_2IrO_4 and Sr_2IrO_4 [20]. Several other x-ray techniques such as x-ray absorption spectroscopy (XAS), resonant elastic (REXS) and resonant inelastic (RIXS) x-ray scattering have been used to estimate that Δ is between 2.5 eV and 4 eV for Sr_2IrO_4 and $Sr_3Ir_2O_7$ [90][104] and that λ for Sr_2IrO_4 is 0.4 eV [68], which fulfils the second condition for the existence of a $J_{eff} = 1/2$ ground state.

2.5 Magnetism

In this thesis materials with a plethora of different ground states that exhibited different magnetic properties were synthesised. The main magnetic phenomena pertaining to the materials studied are described in the following section as well as the magnetic interactions which facilitate long-range magnetic order.

2.5.1 Magnetism in insulators

Diamagnetic and Paramagnetic Behaviour

All ions that possess unpaired electrons and hence a non-zero spin quantum number exhibit paramagnetic behaviour whilst ions with a spin quantum number of zero are diamagnetic. Paramagnetic behaviour is restricted to transition metal and lanthanide ions with unpaired d and f electrons as s and p block ions such as Li^+ (s^0) and Sb^{5+} (d^0) possess no unpaired electrons. Simple paramagnetic behaviour occurs when the magnetic moments of the ions in a material are independent and non-interacting. The observed molar magnetic susceptibility, χ_m, is dependent on the competing interactions between the alignment of the spins with an external magnetic field and the randomisation of the spins due to thermal energy. In cases where the molar magnetic susceptibility, χ_m, is much less than 1, as is the case for all diamagnetic and paramagnetic materials, the molar magnetic susceptibility can be defined as:

$$\chi_m = \frac{M_m}{H} \tag{2.3}$$

where M_m is the molar magnetisation (emu mol^{-1}) and H is the applied magnetic field (Oe). This equation also holds true for other magnetic materials when the applied field is small. In the simplest examples of paramagnetic behaviour the molar magnetic susceptibility is inversely proportional to the temperature and can be described by the Curie law:

$$\chi_m = \frac{C}{T} \tag{2.4}$$

where C is the Curie constant of the substance in question. The Curie constant

can be related to the effective magnetic moment, μ_{eff}, of the metal cations present in the sample by:

$$C = \frac{N_A \mu_B^2 \mu_0}{3k_B} \left(\frac{\mu_{eff}}{\mu_B} \right)^2 \tag{2.5}$$

where N_A is Avogadros number, k_B is the Boltzmann constant, μ_0 is the vacuum permeability and μ_B is a Bohr magneton. For general purposes of this thesis, this relation can be approximated to:

$$C = \frac{1}{8}\mu_{eff}^2 (\text{cm}^3 \text{ K mol}^{-1}) \tag{2.6}$$

Theoretically for a paramagnet, a plot of χ_m against T^{-1} should give a straight line that passes through the origin, however, in reality a substance is not magnetically dilute enough for the cations to be completely localised and non-interacting so there is a deviation from this linear relationship. Onnes and Perrier[15] showed that a more accurate relationship for most paramagnets, later theoretically justified by Weiss, is:

$$\chi_m = \frac{C}{T - \theta} \tag{2.7}$$

where θ is the Weiss constant, which can either be positive or negative depending on the nature of the interactions between the cations. A positive Weiss constant indicates ferromagnetic or ferrimagnetic behaviour whilst a negative Weiss constant indicates that there is antiferromagnetic coupling between the cations. Paramagnetic substances are composed of paramagnetic centres mixed with diamagnetic groups. Even a monatomic paramagnetic ion has an underlying diamagnetism, thus, when calculating the molar magnetisation of a sample a diamagnetic correction factor, otherwise known as Pascal's constants, needs to be taken into account for each ion present. The diamagnetic correction factors are cumulative so that the molar susceptibility is given by:

$$\chi_m = \chi_T - \sum \chi_D \tag{2.8}$$

where χ_T is the total molar magnetisation and χ_D is the molar diamagnetic susceptibility or diamagnetic correction factor of each ion. The diamagnetic

correction factors of each ion used in the magnetic calculations in this thesis are listed in appendix G.

Antiferromagnetic Behaviour

In cases where ions have a non-zero spin quantum number, a long-range anti-parallel alignment of the spins can occur below a specific temperature, known as the Néel temperature, T_{N}. The case where there is a long-range parallel alignment of spins is known as ferromagnetic order. This anti-parallel alignment of spins can also be viewed as the anti-parallel alignment of two interpenetrating ferromagnetic sub-lattices and results in there being no net magnetisation. In some compounds the moments of the two interpenetrating sub-lattices are not equivalent, which results in a net magnetisation. This type of long-range magnetic order is known as ferrimagnetism. At temperatures above the Néel temperature the thermal energy is enough to overcome the interatomic spin-coupling that produces the antiferromagnetic state, causing the metal-oxide to behave as a paramagnet. From this paramagnetic region approximate magnetic moments can be calculated from the Curie-Weiss law.

There are multiple types of long-range antiferromagnetic order, the three most common for perovskite and simple cubic lattices, type A, C and G, are shown in figure 2.6. These models can also be used to describe the type of magnetic order within the perovskite layers of a Ruddlesden-Popper compound (general formula of $(\mathrm{AO})_{(\mathrm{n})}(\mathrm{AMO_3})_{\mathrm{n}}$) when n$>$ 1. Type G order occurs when superexchange causes all nearest neighbours interactions to be antiferromagnetic and can be found in a wide range of transition metal oxides including $Sr_3Ir_2O_7$[18]. $LaMnO_3$ exhibits A-type antiferromagnetic order, which is a result of orbital order from the Jahn-Teller distortion of the Mn^{3+} ions[94]. C-type antiferromagnetic order also arises as a consequence of orbital ordering, as seen in $La_{2-2x}Sr_{1+2x}Mn_2O_7$ for $0.74<x<0.90$ [80].

Magnetic Superexchange

Superexchange is the mechanism by which electrons are correlated between two atoms with a shared anion and is facilitated by a combination of the coulomb interaction and the Pauli principle. The Goodenough-Kanamori rule governs the nature of the superexchange interaction between the two ions. This states that

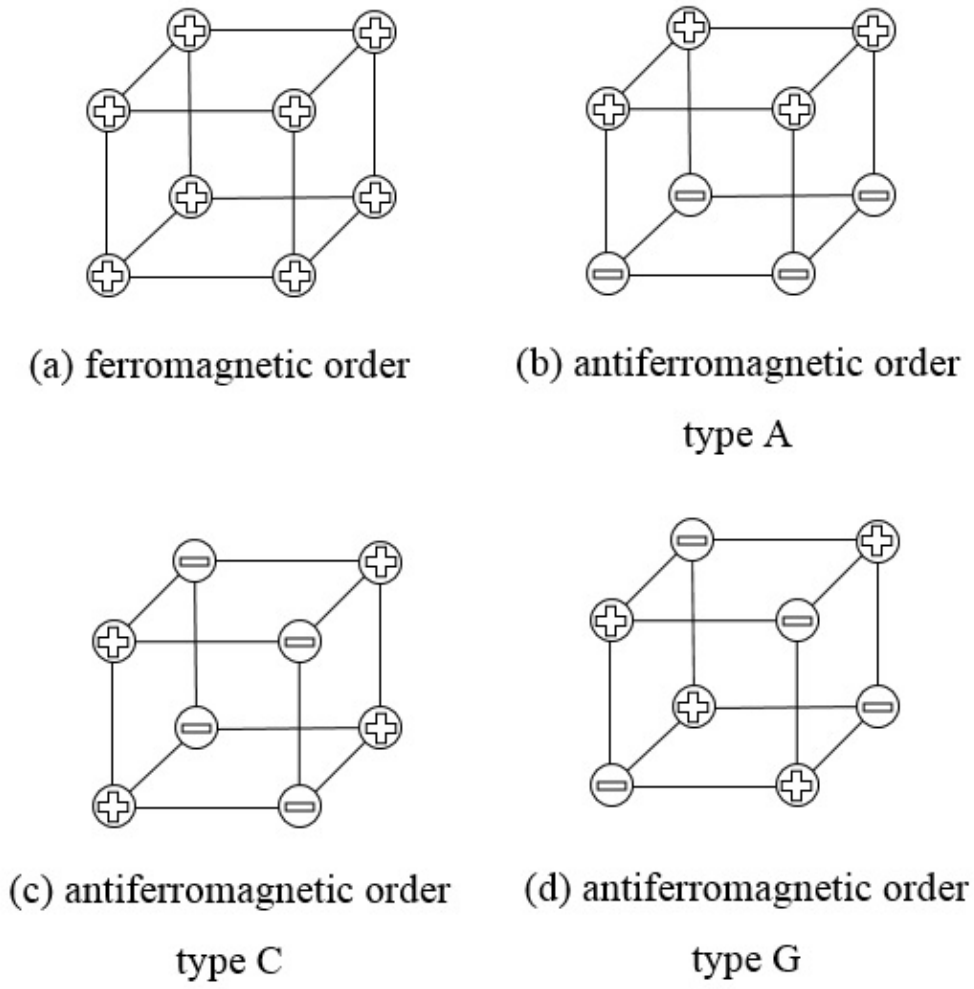

Figure 2.6 *The four most common types of magnetic order found on a simple cubic lattice. + and - denotes the two possible spin states*

when the overlapping orbitals are both half-filled the superexchange interaction is antiferromagnetic. In the case where the overlapping orbitals consist of one half-filled orbital and one empty orbital or one half-filled and one full orbital then the superexchange interaction is ferromagnetic. In a 180° cation-anion-cation bridge with a p-orbital shared between the two cations where both cation d-orbitals are half-filled, such as shown in figure 2.7, the resulting superexchange interaction is antiferromagnetic. The strontium iridate compounds studied in this thesis have a Ir-O-Ir bond angle close to 180° so the superexchange mechanism described is dominant in facilitating the observed long-range antiferromagnetic order.

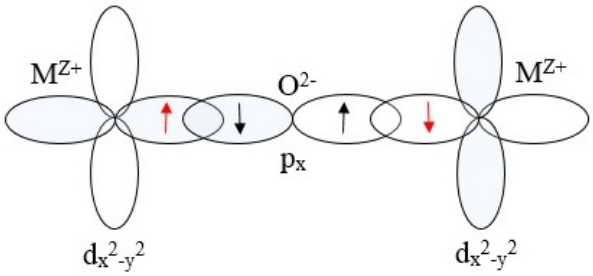

Figure 2.7 *Superexchange through a 180° M-O-M bond angle resulting in antiferromagnetic order*

2.5.2 Magnetism in metals

Metals can exhibit a range of magnetic phenomena such as the Kondo effect, itinerant ferromagnetism, ferromagnetic and antiferromagnetic order; however these are not the focus of this thesis. Instead the magnetic behaviour more commonly found in metallic transition metal oxides, namely Pauli paramagnetism and Landau diamagnetism, will be discussed.

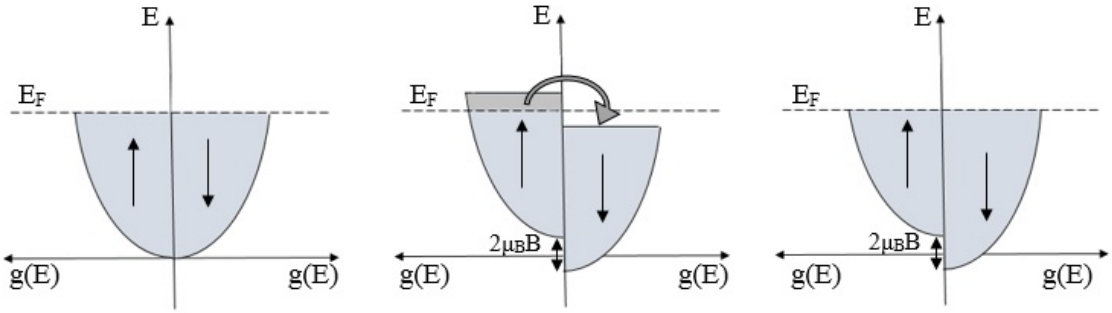

Figure 2.8 *The splitting of the density of states of a free electron gas in a field, B*

In the free electron gas model of a 3D metal at T=0, electrons fill k states up to the Fermi energy, E_F. As the temperature is increased some electrons below the fermi level populate k states above the fermi level, which facilitates electron conduction. In accordance with Hund's rules and the Pauli exclusion principle, each k-state can be doubly occupied with electrons of opposite spin states. When a magnetic field is applied the energy of each spin state is raised or lowered depending on the orientation of the magnetic field with respect to the spin state resulting in a split in the density of states as shown in figure 2.8. This gives rise to the electron gas having a paramagnetic response, which is known as Pauli paramagnetism or χ_{P}. χ_{P} is given by:

$$\chi_P = \frac{n\mu_0\mu_B^2}{2E_F} \tag{2.9}$$

where n is the number of electrons per unit volume. This means that, unlike an insulator, the paramagnetic response of a metal is temperature independent and, as only the electrons close to the fermi surface are involved, quite small. A temperature dependent correction resulting from the thermal population of states above the fermi level can be applied to the above equation, but it only has a very small effect on χ_{P} as $k_{\mathrm{B}}T \ll E_F$.

Pauli-paramagnetism arises from the spin of the electrons. Landau diamagnetism arises from the orbital contribution of the electrons. In a free electron gas Landau diamagnetism is three times smaller than the Pauli paramagnetism so naively, all metals would be expected to be paramagnetic. However, once band structure effects are taken into consideration, a metal can be diamagnetic if the electron has a small effective band mass, m^* in comparison to the classical mass of an electron, m_e, as demonstrated by the following equation:

$$\chi = \chi_P \left[1 - \frac{1}{3}\left(\frac{m_e}{m^*}\right)^2\right] \tag{2.10}$$

where χ is the total susceptibility of the metal. From equation 2.10, a metal will be diamagnetic if $\frac{m_e}{m^*} < \sqrt{3}$. Naturally, there is also a small additional diamagnetic contribution from the electrons in the core s and p orbitals.

2.6 Crystallography

In order to understand the physics of a material it is crucial to accurately determine its crystal structure as it defines the crystal field, interatomic distances and nearest-neighbour interactions. With the exception of quasicrystals, a crystal is an ordered periodic array of atoms that can be described as a single repeating motif or unit cell translated in three dimensions. The unit cell is a fixed volume containing one or more atoms and is bound by the unit cell vectors $\bar{a}$, $\bar{b}$ and $\bar{c}$ with angles between the vectors of α, β and γ. There are seven parallelepiped geometries that a unit cell can adopt and these are known as crystal systems. These 7 lattice systems can be combined with 4 different types of lattice centerings, primitive (P), body centered (I), face-centered (F) and base centered (A, B or C), to obtain 14 crystallographically distinct Bravais lattices that still retain the symmetry of the crystal system. In a primitive cell there are lattice points only on the corners of the unit cell, with the other centerings having additional lattice points either at the centre of the cell (I) on the centre of each face of the cell (F) or at the centre of just one pair of faces (A,B or C depending on the pair of faces).

The position of an atom in the unit cell can be described by a coordinates made up of a fraction of each of the unit cell vectors. For example an atom located in the centre of the unit cell can be described by atomic coordinates of ($0.5\bar{a}$ $0.5\bar{b}$ $0.5\bar{c}$). The atoms in a unit cell can often be related to each other by a set of symmetry operators, the combination of which is described by the space group of the unit cell. This means that only one atomic position, or generating coordinate, needs to be defined in a unit cell for multiple symmetry equivalent atoms to be generated. The number of atoms generated per atomic coordinate is given by the Wyckoff symbol of a site. For example if an atom is on a site described by the Wyckoff symbol $16n$, 16 symmetrically equivalent atoms will be generated in the unit cell. The space group of a unit cell is described in 4 (sometimes 5) parts. The first letter describes the type of lattice centering and can be P, I, F, A, B or C. The next three terms are a combination of symmetry operators. A fifth term occasionally arises to distinguish between two different origin choices for a unit cell. The main symmetry operators possible in a unit cell are 2,3,4 or 6 fold rotational axes, mirror planes (denoted m in the space group), glide planes along a particular axis (a, b or c) or a combination of axes (denoted as d or n), screw axes (a combined rotation plus a reflection) and rotoinversion axes (e.g $\bar{3}$). For

example the space group $I4/mmm$, which is used in this thesis, means that the unit cell of the crystal is body centered and has four-fold rotational symmetry about the a axis. There is also a mirror plane perpendicular to the four-fold rotation axis, and two other mirror planes perpendicular to the b axis and the c axis. More information about each of the symmetry operations and the symbols associated with them plus information about all of the 230 possible space groups are given in the International Tables of Crystallography[43].

Atom	Wyckoff Symbol	x	y	z	B	Occupancy
Ir(1)	4e	0	0	0.09743(3)	0	1
Sr(1)	2b	0.5	0.5	0	0	1
Sr(2)	4e	0.5	0.5	0.1872(1)	0	1
O(1)	4a	0	0	0	1.4(2)	1
O(2)	2e	0	0	0.1939(4)	0.5(1)	1
O(3)	16n	0.1043(19)	0.5	0.0960(3)	0.8(1)	0.5

Table 2.1 *The unit cell of $Sr_3Ir_2O_7$ for the I4/mmm space group model*

Table 2.1 gives the unit cell of $Sr_3Ir_2O_7$ for $I4/mmm$ space group model proposed by Subramanian et al [129]. From the table it can be seen that only 4 generating coordinates are required to generate all of the atoms in the unit cell. From the Wyckoff symbols provided next to each generating coordinate and the fractional occupancy of atoms on each site it can be easily calculated that there are six strontium atoms, four iridium atoms and fourteen oxygen atoms in one unit cell and thus a total of two formula units, Z, per unit cell.

The atoms within a unit cell form planes and the number of times that a plane intercepts the a, b and c unit cell axes are described by respective h, k and l values known as Miller indices. As outlined in section 2.7, x-rays and neutrons can diffract off these planes of atoms to give a set of Bragg reflections the positions of which depend on the interplanar spacing. This interplanar or d-spacing is related to the lattice parameters of the unit cell and the h, k and l values associated with the plane of atoms. As the unit cell parameters of a cell are constant for a given sample, each Bragg reflection can be associated with a particular value of h, k and l.

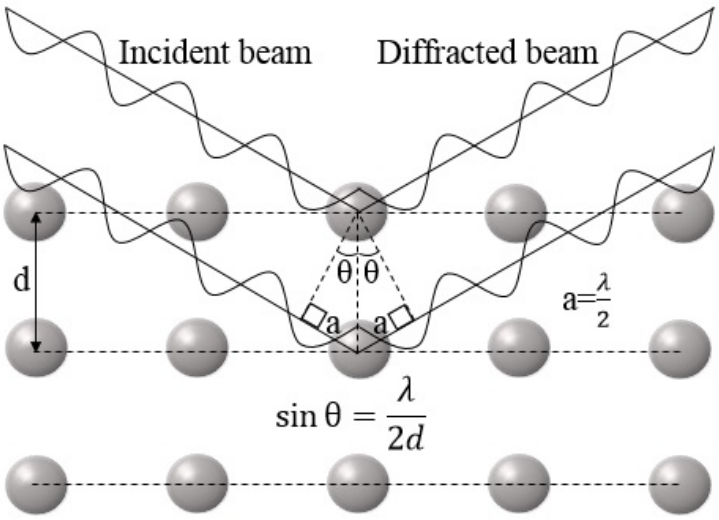

Figure 2.9 *The derivation of Bragg's law from considering the geometry of an x-ray or neutron beam diffracted by a plane of atoms.*

2.7 X-ray diffraction

As explained in section 2.6 a crystal is made up of a periodic array of unit cells. This regular array of atoms can interfere with a wavefront in a similar way to Young's double split experiment - the wavefront is scattered constructively and destructively by the atoms to produce a characteristic diffraction pattern for a particular material. For constructive interference to occur the path difference between the waves diffracted by two planes of atoms needs to be equal to the wavelength, as shown in figure 2.9. From this condition Bragg's law is derived, which is given by equation 2.11

$$n\lambda = 2dsin\theta \tag{2.11}$$

where d is the distance between two planes of atoms. If the wavelength is known and kept constant and the angle between the incident and scattered beam, 2θ, is varied the interplanar d-spacings can be calculated from the limited number of reflections that obey Bragg's law. The interplanar spacing is related to the dimensions, or lattice parameters, of the unit cell. This relation varies depending upon the Bravais lattice type of the unit cell. For example the relationship between the lattice parameters and the d-spacing of an orthorhombic unit cell is

given by equation 2.12 while for a hexagonal unit cell it is given by equation 2.13.

$$\frac{1}{d^2} = \frac{h^2}{a^2} + \frac{k^2}{b^2} + \frac{l^2}{c^2} \tag{2.12}$$

$$\frac{1}{d^2} = \frac{4}{3}\frac{h^2 + hk + k^2}{a^2} + \frac{l^2}{c^2} \tag{2.13}$$

The h, k and l values of a plane are known as Miller indices. A crystal structure has a symmetry that is described by a space group (see section 2.6) and this space group imposes a set of conditions upon the allowed integer values of h, k and l. For example a cubic face centred unit cell has the conditions that h, k and l must either be all odd or all even for the diffracted intensity to be non-zero. Reflections that are not allowed by the symmetry conditions of a specific space group are known as systematic absences. Thus from the angular dependence of the reflections the space group and lattice parameters of a unit cell can be calculated.

The incident wave can be either x-ray or neutron radiation. The x-rays are diffracted by the electrons while the neutrons are diffracted by the nuclei of the atoms. The intensity of the Bragg reflection is proportional to the square of the structure factor, which is calculated from the positions, x_n, y_n and z_n, of all n atoms in the unit cell and is given by equation 2.14.

$$F_{hkl} = \sum_{1}^{N} a f_n exp(2\pi i(hx_n + ky_n + lz_n)) exp(-\frac{B_{iso} sin^2\theta}{\lambda^2}) \tag{2.14}$$

$$\text{where } U_{iso} = \frac{B_{iso}}{8\pi^2} \tag{2.15}$$

where N is the number of atoms in the unit cell, a is a factor to account for the fractional occupancy of a particular site and U_{iso} and B_{iso} are isotropic atomic displacement parameters, which are dependent on the thermal energy available. The f_n term accounts for a variety of atomic scattering factors including the form factor, $f(H)$, which for a spherically symmetric distribution of electrons of distance r from the nucleus is given by equation 2.16.

$$f(H) = 4\pi \int r^2 \rho(r) \left(\frac{\sin Hr}{Hr}\right) dr \tag{2.16}$$

$$\text{where } H = \frac{2sin\theta}{\lambda} \tag{2.17}$$

where ρ(r) is the charge of the electron density. The form factor arises from the fact that the distance between electrons is similar to the wavelength of the x-rays and so the scattering power of an atom is dependent on the scattering angle. It has been tabulated as a function of $\frac{sin\theta}{\lambda}$ in the *International Tables for Crystallography* for most atoms and ions. As shown in figure 2.10 the form factor is dependent on its atomic mass and rapidly falls off as theta is increased. This means that the scattering power of an atom is also related to its number of electrons so low Z atoms such as oxygen and lithium have much smaller scattering powers than high Z atoms auch as platinum and iridium.

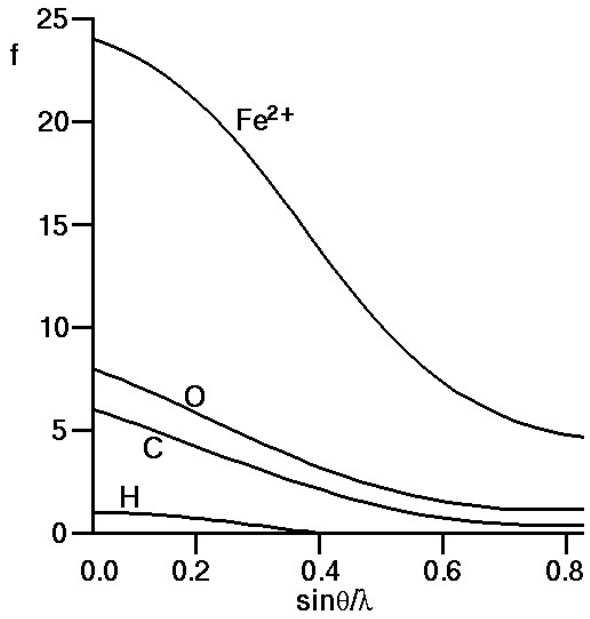

Figure 2.10 *The form factors of several common ions as a function of* $\frac{sin\theta}{\lambda}$ *[6].*

As well as the form factor f_n consists of a multiplicity factor, corrections for preferred orientation and the Lorentz-Polarization factor (LP). The multiplicity factor corrects for a fact that in a powder sample, in which the Bragg reflections are condensed down to two dimensions, different miller indices can give the same d spacing and hence value of theta. For example in a cubic lattice the (1-1 0), (1 0 -1), (0 1 -1), (0 -1 1), (-1 0 1) and (-1 1 0) reflections would all appear to be equivalent. The preferred orientation correction term is needed when, in a powder sample, the polycrystalline grains are preferentially orientated in one direction (a common problem with platelet shaped polycrystals) causing a particular set of

Bragg reflections to be of a greater intensity than expected if the crystallites were randomly orientated.

The Lorentz-Polarization factor corrects for the fact that more crystallites are orientated in a way that satisfies Bragg's law at low angles, that more diffracted electrons intersect the detector at low angles and that x-rays have an electric field vector the angle of which will vary with respect to the scattered beam. The LP factor is given by equation 2.18

$$I \propto \frac{1 + cos^2 2\theta}{8 sin^2 \theta cos\theta} \tag{2.18}$$

2.8 Neutron diffraction

There are several advantages to using neutron instead of x-ray scattering. Firstly, neutrons have a greater penetration depth in the order of centimetres-decimetres and so can probe the bulk of the sample while x-rays only have a penetration depth in the order of microns-millimetres so only the surface of the sample is measured. Secondly, while the scattering power of an element is proportional to its effective nuclear mass for x-ray diffraction, in neutron scattering the scattering power of an element is dependent on the coherent scattering cross section of an atom. The coherent scattering cross section varies irregularly with atomic number so neutron scattering is more sensitive to lighter elements and isotope distributions than x-ray scattering. For example ^{1}H, ^{2}H and Ir have coherent scattering cross sections of 1.7583barn, 5.592barn and 14.1barn[120] respectively (1 barn $= 1\times10^{-24}$cm^2). Finally neutrons also have a spin and thus an intrinsic magnetic moment that interacts with the electron spins and induced orbital moments. This magnetic neutron scattering can be used to determine the magnetic structure of a compound. The magnetic scattering has a form factor that falls off with angle in the same way as x-ray scattering because the neutrons interact with electrons over distances similar to the neutron wavelength. The form factor of neutrons scattered by atomic nuclei, however, is independent of scattering angle as the interaction between the neutron and the atomic nuclei is much smaller than the neutron's wavelength.

Each element also has an absorption cross section, which affects the number of diffracted neutrons that actually emitted from the sample. Iridium has a very

high absorption cross section of 425barn so larger sample masses of sample are required in neutron scattering experiments to compensate for the large amounts of diffracted neutrons lost due to absorption. For highly absorbing samples, the sample should also be thin to reduce the distance that a scattered neutron has to travel through the sample and thus the probability of the neutron being absorbed.

The structure factor in neutron diffraction is identical to that from x-ray diffraction so the same systematic absences are observed for a sample. The function to determine the intensity of the reflections for time-of-flight powder neutron diffraction (to be discussed more in section 3.2) is different however and is given by equation 2.19, which is from Buras and Gerward[24].

$$I_{hkl} = cI_0(\lambda)\epsilon(\lambda)\lambda^4 V_{\mathrm{S}} A_{hkl}(\lambda) \times E_{hkl}(\lambda) j |F_{hkl}|^2 \frac{cos\theta\Delta\theta}{4V_c^2 sin^2\theta} \tag{2.19}$$

where...
c = normalising constant ($\propto$ counting time)
$I_0(\lambda)$ = incident neutron flux at wavelength λ
$\epsilon(\lambda)$= detector efficiency at wavelength λ
$A_{hkl}(\lambda)$ = attenuation coefficient for reflection hkl
$E_{hkl}(\lambda)$ = extinction coefficient for reflection hkl
V_{S} = sample volume
j = reflection mulitplicity
F_{hkl} = structure factor
2θ = Bragg angle
$\Delta\theta$=angular width of the detector

When magnetic neutron scattering is taken into account the total intensity of a Bragg reflection becomes the sum of the nuclear and magnetic scattering as shown in equation 2.20

$$F^2 = F_{\mathrm{nuc}}^2 + F_{\mathrm{mag}}^2 \tag{2.20}$$

The structure factor for magnetic scattering F_{mag} is dependent on scattering vector, $\mathbf{h}$, the magnitude of the magnetic scattering length, p, the magnetic interaction vector, $\mathbf{q}$ and the position vectors, x_j of all of the magnetic atoms as shown in equation 2.21. p is calculated from the magnitude of the magnetic moment, S, of an atom and the magnetic form factor, f_m (equation 2.22) while

q depends on the magnetic moment and scattering vector of a particular atom (equation 2.23).

$$F_{\text{mag}} = \sum_j p_j exp(2\pi i \mathbf{h}.\mathbf{x_j}) \tag{2.21}$$

$$p = Sf_m \times 0.54 \times 10^{-12} cm \tag{2.22}$$

$$\mathbf{q_j} = \overline{\epsilon}(\epsilon.\bar{\mathbf{K}}_\mathbf{j} - \mathbf{K_j}) \tag{2.23}$$

where $\overline{\epsilon}$ is the unit vector in the direction of the scattering vector, **h** and **K** is the unit vector in the direction of the magnetic moment. Due to chemically and symmetrically equivalent atoms potentially possessing magnetic moments of differing orientation, the nuclear and magnetic unit cells of a crystal can have different dimensions and space groups. In a neutron diffraction experiment magnetic phase transitions can often be identified by the appearance of additional peaks or a change in the intensity of existing peaks below a particular temperature. A classic example of this is MnO, a cubic material that adopts the rock salt structure, that undergoes G-type antiferromagnetic order below 118K[124]. The magnetic phase transition is accompanied by the appearance of additional peaks in the powder neutron diffraction pattern that can be indexed by doubling the magnetic unit cell. From equation 2.23 it is also evident that a component of the magnetic moment of an atom must be perpendicular to the scattering vector for it to make a contribution to the scattered intensity.

2.9 Rietveld Refinement

Structure determination is more facile if a single crystal sample can be produced, as data can then be collected over four angular ranges, φ, κ, ς and 2θ, as opposed to powder diffraction, where only one angular range is measured and the data is projected onto one axis. This results in a superposition of peaks where there are composite peaks consisting of multiple reflections with similar 2θ values. In single crystal diffraction there are no composite peaks as the data is collected over the entire Ewald sphere to cover all three dimensions. This causes problems in powder x-ray diffraction in partitioning the intensity of the composite peak

into that of individual reflections and there are cases where randomly orientated degenerate planes, such as the (1 0 0), (0 1 0) and (0 0 1) planes in a cubic system, are no longer distinguishable whereas these planes are distinguishable in single crystal diffraction. However in cases where single crystals of a sample are unavailable, structural analysis can be conducted on powder diffraction data. Depending on the composition of the sample and whether the sample shows magnetic properties, a combination of x-ray and neutron powder diffraction is useful. Also powder diffraction can be useful to average out sample to sample variation found in single crystal samples. This is useful when following general structural trends such as looking at the evolution of the lattice parameters with varying temperature, pressure or crossing a solid solution.

Rietveld refinement[18] is an invaluable technique for extracting important structural information from powder diffraction data, particularly when there is partial peak overlap, as it apportions the intensity of a composite peak into the contributing Bragg peaks. Normally a computer program is used for such analysis and in this thesis Rietveld refinement was carried out using GSAS, the General Structure Analysis System program suite[19], which models Bragg peaks using a pseudo-Voigt peak shape function[20]; a combination of Lorentzian and Gaussian functions. The background intensity was modelled using a shifted Chebyshev function. In Rietveld analysis the positions of the Bragg reflections are optimised from an initial starting model using a least squares refinement method. This means that if the initial starting model is not close enough to the actual model for the observed and calculated peak positions to be of a fairly closely match, the refinement will not work.[21] During the refinement the lattice parameters, atomic coordinates, isotropic thermal parameters, profile functions (discussed in sections 2.9.1 and 2.9.2) and the fractional occupancies were altered from the initial model and the phase fractions of multi-phased samples were calculated.

The least squares refinement method outlined by Rietveld aims to minimise the quantity, S_y, which is the weighted sum of the squared difference between the observed and calculated diffraction patterns (equation 2.24)

$$S_y = \sum_i w_i (y_i - y_{ci})^2 \tag{2.24}$$

where w_i is a weighting factor equal to $1/y_i$, y_i is the observed intensity at the ith step and y_{ci} is the calculated intensity at the ith step.

On the Rietveld refinements in this thesis a difference curve along the bottom of the refinement shows how good a fit the observed data (marked as crosses) is compared to the calculated data (a line). If the observed and calculated profiles are in good agreement the difference curve should be a relatively flat line. The goodness of fit is also checked using statistical quantities such as the weighted profile parameter, R_{wp} equation (2.25), and the statistically best profile parameter, R_{exp}.

$$R_{\mathrm{wp}} = \left(\frac{\sum_i w_i (y_i - y_{ci})^2}{\sum_i w_i (y_i)^2} \right)^{\frac{1}{2}} \tag{2.25}$$

A perfect fit would have an R_{wp} value equal to zero but in reality a R_{wp} value of less than $\sim$7% equates to a good fit. The same is true for R_{exp}. Another useful statistical parameter is $\chi^2 = R_{\mathrm{wp}}/R_{\mathrm{exp}}$, which approaches unity as the fit improves although note that the R values can be affected by instrument-related parameters.

2.9.1 Refinement of constant wavelength x-ray powder diffraction data

A refinement aims to optimise the least squares fit of a model to the observed data over a set number of cycles. It is possible to end up in a false minimum in the value of χ^2 during a refinement, particularly if all the parameters are refined simultaneously as certain parameters such as fractional occupancies and thermal displacement parameters are strongly correlated with each other, so parameters should be tuned slowly with the parameters furthest away from their true values being refined first. The optimum order of refinement regardless of whether the data has been collected by constant wavelength (CW) or time-of-flight(TOF) powder x-ray or neutron diffraction are as follows:

- Background terms and scale factors
- Unit cell parameters
- Fit 2 theta zero (for neutron/synchrotron CW data only. Refine $shft$ and $trns$ instead for Bragg-Brentano geometry)
- Sample dependent profile parameters (if peak shapes are a poor fit)

- Atomic coordinates
- Displacement parameters and fractional occupancies
- Optimise all refineable profile parameters

In this thesis powder CW and TOF neutron data were collected and refined. This section covers refinements terms specific to CW x-ray data using the refinement program GSAS. The terms associated with TOF powder neutron refinements are covered in section 2.9.2.

The background was fitted using a Chebyshev polynomial with as many terms as needed to ensure a good fit without accidently fitting peaks. Typically 8-15 terms were used. Scale factors are refined when there are multiple histograms contributing to the refinement or multiple phases in one diffraction pattern. From these phase fractions the percentage weight of each phase in a sample can be determined. The unit cell parameters need to be manually refined so that the positions of the model Bragg reflections are close to those of the experimental data before the lattice parameters can be freely refined, otherwise the refinement will diverge later or a false minimum will be found.

The samples were measured using diffractometers aligned in Bragg-Brentano geometry (see section 3.2.5). In Bragg-Brentano geometry samples are ideally placed at the centre of the rotation and all diffraction occurs from the sample surface. However as neither of these is true and this effects the two theta zero point. The sample displacement term ($shft$) corrects for displacement from the centre of rotation and the sample transparency term ($trns$), which is dependent on sample absorption, corrects for diffraction that is not from the surface of the sample. X-ray and neutron CW instruments are highly tolerant to changes on $shft$ and $trns$ so ZERO is refined instead. As ZERO highly correlates with $shft$ and $trns$ it should not be refined for samples in Bragg-Brentano geometry.

Structural parameters

The refinement of the unit cell has already been covered in the previous section. If the starting calibration file for the instrument has profile parameters that reasonably model the peak width and shape of the Bragg reflections then the other structural parameters can be refined. If the fit is poor then the sample dependent terms of the profile parameters should be refined first otherwise the

structural parameters will converge on a false minimum. As x-ray rays are scattered more strongly by atoms with a high atomic number, the position of heavy atoms contribute more to the intensity of a Bragg reflection and should be refined first. Once refined it is sometimes possible to refine the position of lighter atoms such as oxygen, the position of which makes little difference to the least squares fit, by fixing the position of heavier atoms. However, neutron diffraction is often needed to accurately refine the atomic positions of lighter atoms.

Displacement parameters and fractional occupancies are strongly correlated to each other so should not be refined simultaneously. Restraints should be used to link the displacement parameters of light atoms and atoms sharing the same atomic coordinates. Once the displacement parameters are close to their true minimum, some of the restraints can be relaxed. The fractional occupancies of atoms sharing and/or split across different atomic sites need to be restrained so that the correct stoichiometry is maintained across all sites during a refinement. For example, if there are two sites of the same multiplicity labelled A and B that contain atom type A and B respectively, if x amount of atom A mixes onto site B, x amount of atom B needs to mix onto site A for a 1:1 ratio of atom types A and B to be maintained. As with refining the atomic coordinates, the displacement parameters and fractional coordinates of the heaviest atoms should be refined first.

Profile parameters

While the intensity of a peak is dependent only on structural parameters, the profile (or shape) of the peak is dependent on instrumental parameters and sample dependent parameters. These include the resolution of the instrument, low angle asymmetry (or axial divergence), sample placement and transparency, crystallite and strain broadening, stacking faults, compostional inhomogeneity and modulated structures. These contributions normally can be described by either Gaussian or Lorentzian function, the combination of the weighted sum of these can be described by a pseudo-Voigt function. The Gaussian part of the pseudo Voigt function is given by equation 2.26. U, V and W are Cagliotto terms that are denoted in GSAS as GU, GV and GW. They are derived from the instrument response function for CW neutron diffraction and are incomplete for CW x-ray diffraction and so can be refined. P is the contribution of crystallite broadening and is denoted GP in GSAS. Due to high correlations between terms,

it is recommended that GP is fixed at zero if GU, GV and GW are refined or if GP is allowed to refine the Cagliotti terms should be fixed at instrumental values.

$$\Gamma_g^2 = U\tan^2\Theta + V\tan\Theta + W + \frac{P}{\cos^2\Theta} \tag{2.26}$$

$$\gamma = \frac{X}{\cos^2\Theta} + Y\tan\Theta \tag{2.27}$$

The Lorentzian part of the pseudo-Voigt function is described by equation 2.27. Both X and Y are sample dependent terms and cover crystallite broadening and strain broadening respectively. In GSAS these terms are denoted LX and LY and should both be refined. There are 4 different profile types in GSAS of which type 2 - the standard pseudo-Voigt function was used in this thesis. In profile type 2 there are several additional profile parameters that can be refined. Firstly there is a parameter denoted as asym, which treats low angle peak asymmetry, although this correction is only applicable if the assymetry is small and the data has not been collected to very low angles. For refinements involving data collected to very low angles profile types 3 and 4 are more suited. As mentioned earlier there are also $trns$ and $shft$ terms for accounting for sample misalignment and transparency. Finally there are terms to account for anisotropic broadening. stec corrects for anisotropic strain broadening, ptec corrects for anisotropic crystallite size broadening and sfec corrects for sublattice anisotropic broadening. For samples that show large anisotropic broadening it is better to use profile type 4 that includes additional S_{xxx} profile terms that are dictated by the symmetry of the unit cell. The ratio of the lorentzian to the gaussian components of the pseudo-Voigt function can also be refined using the eta profile term. More information about the different refinement parameters can be found in the GSAS manual [10].

2.9.2 Refinement of time-of-flight neutron powder diffraction data

There were no additional peaks from magnetic neutron scattering in the powder neutron diffraction data collected in this thesis so only the nuclear part of the structure factor needed to be considered. In order to fit the data two sets of information, the diffractometer constants and profile parameters, are

required. The diffractometer constants are needed to convert the d-spacings and consequently the Bragg reflections of the structure into time-of-flight positions. The profile parameters are needed to model the shape and width of the Bragg reflections. Starting values for both sets of these parameters were provided by the beamline scientist of HRPD at ISIS, Dr Kevin Knight, upon which the neutron diffraction data were collected.

Diffractometer constants

As mentioned in earlier the time-of-flight powder neutron data was refined in GSAS. In GSAS there are three diffractometer constants - DIFC, DIFA and ZERO - that relate the time of flight, t, to the d-spacing via equation 2.28

$$t = DIFC\ d + DIFA\ d^2 + ZERO \tag{2.28}$$

Of these three parameters only DIFA, which corrects for peaks shifts due to absorption of neutrons by the sample can be refined and this should only be refined in the later stages of the refinement. ZERO corrects for slight difference in the timing signals between the ISIS accelerator and the instrument data acquisition system. DIFC relates the theoretical time of flight (when DIFA and ZERO are equal to zero) position of a Bragg reflection to its d-spacing by substituting equation 2.29, where L is the flight path (units of m), d is in units of Å and t in μs, into equation 2.28. This is derived from combining Bragg's law with the de Broglie relation (equation 2.30) and substituting Planck's constant, h, and the neutron mass, m, while converting quantities to appropriate units to obtain equation 2.31.

$$DIFC = 505.56 L sin\theta \tag{2.29}$$

$$t = \left(\frac{2m}{h}\right) L sin\theta d \tag{2.30}$$

$$d = \frac{1.977 \times 10^{-3}}{L sin\theta} t \tag{2.31}$$

Profile Parameters

The neutron powder data was refined in GSAS using peak shape function 3, which is a combination of a pseudo-Voight function with two back-to-back exponentials. The exponentials model the nature of neutron production at ISIS where there is a rapid increase in intensity when the proton beam strikes the neutron target followed by a slower drop off in intensity as neutrons emerge from the moderator. The rise and decay coefficients of the two exponential functions are described by the parameters alp, bet-0 and bet-1. These coefficients are instruments specific and should remain fixed during the refinement.

The pseudo-Voigt function models the peak shape and full width half maximum (FWHM) of the Bragg reflection and is a linear combination of Gaussian and Lorentzian functions. The function covers the effects of peak broadening due to sample strain and particle size plus the effects of instrument design and detector geometry on the FWHM. The widths of the Gaussian part, σ, and the Lorentzian part, γ of the pseudo-Voigt function are described by equations 2.32 and 2.33. In GSAS σ_0, σ_1 and σ_2 are referred to as sig-0, sig-1 and sig-2 and γ_0, γ_1 and γ_2 are referred to as gam-0, gam-1 and gam-2. Sig-1 and gam-1 describe the linear relationship between peak width and the d-spacing and sig-2 and gam-2 describe particle size and strain broadening all of which can be refined. However sig-0 and gam-0 cannot be refined.

$$\sigma^2 = \sigma_0^2 + \sigma_1^2 d^2 + \sigma_2^2 d^4 \tag{2.32}$$

$$\gamma = \gamma_0 + \gamma_1 d + \gamma_2 d^2 \tag{2.33}$$

In the case where there is anisotropic strain broadening, which is when different classes of reflections are broadened to differing degrees, a refinement of sig-1, sig-2, gam-1 and gam-2 will fail to provide an adequate fit to the observed reflections. In this case there are extra profile parameters in the Lorentzian component of the pseudo-Voigt function that can be refined. More information about the refinement of TOF powder neutron diffraction data can be found in the data analysis guide for the Polaris instrument at ISIS[5].

2.9.3 Structure solution and refinement via single crystal x-ray diffraction

In this thesis single crystal x-ray diffraction is used to solve the structure of the novel platinate compound, $K_2CaPt_{3-\delta}O_6$, and to refine the oxygen positions in $(Sr_{(1-x)}La_x)_3Ir_2O_7$. Experimental details are discussed in more detail section 3.2.5. In single crystal x-ray diffraction data is collected over four angular ranges to cover φ, κ, ς and 2θ, which produces a map of Bragg reflections over the entire Ewald sphere. In a similar way to powder x-ray diffraction, the positions of the Bragg reflections across the Ewald sphere is determined by the lattice and the intensity of the Bragg reflections is proportional to the square of the structure factor, $F(hkl)$.

The first step in solving the structure of a crystal is determining the lattice parameters of the unit cell. These can be determined by measuring the distance between Bragg reflections in reciprocal space. If the density of the compound is known then the number of formula units per unit cell, Z can be calculated from the volume of the unit cell. Next the crystal system is determined (i.e tetragonal or hexagonal) and the Laue class. Then systematic absences can be used to look for certain symmetry planes within the structure. For example if reflections only appear at $l = 2n$ when looking in the $(h0l)$ plane then there is a glide along c that is perpendicular to the b axis. As well as this, systematic absences give information about the lattice centering, such as whether the lattice is body centred or face-centred.

A single crystal diffraction pattern will always appear to be centrosymmetric as the structure factors at reciprocal space vectors Q and $-Q$ (e.g (001 and 00-1) are complex conjugates so that $F(hkl) = F^*(hkl)$. These opposing reflections are called Friedel pairs and have equal diffraction intensities. In order to differentiate between a centrosymmetric and an acentric space group Wilson statistics can be used as centrosymmetric and acentric crystals give rise to a different distribution of intensities. Wilson statistics make use of the fact that the relative structure factor is related to the motion free structure factor by equation 2.34, where s is a scaling factor between the relative structure factor, $F_{\mathrm{rel}}(hkl)$, and the real structure factor and K is given by equation 2.35. s and B can be determined by plotting ln K against $\sin^2\theta/\lambda^2$ as the resulting straight line will have a gradient of -2B and a y intercept of 2 ln s. This allows the motion free structure factor, $F_{\mathrm{mf}}(hkl)$ to be calculated, which is related to the normalised structure factor,

$E(hkl)$, by equation 2.36. The normalised structure factors have the same phase as the real structure factors. Both centrosymmetric and acentric crystals have an $\langle E^2\rangle$=1 but centrosymmetric crystals have a value of $\langle E\rangle$ of 0.798 and a value of$\langle|E^2\text{-}1|\rangle$ of 0.968. On the other hand acentric crystals have an $\langle E\rangle$ of 0.886 and an $\langle|E^2\text{-}1|\rangle$ of 0.736.

$$F_{\mathrm{rel}}(hkl) = s\ exp(-B\sin^2\theta/\lambda^2)|F_{\mathrm{mf}}(hkl)| \tag{2.34}$$

$$K = \frac{\langle F^2_{\mathrm{rel}}(hkl)\rangle}{\sum_i f_i^2} \tag{2.35}$$

$$|E(hkl)|^2 = \frac{|F_{\mathrm{mf}}(hkl)|^2}{\epsilon\sum_i f_i^2} \tag{2.36}$$

From all this information it may be possible to determine the space group of the crystal structure. In this thesis CrysAlis^{Pro}[12] was used in order to determine the lattice parameters and space group of the crystal and reduce the data ready for refinement in Jana2006[107]. To solve and refine the structure of a crystal the heaviest atom is located first - normally through a Patterson map or charge flipping or the direct method. The structure factor is calculated from the position of the one heavy atom and the position of lighter elements can be assigned from residual electron intensity. This process is repeated until all of the atoms in the unit cell have been identified. Then the thermal parameters are refined, including anisotropic displacement parameters.

During the refinement the position of the atoms and thermal displacement parameters are adjusted so that the structure factor from the model, $F_{\mathrm{calc}}(hkl)$, matches better the observed structure factor, $F_{\mathrm{obs}}(hkl)$. The goodness of fit is assessed by an R_1 factor that is given by equation 2.37 and a weighted R factor, wR_2 (equation 2.38. A good refinement will typically have an R_1 value of less than 5% and a wR_2 value of less than 15%. There should also not be any significant maxima or minima in the residual electron intensity and the standard deviation on each refined value should be small (<0.01 Å for atomic positions).

$$R_1 = \frac{\sum_{hkl}(|F_{\mathrm{obs}}(hkl)| - |F_{\mathrm{calc}}(hkl)|)}{\sum_{hkl}|F_{\mathrm{obs}}(hkl)|} \tag{2.37}$$

$$wR_2 = \frac{\sum_{hkl}(wF_{\mathrm{obs}}(hkl)^2 - F_{\mathrm{calc}}(hkl)^2)^2}{\sum_{hkl}(wF_{\mathrm{obs}}(hkl)^2)^2} \tag{2.38}$$

Chapter 3

Experimental methods

3.1 Methods of single crystal growth

There are a multitude of techniques available for the growth of single crystals and the most suitable is highly dependent on the nature of the compound that needs to be crystallised. If the material melts congruently then it may be possible to produce large crystals (in order of centimetres) via a melt growth technique such as the Czochralski process or the floating zone method. The Czochralski method is often used to obtain single crystals of semiconductors such as silicon and gallium arsenide or metals and metal alloys such as $Co_{1-x}Fe_x$[14] and $Ce_3Pt_{23}Si_{11}$[102]. For non-metallic samples the floating zone method is preferable to the Czochralski process as the crystal growth can be containerless. This avoids introducing contaminants into the crystal from the crucible unlike partially melting or reacting with the sample. Large, very high purity crystals have been made via the floating zone method including Sr_2RuO_4[105] and $Dy_2Ti_2O_7$[115]. In these two cases it was the high purity of the samples that allowed novel phenomena such as unconventional superconductivity[85] and magnetic monopoles to be discovered[93].

It is often the case, particularly with 5d transition metal containing compounds, that crystals cannot be grown by either of the above techniques due to the material melting inhomogeneously (as with $YBa_2Cu_3O_{7-x}$[116]), having too high a melting point, being thermally unstable (decomposing before it melts) or one or more of the constituent elements having low vapour pressures, making it very

difficult to grow stoichiometric crystals due to the high evaporation rate. In some cases the crystal undergoes a phase transition whilst cooling, which can destroy the crystal. In these cases low temperature methods of growing crystals such as hydrothermal synthesis and flux growth need to be utilised or the highly volatile nature of the constituents exploited to grow crystals via vapour transport.

The platinate compounds being studied have relatively low decomposition temperatures of circa 800-950°C, which makes it impossible to grow crystals from their melt and rules out the Czochralski and floating zone techniques. Thus the method of choice is flux growth, which involves mixing the powder of the sample with a flux (or solvent) - a compound possessing a lower melting point and in which the sample will readily dissolve. This effectively lowers the temperature of crystal growth below the decomposition temperature of the target compound and makes it possible to obtain single crystals. The disadvantage of flux growth is that sometimes the flux can become incorporated into the crystal and that the crystal size is normally quite small (a few millimetres at most) but it is preferable to having no crystals of a compound.

A recent review by Daniel Bugaris and Hans Zur Loyle gives a very good overview of flux growth[23] and a text book by Elwell and Scheel[44] gives a more in depth account, however a brief overview of the key factors to take into consideration when attempting to grow single crystals via flux growth is given below.

The type of flux

An ideal flux should most importantly melt at a lower temperature than the target compound and should preferentially be cheap, non-toxic and easily removable after the crystal growth. Commonly used fluxes are NaOH, K_2CO_3 and $BaCl_2$. Careful consideration needs to be taken on whether the flux is likely to react with the dissolved compound to produce an unwanted phase or if the ions of the flux are likely to become incorporated into the crystal structure. The platinate compounds are commonly grown from alkali fluxes such as sodium carbonate and potassium hydroxide as they melt at relatively low temperatures (KOH melts at 406°C) and their alkali nature helps to stabilise the platinate ion rather than the platinum cation[97]. The viscosity of the flux is also important as a too viscous flux will prevent the ions from sufficiently diffusing through the melt to nucleation points but a flux of too low a viscosity will cause spontaneous nucleation with many small crystals rather than a few larger crystals.

The temperature

For crystallisation of the target compound to occur the melt needs to pass through a supersaturation point. This can be achieved in two principle ways. Either the temperature can be slowly lowered, typically between 1 and 10°C per hour, so that crystals precipitate out of the flux as the solubility of the reagent in the flux gradually decreases or the melt can be held at a constant temperature so that the melt becomes supersaturated as the flux evaporates. A temperature range or temperature needs to be found that is below the decomposition temperature or structural phase transition of the target compound, has a relatively slow or minimal rate of flux evaporation, where the flux is initially of a low enough viscosity to solvate the metal oxide (viscosity decreases with increasing temperature) and needs to be such that the supersaturated region is passed through at a sufficiently slow rate for nucleation to occur.

The ratio of solute to flux

The ratio of solute to flux needs to be large enough for the molten solution to become supersaturated but small enough for all of the solute to be solvated by the flux. If the solution is too supersaturated then dendritic crystal growth will occur as the growth rate will be too fast, however, too low a degree of supersaturation will prevent nucleation from occurring. When determining the growth conditions for a particular material it is good to initially use a 10:1 ratio of flux to reagent and to then adjust this ratio depending on the crystal morphology.

3.2 Experimental probes

In order to investigate the ground state of the iridate and platinate compounds synthesised in this thesis a variety of experimental probes were used. This section gives information about how each technique works and how the measurements were conducted.

3.2.1 SQUID magnetometry

A SQUID (Superconducting QUantum Inference Device) is the one of the most sensitive detectors available for measuring the magnetic moment of a sample as it can resolve changes in the magnetic field of 10^{-15}T[35] at varying temperatures, frequencies and fields[63]. By measuring how the magnetic moment of a sample varies as a function of temperature or field magnetic, transitions such as long-range magnetic order or spin-flop transitions can be detected. If the magnetic susceptibility follows Curie-Weiss type behaviour the magnetic moment of an ion can be determined. The magnetic moment gives the magnetisation of a sample, which is a thermodynamic variable that relates to the free energy and hence the ground state of the system. For more information on the different types of magnetism that occur in transition metal oxides, see section 2.5.

The SQUID consists of a superconducting ring separated in half by two insulating Josephson junctions[134] (see figure 3.1). The Cooper pairs in each half of the superconducting ring can be described by a single wave function, which can penetrate into the forbidden region of the Josephson junction. The Josephson junction is narrow enough to allow the wave functions to overlap and transfer Cooper pairs across the barrier via quantum mechanical tunnelling[79], generating a weak superconductor with a measurable critical current. When a magnetic field is applied to the ring, the critical current oscillates between a maximum and a minimum value[35]. In D.C magnetometry the sample interferes with the magnetic field as it passes through the ring, which alters the critical current. The SQUID measures and records the change in the output voltage across the ring, which is directly proportional to the change in the current and is calibrated against a palladium reference, resulting in the very accurate measurement of the magnetic moment of the sample.

D.C measurements were carried out on a Quantum Design MPMS instrument.

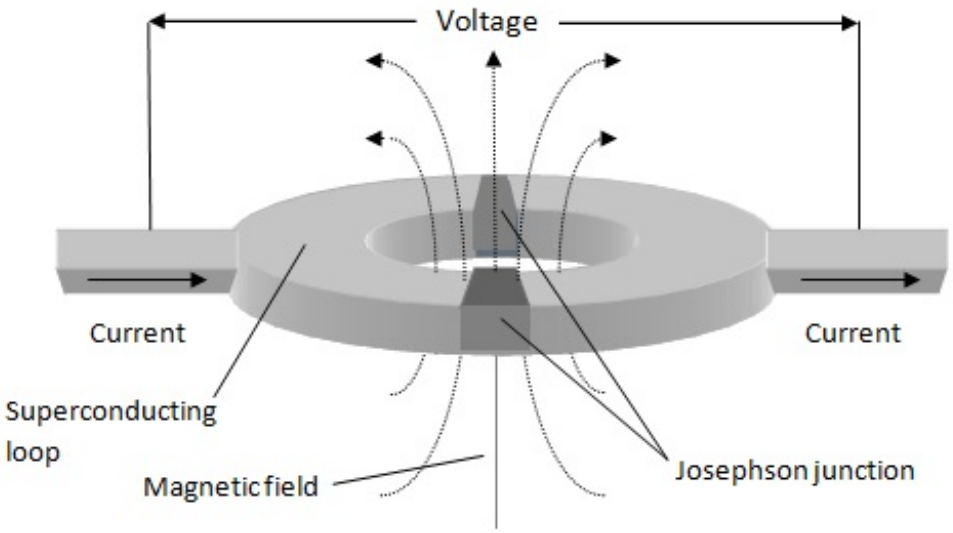

Figure 3.1 *A superconducting ring separated by two Josephson junctions.*

For polycrystalline powder samples about $30 \leq$ mg ≤ 40 of material was accurately weighed and placed in an empty gelatin capsule and sealed in such a way as to restrict the movement of the sample. The filled capsule was inserted into a plastic straw with a small amount of diamagnetic tape between the capsule and the straw to prevent any movement of the capsule. A needle was used to pierce small holes in the straw to allow for free aerodynamic movement. This was essential as before samples entered the SQUID, the airlock and the sample were purged with helium to remove paramagnetic oxygen. The straw was sealed and attached to a metre long stainless steel rod using diamagnetic tape before being purged and lowered into the SQUID. A relatively large field of 10,000Oe was used to centre the sample as the response from the samples used was weak due the the relatively low magnetic moments of iridium and platinum based compounds. A background measurement was conducted on a plastic straw containing an empty capsule to be as identical as possible to the sample straw set-up with data collected over the same temperature range and using the same applied field as the sample. This background measurement was subtracted from the sample data collected.

For single crystals samples, a window was cut out at 8cm from the top of the straw to be at the correct height for centering and then the crystal was attached to the inside of the straw in the area of the window using a small amount of araldite glue. The mass of the crystal was measured beforehand using a balance with an accuracy of $\pm$ 0.05mg. The sample straw was attached to the stainless steel pole, lowered into the SQUID and centred in the same way as the polycrystalline

samples described above. The crystals measured typically had a mass of 1mg, which in a 10,000Oe field gave a measured sample moment of about 2×10^{-5} emu. This is only an order of magnitude greater than the background from the straw and araldite glue so a background measurement was conducted on the same straw after each measurement using a similar amount of araldite glue in the sample position, which was then fitted with a fourth order polynomial and subtracted from the sample moment before the data was analysed.

$$B = \mu_0(H + DM) \tag{3.1}$$

When a sample is magnetised it will generate its own internal magnetic field, known as the demagnetising field, which reduces the magnitude of the applied field acting on the sample. This demagnetising effect is outlined in equation 3.1 where B is the total field, H is the applied field, D is the demagnetisation factor and M is the magnitude of the demagnetising field. The demagnetisation factor is dependent on the shape of the sample. For example the demagnetisation factor is a third for a spherical sample and a half for an infinite rod with the field applied parallel to its axis. For ferromagnets the demagnetising field is large so it is important to select a sample shape and applied field direction that results in a low demagnetisation factor so that the whole applied magnetic field is experienced by the sample. However, for paramagnets where the sample magnetisation is much smaller ($\chi \ll 1$), M is negligible so the sample shape it not such an important consideration and the applied field is roughly equal to the field experienced by the sample.

A SQUID magnetometer gives the magnetic moment of a sample in electromagnetic units (emu). Equation 3.2 is used to convert the magnetic moment of a sample to its molar susceptibility, χ_{m}, which is in units of emu mol^{-1}. In equation 3.2, M is the measured moment of the sample (units of emu), A_r is the molar mass of the sample (units of mol g^{-1}) and m is the mass of the sample (units of g). In this thesis the magnetic susceptibility is occasionally reported per mole of a particular magnetic ion in a sample, in which case the units are emu mol^{-1} per X, where X is the magnetic ion. These are CGS units of the molar susceptibility. To convert χ_{m} into SI units of m^{3}mol^{-1}, the CGS value needs to be multiplied by $4\pi\times10^{-6}$. The CGS unit for the strength of the applied magnetic field is the Oersted (Oe), however, this is commonly reported in the SI units of Tesla (T)

with a conversion factor of 1T=1×10^4Oe.

$$\chi_{\mathrm{m}} = \frac{M}{H}\frac{A_{\mathrm{r}}}{m} \tag{3.2}$$

As mentioned in section 2.5 all ions have an underlying diamagnetic response that arises from the s orbitals, which contributes to the total magnetic susceptibility measured. These were calculated using Pascal's constants and subtracted from the total moment. The values of the Pascal's constants used are given in appendix G.

3.2.2 Electrical resistivity

The resistivity of a sample gives information on states that are close to the chemical potential of the system. On a basic level electrical resistivity measurements can help to identify electronic phase transitions such as a metal-insulator transition or the onset of superconductivity. The low temperature dependence of the resistivity of a metal follows the relationship as given in equation 3.3[126]. At high temperatures the resistivity is linearly proportional to the temperature.

$$\rho = \rho_0 + AT^2 + A'T^5 \tag{3.3}$$

The quadratic temperature dependence is due to electron-electron scattering and the T^5 dependence is due to electron-phonon scattering. The residual resistivity, ρ_0, gives an indication of the purity of a metal and the quadratic constant, A, is proportional to the square of the effective free electron mass, m^*. If the purity of the metal is sufficient a T^2 power law in the resistivity is observed at low temperatures as the electron-electron scattering term dominates. From a knowledge of the effective free electron mass the electron mobility, μ, and the scattering rate of electrons during the scattering process, τ, can be calculated using the Drude equation 3.4.

$$\mu = \frac{e\tau}{m^*} \tag{3.4}$$

For an insulator, the resistivity of a sample as a function of temperature can give

information about the band gap, E_g, of a sample, using the relation given by equation 3.5. From this the easiest way to obtain E_g is to plot $\ln(1/\rho)$ against the 1/T, which should give a straight line with a gradient equal to $-E_g/k_{\mathrm{B}}$.

$$\frac{1}{\rho} = exp\left(\frac{-E_g}{2k_B T}\right) \tag{3.5}$$

Electrical resistivity measurements were conducted on two different pieces of equipment. The majority of the measurements were done on the CCR machine in the Centre for Science at Extreme Conditions (CSEC) in Edinburgh but some measurements, particularly on the lanthanum doped $Sr_3Ir_2O_7$ were conducted using the Quantum Design PPMS in the Materials Characterisation Laboratory at ISIS. In both cases the crystals needed to be suspended on a quartz plate using 100μm thick gold wire goalposts, which also served as current contacts. Two (or four in the case of a 6 point measurement) further gold wires were attached to the crystal to serve as voltage contacts. This 4 or 6 point measurement prevents the contact resistance from being measured. All of the wires were attached to the crystal and to the quartz plate using 6838 silver paint, which needed to be annealed at 450°C for 15 minutes to cure. During annealing some of the silver paint diffuses into the crystal, creating a good contact with minimal contact resistance. An example of crystal prepared for a 6 point measurement is shown in figure 3.2, which was used to measure the homogeneity of La doping across a sample of $Sr_3Ir_2O_7$. The quartz plate is then stuck to a puck using double sided tape. The puck used for the PPMS is shown in figure 3.3. Copper wires with an insulating coating to help prevent short circuiting were used to attach the current and voltage contacts on the puck to the current and voltage contacts on the quartz plate. The ends of the wires were tempered first using an acidic gel to reduce the contact resistance.

A.C. resistivity data was collected on the CCR in CSEC at the University of Edinburgh. A.C. resistivity is preferable to D.C. resistivity as data is measured at a selected frequency, which substantially reduces the noise. It is a more sensitive resistivity probe ideally to be used on samples such as metals with a low impedance with $R < 100\Omega$. The voltage was measured using a Stanford SR830 Lock in Amplifier (LIA) and a frequency of 85Hz was selected for all measurements. The voltage is measured as two components - in phase and out of phase. The in-phase component corresponds to the sample voltage and is used to calculate the sample resistivity while the out of phase component is used

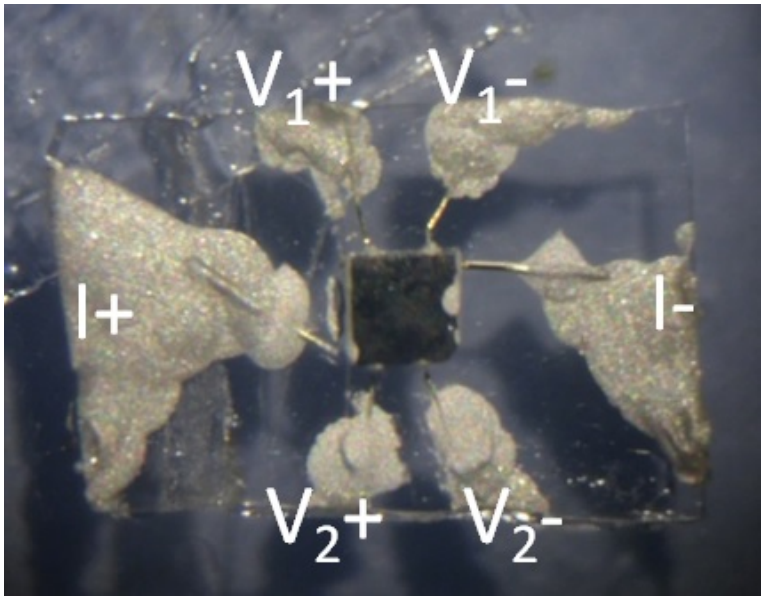

Figure 3.2 *The configuration of the contacts on a sample of La doped $Sr_3Ir_3O_7$ for a 6 point resistivity measurement.*

Figure 3.3 *The puck used to conduct resistivity measurements on a ppms. [4]*

for diagnostic purposes. A large out of phase component implies that there is capacitance or inductance in the circuit, which is likely to be caused by a bad contact. Thus samples were only measured if the out-of plane component was less than 5% of the in-plane component. Although the change in voltage of the sample was measured on the PPMS the LabVIEW based software on the instrument automatically converted the voltage to Ohms so the separate x and y components were not recorded. The LIA displays two temperature values - A and B. Temperature A is the temperature at the base of the CCR and is normally cooler than temperature B, which is from the thermometer on the probe that the sample is on. As temperature B is closer to the sample these readings are taken to be the temperature of the sample. The slow cooling rate of 0.5K/min that was used means that the actual temperature of the sample should be very close to the temperature reading of thermometer B.

The voltage is converted into electrical resistivity according equation 3.6, where V is the voltage measured between 2 points, A is the cross-sectional area of the sample, I is the applied current and L is the length between the voltage contacts (see figure 3.4). This normalises the data to take the differing sizes of the sample into account. However, it does assume that the crystals are rectangular prismatic in shape, which introduces an absolute error for each reading. As this measurement error will vary randomly from crystal to crystal the relative error when comparing samples will be much smaller.

$$\rho = \frac{V \times A}{I \times L} \tag{3.6}$$

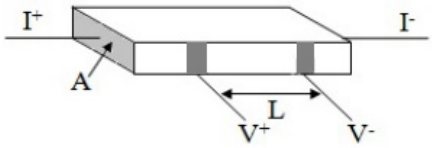

Figure 3.4 *Sample dimensions used to calculate the resistivity*

3.2.3 Heat Capacity

The molar heat capacity of a material is thermal energy required to raise its temperature by 1K per mole of material, however the heat capacity of a material is not constant and is temperature dependent. By keeping the pressure or

volume of the sample constant, this bulk measurement can locate the exact temperature at which first or second order transitions occur by monitoring the temperature dependence of the heat capacity. For metals the low temperature heat capacity follows equation 3.7[126] where the second term is the phonon (or Debye) component and the first term is C_{el}, or the electronic heat capacity.

$$C_{\mathrm{P}} = \gamma T + \alpha T^3 \tag{3.7}$$

With decreasing temperature the phonon or lattice component to the heat capacity approaches zero and the electronic contribution to the heat capacity becomes more significant, allowing the separation of the electronic contribution to the heat capacity from the lattice component of the heat capacity. The linear electronic specific heat coefficient, γ, can be extracted from the electronic heat capacity which, is proportional to the density of states at the Fermi energy and when combined with magnetisation or electrical resistivity data, gives the Wilson ratio (equation 3.8) and Kadowaki - Woods relation (equation 3.9) for the material.

$$R_{\mathrm{W}} = \frac{B\chi}{\gamma} \; (B = \frac{4\pi^2 \; k_{\mathrm{B}}^2}{3(g\mu_{\mathrm{B}})^2}) \tag{3.8}$$

$$R_{\mathrm{KW}} = \frac{A}{\gamma^2} \tag{3.9}$$

The Wilson ratio R_{W} is unity for a non-interacting gas of fermions and scales to two according to the number of impurities in the metal. For a heavy fermion metal both the specific heat and the susceptibility are enhanced by the same amount so the ratio is close to unity. Transition metal compounds tend to have a $\mathrm{R_{KW}}$ value of about 0.4 $\mu\Omega\mathrm{cmmol^2K^2J^{-2}}$ while heavy fermion systems $\mathrm{R_{KW}}$ is roughly 10 $\mu\Omega\mathrm{cmmol^2K^2J^{-2}}$[62].

A schematic of the calorimeter puck used for heat capacity measurements is shown in figure 3.5. It contains a resistive platform heater that is used to heat the sample, a platform thermometer to measure the sample temperature and a puck thermometer to monitor the temperature of the puck, which acts as a thermal bath to the calorimeter. The key feature is that the platform is suspended in the middle of the puck frame by eight thermally conducting wires, which electrically connect the sample thermometer and the resistive sample heater to the rest of

the puck and also thermally connect the platform to the puck frame.

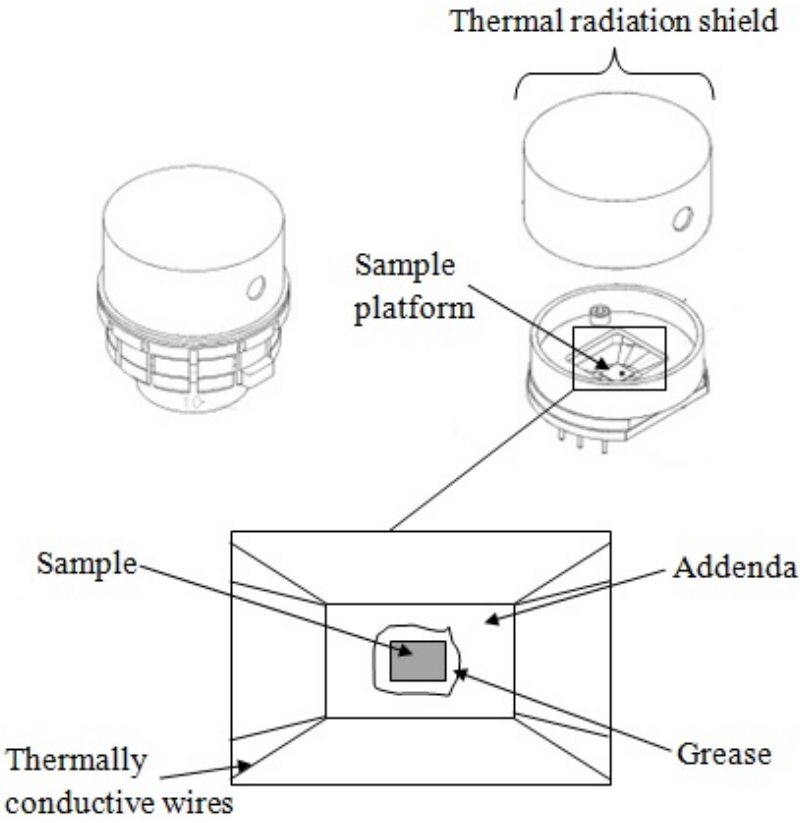

Figure 3.5 *A schematic of the PPMS puck used for heat capacity measurements modified from the Quantum Design Heat Capacity Option User's Manual[38].*

In order to conduct a heat capacity measurement a small amount of N or H type grease should be added to the platform using the sample mounting state, which uses a small vacuum to hold the sample platform in place and thus prevent damage to the thermally conductive wires. it is good experimental practice to clean the addenda with toluene beforehand and using a small amount of grease limits the value of tau2. The N type grease is best suited to heat capacity measurements below 200 K but it can be used up to 300 K. At higher temperatures N type grease melts so H type grease should be used instead as it has a temperature range from 200 to 400 K. A background heat capacity or addenda measurement must be performed on the small amount of grease over the temperature range and at the field that will be used to perform the sample heat capacity measurement. After the addenda measurement has been conducted a sample is added to the platform using the same mounting stage, the mass of which has been measured to ± 0.05 mg using the weighing balance. A flat side of the sample is placed on the grease to provide good surface and thermal contact between the sample and

the platform. The outputted data includes a sample coupling percentage, which gives a guide to the quality and reliability of the data. If the sample coupling is below 80% the data obtained is unreliable.

The PPMS measures the heat capacity at a constant pressure, which is at a high vacuum of less than 10^{-6} mbar. Activated charcoal is installed above the puck to soak up excess Helium atoms in the atmosphere. The resistive platform heater transfers a known amount of heat to the sample for a fixed duration of time, which is followed by a cooling period for the same amount of time. This fixed amount of cooling time, or relaxation time, is known as the time constant, tau. Insulating samples have a low thermal conductivity and so should be thin to avoid a temperature gradient in the sample. Powder samples were pressed into a pellet under a pressure of 3 GPa to increase the density and hence thermal conductivity of the sample. The trace of the variation of the temperature during the relaxation time is fitted using the two tau model, which simulates both the effect of heat flowing between the sample platform and the sample (equation 3.10) and the effect of heat flowing between the sample platform and the puck (equation 3.11). In these equations $P(\mathrm{t})$ is the power applied by the heater, K_{w} is the thermal conductance of the wires, K_{g} is the thermal conductance of the grease, $T_{\mathrm{s}}(\mathrm{t})$ and $T_{\mathrm{p}}(\mathrm{t})$ are the temperatures of the platform and the sample, T_{b} is the temperature of the thermal bath (or puck frame) and C_{pl} and C_{s} are the heat capacities of the platform and the sample.

$$C_{\mathrm{pl}}\frac{dT_p}{dt} = P(t) - K_{\mathrm{w}}(T_{\mathrm{p}}(\mathrm{t}) - T_{\mathrm{b}}) + K_{\mathrm{g}}(T_{\mathrm{s}}(\mathrm{t}) - T_{\mathrm{p}}(\mathrm{t})) \tag{3.10}$$

$$C_{\mathrm{s}}\frac{dT_{\mathrm{s}}}{dt} = K_{\mathrm{g}}(T_{\mathrm{s}}(\mathrm{t}) - T_{\mathrm{p}}(\mathrm{t})) \tag{3.11}$$

An example of a trace showing the temperature of a sample as a function of time is shown in figure 3.6. You can see the temperature increase as heat is transferred to the sample of a known power and the following decrease in sample temperature. In this case tau 2 is negligible as there is good sample to platform surface contact (100%) and only a thin coating of grease has been applied. The parameters that are used in the two tau measurement, which are visible in the measurement status viewer window are given in table 4.10. In this table α is given by equation 3.12 and β is given by equation 3.13. From the fit the sample heat capacity is calculated in units of $\mu\mathrm{JK}^{-1}$ but in this thesis the units are converted

to mJK^{-1}mol^{-1} per X, where X is the magnetic ion. More information about conducting heat capacity measurements using a quantum design PPMS can be found in the PPMS heat capacity user manual[38].

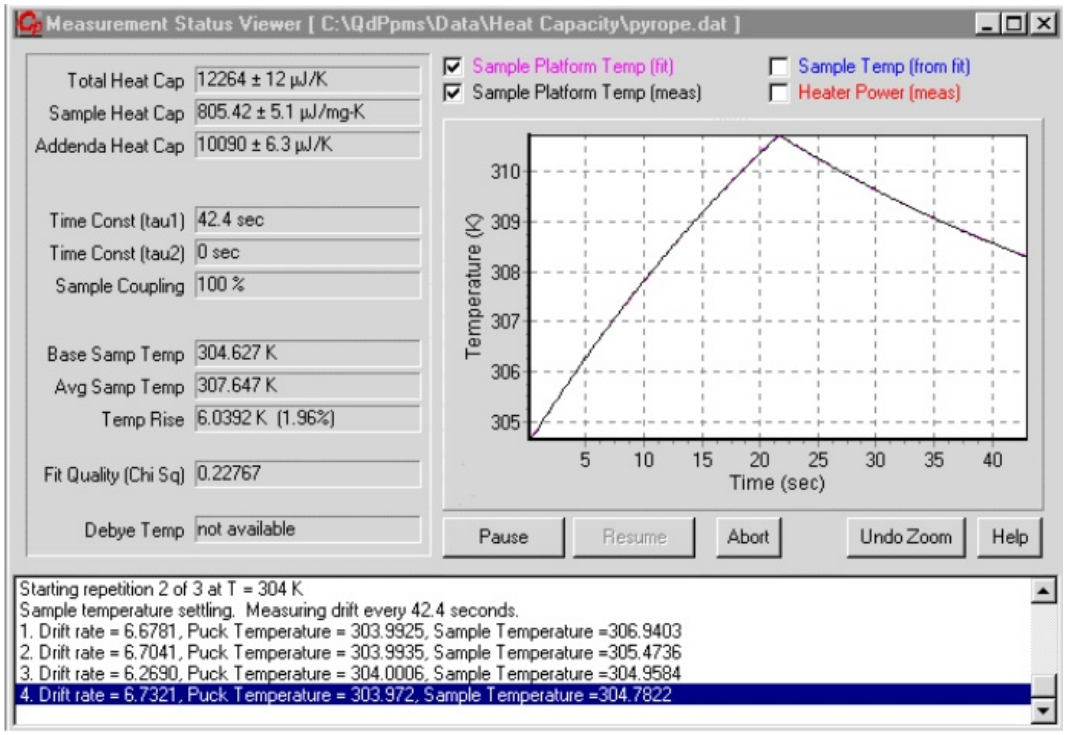

Figure 3.6 *Measurement status viewer window on the ppms instrument showing a trace of the temperature of the samples as a function of time, to which the two tau model is fitted. [38]*

Status viewer field	**Expression from model**
Total Heat Capacity	$C_{\mathrm{pl}} + C_{\mathrm{s}}$
Sample Heat Capacity	C_s
Addenda Heat Capacity	C_{pl}
Time Constant (tau1)	$\frac{1}{\alpha+\beta}$
Time Constant (tau2)	$\frac{1}{\alpha-\beta}$
Sample Coupling	$100\times\frac{K_{\mathrm{g}}}{K_{\mathrm{g}}+K_{\mathrm{w}}}$

Table 3.1 *Two-tau model parameters used for heat capacity measurement.*

$$\alpha = \frac{K_{\mathrm{w}}}{2C_{\mathrm{pl}}} + \frac{K_{\mathrm{g}}}{2C_{\mathrm{pl}}} + \frac{K_{\mathrm{g}}}{2C_{\mathrm{s}}} \tag{3.12}$$

$$\beta = \frac{\sqrt{K_{\mathrm{g}}^2C_{\mathrm{g}}^2 + 2K_{\mathrm{g}}^2C_{\mathrm{s}}C_{\mathrm{pl}} + K_{\mathrm{g}}^2C_{\mathrm{pl}}^2 + K_{\mathrm{w}}^2C_{\mathrm{s}}^2 + 2K_{\mathrm{w}}C_{\mathrm{s}}^2K_{\mathrm{g}} - K_{\mathrm{w}}C_{\mathrm{s}}K_{\mathrm{g}}C_{\mathrm{pl}}}}{2C_{\mathrm{pl}}C_{\mathrm{s}}} \tag{3.13}$$

3.2.4 Angle resolved photoemission spectroscopy (ARPES)

Angle resolved photoemission spectroscopy (ARPES) is a surface sensitive technique that measures the angular distribution, momentum and energy of emitted valence electrons of the material of interest. From this information is gained about the material's Fermi surface and band dispersion. ARPES is more effective for 2D materials, which are easily cleaved, as the momentum directions of interest are parallel to the surface. It is also a technique that is best suited to materials that are metallic or near metallic as the electron density needs to be at or just below the chemical potential.

In ARPES an incoming photon of a known energy, hv, and momentum is directed at and absorbed by the sample. This results in an electron being promoted out of the valence band, which has an energy, $|E_{\mathrm{B}}|$, of typically between 0-1eV, to an occupied energy level from which it can escape. The emitted electron has a kinetic energy, $|E_{\mathrm{kin}}|$ that is given by equation 3.14 and relates to $|E_{\mathrm{B}}|$ through the conservation of energy and momentum where W is the work function or the energy required to escape the sample. The electrons are emitted over an angular range given by θ and ϕ, which are detected by a kinetic energy analyser, as shown in figure 4.49. The kinetic energy analyser consists of a hemispherical analyser with an entrance slit that can resolve the energy and momentum of the incoming electrons. By rotating and moving the sample not only can the energy of the valence bands be determined, but also the band structure of the valence bands at or just below the fermi surface.

$$E_{\mathrm{kin}} = hv - W - |E_{\mathrm{B}}| \tag{3.14}$$

In free space momentum cannot be conserved as a single electron cannot absorb a photon, however, in a solid the lattice provides extra momentum that allows the component of the momentum that is parallel to the surface of the crystal, $k^{||}$, to be conserved. The relationship between parallel momentum of the electron in the valence band to the surface, $k_{\mathrm{i}}^{||}$, and the parallel momentum of the emitted electron to the surface, $k_{\mathrm{f}}^{||}$, is given by equation 3.15 where $G^{||}$ is the surface reciprocal lattice vector. $G^{||}$ is dependent on the symmetry of the crystal at the surface, which may be different to that of the bulk if surface reconstruction has occurred. Due to this surface sensitive nature of ARPES it is important that the crystal has been freshly cleaved under ultra-high vacuum so that the surface is

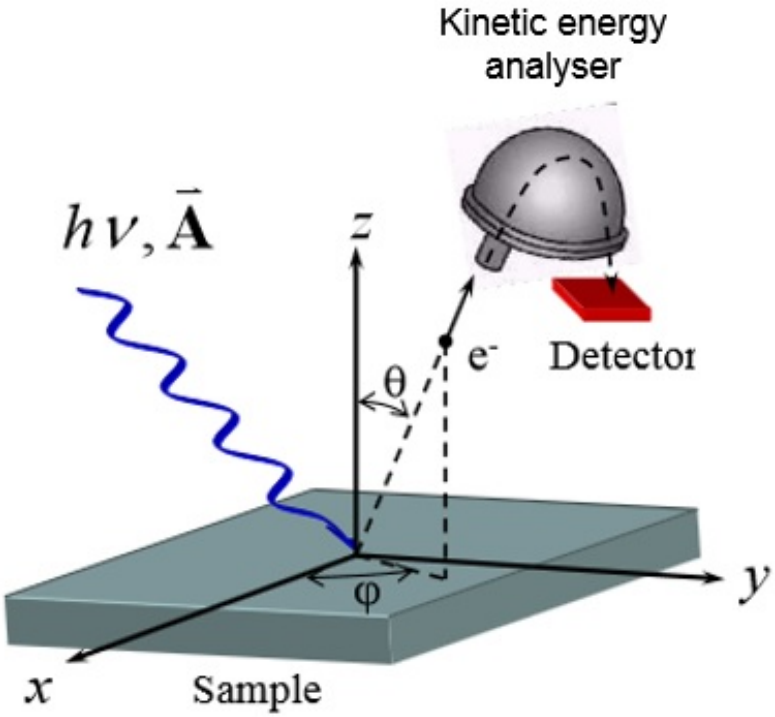

Figure 3.7 *The angular range of detection of the emitted electrons from a sample after irradiation by x-rays during ARPES. The sample moves and rotates rather than the detector to scan through θ and ϕ.*

atomically flat, very clean and representative of the bulk. $k_{\mathrm{f}}^{||}$ can be calculated from $|E_{\mathrm{kin}}|$ by equation 3.16, allowing $|E_{\mathrm{B}}|$ and $k_{\mathrm{i}}^{||}$ to be determined through equations 3.14 and 3.15.

$$k_{\mathrm{i}}^{||} = k_{\mathrm{f}}^{||} + G^{||} \tag{3.15}$$

$$|k_{\mathrm{f}}^{||}| = \frac{(2m_{\mathrm{e}}E_{\mathrm{kin}})^{\frac{1}{2}}}{\hbar}\sin\theta \tag{3.16}$$

In section 4.4 ARPES is used to measure the evolution of the band structure of lanthanum doped $Sr_3Ir_2O_7$ upon electron doping. The ARPES experiment was conducted on the high resolution branch of beamline I05 at Diamond Light Source, which has an energy analyser that is capable of resolving the energy of the incoming electrons to 10meV and an angular resolution of 0.1°. The synchrotron (x-ray) radiation provides photons in an energy range from 18-240 eV to a spot size of less than 50×50 μm^2 and the samples were cleaved in situ under an ultra-high vacuum of 5×10^{-11} mbar at 10K to avoid surface reconstruction.

3.2.5 X-ray diffraction

Powder and single crystal X-ray diffraction yields valuable structural information about a material. Single crystal x-ray diffraction allows the reciprocal space of the material to be mapped, which quickly allows its lattice parameters and space group and eventually the complete crystal structure to be determined. In the absence of a single crystal sample the structure can still be solved using powder x-ray diffraction by matching a theoretical model of the structure to the experimental diffraction pattern using a programme such as GSAS[10] or TOPAS. Powder x-ray diffraction is also used to check the phase purity of a sample and to monitor the progress of a solid-state reaction. Information about the theory behind x-ray diffraction is given in section 2.7 including the different parameters that are fitted in a Rietveld refinement. This section provides information about the instruments and the experiment setup used to collect x-ray powder and single crystal diffraction data.

Powder x-ray diffraction

Multiple x-ray diffractometers have been used to collect data throughout this thesis, however, the experimental setup for all of the diffractometers is very similar. X-rays of a fixed wavelength are focused and diffracted off a sample in theta-2theta Bragg-Brentano geometry as shown in figure 3.8. 2θ is the angle between the incident beam and the detector and is double the incident angle. The intensity of the diffracted photons varies as a function of angle depending on the crystal structure of the sample. During a measurement the sample rotates at $\theta°$/min and the 2D detector rotates at $2\theta°$/min to builds up a diffraction pattern showing the angular dependence of the number of counts. Different width divergence slits can be used to change the area that the x-ray beam interacts with the sample and soller slits are used to reduce noise and both slits can be used to reduce the number of scattered electrons detected, which can prevent the detector from becoming oversaturated.

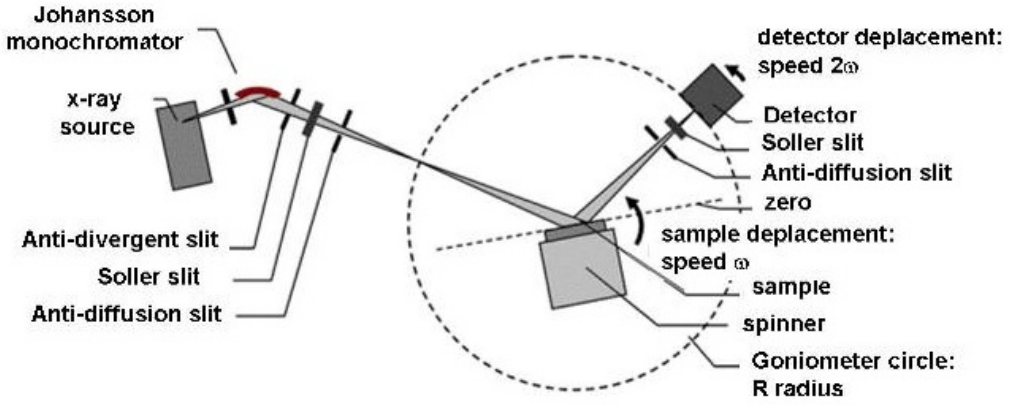

Figure 3.8 *The theta - 2 theta Bragg-Brentano geometry experimental setup on a D8 advanced Bruker diffractometer. [7]*

In this thesis x-ray powder diffraction data were collected on the D2 and D8 Bruker diffractometers in the department of Chemistry and in CSEC at the Univeristy of Edinburgh and on the Rigaku Smartlab and Miniflex diffractometers in the materials characterisation laboratory at ISIS. All the diffractometers used had a Cu source to generate the x-rays. Cu emits x-ray radiation on the relaxation of excited electrons from the 2p and 3p energy levels back to the 1s level. This produces x-rays of three different wavelengths, Cu $K_{\alpha 1}$ and $K_{\alpha 2}$, which have wavelengths of 1.5406 Å and 1.5444 Å (2p to 1s transitions), and Cu K_{β} (3p to 1s transition), which has a wavelength of 1.3922 Å. K_{β} radiation is removed from all

of the diffractometers, however, the D8 advanced, Rigaku Smartlab and Minifflex diffractometers had a monochromator to also remove the $K_{\alpha 2}$ radiation. The D2 diffractometer does not contain a monochromator so an edge is visible on the right of all of the Bragg reflections from the diffraction of the $K_{\alpha 2}$ radiation.

The D2 diffractometer could scan other a 2θ range of 10-90° in 20 minutes and so was used as an initial check of the phase purity of a sample and at intermediate steps of a reaction to check whether the reaction had gone to completion. The Miniflex diffractometer at ISIS could cover a similar angular rangle within half an hour when a step size of 0.01° and a scan rate of 2°/min was used and so was also used for checking phase purity and the progress of the reaction. The Bruker D8 diffractometer at the University of Edinburgh was used to collect refinement quality data, but as the intensity of the x-ray source was poor data was collected typically collected over12 hours from 10° to 125°. At ISIS refinement quality data was collected on the Rigaku Smartlab diffractometer from 10° to 125° in 0.01° steps at 0.5°/min so a typical scan took just under 4 hours.

The samples were prepared by sprinkling about 10mg polycrystalline powder, either from crystals ground up in a pestle and mortar or a ground up powder pellet, onto a glass or low background silicon disk that was in the centre of a circular plastic sample holder. The sample was sprinkled across the disk as evenly as possible to minimise the background and held in place by either using a thin coating of vacuum grease or by adding a few drops of ethanol to the powder before letting it evaporate off the disk. The ethanol method produces a lower background but the grease method is better if the sample is soluble in or reacts with ethanol or is there is significant preferred orientation in the powder. Given that only a small fraction of the crystallites in the powder are in the correct orientation for diffraction to occur off one of the *hkl* planes, the sample is rotated to increase the number of crystallites that can contribute to the overall diffraction pattern.

After the diffraction data had been collected the compounds present could be identified by matching the diffraction pattern to those stored in a computer database. These databases were Eva in Edinburgh and PDXL at ISIS. From this preliminary fitting the lattice parameters of the compound could be estimated and the weight percentage of any impurity phases could be approximated. Rietveld refinement was then conducted on the diffraction patterns using GSAS to test the accuracy of a proposed structural model and to refine structural parameters such as the lattice parameters and the occupancy of a particular atomic site.

Single crystal x-ray diffraction

Single crystal x-ray diffraction allows a 3D picture the Bragg reflections in reciprocal space to be built up by scanning across a hemisphere of a crystal. It is very useful for solving the structure of a compound as the space group, lattice parameters and atomic positions of a crystal structure can be refined with relative ease once a complete data set has been collected. Single crystal x-ray diffraction data were mainly collected on the Agilent Gemini x-ray diffractometer at ISIS; however, data on the crystal of the novel platinate compound were collected on the Agilent Supernova x-ray diffractometer in the Chemistry department at the University of Edinburgh, which is run by the crystallography service. Further data were also collected on the Agilent Supernova diffractometer at the Research Complex at Harwell.

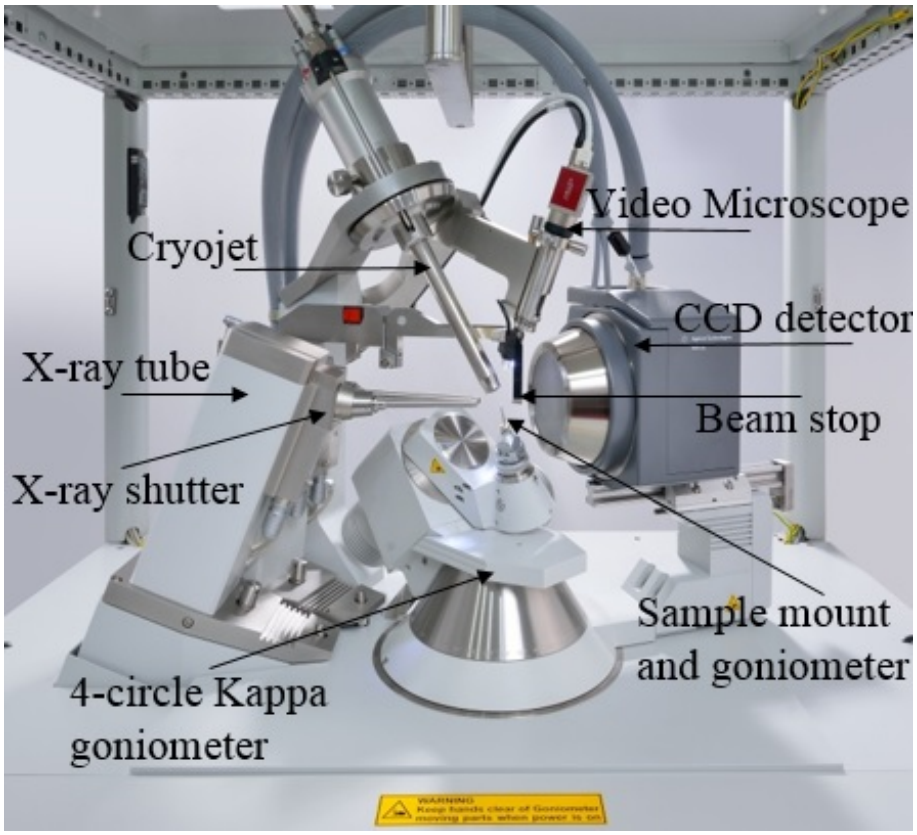

Figure 3.9 *The different components of an Agilent Gemini x-ray diffractometer.*

Figure 3.9 is a labelled photo of an Agilent Gemini x-ray diffractometer. There are two x-ray tubes corresponding to a Cu or Mo x-ray source, which are interchangeable. For my measurements I used the Mo source as the shorter wavelength of 0.71074 Å gives higher resolution data. The x-ray rays are collimated and directed onto the sample, which is mounted in a MiTeGen loop

with a 200 μm aperture that is on the end of a needle. The needle is secured in a separate sample goniometer that is used to centre the crystal. The crystal is coated with BioOil, which uses hydrosuction to keep the crystal attached to the loop and to prevent the crystal from moving during the measurement. The x-ray rays are diffracted off the crystal and any Bragg reflections are detected by the sensitive CCD area detector. In the detector the x-rays first pass through a Beryllium window into a vacuum-sealed detector unit. The x-ray photons hit a scintillation detector that converts the photons to light, which is conducted along a fibre optic cable to the CCD chip and then digitalised. There is a beam stop in line with the x-ray beam and the CCD detector to prevent the beam from oversaturating the detector. The sample mount is on a 4-circle Kappa goniometer, which can rotate the sample through phi, kappa, omega and theta so that data can be collected over a complete hemisphere of reciprocal space. A visual microscope, the output from which is shown on a monitor, is used to help to centre the sample so that it remains in the centre of the beam for all possible angles of rotation. There is also a cryojet attachment that can cool the sample to 85 K by covering the sample in a stream of nitrogen gas, although most of my measurements were conducted at room temperature.

Small crystals of about 100 μm or less were selected for single crystal x-ray diffraction. These were centred by using the visual microscope to adjust the crystal position so that it was always contained within the central four squares on the monitor, which is approximately the area of the x-ray beam. To centre the x, y and z position of the crystal is adjusted on the sample goniometer by turning certain screws with an Allen key when the sample is at theta positions of 0°, 90°, 180° and 270°. After the sample is centred some preliminary diffraction images are collected to check that the sample is indeed a single crystal, to determine a good x-ray exposure time and to check the quality of the Bragg reflections to see if the reflections are twinned or smeared from stacking faults. If the crystal appears to be of a good quality from the images a preliminary images a pre-experimented is conducted where 30 frames are collected, which is used to check the space group and lattice parameters of the crystal, from which a strategy will be determined to collect a complete data set (at least 98.5% completeness is required for publication in a IUCr journal) in the minimum amount of time. Due to the short exposure time of 2s required for crystals of 5d transition metal oxides to prevent oversaturation of the detector it only takes about 4 hours to collect a complete data set for a crystal of a known space group, however I often collected a full hemisphere of data so I could check the

space group determination again later which took about 8 hours. At the start of the run a set of photos is taken of the crystal as it is rotated through 360° that can be used for face-indexing later to calculate the absorption correction due to sample asymmetry later. Both single crystal diffractometers used were controlled by software programme called CrysAlis^{Pro}[12]. During data collection, data reduction is automatically carried out every 25 frames to re-check the space group and lattice parameters. It also applies an absorption correction, corrects for instrument effects, scales the reflections and calculates the crystal mosaicity and reports parameters that relate to the data quality such as R_{int}, I/sig, the Redundancy and the Completeness. After a final data reduction the data is outputted as a *.ins file that gives information about the conditions used on the experimental run and instrumental parameters and an *.hkl file, which is a list of Bragg reflections and their corresponding integrated intensity. These files are inputted into Jana2006[107] and the structure initially solved using superflip. For more information about the process of single crystal refinement, see section 2.9.3.

3.2.6 EDX and EPMA

Energy-dispersive X-ray Spectroscopy (EDX but also known as EDS and XEDS) and Electron Probe MicroAnalysis (EPMA) are both techniques that use electron microscopy to determine the chemical composition of the surfaces of crystals. In this thesis EDX measurements were conducted at the Research Complex at the Rutherford Appleton Laboratory, Harwell, under the supervision of Jennifer Holter and EPMA measurements were conducted in the department of Geosciences under the supervision of Chris Hayfield.

EDX

EDX relies on the fact the each element has a unique set of peaks in their emission spectrum due to differences in their atomic structure. To stimulate the emission of x-rays from the sample a beam of high energy electrons is focused on a spot on the sample using an electron microscope. For the EDX measurements conducted in this thesis the incoming beam of electrons had an energy of 20 keV, which are generated from a tungsten filament. This excites electrons from the core levels of the elements, creating an electron hole that is filled by an electron from a higher energy level, releasing an x-ray that has an energy that corresponds to

the difference in energy between the two levels. Electrons occupying the valence energy levels are usually not involved in the generation of x-ray emission lines so the observed emission lines are not affected by the local crystal structure around the element. The emitted x-rays are detected by a solid state detector that consists of channels that each detect the number of photons within a particular energy range. With an incident energy of 20 keV each channel has a resolution of around 10 eV. A histogram is built up of the number of counts per channel (or per eV). To reduce noise, data was collected until the total area under the histogram reached 500,000 counts, which was then divided by the total acquisition time to give the number of counts per second. This gives a spectra of the number of counts per second per eV as shown in figure 3.10. Each peak in the spectrum corresponds to a transition of an electron between a valence state and a core hole and with a knowledge of the energy that these transitions occur at the chemical composition of a sample can be determined. The weight percentage of each element can be determined by comparing the intensities of the fitted peaks, which are calibrated against a cobalt standard.

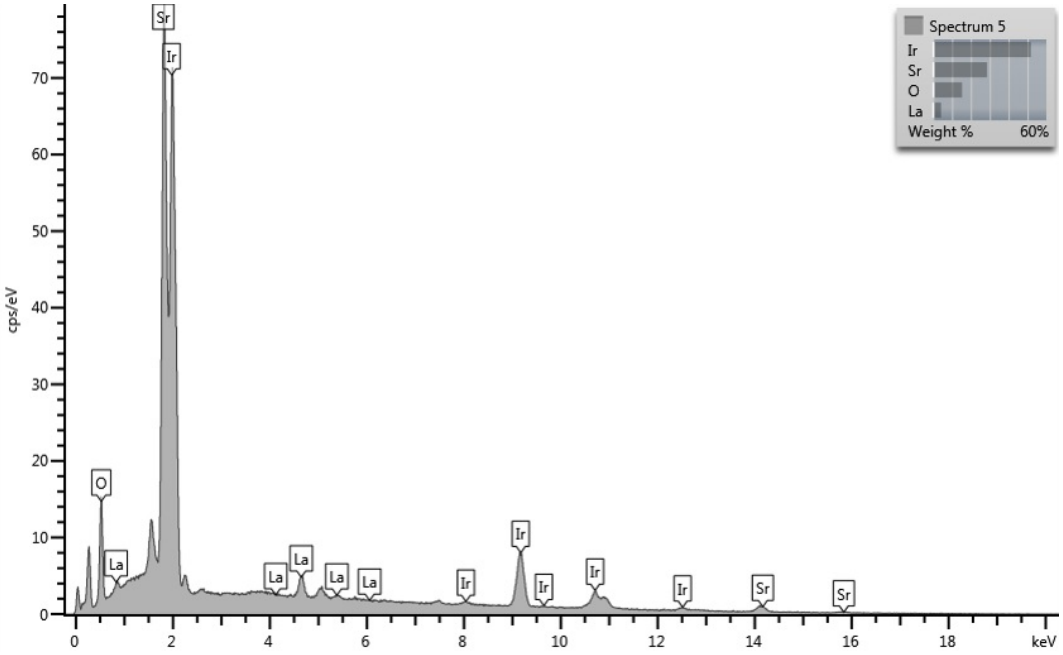

Figure 3.10 *A typical peak fitted spectra from an EDX measurement on a sample of La doped $Sr_3Ir_2O_7$ with the weight percentage of each element from the fit given in the top right-hand corner. Peaks that correspond to the carbon coating of the sample have been excluded from the fit.*

EDX should be conducted on conducting samples to prevent surface charge build up so all samples were coated in a thin layer (about 10 nanometres) of carbon

using carbon sputtering, which is conducted under vacuum with the source of the carbon being a carbon rod that volatises when a large current is passed through the rod. Carbon is used, rather than for example gold, on account of its low atomic number so that it has minimal influence on the fitted intensities of other peaks, which usually occur at a higher energy. The samples are placed on a conductive sticky pad so that incident electrons have a path to flow to the ground. The bombarding electrons give rise to a continuous spectrum that is higher at lower energies and there are also some emission lines corresponding to carbon from the carbon coating. Using the AZtec software that also controlled the data collection, these emission lines were excluded and the EDX profile fitted to calculate the chemical composition of a sample. The continuous background does mean that small peaks are hard to detect as they can be below the background. This meant that it was not possible to accurately detect the amount of La in nominally doped 1% and 3% crystals of La doped $Sr_3Ir_2O_7$. However, it was possible to detect the small amounts of La in the crystals using EPMA. For EDX measurements samples should be well polished before carbon coating so that surface roughness does not affect the results. To achieve this, samples were cleaved before coating to provide a clean, near atomically flat surface that would be smoother than what was achievable in our laboratory from polishing crystals with a colloidal diamond slurry.

By tracking changes in the intensity of a certain emission line that corresponds to a particular element as the beam systematically scans across an area of the sample it is possible to build up a 2D map of the relative distribution of an element across a sample. Also on the EDX in the research complex it is possible to use the scanning electron microscope (SEM) to take electron images of the crystal.

EPMA

EPMA works in a similar way to EDX in that a spot on a sample is bombarded with an electron beam, which causes the sample to emit an emission spectra of x-rays at energies characteristic of the elements present in the samples, which allows the chemical composition of the sample to be determined. However the detection limit for EPMA is much lower for EPMA than EDX with the concentrations of all of the elements from Boron to Plutonium being detectable to levels as low as 100 parts per million. This is because only one wavelength for each element is counted in EPMA. In EPMA EDX is used first to check which elements are present and select a specific wavelength for an emission line for each element (an α line if possible as it is of the highest intensity) that do not overlap in energy. These specific wavelengths are counted using wavelength dispersive X-ray spectroscopy, which utilises Bragg diffraction to select a narrower energy range for each peak. These measured intensities are compared to the intensities of x-rays from a range standards of a known composition that together contain all of the elements that are present in the sample and then corrected for matrix effects such as the depth of production of the x-rays, absorption and secondary fluorescence before yielding quantitative chemical compositions.

All EPMA measurements in this thesis were conducted using a CAMECA SX100 instrument under the supervision of Chris Hayward who runs the Electron Probe Microanalysis Facility in the School of GeoSciences at the University of Edinburgh. The instrument is operated using Cameca's *Peaksight* software, which also automatically analysed the data to give the weight percentage of each element present. The CAMECA SX100 contains five vertical crystal spectrometers containing crystals that enable the analysis of all elements between boron and uranium. The standards used for each compound measured are given in the relevant section. All samples were mounted in a polished block and carbon coated prior to the experiment by Dr Mike Hall.

3.2.7 Neutron Diffraction

Neutron diffraction and scattering experiments need to be conducted at a neutron source such as the Institut Laue-Langevin (ILL) in Grenoble, France or the Spallation Neutron Source (SNS) in Oak Ridge, U.S. . In chapter 5 powder neutron diffraction data were collected at ISIS spallation source near Didcot, UK.

A pulsed neutron source such as ISIS generates produces pulses of neutrons (50 times a second) in a three step process. The key components required are shown in figure 3.11, which only shows the neutrons being delivered to instruments in target station 1 (TS1). Firstly H^- ions, created from the electrical discharge of an ion source, are accelerated to 37% of the speed of light along a linear accelerator (Linac) and injected into a synchrotron ring. As the H^- ions enter the synchrotron, their electrons are stripped away by aluminium foil to create a beam of photons that are further accelerated around the ring by radio frequency electric fields until the photons are travelling at 84% of the speed of light. These protons are then ejected from the synchrotron ring by a fast-kicker magnet and collide with a tungsten target. This drives neutrons from the nuclei of the tungsten target that are then slowed down to more useful speeds for condensed matter research using an array of hydrogenous moderators around the target and directed towards an array of different instruments around the spallation source.

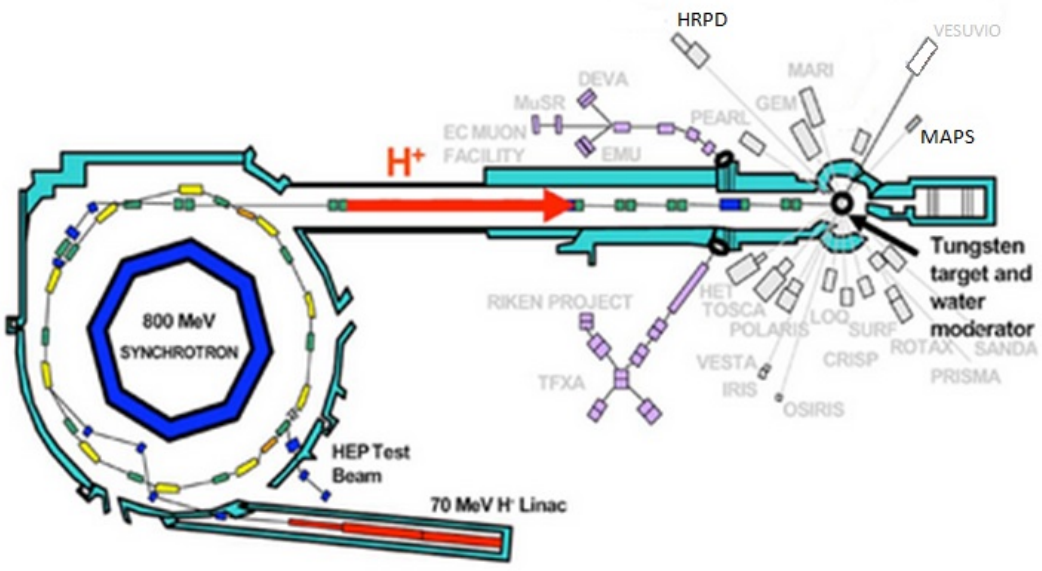

Figure 3.11 *Overview of the components needed to generate neutrons for use in TS1 at ISIS.[2]*

For a pulsed neutron source the time-of-flight (TOF) of neutrons from the spallation source to the sample and from the sample to the detector is measured. By using the equation 3.17, which relates the energy of a neutron to its wavelength, the time of flight, T, of a neutron over a known distance, L can be related to its wavelength via equation 3.18. Unlike in laboratory x-ray diffraction where a constant wavelength of incident radiation is used and the position of the detector is varied to scan across 2θ, in TOF a polychromatic neutron source is used and the detector angles are fixed. Bragg reflections are discriminated from each other by the difference in their time of arrival at the detector. By combining equation 3.18 with Bragg's law the time of arrival of a neutron in μs at the detector can be directly related to the d-spacing in Å via equation 3.19. The advantage of TOF over fixed wavelength diffraction is that data can be collected much more quickly.

$$\lambda = [h^2/2mE]^{\frac{1}{2}} = 9.04/E^{\frac{1}{2}} \tag{3.17}$$

$$\lambda = 0.003955T/L \tag{3.18}$$

$$t_{hkl} = 505.55685Ld_{hkl}sin\theta \tag{3.19}$$

Powder neutron diffraction using HRPD at ISIS

For section 5.2.3 of this thesis powder neutron diffraction data was collected on HRPD (High Resolution Powder Diffraction) at ISIS. Time was applied and successfully obtained on this instrument because its backscattering bank has the highest resolution in the world of Δd/d= 4×10^{-4} due to the instrument being situated 100 m away from the ISIS target. HRPD actually consists of three different detector banks, the configuration of which is shown in figure 3.12 The main backscattering bank covers a d-spacing range of 0.6-4.6 Å, a bank at 90° covers a d-spacing range of 0.9-6.6 Å and the low angle detector banks cover a d-spacing range of 2.2 Å to 16.5 Å. Despite the ability of the low angle detector banks to measure Bragg reflections to very large d-spacings, the resolution of the peaks is poor at 2×10^{-2} Å so the low angle data is mainly used to check for peak positions. The sample was placed in the 1 metre position so that data could be

recorded simultaneously on all three detector banks.

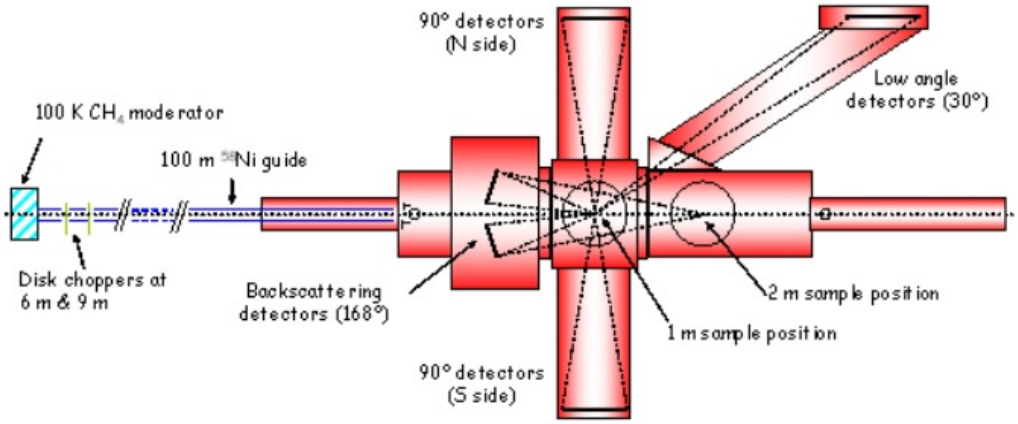

Figure 3.12 *Schematic plan view of the HRPD detector configuration as shown in the HRPD user manual.[3]*

Chapter 4

Investigating and tuning the ground state of $Sr_{n+1}Ir_nO_{3n+1}$ (n=1, 2, ∞) iridates

4.1 Literature review of $Sr_{n+1}Ir_nO_{3n+1}$

4.1.1 The proposed structures of $Sr_3Ir_2O_7$

As mentioned in section 1.2, $Sr_3Ir_2O_7$ is the n=2 member of the Ruddlesden-Popper series $(SrO)_{(n)}(SrIrO_3)_n$ in that the structure has perovskite bilayers of $SrIrO_3$ separated by single layers of rock-salt SrO. However the IrO_6 octahedra within the perovskite layers can undergo various tilts and rotations, the nature of which are still under debate. So far a multitude of different space groups have been proposed for $Sr_3Ir_2O_7$, which differ in their placement of the oxygen atoms in the unit cell, which are hard to identify by x-ray diffraction due to iridium being a very strong x-ray scatterer in comparison to oxygen. Up until recently neutron scattering experiments, which are more sensitive to oxygen, had not been conducted on $Sr_3Ir_2O_7$ due to the small size of single crystals available and the high neutron absorption cross section of iridium. The results of a powder neutron diffraction study reported in the literature by C. Dhital et al [39] are expected to be published soon, which may clarify the structure.

The I4/mmm model

The crystal structure of $Sr_3Ir_2O_7$ was originally proposed in 1994 by M.A. Subramanian, M.K. Crawford and R.L. Harlow as a result of a single crystal x-ray diffraction experiment as belonging to the space group I4/mmm[129]. This tetragonal unit cell is body centred and has 4-fold rotational symmetry and 3 mirror planes that are perpendicular to each other. Out of all the proposed structural models of $Sr_3Ir_2O_7$, this one has the highest symmetry unit cell. Due to the space group being tetragonal the a and b lattice parameters are of equal length. In this structural model proposed by Subramanian the IrO_6 octahedra are not tilted and the O3 site is displaced about 0.4 Å away from the mirror plane and assigned an occupancy of a half. This half occupancy means that the IrO_6 octahedra are alternately rotated about the c-axis within a layer although the direction of rotation is not correlated between bilayers (see figure 4.1). This averaged structure, with the two possible directions of rotation, maintains the 4-fold rotational symmetry characteristic of the I4/mmm space group. Due to the uncertainty in the correct space group for $Sr_3Ir_2O_7$ and the simplicity of the I4/mmm model, it is often employed in band structure calculations and other theoretical models.

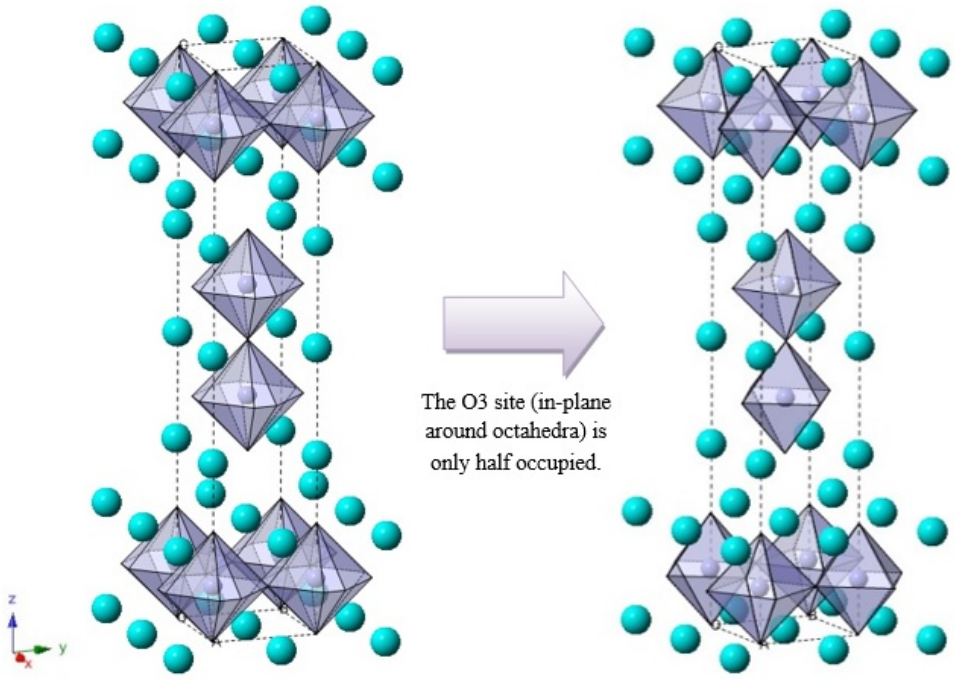

Figure 4.1 *The unit cell of $Sr_3Ir_2O_7$ in the I4/mmm space group model as proposed by Subramanian et al [129].*

For example the I4/*mmm* model was used as the basis of calculations on Resonant Elastic X-ray Scattering (REXS) data collected on $Sr_3Ir_2O_7$ using I16 at Diamond to determine its magnetic structure[18]. By doing this, S. Bossegia et al found that $Sr_3Ir_2O_7$ had a collinear G-type antiferromagnetic structure with the spins on the iridium ions orientated parallel to the applied magnetic field as shown in figure 4.2. They also found that there were two magnetic domains present (labelled A and B) of size $0.02mm^2$.

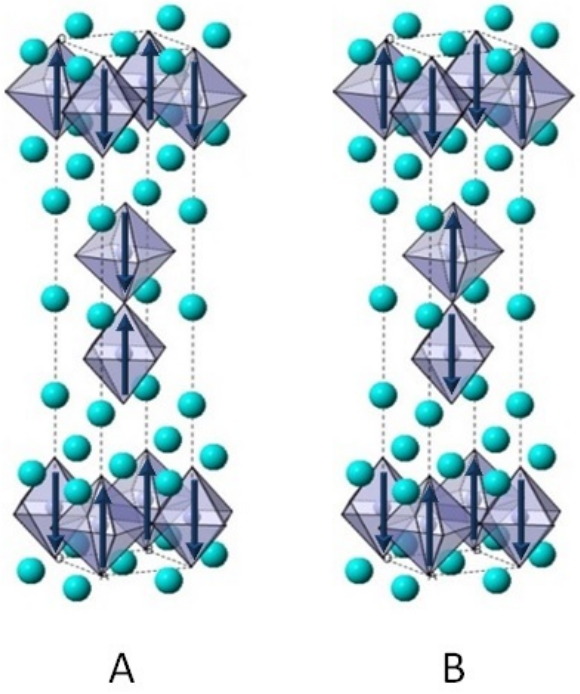

Figure 4.2 *The two magnetic domains of $Sr_3Ir_2O_7$ as characterised by S. Bossegia et al [18].*

The IrO_6 octahedra are not perfectly cubic in Subramanian's model for $Sr_3Ir_2O_7$ with the axial Ir-O3 bond lengths being shorter at 1.990 Å, than the axial Ir-O2 and bridging Ir-O1 bond lengths of 2.014 Å and 2.034 Å respectively. This could potentially move the ground state away from the J_{eff}=1/2 model as discussed in section 2.4.

The B*bcb*/B*beb* model

The B*beb* or B*bcb* structure (space group number 68) is another popular model used to describe the structure of $Sr_3Ir_2O_7$. The B*bcb* and B*beb* space groups appear interchangeably in the literature - the *e* term was introduced by the International Union of Crystallography recently to avoid confusion in cases where the *a* and *c*

symmetry operations become interchangeable depending on how the unit cell axes are labelled and it still hasn't been fully adopted. The B*beb* structure is supported by a single crystal x-ray synchrotron experiment conducted by S. Fujiyama et al at Sping8[46] and by a detailed electron diffraction experiment[87] that compared the goodness of fit of the B*bcb* and A*caa* models (both from space group 68) and the B*bcm* and A*cam* models (space group number 64) to the data before deciding on B*bcb*. This is strong evidence for the B*bcb* structure as synchrotron x-ray sources are more intense and so can detect weak superlattice reflections that may be missed by laboratory based x-ray sources while electron diffraction has a very small spot size so can measure the structure of different domains within the sample.

The difference between the B*bcb* space group model and the I4/*mmm* space group model is that the rotation about the c-axis is ordered and not random, which destroys the 4-fold rotational symmetry about c. The I4/*mmm* unit cell can be transformed to the B*bcb* unit cell by a 45° rotation of the I4/*mmm* unit cell about c and an increase in the a and b lattice parameters by $\sqrt{2}$ so that overall the unit cell is doubled. As the tetragonal symmetry is lost the a and b lattice parameters of the now orthorhombic unit cell can be non-equivalent but in practice they are of a very similar length. Thus the structure of $Sr_3Ir_2O_7$ in the B*bcb* unit cell is often described as being pseudo-tetragonal as the lattice parameters can described by a tetragonal unit cell as $a \approx b \neq c$ and $\alpha = \beta = \gamma = 90°$ but the symmetry condition of a tetragonal unit cell, i.e. that there is four-fold rotational symmetry about c, is not obeyed. The unit cell of $Sr_3Ir_2O_7$ in this model is analogous to the structure of $Sr_3Ru_2O_7$, which is a n=2 Ruddlesden-Popper phase that also belongs to the B*bcb* space group.

Other structural models

There are several other structural models for $Sr_3Ir_2O_7$ that have been mentioned in the literature but not fully published. Firstly, there is a B*bca* model that was proposed by Cao et al in 2002 from a single crystal x-ray diffraction study[32]. Although the paper stated that "detailed results of the crystal structure of $Sr_3Ir_2O_7$ will be published elsewhere" no such paper was ever published. Secondly there was an ESRF experimental report submitted in 2005[16] that found some additional weak reflections in the single crystal synchrotron x-ray diffraction data. These reflections violated the B centering condition: (hkl), $h + l = 2n$ and were

attributed to the primitive space group P*ban*. The key difference between the B*beb* and the P*ban* structural models are that the two perovskite bilayers in the unit cell become inequivalent due to the octahedra having significantly different rotation angles and bond lengths in P*ban* (see figure 4.3). However a full crystal structure or paper from this experiment has never been published and this space group has not been reported since. Finally a recent paper in 2014 by C. Dhital et al stated that additional (1, 0, l)-type superlattice reflections were apparent in polarised powder neutron diffraction data collected at 300 K on the BT7 triple-axis spectrometer at NIST[39]. These extra reflections were attributed to the space group $Bb2_1/m$, which make $Sr_3Ir_2O_7$ isostructural with $Ca_3Ru_2O_7$. The key difference between this structural model and the B*beb* model is that the IrO_6 octahedra are tilted as well as rotated. However, as stated in the paper, a full neutron data set has yet to be collected and refined.

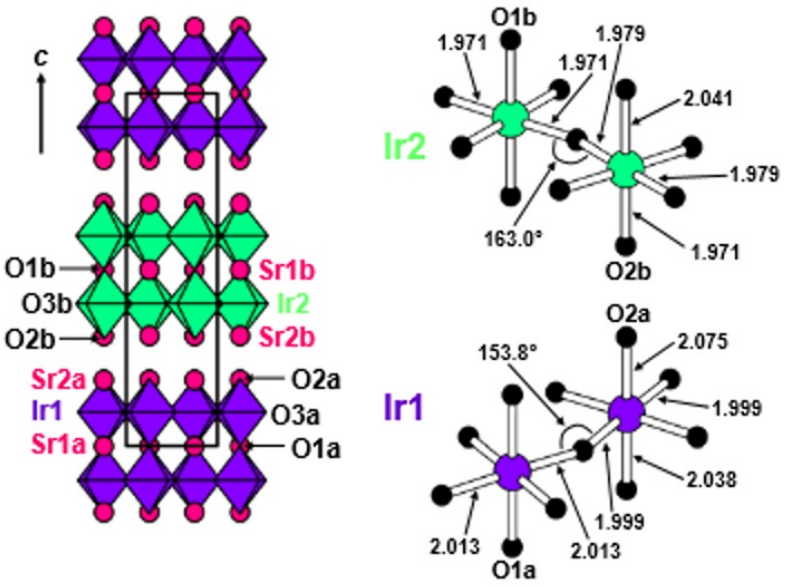

Figure 4.3 *The Pban structural model of $Sr_3Ir_2O_7$ as shown in ESRF experimental report HS2386[16].*

Structural similarities to $Sr_3Ru_2O_7$

$Sr_3Ru_2O_7$ is the n=2 member of a Ruddlesden-Popper series $(SrO)_{(n)}(SrRuO_3)_n$. As with $Sr_3Ir_2O_7$, there was some debate other the correct space group. From single crystal x-ray diffraction the structure was initially identified as being of the $I4/mmm$ space group[89], however, in 1998 and 2000 two neutron powder

diffraction experiments assigned $Sr_3Ru_2O_7$ two different space groups of P*ban*[58] and B*bcb*[121]. Both unit cells were pseudo-tetragonal as the a and b lattice parameters were almost identical. The second study compared the fit of 10 different space groups to the data including B*bmm*, B$b2_1/m$ and P$4_2/mcm$ before settling on the B*bcb* structure. It wasn't until 2004 that single crystal neutron diffraction on a sample grown via the floating zone method was able to confirm the correct space group as B*bcb*[73]. This dilemma of differentiating between tetragonal and pseudo-tetragonal cells with only subtle differences in the oxygen positions that cause a lowering of the symmetry is the same as faced for $Sr_3Ir_2O_7$. However, resolving the structure of $Sr_3Ir_2O_7$ is even more complex than for $Sr_3Ru_2O_7$ as no crystals have been grown by floating zone method so single crystal samples are smaller and iridium has a much larger neutron absorption cross section so single crystal neutron diffraction experiments are much more challenging.

4.1.2 The structure of Sr_2IrO_4 and $SrIrO_3$

Sr_2IrO_4

Sr_2IrO_4 is the n=1 member of the Ruddlesden-Popper series $Sr_{n+1}Ir_nO_{3n+1}$ so has monolayers of corner-sharing IrO_6 octahedra instead of bilayers. The unit cell coordinates for the I4_1acd space group model of Sr_2IrO_4 as originally published by M.K. Crawford et al[36] are given in table 4.1. The unit cell has a body-centered tetragonal lattice so the a and b lattice parameters are equivalent with a published value of 5.4979(2)Å and the c lattice parameter was given as 25.798(1)Å. This structure was recently verified by single crystal neutron diffraction using HB3A at the Oak Ridge National laboratory[141]. As with $Sr_3Ir_2O_7$, the IrO_6 octahedra undergo a tetragonal distortion but there are only two rather than three oxygen environments. The O1 atoms are on the apical positions of the IrO_6 octahedra and the O2 ions are in-plane as shown in figure 4.4. The in-plane Ir-O2 bond lengths are slightly shorter than the apical Ir-O1 bond lengths with respective values of 1.981(1)Å and 2.058(2)Å. In the single crystal neutron diffraction study the magnetic structure was also refined, which showed that Sr_2IrO_4 has a canted antiferromagnetic structure with the spins pointing in the plane. This is different to the collinear antiferromagnetic structure of Sr_3Ir_2O7.

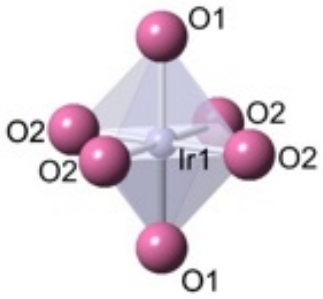

Figure 4.4 *The arrangement of the O1 and O2 atoms within the IrO_6 octahedron in Sr_2IrO_4.*

Atom	Wyckoff Symbol	x	y	z	B	Occupancy
Ir1	8a	0	0.25	0.375	0.0031(4)	1
Sr1	16d	0	0.25	0.55060(5)	0.0050(4)	1
O1	16d	0	0.25	0.45472(6)	0.0053(4)	1
O2	16f	0.2001(2)	0.4501(2)	0.125	0.0090(5)	1

Table 4.1 *The unit cell of Sr_2IrO_4 as published by M.K Crawford et al[36].*

Ambient pressure $SrIrO_3$

The ambient pressure structure $SrIrO_3$ has the lowest symmetry space group, $C2/c$, of all of the strontium oxide compounds. The unit cell, as published by I. Qasim [109], is monoclinic with β=93.202(4)° and the unit cell lengths a, b and c equalling 5.60401(29)Å, 9.6256(4)Å and14.1834(7)Å respectively. The crystal structure (see figure 4.5) itself is a monoclinic distortion of the 6H hexagonal perovskite structure and so does not belong to the Ruddlesden-Popper series.

From the unit cell shown in table 4.2, there are two different iridium sites within the unit cell. The octahedron that forms around Ir(1) site is corner-shared with four other IrO_6 octahedra while the octahedron that forms around the Ir(2) site is face-shared with another $Ir(2)O_6$ octahedron to form a dimer unit. The iridium ions located on both of these sites types are surrounded by a non-regular array of oxygen anions. The $Ir(2)O_6$ octahedra are particularly distorted with the bond angle between opposing oxygen anions moving away from 180° and all of the bond lengths to the 5 different oxygen sites being different, ranging in length from 1.974Å to 2.129Å. In comparison the $Ir(2)O_6$ are less distorted. Although the O-Ir-O bond angles are not the ideal 90°, opposing oxygen atoms are still all at 180° to each other and there are only three different Ir(1)-O bond lengths of

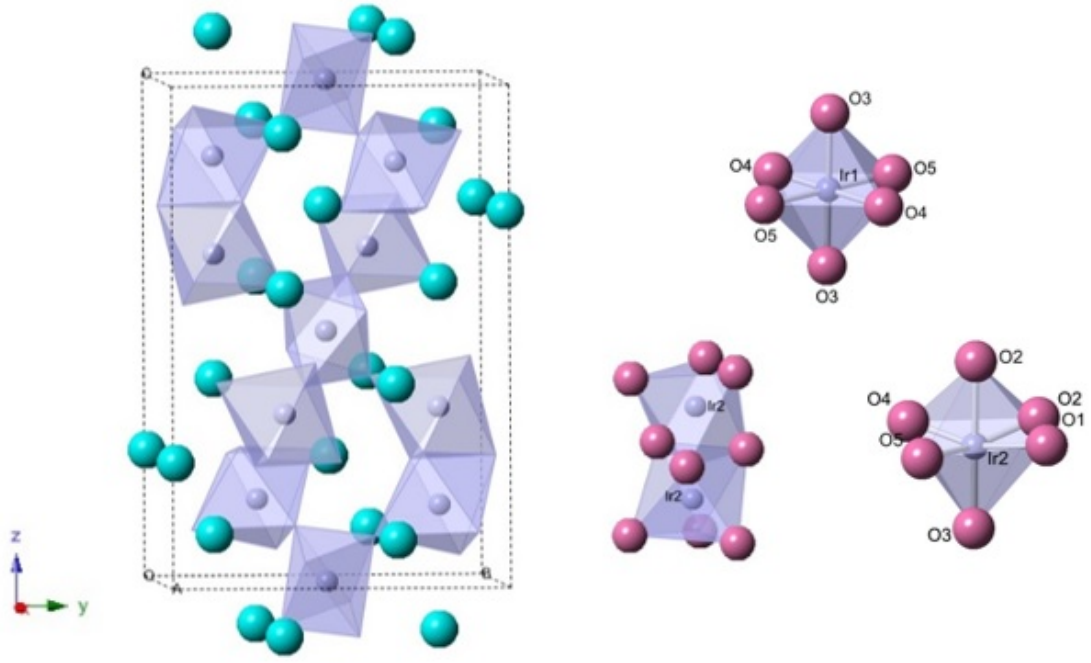

Figure 4.5 *The ambient pressure crystal structure of $SrIrO_3$ plus the three different local coordination environments around the iridium ions.*

1.847Å, 1.995Å and 2.038Å, which correspond to each of the three types of oxygen site surrounding the iridium ion. $SrIrO_3$ is metallic rather than insulating like Sr_2IrO_4 and $Sr_3Ir_2O_7$ so perhaps the highly distorted octahedra are responsible for moving the ground state away from the J_{eff}=1/2 ground state.

Atom	Wyckoff Symbol	x	y	z	Occupancy
Sr1	4e	0.0	0.0092(1)	0.250	1
Sr2	8f	0.0122(1)	0.6667(8)	0.0957(4)	1
Ir1	4a	0	0	0	1
Ir2	8f	0.9820	0.6660(5)	0.84698(3)	1
O1	4e	0	0.4981(3)	0.250	1
O2	8f	0.2411	0.2649(7)	0.2630(5)	1
O3	8f	0.8112	0.4077(8)	0.0474(5)	1
O4	8f	0.9407	0.1344(9)	0.4087(5)	1
O5	8f	0.3238	0.4204(8)	0.1058(6)	1

Table 4.2 *The unit cell of the ambient pressure phase of $SrIrO_3$ as published by Longo et al [83]*

There is also a high pressure form of $SrIrO_3$, which adopts the perovskite structure to be the n=∞ member of the Ruddlesden-Popper series. In this orthorhombic compound the IrO_6 octahedra are rotated about and tilted away from the y axis and the octahedra themselves are also highly distorted. However, this compound

is not studied in this thesis.

4.1.3 Discrepancies in the reported bulk properties of $Sr_3Ir_2O_7$

The bulk properties of single crystal $Sr_3Ir_2O_7$ were first published by G. Cao et al in 2002[32]. Magnetisation measurements between 2 and 350 K (in figure 4.6a and 4.6b) showed that there were three magnetic transitions below an applied field of 2500 Oe. These were a transition at 285 K that was described as ferromagnetic in the original paper, a change in slope at 260 K, labelled as T^*, and a diamagnetic cross-over below 50 K. This diamagnetic cross-over was quenched by higher fields and replaced by an upturn, although the other two magnetic transitions remained and the magnitude of the magnetic susceptibility dropped with increasing field. By a field of 70,000 Oe all features in the magnetisation had disappeared apart from a paramagnetic-like response. This field variation of the magnetisation suggests that there may be a paramagnetic impurity present in the crystals especially as it is difficult to grow pure crystals by flux growth. A paramagnetic impurity would appear as an upturn in the magnetisation at low temperatures and would become more apparent with increasing field. A measurement of the isothermal magnetisation as a function of field found no hysteresis at any of the temperatures measured but as the isothermal magnetisation is non-linear $Sr_3Ir_2O_7$ cannot be a simple antiferromagnet. At temperatures above 150 K the isothermal magnetisation saturates quickly with increasing applied field to yield a low moment of just $0.003\mu_B$ per iridium ion, showing that the Ir^{4+} does not behave as a simple S=1/2 ion but has an orbital contribution.

In the analogous strontium ruthenate Ruddlesden-Popper series it is possible to grow eutectic mixtures of Sr_2RuO_4 and $Sr_3Ru_2O_7$ where there are monolayers of Sr_2RuO_4 intercalated between $Sr_3Ru_2O_7$ bilayers[72][1]. These intercalated Sr_2RuO_4 monolayers have a noticeable effect on the physical properties of eutectic $Sr_3Ru_2O_7$ in that it superconducts at temperatures between 1 K and 1.5 K[71] while pure $Sr_3Ru_2O_7$ does not exhibit superconductivity down to 15 mK[72]. The presence of monolayer defects is also apparent in the magnetisation where three transitions are evident below 2 K[71]. It is possible that defect layers of Sr_2IrO_4 could also be present in $Sr_3Ir_2O_7$ and could be responsible for the T^* transition observed at 260 K.

Resistivity data taken over a temperature range from 2 K to 1000 K revealed two changes of gradient at 285 K and 50 K that coincide with two of the proposed magnetic transitions from the magnetisation measurements. The fact that the T^* transition is not present in the resistivity suggests that it could be from an impurity phase. The increase in the resistivity with decreasing temperature showed that $Sr_3Ir_2O_7$ was an insulator. The *c*-axis resistivity is significantly higher than the resistivity in the *ab* plane at 200 mΩcm compared to 30 mΩcm at 300 K showing that the transport properties of $Sr_3Ir_2O_7$ are anisotropic. This is not surprising as $Sr_3Ir_2O_7$ has a layered structure. Resistivity measurements conducted under varying fields showed only a mild magnetoresistive effect below 15 K.

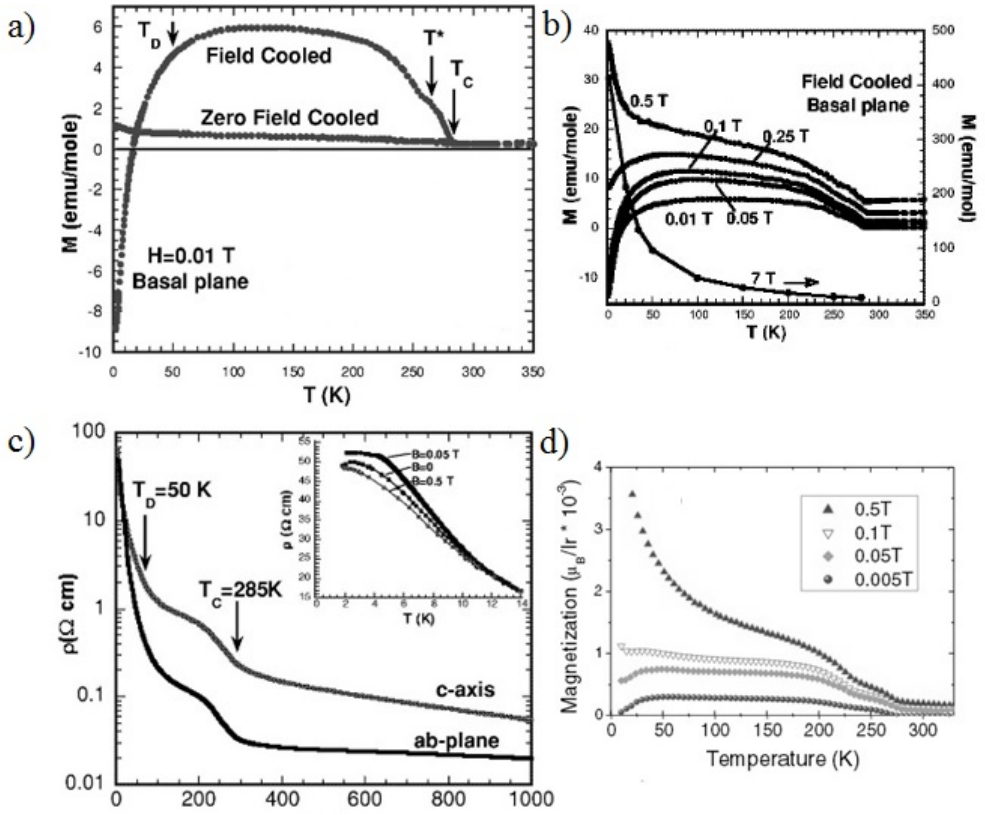

Figure 4.6 *Some of the bulk measurements on $Sr_3Ir_2O_7$ that have been previously published [19][32]. a) Field and Zero Field cooled magnetisation in the basal plane between 2 K and 350 K. b) field cooled magnetisation in the basal plane between 2 K and 350 K in different applied fields c) c-axis and ab plane resistivity between 2 K and 1000 K. Inset shows the field dependence of the resistivity as a function of temperature d) Magnetisation between 2 and 350 K in different applied fields taken from S. Boseggia et al's paper.*

Magnetic susceptibility data on single crystal $Sr_3Ir_2O_7$ that was later published by S. Boseggia et al [19] (again see figure 4.6) also showed that there were three

features between 2 K and 350 K but these were at different temperatures of 50 K, 230 K and 275 K. This difference in the transition temperatures to the original paper was attributed to "variations in the sample quality or small differences in oxygen stoichiometry". Apart from this their data was in agreement with Cao's in that a diamagnetic cross-over occured below 50K and was seen only at small fields to be replaced by a paramagnetic-like upturn at higher fields. In isothermal magnetisation measurements the magnitude of the moment per iridium ion was also in agreement with Cao's work below $0.003\mu_B$ for all fields used. However in their case the diamagnetic cross-over was quenched using a much smaller field of 0.1 T. This suggests that samples used in S. Boseggia's work are of lower quality that those in Cao's work as the paramagnetic impurity is apparent when using smaller fields and if the T^* transition is from single layer intergrowths then the lower value of T^* of 230 K rather than 260 K, which is closer to the magnetic transition of 240 K of Sr_2IrO_4, suggests that there could be more single layer intergrowths in S. Boseggia's samples. The fact that the magnetic transition at 285 K has been lowered to 275 K is also an indication of poorer sample quality.

The bulk properties of polycrystalline samples of $Sr_3Ir_2O_7$, made via high pressure synthesis, have also been measured by Nagai et al. In the magnetisation measurements in Nagai et al's paper [95] the diamagnetic cross-over at 50 K was not observed even in fields as low as 10 Oe. Although the magnetic transition at 280 K occurs, there is no evidence of another transition between 230 K and 260 K. There are also some differences in the isothermal magnetisation data as there is hysteresis at temperatures below 280 K. However, the sample was found to contain an impurity phase of $SrIrO_3$ that made up an estimated 2% of the sample by weight and the powder averaging of the anisotropic nature of the magnetisation seen in single crystal measurements may be responsible for some of the differences seen.

The resistivity of a polycrystalline pellet of $Sr_3Ir_2O_7$ was also measured by Nagai et al and found to be 250 mΩcm at 300 K[95]. This is similar to the c-axis resistivity of a single crystal sample. There is also a feature in the resistivity at 280 K that corresponds to the magnetic phase transition observed.

Depending on the paper there are key differences in the number, transition temperature and the field dependent behaviour of the magnetic transitions in $Sr_3Ir_2O_7$. The authors of the paper measured samples of $Sr_3Ir_2O_7$ prepared by different people so it is possible that these differences are due to sample variation. Some of these differences may also arise from slight differences in the measurement

technique. Considering that the slight changes to the oxygen stoichiometry of Sr_2IrO_4 has a large effect on its bulk properties, I will investigate how sample quality affects the bulk properties of $Sr_3Ir_2O_7$.

4.2 Crystal growth of $Sr_{n+1}Ir_nO_{3n+1}$ (n=1, 2, ∞)

4.2.1 Review of crystal growth conditions for $Sr_{n+1}Ir_nO_{3n+1}$ (n=1, 2, ∞) in the literature

There are four different reported sets of crystal growth conditions for forming $Sr_3Ir_2O_7$, the details of which are given in table 4.3. These conditions were published by separate groups of collaborators and there are some key variations, the most significant being the temperature regime used for the flux growth. Subramanian et al use a much lower dwell temperature of 1050°C with a shorter dwell time and a 2-3 times faster cooling rate than the other syntheses. G.Cao et al and S. Boseggia et al use surprisingly high dwell temperatures of 1480°C and 1440°C respectively given that an open platinum crucible was used and that the boiling point of the $SrCl_2$ flux is 1250°C. C. Dhital et al also use a dwell temperature higher than the boiling point of the flux but reduce the rate of flux loss by partially sealing the platinum crucible with a platinum lid and then enclosing it in an alumina crucible. Flux loss is not a problem in the conditions given by Subramanian et al as the growth is conducted in a sealed platinum tube below the boiling point of $SrCl_2$.

The ratio of the starting materials or the amount of flux used is not given in the conditions provided by G.Cao et al and S. Boseggia et al, just that off-stoichiometric quantities of IrO_2, $SrCO_3$ and $SrCl_2$ were used. The other two syntheses use stoichiometric ratios of $SrCO_3$ to IrO_2 and the molar ratio of flux used was 5 and 15. The smaller molar ratio of flux used in the sealed Pt tube growth is not surprising as there is no flux loss that needs to be considered.

All of the samples appear to be plate-like in morphology, although their reported size differs. The crystals grown by S. Boseggia et al and C. Dhital et al are the largest with dimensions of $2\times2\times0.1mm^3$. Whether this is correlated to the cooling rate of these two growths being the slowest or whether the larger crystals are due to a more optimal temperature regime is unclear.

Paper	Starting materials	Temperature	Cooling rate	Crucible type	Sample details
M.A Subramanian et al, Materials Research Bulletin, 29 (1994) 645	3:2 mixture of SrO_2:IrO_2 and a 5-fold excess of anhydrous $SrCl_2$	1050°C for 6 hours	10°C/hour to 600°C before quenching	Sealed Pt tube	Plate-like crystals. Crystal used for x-ray diffraction had dimensions of $0.09\times0.02\times0.13mm^3$. ICP found no traces of Cl from flux in crystals. Microprobe analysis found Sr:Ir ratio to be close to 3:2
G.Cao et al, Physical Review B, 66 (2002) 214412	Off-stoichiometric quantities of IrO_2, $SrCO_3$ and $SrCl_2$	1480°C for 20 hours	5°C/hour to 1440°C before being quenched to room T	Open platinum crucible	Plate-like crystals of average dimensions of $0.6\times0.5\times0.1mm^3$. EDX found Sr:Ir ratio to be 3:2.
S.Boseggia et al, Physical review B, 85 (2012) 184432	Off-stoichiometric quantities of IrO_2, $SrCO_3$ and $SrCl_2$	1440°C for 20 hours	3°C/hour. No temperature range given.	Open platinum crucible	Plate-like crystals with typical dimensions of $2\times2\times0.1mm^3$
C.Dhital et al, Physical Review B, 86, (2012), 100401(R).	IrO_2, $SrCO_3$ and anhydrous $SrCO_3$ in a 2:3:15 molar ratio	1300°C. No dwell time given.	3.5°C/hour to 850°C then furnace-cooled to room temperature.	Pt crucible partly sealed with a Pt lid enclosed in an alumina crucible.	Crystals had typical dimensions of $2\times2\times0.1mm^3$. Sr:Ir ratio confirmed to be 3:2 via EDS and phase purity checked by x-ray powder diffraction.

Table 4.3 *An overview of the different crystal growth for $Sr_3Ir_2O_7$ reported in the literature*

A search of the literature reveals only one complete set of crystal growth conditions for Sr_2IrO_4, which is by K.Ishii et al[60], and is commonly cited when people describe how they obtained their samples. G. Cao et al also published a paper on the growth of Sr_2IrO_4 but the details are vague with the description as follows: " Single crystals were grown in Pt crucibles using flux techniques from off-stoichiometric quantities of IrO_2 or Ir, $SrCO_3$, and $SrCl_2$. Details are described elsewhere."[28]. The further details referenced refer to a paper that outlines the crystal growth conditions for $Ca_3Ru_2O_7$ and $(Sr_{1-x}Ca_x)_3Ru_2O_7$ and so is unrelated. Unfortunately this paper is often cited in further publications by this group as to how the samples were made.

The crystal growth paper by K.Ishii et al[60] uses a stoichiometric ratio of $SrCO_3$ and IrO_2 and a 15 molar ratio of $SrCl_2$. In conditions similar to C. Dhital et al in the growth of $Sr_3Ir_2O_7$, the mixture is heated to 1300°C before being cooled to 900°C at a faster cooling rate of 8°C/hour. The similarity of these two conditions suggest that the ratio of $SrCO_3$ to IrO_2 is important in determining which phase of $Sr_{n+1}Ir_nO_{3n+1}$ is formed.

As outlined in section 4.1.2, there is a ambient pressure and high pressure form of the x=∞ member of the $Sr_{x+1}Ir_xO_{3x+1}$ series. To date crystals of the high pressure form of $SrIrO_3$ have not been synthesised but a polycrystalline powder can be made by heating a pellet of the ambient form of $SrIrO_3$ to 1000°C at a pressure of 5GPa[83].

Single crystals of the ambient form of $SrIrO_3$, of typical dimensions of $0.4 \times 0.4 \times 0.6 mm^3$, have been grown by G.Cao et al using off-stoichiometric quantities of IrO_2, $SrCO_3$,and $SrCl_2$ in a platinum crucible[30]. Further technical details relating to the crystal growth conditions are referenced back to the paper on the crystal growth of $Sr_3Ir_2O_7$. This enforces the notion that the crystal growth conditions for growing $Sr_3Ir_2O_7$ and $SrIrO_3$ are very similar with just slightly different quantities of $SrCO_3$, IrO_2 and $SrCl_2$ being used each time.

4.2.2 The crystal growth of $Sr_{n+1}Ir_nO_{3n+1}$ (n=1, 2, ∞)

While most papers use a mixture of $SrCO_3$, IrO_2 and $SrCl_2$ to grow crystals of SrO-IrO_2 systems, the conditions used vary widely and it is possible that these variations from group to group are responsible for the variations in the bulk properties observed in the literature. Given the uncertainty in the crystal

growth conditions required for each phase of $Sr_{n+1}Ir_nO_{3n+1}$ (n=1, 2, ∞) it was important to fully explore the SrO-IrO_2 phase diagram. In order to do this 36 flux growth attempts were made using a variety of different temperature ranges, cooling rates, ratios of starting materials and different types of crucible. The conditions used and the corresponding results of key crystal growth attempts are listed in table A.1 in Appendix A. The motivation behind exploring the SrO-IrO_2 phase diagram was to find the optimum conditions for producing good quality crystals of $Sr_3Ir_2O_7$. Later on the properties of crystals of $Sr_3Ir_2O_7$ that have been grown under slightly different conditions are compared to see if observed variations in published results can be linked to slight differences in the samples used.

The phase of $Sr_{x+1}Ir_xO_{3x+1}$ grown is dependent on an interplay of many factors. Although the results of varying these factors are not always repeatable, some general trends are discussed below.

Starting temperature

It appears that lower starting temperatures favour the formation of $SrIrO_3$ over Sr_2IrO_4 and $Sr_3Ir_2O_7$ and that too low a starting temperature makes it more difficult for crystal nucleation to occur. For example all of the growths starting at a temperature of 1150°C or below only produced very small crystals of $SrIrO_3$ with the exception of SIO#24A+B where some small flakes of Sr_2IrO_4 were also formed. However in both of these cases a very low molar ratio of IrO_2:$SrCl_2$ of 1:6.5 was used. At temperatures above 1200°C the temperature does not seem to be a major factor in determining the phase grown as reactions SIO#F1 and F3 had identical temperature regimes and cooling rates but one produced crystals of $Sr_3Ir_2O_7$ while the other produced crystals of Sr_2IrO_4. Large single phase crystals of Sr_2IrO_4 were grown in reactions with starting temperatures of 1250°C (SIO#F2), 1245°C (SIO#F15) and 1300°C (SIO#F15). On the other hand large crystals of $Sr_3Ir_2O_7$ were grown at initial starting temperatures of 1200°C (SIO#F17) and 1300°C (SIO#F1). Other reaction conditions, namely the ratio of $SrCO_3$:IrO_2 seem to be more important in determining the phase formed.

Cooling rate

The cooling rate, while perhaps not the most important factor in determining which phase is formed, can affect the crystal size and quality. For example SIO#F11 and SIO#F12 are near identical except that SIO#F12 is cooled over a narrower temperature range. This means that SIO#F11 has a cooling rate of 4.57°C/hr while SIO#F12 has a cooling rate of 1.14°C/hr. Both growths produce crystals of Sr_2IrO_4 but the slower cooling rate produces thick globular shaped crystals while the faster cooling rate produces plate-like crystals. SIO#F13, although not directly comparable as the molar ratio of IrO_2:$SrCO_3$ is slightly lower, has a much faster cooling rate still at 5.26°C/hr and produces much smaller flakes of Sr_2IrO_4. Clearly the cooling rate has to be just right for large good quality crystals to form. From conducting these crystal growths the best cooling rate was found to be around 4°C/h.

Amount of flux

There are very few direct comparisons that can be made where only the flux ratio has been changed and there seems to be no direct correlation between the flux ratio and the phase formed. The amount of flux is not the key factor in affecting crystal size or quality either. For example using 15$SrCl_2$ in SIO#F5 produces large thick crystals of $Sr_3Ir_2O_7$ and large (although thin) crystals of $Sr_3Ir_2O_7$ can also be formed using a IrO_2:$SrCl_2$ molar ratio of 1:7.5. Other factors such as the cooling rate and temperature range appear to be more important as crystals could be formed for all IrO_2:$SrCl_2$ molar ratios used, which were between 1:6.5 and 1:20.

The ratio of $SrCO_3$:IrO_2

It seems fairly clear that as the amount of $SrCO_3$ is increased relative to the amount of IrO_2 the phase preference changes from $SrIrO_3$ to $Sr_3Ir_2O_7$ to Sr_2IrO_4. This makes sense as the amount of strontium increases compared to the amount of iridium in the crystal structure as you go along this series. Some examples:

- SIO#F17,18A+19A had identical reaction conditions except for a varying IrO_2:$SrCO_3$ molar ratio. When 1:1.35 moles molar ratio was used only Sr_3IrO_7 formed. As the proportion of strontium carbonate is reduced

relative to IrO_2 more $SrIrO_3$ starts to form as well as the $Sr_3Ir_2O_7$ until by a 1:0.8 molar ratio only $SrIrO_3$ forms.

- SIO#F1+3 had identical reaction conditions except that SIO#F1 used IrO_2:$SrCO_3$ molar ratio of 1:1.8 moles while SIO#F3 used 1:2.2 molar ratio. Mainly $Sr_3Ir_2O_7$ formed in reaction SIO#F1 while only Sr_2IrO_4 formed in reaction SIO#F3

- SIO#F5+F11 had identical reaction conditions except that SIO#F5 used a IrO_2:$SrCO_3$ molar ratio of 1:1.35 moles while SIO#F11 used a IrO_2:$SrCO_3$ molar ratio of 1:1.45. SIO#F5 produced large thick crystals of $Sr_3Ir_2O_7$ while SIO#F11 produced large flakes of Sr_2IrO_4.

Crucible type

The first choice of crucible material for growing $Sr_{x+1}Ir_xO_{3x+1}$ crystals was platinum as it is reasonably inert and survives to high temperatures. Also all the published literature used platinum crucibles for the growth. A platinum lid was used and the filled crucible was enclosed in firebricks to minimise flux loss and to stabilise the temperature. However, during EPMA measurements it was found that a PtIr alloy had been incorporated into the crystals, encouraging us to try other types of crucible in an effort to eliminate this impurity. The use of an alumina crucible resulted in almost complete loss of the flux, although the reason for this is unknown, so only one growth was attempted with this crucible type. Zirconia crucibles appeared to be more promising with large crystals of $Sr_3Ir_2O_7$ being formed with less of the metal impurity (in this case just Ir) forming. However, x-ray of the crystals revealed additional unknown impurity peaks, perhaps some zirconium iridate phase, and the zirconia crucibles cracked and broke after a maximum of two crystal growth attempts so the platinum crucibles were returned to.

Crucible size does make a difference, as well as the mass of the starting materials, as it effects the surface area of the flux exposed to the atmosphere and thus the evaporation rate of the flux. A smaller crucible has a small cross-sectional surface area so has a smaller evaporation rate (in $g/cm^2/s$) than a larger crucible. However a smaller crucible also contains less material so although the evaporation rate is lower it will take less time for all of the flux to evaporate than for a large crucible containing a lot of material. This means that scaling up a reaction can

produce completely different results. To prevent variations in the evaporation rate effecting the outcome of the flux growth the same sized platinum crucible and similar masses of starting material were used as much as possible. However, a smaller platinum crucible had to be used for reactions carried out in the tube furnace (growths SIO#14A+14B) and the alumina and zirconia crucibles used would have had a slightly larger cross-sectional area than the platinum crucible.

4.2.3 Other factors

Adding seed crystals of the desired phase seemed to aid the formation of large crystals of that particular phase (as seen in SIO#F7 and SIO#F32) but ultimately other crystal growth conditions were more dominant in determining the phase formed and crystals of a useable size could still be formed without adding seed crystals.

Carrying out the flux growth under flowing oxygen does seem to help the amount of IrPt impurity formed but results in only a few very small crystals being produced. It is possible that small pieces of the IrPt alloy help to seed crystals of $Sr_{x+1}Ir_xO_{3x+1}$.

4.2.4 Summary of optimum crystal growth conditions

Table 4.4 summarises the crystal growth conditions used to grow six batches of $Sr_3Ir_2O_7$ crystals, the quality of which are investigated in section 4.4. These crystal growth conditions appear to be most similar to those used by C. Dhital et al (see table 4.3), however for most of these growths a slightly lower dwell temperature and off-stoichiometric quantities of $SrCO_3$ and IrO_2 were used. This has produced a much thicker and regular morphology of crystal than those reported in the literature.

The optimum crystal growth conditions for Sr_2IrO_4 and $SrIrO_3$ were from growths SIO#F11 and SIO#F15 and SIO#F7, which are shown in table 4.5. The Sr_2IrO_4 crystal growth conditions are similar to those of K. Ishii et al except that the cooling rate is twice as fast for SIO#F11 and the dwell temperature for SIO#F15 is lower. A less than stoichiometric ratio of $SrCO_3$ was also used.

Name	Starting materials	Temperature	Cooling rate	Crystal morphology
SIO#F1	$1.8SrCO_3$:$1IrO_2$:$15SrCl_2$	1300°C for 12 hours	8.00°C/hour to 900°C	Thick cuboidal.
SIO#F5	$1.35SrCO_3$:$1IrO_2$:$15SrCl_2$	1300°C for 12 hours	4.57°C/hour to 900°C	Thick cuboidal.
SIO#F17	$1.35SrCO_3$:$1IrO_2$:$7.5SrCl_2$	1200°C for 12 hours	4.00°C/hour to 1100°C	Plate-like.
SIO#F18A	$1.20SrCO_3$:$1IrO_2$:$7.5SrCl_2$	1200°C for 12 hours	4.00°C/hour to 1100°C	Square.
SIO#F18B	$1.00SrCO_3$:$1IrO_2$:$7.5SrCl_2$	1200°C for 12 hours	4.00°C/hour to 1100°C	Square.
SIO#F19B	$1.00SrCO_3$:$1IrO_2$:$12SrCl_2$	1200°C for 12 hours	4.00°C/hour to 1100°C	Square.

Table 4.4 *Crystal growths conditions found for growing $Sr_3Ir_2O_7$*

Name	Starting materials	Temperature	Cooling rate	Product
SIO#F11	$1.45SrCO_3$:$1IrO_2$:$15SrCl_2$	1300°C for 12 hours	4.57°C/hour to 900°C	Plate-like crystals of Sr_2IrO_4.
SIO#F15	$1.35SrCO_3$:$1IrO_2$:$15SrCl_2$	1245°C for 12 hours	7.92°C/hour to 1150°C	Plate-like crystals of Sr_2IrO_4.
SIO#F7	$1.35SrCO_3$:$1IrO_2$:$10SrCl_2$	1200°C for 12 hours	4.00°C/hour to 1000°C	Hexagonal bipyramidal crystals of $SrIrO_3$.

Table 4.5 *Crystal growths conditions found for growing Sr_2IrO_4 and $SrIrO_3$*

4.3 Structural and bulk characterisation of $SrIrO_3$

While exploring the SrO-IrO_2 phase diagram, crystals of ambient pressure monoclinic form of $SrIrO_3$ were grown. These were easily distinguishable from other crystals by their hexagonal bi-pyramidal morphology and were up to 600 μm in size in batch number SIO#F7 (see figure 4.7). The same ratio of starting materials were used for this batch as for growths that produced crystals of $Sr_3Ir_3O_7$. The different outcomes may be due to seed crystals of $SrIrO_3$ being added to the mixture or the fact that the average temperature was lower than in other growths. The bulk properties of these crystals were measured to confirm published work by Cao et al [30] that claimed that $SrIrO_3$ was a non-fermi liquid metal close to a ferromagnetic instability. We also wished to test their hypothesis that $SrIrO_3$ would superconduct at sub 1.7 K temperatures.

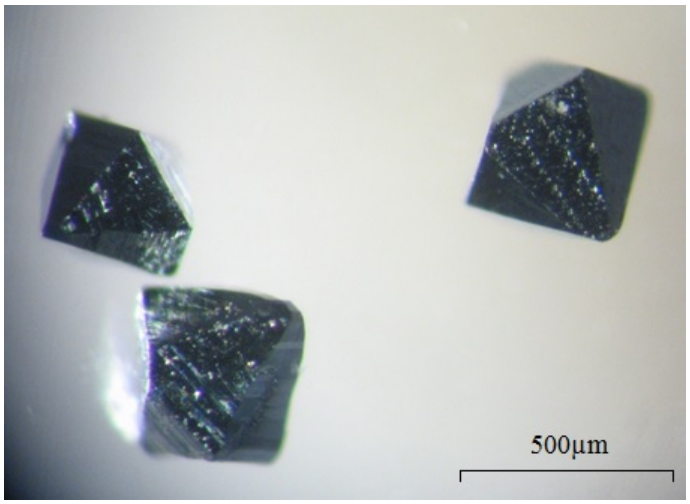

Figure 4.7 *Crystals of $SrIrO_3$ as grown by flux growth.*

Approximately 5-10mg of $SrIrO_3$ crystals were ground in a pestle and mortar and powder x-ray diffraction data were collected on the Bruker D8 diffractometer at the Centre for Science at Extreme Conditions (CSEC) at the University of Edinburgh. The data was refined using GSAS and was found to be a reasonably good fit to the structural model determined by I. Qasim et al by powder neutron diffraction[109]. The refinement is shown in figure 4.8 and has a reduced χ^2 value of 5.225 and a R_{wp} of 0.882. The diffraction pattern also appeared to be phase pure with no sign of elemental iridium. The lattice parameters were refined to be a=5.604(7) Å; b=9.608(1) Å and c=14.173(2)Å with a beta angle of 93.265(4)°, which differ slightly from the unit cell found be powder neutron diffraction of a=5.60401(29) Å; b=9.6256(4) Å; c=14.1834(7) Å and β=93.202(4)°.

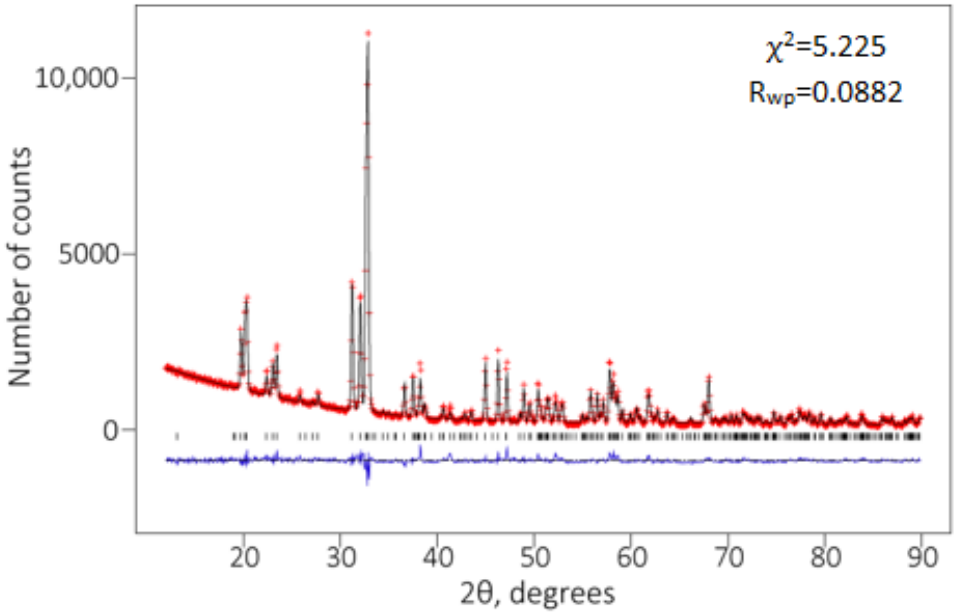

Figure 4.8 *Rietveld refinement of x-ray powder diffraction data collected on crushed crystals of $SrIrO_3$.*

In Cao et al's paper [30] the ferromagnetic instability is evidenced by a sharp upturn in the magnetic susceptibility below 15 K, the inverse of which follows non-standard power laws between linear T and $T^{1/2}$ depending on the magnitude of the applied field. However, this upturn could also be due to the crystals containing a paramagnetic impurity particularly as the reported *RRR* (Residual resistance ratio) of the crystal was only 3 and the fact that the upturn is field dependent. In the heat capacity there is an upturn below 2.5 K in an applied field less than 3 T that has a -log T temperature dependence, which is used as evidence for $SrIrO_3$ being a non-fermi liquid. The *ab* plane resistivity has a $T^{3/2}$ power law below 120 K (see figure 4.9) rather than the T^2 power law expected of a Fermi-liquid material, however, in a dirty metal the low temperature T^2 power law can be disrupted by electron scattering as the residual resistivity is approached. The reported *ab* plane residual resistivity of 2.2 $\mu\Omega$cm also seems unrealistically small considering the crystal's low *RRR* and the fact that the sample was grown by flux growth. In comparison ultra pure Sr_2RuO_4 grown by the floating zone method has a room temperature resistivity of around 1.2 $\mu\Omega$cm at room temperature. The low temperature mass enhancement of the Wilson ratio provides more compelling evidence for the proximity of the system to a quantum critical point, which the paper predicts should occur at fields below 0.3 T and temperatures below 1.7 K. From these observations, the author predicts that $SrIrO_3$ may be a triplet-paired superconductor due to the phenomena's association with weak ferromagnetism

near a quantum critical point.

The resistivity of as grown $SrIrO_3$ from batch SIO#F7 from 300 K to 2 K is shown in figure 4.10. The resistivity was measured in the *ab* plane, the same as in Cao's paper. Due to the difficult sample morphology the crystals had to be polished along the (001) direction to create a large surface area in the *ab* plane to which the gold wires could be attached. Similar to Cao's sample, the resistivity has a $T^{3/2}$ temperature dependence but only from 100 K to 34 K. At temperatures below 15 K the resistivity exhibits a T^2 temperature dependence that would be expected of a Fermi liquid metal. The magnitude of the residual resistivity, ρ_0, of my samples is an order of magnitude higher than those studied by Cao at 40 $\mu\Omega$cm but despite indicating a poorer quality sample this value is more realistic for a sample grown by flux growth. The ρ_0 of Cao's sample seems too low when compared to other samples in the literature. Comparing values of ρ_0 between my sample and Cao's is unreliable as there could be a large error on the magnitude of the resistivity due to the non-rectangular dimensions of the sample. Comparing the RRR values of samples is a better way to assess sample quality as it is a dimensionless quantity that is independent of the absolute magnitude of the resistivity. The RRR of my samples is about 15 compared to 3 for Cao's samples so my samples are 5 times better in quality. Thus the absence of the T^2 low temperature power law in Cao's data may have been due to poor sample quality.

Despite the T^2 power law at low temperatures, the sample was measured down to 20 mK using the dilution fridge at St Andrew's University to look for evidence of superconductivity. Jack Barraclough and Ed Yelland conducted the measurement, although I assisted with the sample set up. The data is shown in part (d) of figure 4.10. From the data there appears to be an onset of superconducting transition, T^*, at 78 mK, however the transition is incomplete as the resistance does not reach zero. The superconductivity disappeared on the application of a field of 0.5 T and could not be recovered, however, the critical field of the sample must be at most 0.0015 T, which was the residual field left when we tried to re-measure the resistivity at 0 T. This very small critical field is indicative of a type I superconductor and given that metallic elements often exhibit type I superconductivity we checked the superconducting transition temperatures of the elements in $SrIrO_3$. It was found that the superconducting transition temperature of Ir metal is 112.5 mK while it is 1.9 mK for Pt metal and given the small critical field it is likely that the transition at 78 mK is from induced superconductivity

from the sample containing a small amount of a $Ir_{0.9}Pt_{0.1}$ alloy at levels below the background in the powder x-ray diffraction pattern. The sample was measured up to 15 T at 20 mK, with the field applied along the (001) axis, but no dHvA quantum oscillations were observed.

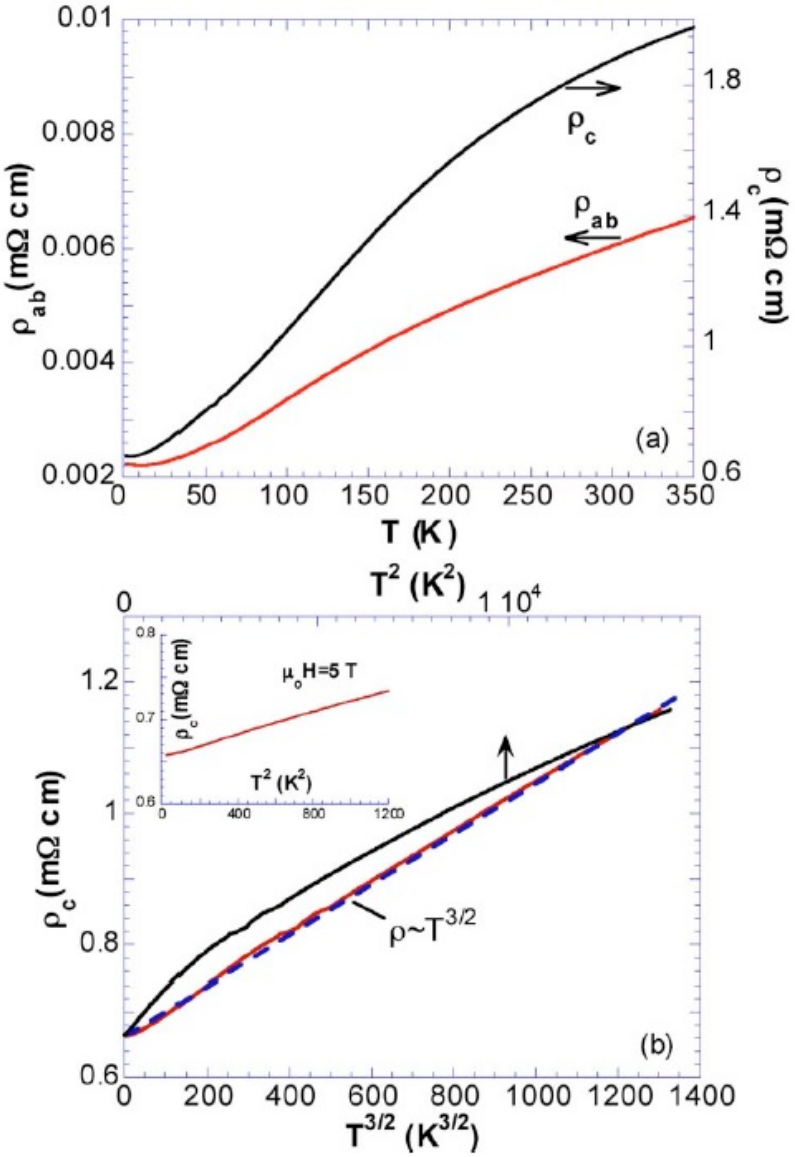

Figure 4.9 *Data from Cao's paper to demonstrate the $T^{3/2}$ power law in the ab plane resistivity.*

The heat capacity and magnetic susceptibility of the sample was also re-measured to compare our crystals to those in the literature. As shown in figure 4.11 the magnetic susceptibility of $SrIrO_3$ was largely temperature independent, as would be expected of a metal, with a small upturn below 30 K. χ_0 was measured to be around 8.8×10^{-4}, which is around a factor of three smaller than published in

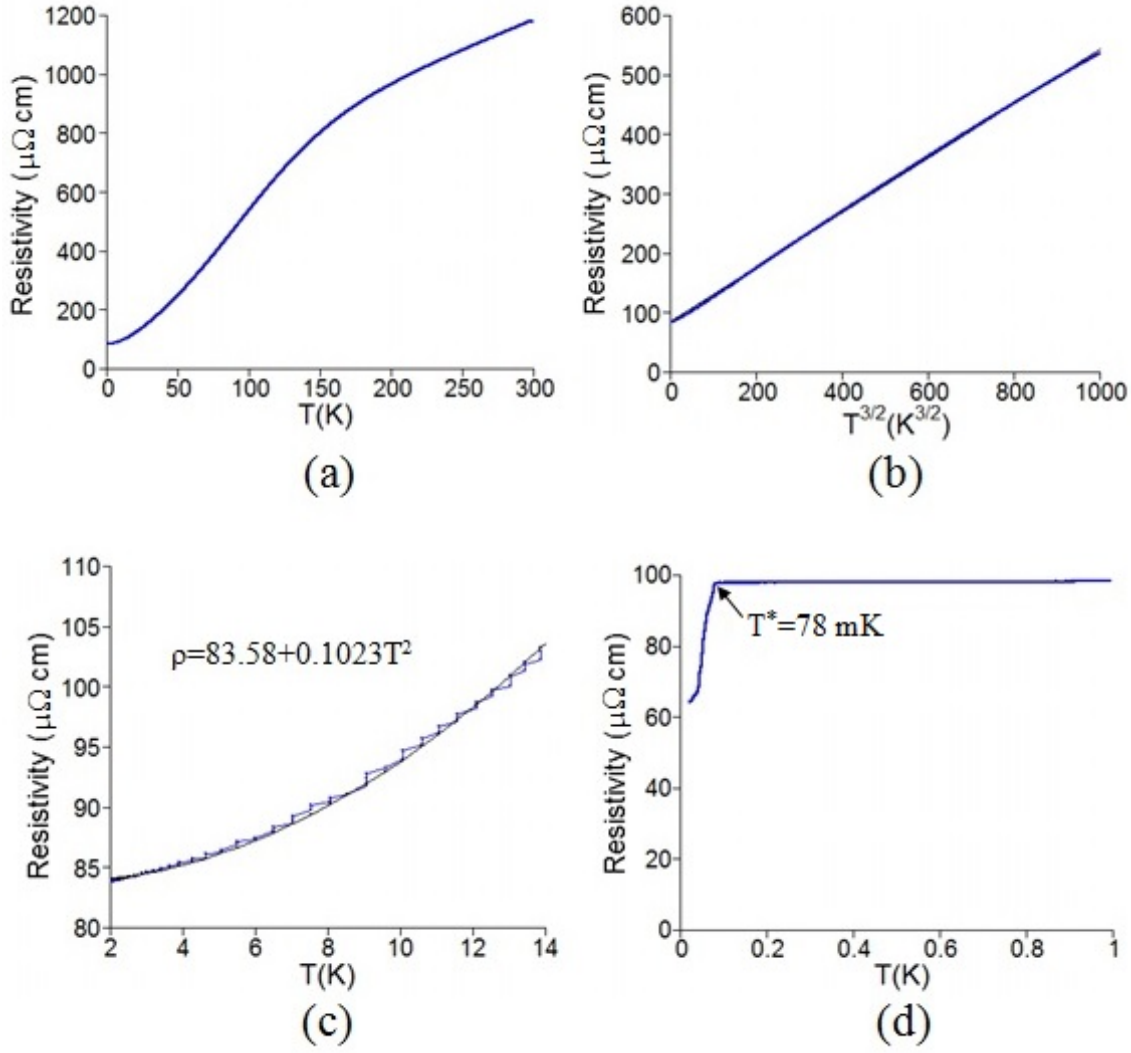

Figure 4.10 *The temperature dependence of the resistivity of $SrIrO_3$ in zero field. (a) The resistivity from 2-300K. (b) The $T^{3/2}$ dependence of the ab plane resistivity from 34-100 K. (c) The T^2 temperature dependence of $SrIrO_3$ below 14 K. (d) Dilution fridge measurements from 1 K down to 20 mK.*

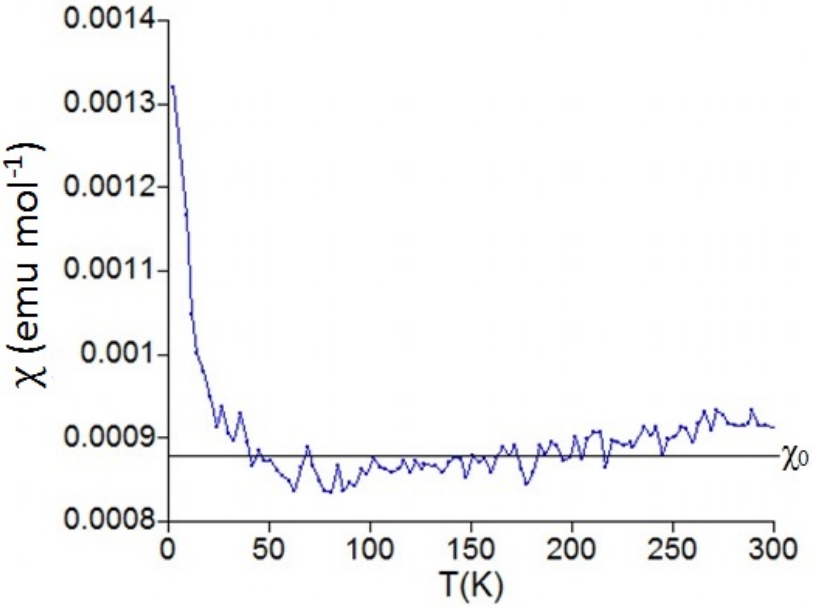

Figure 4.11 *The magnetic susceptibilility of a crystal of $SrIrO_3$ with the field of 20,000 Oe applied parallel to the c axis.*

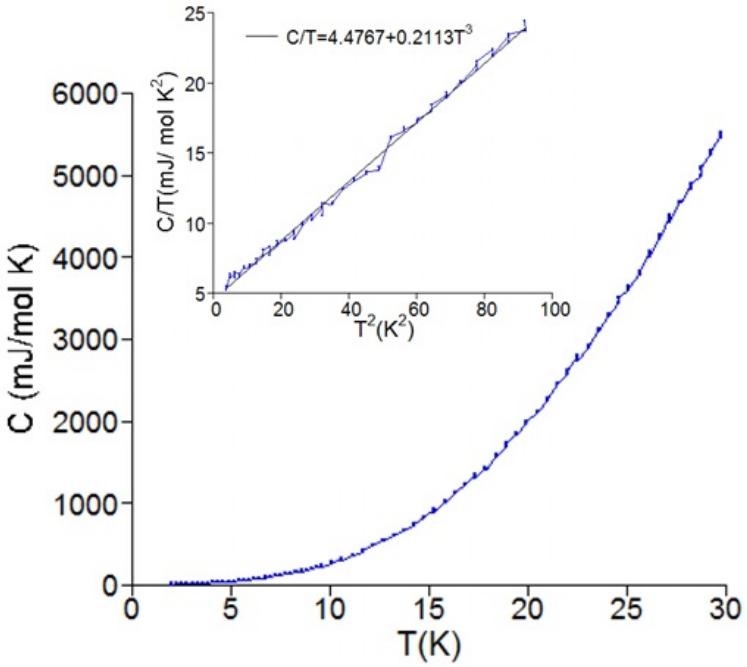

Figure 4.12 *The heat capacity of a 1.7 mg crystal of $SrIrO_3$ measured using an applied field of 7 T from 2-30 K.*

Cao's paper (χ_0=2.5×10^{-3}) and the same order of magnitude as IrO_2. Thus we did not observe a significant exchange enhancement of the moment in our sample. The upturn, which is smaller than published, is probably due to the inclusion of an impurity in the crystals.

The heat capacity, as shown in figure 4.12, was measured at 7 T to prevent any possible upturn so that the Sommerfeld coefficient, γ, could be extracted from a low temperature fit of C/T against T^2. γ gives a measure of the strength of the electron-electron correlations in a material and was found to be 4.48 mJ/Ir mol K^2 for $SrIrO_3$. This means that the electron-electron correlations are relatively weak. The magnitude and behaviour of C/T at 7 T is in agreement with the data published by Cao et al. By combining χ_0 and γ, the Wilson ratio was calculated to be 1.43 in accordance with equation 3.8 in section 3.2.3. A free electron gas has a Wilson ratio of 1 and deviations away from this value are due to electron-electron correlations. This R_W value of 1.43 shows that $SrIrO_3$ possesses some electron correlations but is still a Fermi-liquid. It is also not a heavy fermi material as R_W is less than 2.

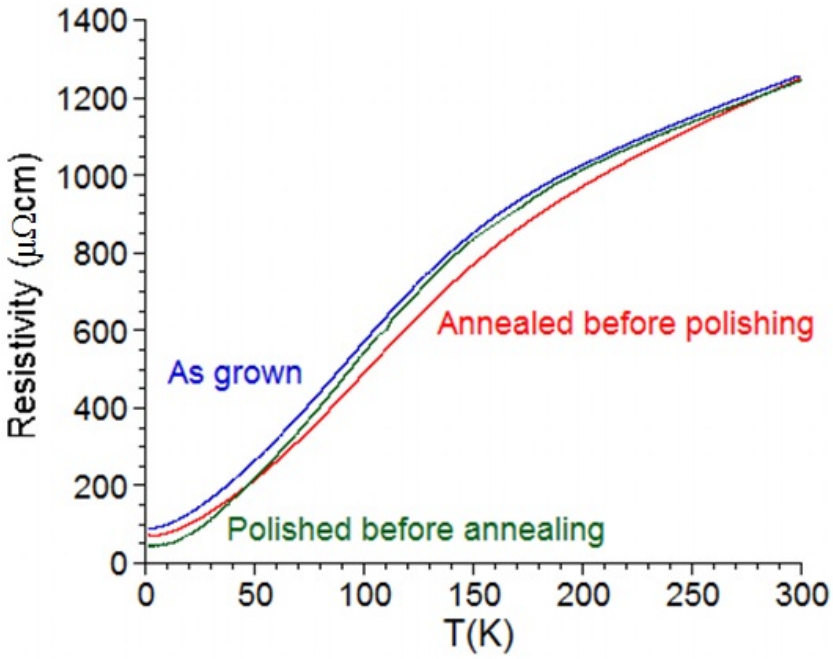

Figure 4.13 *The effect of annealing crystals of $SrIrO_3$ under flowing O_2 at 900°C for a week on the temperature dependence of the resistivity.*

Following the dilution fridge experiment some annealing experiments were conducted on the crystals to see whether the sample quality could be improved. An as grown crystal and a crystal pre-polished to a thin slice were annealed for a week at 900°C under flowing oxygen. The results are shown in figure 4.13. The

as grown crystal that was polished to a thin slice after it had been annealed had an RRR of 18, which is a slight improvement on the non-annealed crystal that had an RRR of 15. The crystal that had been polished to a thin slice before annealing under flowing oxygen had an even higher RRR of 27.8. Thus if any further high field dHvA experiments were to be conducted on these samples in the future it would be recommended to anneal a thin slice of the crystal in oxygen for a week first to improve the quality of the sample and the likelihood of observing quantum oscillations.

In conclusion $SrIrO_3$ was found to be a weakly correlated fermi liquid with no exchange enhancement of the magnetic moment. Dilution fridge measurements also found no superconducting transition in the region of the predicted critical point. The non T^2 power law at low temperatures reported by Cao previously may have been due to poor sample quality as we observe a T^2 power law with our better quality samples.

4.4 The effect of crystal quality on the properties of $Sr_3Ir_2O_7$

In section 4.2 crystals of $Sr_3Ir_2O_7$ were grown under different conditions. In this section the structural and bulk properties of the crystals from these different batches are compared to check for batch variation and to investigate how the ground state is effected by crystal quality. Initially six batches containing $Sr_3Ir_2O_7$ were studied. These were SIO#F1, SIO#F5, SIO#F17, SIO#F18A, SIO#F18B and SIO#F19B and the growth conditions used to grow crystals from each of these batches can be found in table 4.4.

4.4.1 EPMA

Electron probe microanalysis (EPMA) was used to determine the chemical composition of the crystals, to firstly check if the crystals were stoichiometric and to secondly check whether there is batch variation in the composition. Five different crystals from each batch were measured to determine compositional variation between crystals within a batch and between batches. On each crystal five points were measured - one towards each corner of the square sample and one in the centre. This ensured that the points were representative of the whole sample rather than one small domain. The small beam size of 1 μm allowed variations in the composition across an individual crystal to be measured. In order to accurately calculate the ratio of Sr:Ir:O at each point the EPMA was calibrated using a range of materials, provided by the Geosciences department, of known composition. These were Ir metal, $SrSO_4$ (also known as celestite) and $HfSiO_4$ (or Hafnon). Pt metal and NaCl calibrants were also used so that the crystals could be checked for inclusions from both the platinum crucible and the $SrCl_2$ flux used to grow the crystals. To get a good resolution, edges for each element were chosen that did not overlap with each other. The edges used were as follows: O K_α, Ir M_α, Cl K_β, Sr L_α, Pt M_β and Cl K_β. The amount of platinum and chlorine detected in the samples was negligible so these elements were excluded from the rest of the analysis.

Only relative ratios of elements can be determined from EPMA and the crystals appeared to be strontium deficient or iridium rich so the amount of iridium was set at 2 as vacancies on the strontium site in the structure are more likely. The results

are shown in figure 4.14. The majority of the crystals appear to be strontium and oxygen deficient with an average chemical composition across all of the crystals of $Sr_{2.87}Ir_2O_{6.27}$. This gives the iridium ion an oxidation state of +3.4 so this oxygen deficiency is having the effect of electron doping the material. When electrons are doped into a Mott-Hubbard insulator the electrons are added to the upper Hubbard band, which raises the Fermi level and turns the material metallic. $Sr_{2.87}Ir_2O_{6.27}$ is not metallic though and that's because adding electrons also increases the onsite coulomb repulsion, U, and can reduce the bandwidth, t, to reduce the ability of electrons to hop between ions so that the carrier electrons remain localised.

There is some compositional variation across a crystal of typically ±0.03 Sr per formula unit and ±0.10 O per formula unit. However this is within the error on each individual measurement of ±0.03 Sr per formula unit and ±0.04 O per formula unit (arising from a 0.5% error on the O weight percentage) so is not statistically significant. Except for a few crystals in batches F18A and F18B there also appears to be little crystal to crystal variation within a batch and between batches. This can be more clearly seen in table 4.6, where the average number of strontium and oxygen ions per formula unit in each batch has been calculated with the standard deviation in brackets. With the exception of batch F18B, the variation in the mean strontium content of the batches is within a standard deviation of the other batches. The variations in the oxygen content are also less than the measurement error on each reading so it is hard to be confident in the small variations in oxygen content seen between the batches.

Batch Name	**Mean number of Sr ions per formula unit**	**Mean number of O ions per formula unit**
F1	2.84(3)	6.203(5)
F5	2.84(2)	6.220(5)
F17	2.82(2)	6.238(1)
F18A	2.87(5)	6.27(2)
F18B	3.0(1)	6.41(6)
F19B	2.86(4)	6.2978(8)

Table 4.6 *The mean number of strontium,* x*, and oxygen ions,* y*, per formula unit per batch of* $Sr_xIr_2O_y$.

Using the high magnification on the transmission light microscope on the SEM it was was possible to see inclusions of other phases in some of the crystals. Some

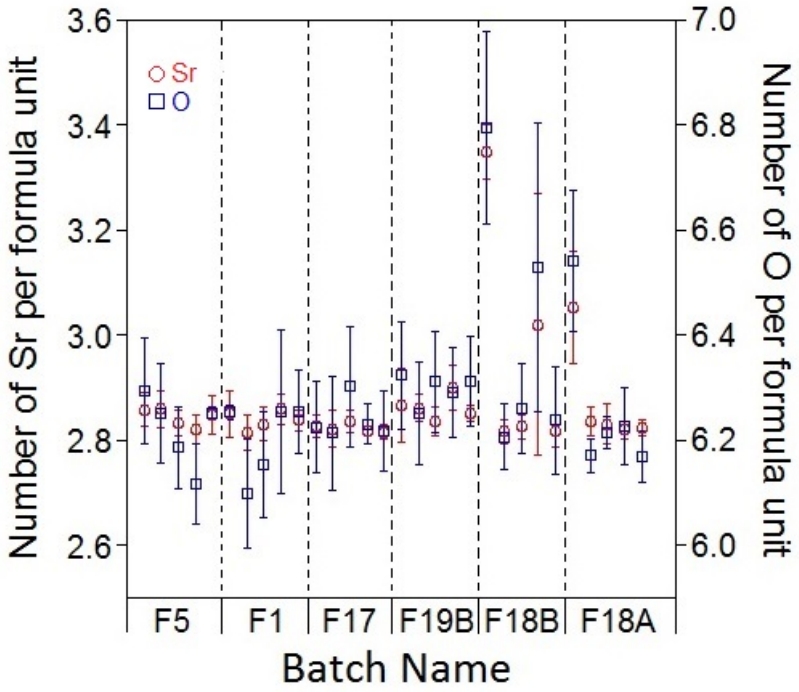

Figure 4.14 *The measured number of Sr ions,* x*, and the number of oxygen ions,* y *in each crystal of* $Sr_xIr_2O_y$.

photos of single phase crystals and photos demonstrating the different impurities seen are shown in figure 4.15. The pinkish coloured impurity was measured to be an iridium platinum alloy of an approximate composition of $Ir_{0.9}Pt_{0.1}$. It was observed in some crystals from every batch but was most prevalent in batches F18B, F19B and F5 with batch F18B qualitatively containing the most $Ir_{0.91}Pt_{0.09}$ alloy. There was also a light blue impurity phase that has a composition and (in the case of the photo of a crystal from F19B) closer to $SrIrO_3$. This impurity was most prevalent in batches F18A and F19B. The crystals from batches F1 and F17 appeared to contain the fewest (if any) impurity phases. Combined with the variation in the strontium and oxygen content of the crystals, which is the largest for batches F18A and F18B batches F1, F17 and F5 appear to be the best quality batches and F18A, F18B and F19B appear to be the lowest quality.

It is interesting to compare the quality of the crystals to the crystal growth conditions. Looking back at the conditions in table 4.4 the poorest quality batches, SIO#F18A,B+19B, have the lowest starting ratios of $SrCO_3$ of 1.2, 1.0 and 0.8 while batches SIO#F1, F5 and F17 have $SrCO_3$ molar ratios of 1.8, 1.35 and 1.35. If the quality was based on the starting molar ratio of $SrCO_3$ alone then SIO#F1 would be expected to be of the best quality and

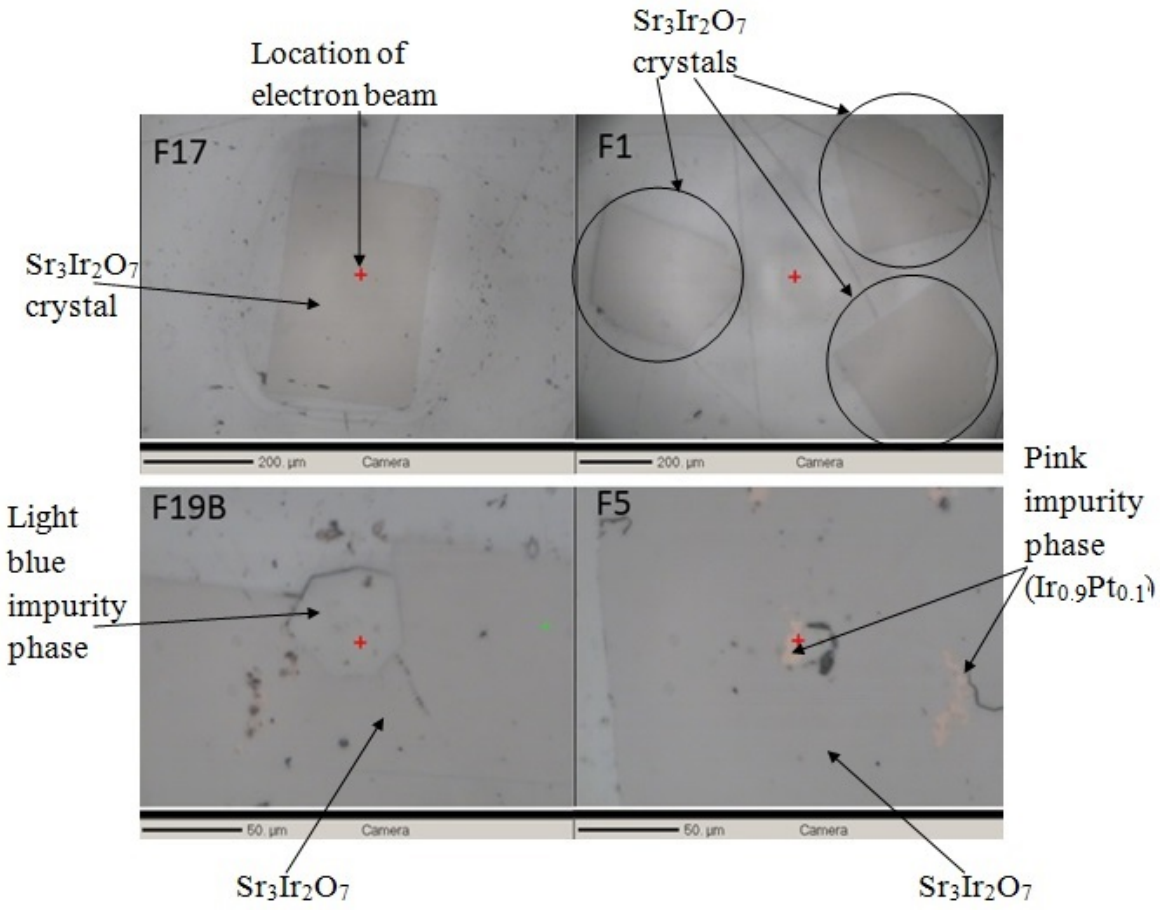

Figure 4.15 *Transmission light microscopy photos of $Sr_3Ir_2O_7$ crystals two phase pure crystals from batches SIO#F17 and SIO#F1, a crystal from batch SIO#F19B possibly containing an intergrowth of $SrIrO_3$ (pale blue area) and a crystal from batch SIO#F5 containing an $Ir_{0.9}Pt_{0.1}$ alloy impurity (pink areas).*

batches SIO#F5 and SIO#F17 would be of a similar quality. However, the initial starting temperature also impacts on the crystal quality as the higher initial starting temperature of 1300°C for batches SIO#F1 and SIO#F5 reduces the quality of these batches by encouraging the formation of the $Ir_{0.8}Pt_{0.2}$ alloy in the more reducing conditions. This results in batches SIO#F1 and SIO#F5 being of lower quality than SIO#F17, which had a lower initial starting temperature of 1200°C. This gives the observed order in crystal quality of SIO#F17 < SIO#F1 < SIO#F5.

The rest of this section focuses on just four batches - SIO#F1, SIO#F5, SIO#F17 and SIO#F19B for simplicity by excluding the two batches that showed the greatest crystal to crystal variation and that were among the worst quality crystals in terms of the number of impurities that they contained. The strontium content of the four chosen batches does not vary significantly but represent average oxygen contents ranging from 6.2 to 6.4 per formula unit. While EPMA is an important tool, bulk measurements will be used to confirm variations in the crystal quality.

4.4.2 Powder x-ray diffraction

To check for phase purity and to refine the structural parameters, powder x-ray diffraction data was collected on approximately 30 ground up crystals from each of the 4 batches over an angular range of 10-125° (with the exception of batch F5, which was only measured up to 90°). More information on the Rigaku diffractometer that was used is given in section 3.2.5. The data were refined using GSAS as detailed in section 2.9.1. Due to the large effective mass on iridium, it scatters x-rays more strongly and dominates intensity of the Bragg reflections in comparison to oxygen. This makes it difficult to refine the occupancy of the oxygen site accurately. The ratio of the elements were known from EPMA, however, efforts to refine all of the occupancies with constraints added to the refinement to maintain this ratio resulted in the oxygen occupancy becoming unrealistically low. Therefore the occupancies were fixed to the values determined by EPMA with the occupancy of the iridium site being set at 1. The z coordinate of the iridium site was refined first, followed by the z coordinate of the Sr(2) site, however the oxygen coordinates were not refined. In order to compare the structural parameters, all of the refinements were carried out using the B*bcb* space group model. The I4/mmm model could have equally been used as it accounted

for all of the peaks but given that the B*bcb* model has been determined to be more accurate from x-ray synchrotron studies and electron diffraction studies, it was chosen to give a more accurate representation of the structure.

Key parameters from the Rietveld refinement are shown in table 4.7. There is some variation in the lattice parameters and the volume of the unit cell from batch to batch that is outside of the error of the refinement. The actual error on each parameter will be larger than stated due to the tendency of the refinement to converge on a particular potential local minimum. In the literature the lattice parameters for undoped $Sr_3Ir_2O_7$ have ranged from 5.50Å to 5.522Å for the a and b lattice parameters and from 20.860Å to 20.93Å for the c lattice parameter so my values are within the correct range (more details of published lattice parameters given in table 4.8). The variation in the lattice parameters in the literature may be due to sample variation caused by differing crystal growth conditions. The z coordinate of the Ir and Sr(2) ion positions are reasonably close for all samples. Despite batches SIO#F1 and SIO#F5 having the most similar chemical compositions the unit cell volumes are the most different so there does not appear to be a correlation between unit cell volume or lattice parameters with the chemical composition of the sample.

Single crystal x-ray diffraction data were collected on three crystals of $Sr_3Ir_2O_7$ taken batch SIO#F17. The refined unit cells of each crystal are in Appendix C. The crystals were refined in the I4/mmm space group as extra reflections associated with the B*bcb* space group were not detectable on the Agilent Gemini diffractometer. The average bond lengths across all three crystals, with a multiplied by $\sqrt{2}$ to be comparable to the B*bcb* space group, are a=5.5140Å and c=20.8963Å. These bond lengths are fairly close to those refined from powder x-ray diffraction. The average Ir z position was found to be 0.0975, which is symmetrically equivalent to 0.4025 and within error of the value of 0.40257 refined for batch SIO#F17. The average Sr(2) z position was found to be 0.1864, which is markedly lower than the values refined from x-ray powder diffraction data. This shows that the position of heavier atoms such as iridium are refined more accurately than lighter atoms from powder x-ray diffraction data. Compared to Subramanian's data [129] where the apical Ir-O3 bond lengths is 1.990 Å, the axial Ir-O2 bond length is 2.014 Å and the bridging Ir-O1 bond length is 2.034 Å the average Ir-O bond lengths of the SIO#F17 crystals differ with the Ir-O3 and Ir-O2 bond lengths being near identical at 1.985Å and 1.984Å respectively while the bridging Ir-O1 bond length is longer at 2.041Å. These differences in the

environment around the iridium ions could be responsible for the slightly different properties seen between batches but neutron diffraction would be required to accurately determine the oxygen positions and hence the Ir-O bond lengths.

In terms of phase purity, no sign of the $Ir_{0.91}Pt_{0.09}$ impurity was seen in any of the powder diffraction patterns, which suggests that it is less than 1% to be below background level. However it was possible to detect $SrIrO_3$ in batches F19B and F5, in agreement with the transmission light microscopy study, and the percentage weight of $SrIrO_3$ in these batches was fitted to be 5% and 3.5% respectively.

Batch Name	χ^2	**a** ($\AA$)	**b** ($\AA$)	**c** ($\AA$)	**Unit cell volume** ($\AA^3$)	**Ir z position**	**Sr z position**
SIO#F1	2.609	5.514(5)	5.514(5)	20.8984(3)	635.8984(3)	0.40284(7)	0.1876(1)
SIO#F5	3.342	5.513(2)	5.512(2)	20.8842(8)	634.57(5)	0.4026(1)	0.1878(2)
SIO#F17	1.312	5.5173(2)	5.5146(2)	20.8969(2)	635.81(2)	0.40257(7)	0.1874(1)
SIO#F19B	1.067	5.5144(2)	5.5182(2)	20.8966(3)	635.88(2)	0.40288(6)	0.18801(9)

Table 4.7 *Key parameters from the Rietveld refinement of the x-ray powder diffraction patterns from different batches of ground crystals of* $Sr_3Ir_2O_7$.

Source	a ($\AA$)	b ($\AA$)	c ($\AA$)	Unit cell volume ($\AA^3$)
H. Matsuhata et al, Journal of Solid State Chemistry, **177**(10), (2004), 3776	5.5191	5.5191	20.9300	637.538
G. Cao et al, Physical Review B, **66** (2002) 214412	5.5221	5.5214	20.9174	637.766
M.A. Subramanian et al, Materials Research Bulletin, **29**, (1994), 645	5.5112	5.5112	20.892	634.560
C.Dhital et al, Physical Review B, **86**, (2012), 100401(R)	5.50	5.50	20.860	631.015
S. Fujiyama et al, Physical Review B, **86** (2012) 174414	5.5108	5.512	20.8832	634.338

Table 4.8 *A range of the lattice parameters for $Sr_3Ir_2O_7$ published in the literature*

4.4.3 Resistivity

The resistivity of up to two crystals from each batch were measured using a 4 point measurement on the CCR system at the Centre for Science at Extreme Conditions in Edinburgh as outlined in section 3.2.2.To focus on the temperature regime where the antiferromagnetic ordering occurs the resistivity was measured between 320 K and 240 K. In this temperature regime the absolute resistivity is below 100 mΩcm, so the A.C. resistivity was measured to get better quality data. The Néel temperature is marked by a discontinuity in the gradient to be more negative (or insulating) below T_{N}. A few of the samples were also measured down to 50 K, to confirm that the crystals were insulating to low temperatures. The sample dependence of T_{N} provides another indication of sample quality as disorder and impurities within a sample are known to supress long-range magnetic order and consequently lower T_{N}. For Sr_2IrO_4, removing just 0.04 oxygens per formula unit had a dramatic effect on the relative magnitude of the resistivity[75] and so the small differences in the oxygen content of crystals from different batches of $Sr_3Ir_2O_7$ may also cause changes to the relative magnitude of resistivity.

The results are shown in figure 4.16 with the derivative shown in figure 4.17. Key values from these two plots are summarised in table 4.9. It can be seen that there is a change in the absolute resistivity at 300 K depending on the

sample with values ranging from 2.9 mΩcm to 9.9 mΩcm. This varies from the literature values of 30 mΩcm, the reason for this variation is unclear. There will be around a large error in the absolute values of ρ due to error in the sample dimensions, particularly from measurement error on the sample thickness, and there are no order of magnitude changes in the resistivity between crystals from different batches. The crystals from batch SIO#F1 have the highest values for ρ_{300K} and are consequently closest to the literature values. The batches in order of the most oxygen deficient first are SIO#F1 > SIO#F5 > SIO#F19B > SIO#F17 so the absolute magnitude of the resistivity bears no correlation to the oxygen composition of the samples.

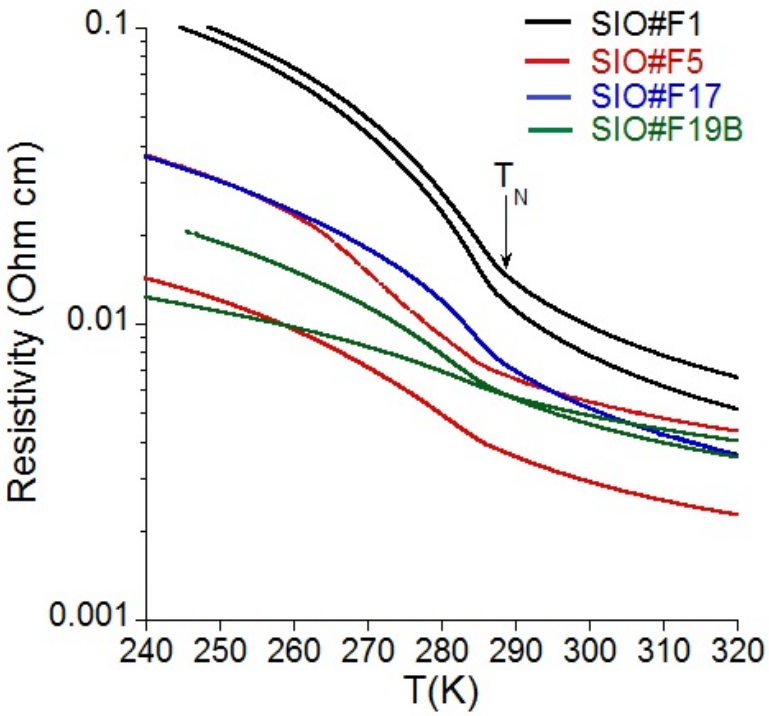

Figure 4.16 *The variation of the resistivity with temperature of crystals of from several different batches of $Sr_3Ir_2O_7$ from 320K to 240K.*

The derivative of the logarithm of the conductivity with respect to inverse temperature allows T_N to be approximated from the onset of the sharp decrease in the derivative on going through the transition. Comparing the derivatives removes the error from the absolute resistivity to provide a more accurate batch comparison, particularly as the derivatives were normalised to be identical at 290 K. The peak broadness or full-width-half-maximum (FWHM) also gives information about the broadness of the antiferromagnetic transition, which correlates to the amount of disorder in the crystal. In theory the better the quality

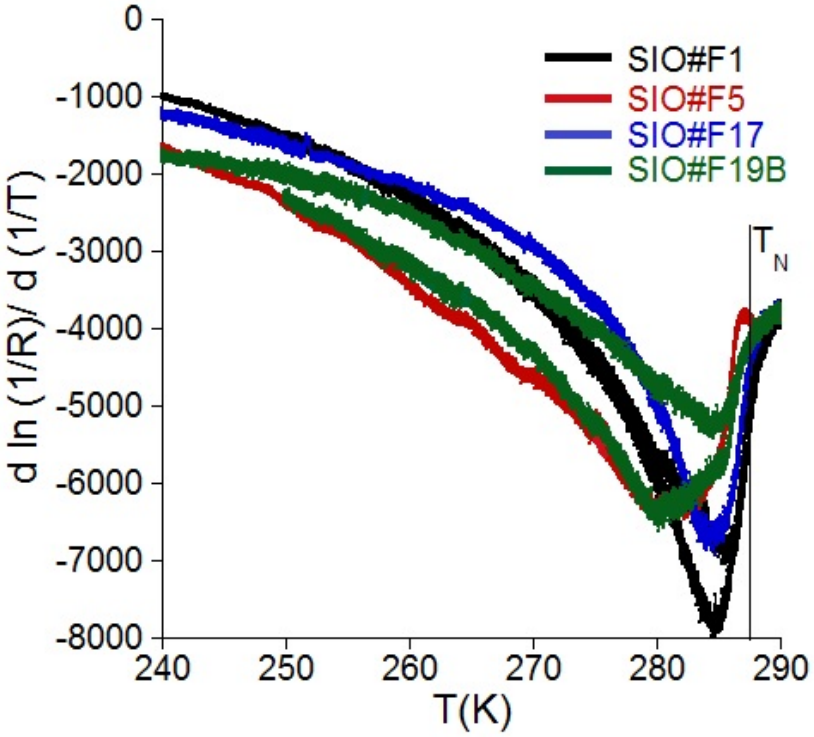

Figure 4.17 *The derivative of the logarithm of the inverse of the resistivity with respect to 1/T for crystals of from several different batches of $Sr_3Ir_2O_7$ from 320K to 240K.*

of the crystal, the sharper the transition and the higher T_N will be as disorder and impurities in a crystal can delay the onset of magnetic order. The crystals from batches SIO#F1 and SIO#F17 appear to have slightly higher values of T_N than crystals from batches SIO#F5 and SIO#F19B, however this difference is only very small at 1 K and so is probably not significant. The crystals from batches SIO#F5 and SIO#F19B seem to have broader and weaker transitions than the crystals from batches SIO#F1 and SIO#F17, which indicates that crystals from these batches may be more disordered. This along with the lower resistivities and the $SrIrO_3$ impurity detected in powder x-ray diffraction makes these two batches lower in quality than batches SIO#F1 and SIO#F17. However all of these variations in the resistivity are very small and do not correlate with the variations seen in the lattice parameters and the chemical composition of crystals from each batch.

Crystal Name	ρ_{300K}**(mΩcm)**	T_N**(K)**	**FWHM(K)**
SIO#F1 C1	9.9	287.5	9
SIO#F1 C2	7.8	287.5	7
SIO#F5 C1	5.5	n/a	n/a
SIO#F5 C2	2.9	286	11
SIO#F17 C1	5.3	287	6
SIO#F19B C1	4.9	286	7
SIO#F19B C2	4.6	286	11

Table 4.9 *Key parameters from the resistivity measurements on the different batches of $Sr_3Ir_2O_7$.*

Annealing experiments

EPMA had shown all of my samples to be oxygen deficient and resistivity measurements have not shown any correlation with the slight differences in the oxygen content of the samples. EPMA is more accurate at determining the oxygen content of a sample than EDX but both techniques struggle with measuring the concentration of lighter atoms. Thermogravimetric analysis (TGA) would be able to more accurately confirm whether the $Sr_3Ir_2O_7$ crystals are truly oxygen deficient. To explore further the effect of the oxygen content in the samples on their bulk properties, annealing experiments were conducted under reducing atmospheres to try and create further oxygen deficiencies. These experiments would determine whether a greater variation in the oxygen content was needed to observe the order of magnitude changes in the resistivity seen in oxygen

depleted Sr_2IrO_4[75]. Creating oxygen deficiencies in the crystals under reducing conditions would have the effect of adding electrons to the system. Initially crystals of $Sr_3Ir_2O_7$ were annealed under a 5% H_2:95% Ar gas mixture at 700°C and 500°C for a few days, however, in both cases x-ray diffraction revealed that the crystals has reduced to Ir metal. Crystals were then annealed under Ar gas for 6 days at 500°C and when no impurities were found in the x-ray diffraction pattern the annealing temperature was increased to 600°C and the crystals were annealed for a further week to make the conditions more reducing and to give more time for oxygen vacancies to infiltrate the crystal. In addition, crystals of $Sr_3Ir_2O_7$ were annealed at 700°C for a week. Several crystals from batch SIO#F17 were placed in a platinum lined alumina crucible for each annealing experiment and once finished some crystals were used for resistivity measurements while others were ground up for x-ray diffraction to check that the conditions used were not too reducing. Resistivity measurements were conducted on two crystals that were annealed in Ar at 600°C and one crystal that was annealed at 700°C . The results are shown in figure 4.18. The absolute resistivity at 300 K of the crystal annealed at 700°C is higher at 89 mΩcm compared to the crystals annealed at 600°C which have ρ_{300K} of 8.3 mΩcm and 6.8 mΩcm. Looking at the derivative, the antiferromagnetic transition appears to become broader as the annealing temperature is increased and when compared to the as-grown crystal. This suggest that annealing the crystals under a reducing atmosphere increases disorder in the sample - perhaps by increasing the number of oxygen vacancies. The increase in ρ_{300K} upon annealing at 700°C may also be correlated to this increased disorder in the sample. It was concluded that annealing crystals under reducing conditions reduces their quality and does not have a large effect on their bulk properties.

EPMA measurements showed that all of the crystals of $Sr_3Ir_2O_7$ were already heavily oxygen depleted so perhaps there is a limited amount of oxygen that can be further removed by annealing the crystals under a reducing atmosphere. Therefore, the effect of annealing the crystals under an oxidising atmosphere was investigated to see if putting oxygen back into the structure would affect the bulk properties. This would remove electrons from the system and oxidise the iridium ion to be closer to +4. To do this crystals from batch SIO#F17 were annealed for nearly 2 weeks at a temperature of 700°C under flowing 100% O_2 gas at a pressure of 2 bar. Resistivity measurements were conducted on two of the crystals that were annealed and the results are shown in figure 4.19. In comparison to an as grown crystal the resistivity at 300 K is a factor of two smaller for one crystal

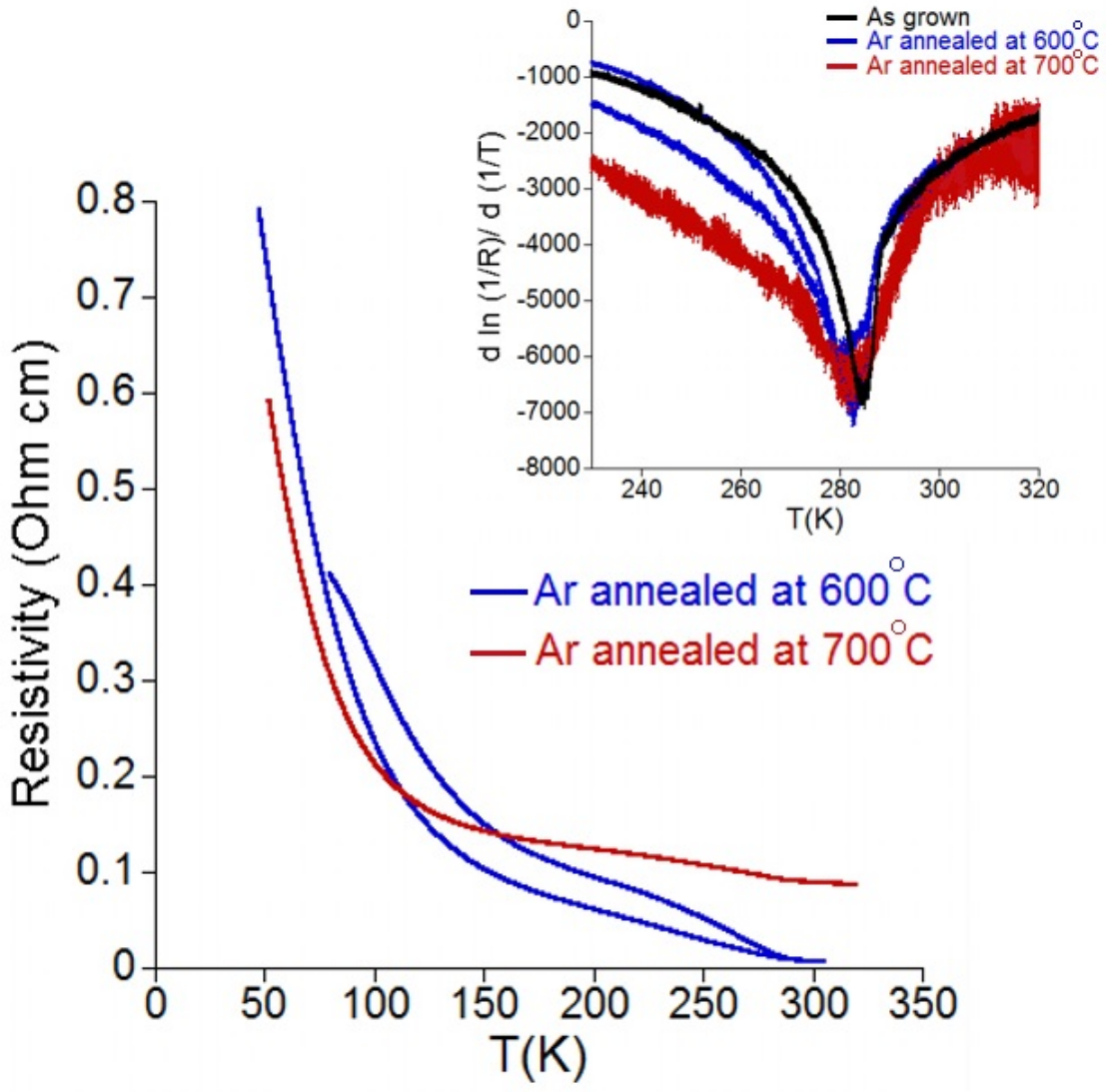

Figure 4.18 *The resistivty as a function of temperature of crystals of $Sr_3Ir_2O_7$ that have been annealed in Ar at 600°C and 700°C. Inset is the differential of the logarithm of the inverse of the resistivity with respect to 1/T of the samples in comparison to an as grown crystal.*

and a factor of two larger for the other crystal. Thus there is no net change in the magnitude of the resistivity upon annealing the crystals under oxygen. The derivative shows that the antiferromagnetic transition is broader and at a slightly lower temperature in the annealed crystals so annealing has not improved the quality of the crystals. Either additional oxygen is not having an effect on the resistivity apart from smearing the transition due to increased sample disorder or higher oxygen pressures are required for additional oxygen to be incorporated into the crystal structure. These results prove that the smaller value of ρ_{300K} in my samples compared to the literature values is not due to differences in the oxygen content. Also in all of the annealing experiments, annealing has been shown not to improve crystal quality or largely affect the bulk properties of the crystals. The lattice parameters of my crystals are also in agreement with the literature so the origin of the difference in ρ_{300K} is still unknown.

4.4.4 Other bulk measurements

Magnetisation

The magnetisation of a crystal of $Sr_3Ir_2O_7$ from batch SIO#F1 was measured as the crystals from this batch have a smaller aspect ratio and a larger mass than the crystals from batch SIO#F17 and from EPMA and resistivity measurements have shown to be of better quality than crystals from batches SIO#F5 and SIO#F19B. From Laue imaging of several crystals the (100) axis was found to be along the diagonal of the flat square face of the crystal and the (001) axis was found to be perpendicular to the plane of the square flat face. The crystal was orientated on the sample straw so that the applied field was parallel to the (110) axis. The sample was field cooled from 300 K to 220 K in a field of 10,000 Oe in order to track the antiferromagnetic transition. The magnetisation was converted to molar susceptibility and the results are shown in figure 4.20. The transition temperature was found to be 287.5 K, which is in agreement with the resistivity measurements. Although a diamagnetic cross-over has been observed on the literature at around 50 K for applied fields of less than 2500 Oe[32], it was not possible to conduct measurements at such a low field due to the small sample mass of the crystal and the weak moment of Ir making the sample too difficult to detect.

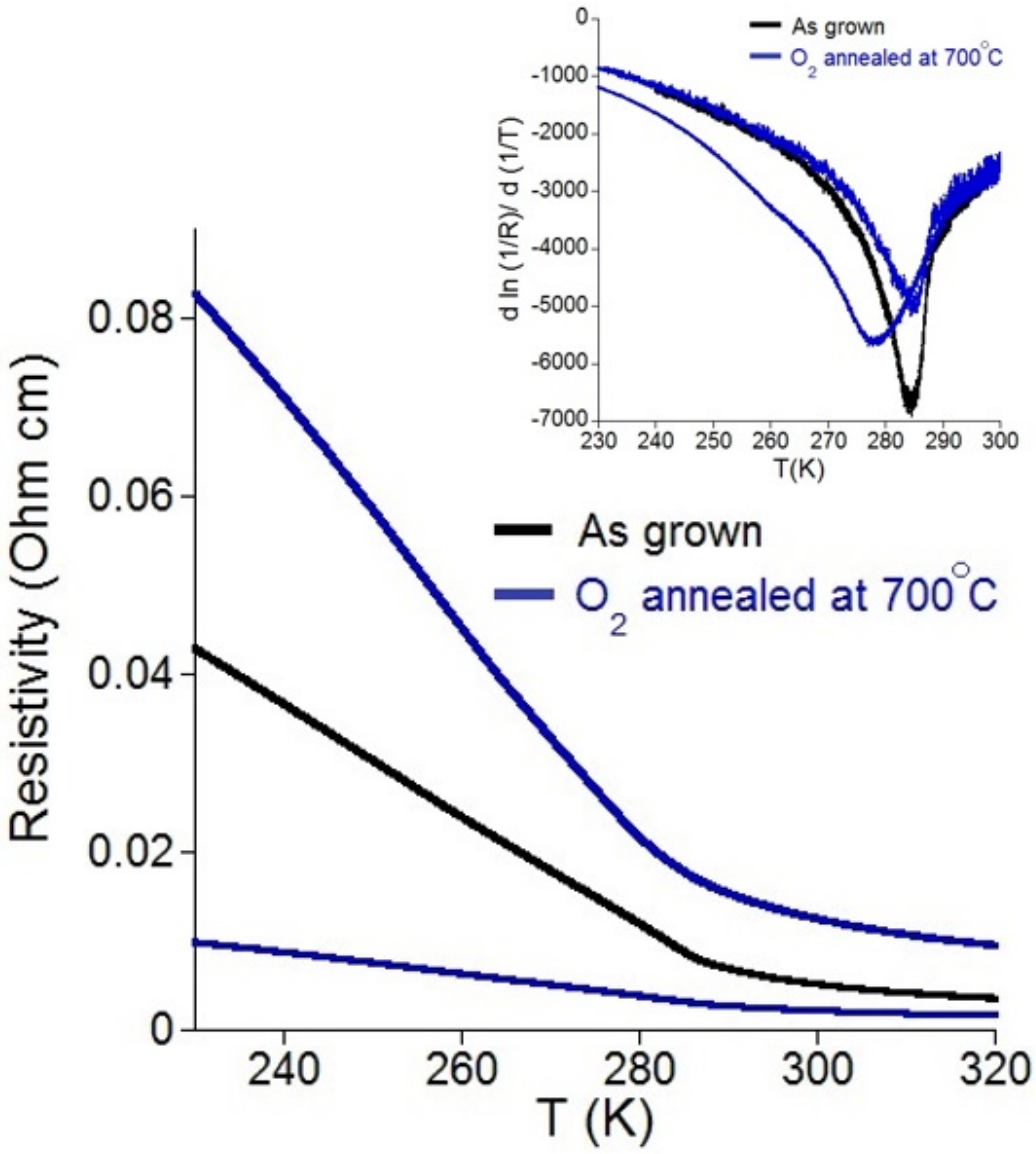

Figure 4.19 *The resistivity as a function of temperature of crystals of $Sr_3Ir_2O_7$ that have been annealed in O_2 at 700°C. Inset is the differential of the logarithm of the inverse of the resistivity with respect to 1/T of the samples in comparison to an as grown crystal.*

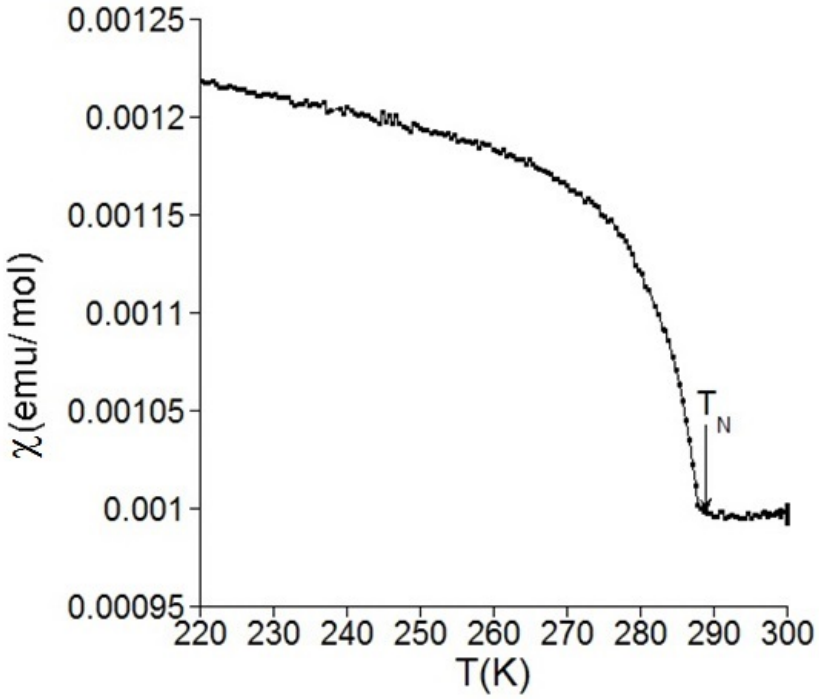

Figure 4.20 *The magnetisation of a crystal of $Sr_3Ir_2O_7$ from batch SIO#F1 measured as a function of temperature with an applied field of 10,000 Oe parallel to the (110) axis.*

Heat capacity

The heat capacity of a separate crystal from batch SLIO#F1 was measured, which had a mass of 0.92 mg. The heat capacity was measured from 320 K to 250 K in a field in order to observe the antiferromagnetic transition and see if there were any other bulk transitions (such as the mysterious T* transition) in this temperature range. In order to measure to high temperatures the high temperature H type grease was used. The results are shown in figure 4.21. Three points per temperature point were measured and on each point the data was averaged to reduce the noise. There is a clear peak in the heat capacity around the temperature of the transition which has an onset of 286.5 K. Considering that there is no discontinuity in the heat capacity at the transition, the slightly lower Néel temperature compared to that obtained from the molar magnetisation is from a smearing of transition due to sample disorder. Thus the Néel transition temperature is consistent with the other bulk measurements. The broadness and relatively small size of the peak suggests that the transition is purely electronic rather than structural, as expected.

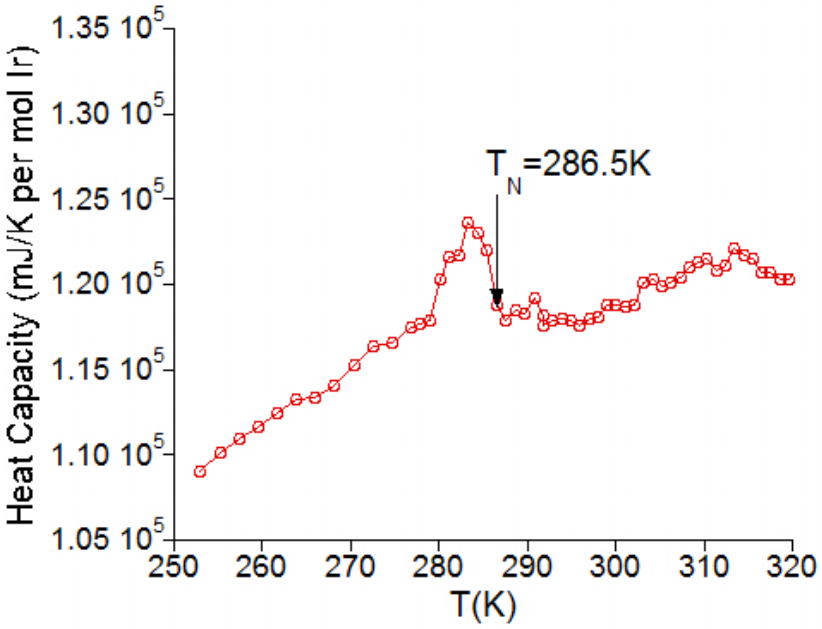

Figure 4.21 *The heat capacity of a 0.92 mg crystal of $Sr_3Ir_2O_7$ from batch SIO#F1 measured between 320 K and 250 K.*

4.4.5 Conclusion

Six batches of $Sr_3Ir_2O_7$ were grown using different crystal growth conditions. From EPMA measurements all of the crystals were found to be naturally oxygen deficient with an average formula of $Sr_{2.87}Ir_2O_{6.27}$, however, annealing the crystals in an oxygen atmosphere had little effect on the resistivity and only appeared to increase the disorder in the samples. The strontium content on the crystals, while also deficient, did not vary significantly from batch to batch. The resistivity of crystals from the four batches that showed the least crystal to crystal variation within a batch was measured. There was no significant difference in the Néel temperature of crystals from these four different batches and although there were differences in the absolute magnitude of the resistivity at 300 K, they were within experimental error, and did not correlate with variations in the strontium and oxygen content or the variations in the lattice parameter. However, in batches SIO#F5 and SIO#F19B $SrIrO_3$ inclusions were detected in agreement with EPMA and a $Ir_{0.91}Pt_{0.09}$ alloy was detected in all batches to varying amounts at levels below background from powder X-ray diffraction. Thus impurities in the crystals are more likely to be responsible for batch variation and discrepancies in the bulk properties in the literature rather than variations in the oxygen content. It is possible that some of the differences reported in the literature are due to

differences in the instruments or measurement technique used rather than from the different crystal growth conditions. Batches SIO#F1 and SIO#F17 appeared to be of the best quality and were used for collaborative experiments and from molar susceptibility and heat capacity measurements the Néel temperature was found consistently to be around 287.5 K. This comprehensive study gave us confidence that crystals of good quality $Sr_3Ir_2O_7$ could be grown reproducibly with little variation in the bulk properties and has provided a stable foundation upon which to conduct advanced physics measurements to elucidate the science of this fascinating material.

4.5 The temperature dependence of the structure of $Sr_3Ir_2O_7$: A high temperature study

The primary reason for collecting high temperature x-ray powder diffraction data over a range of temperatures was to aid in identifying the correct space group of $Sr_3Ir_2O_7$. At room temperature any peak splitting from the space group being orthorhombic is so small that the overlapping intensity from the two peaks is indistinguishable from a single peak. However, if the a and b lattice parameters are not equal the overlapping peaks may evolve with temperature at a different rate, making the peak splitting and B*bcb* space group distinguishable from the tetragonal I4/*mmm* space group model. Another motivation for studying the structural evolution of $Sr_3Ir_2O_7$ at high temperature would be to search for an structural phase transition from the orthorhombic space group to a tetragonal space group. La_2CuO_4 undergoes such a structural phase transition at around T_O=520 K[66] where there is change in space group from the orthorhombic C*mca* below T_O to tetragonal $I4/mmm$ above T_O. Other layered Ruddlesden Popper phases also show high temperature orthorhombic-tetragonal structural transitions [50] and the structure of $Sr_3Ir_2O_7$ has yet to be measured above 300 K.

X-ray powder diffraction data was collected using the hot stage apparatus on the Rigaku diffractometer in the materials characterisation laboratory at ISIS with the help of Gavin Stenning. The sample was placed on a steel holder and a small amount of powder, made from ground crystals of $Sr_3Ir_2O_7$, was held in place with ethanol. This increased the preferred orientation of the sample along (001) compared to when using vacuum grease but there was a risk that the vacuum grease would have decomposed at the high temperatures used. Data was collected at 200°C, 400°C , 600°C and 800°C on warm up and 600°C, 400°C , 200°C and 25°C on cooldown to make sure that any structural transitions or additional features in the diffraction pattern were reversible. Data were collected from 10-125° with a step size of 0.01° and a scan rate of 1°/min and was refined using GSAS using both the tetragonal I4/*mmm* and the orthorhombic B*bcb* structural models for comparison of the quality of fit.

Table 4.10 compares the goodness of fit of the I4/*mmm* and the B*bcb* structural models to the data. The goodness of fit is not as good as previous refinements of $Sr_3Ir_2O_7$ due to crystals being used from a lower quality batch (SIO#18B), which contained a small amount of $SrIrO_3$, to preserve the limited number of crystals

left in the better quality batches. If any structural changes were observed and the sample did not decompose then the experiment could be repeated using better quality samples in preparation for applying for synchrotron time. However, no peak splitting, which would have confirmed the B*bcb* space group or a structural phase transition, was observed. The χ^2 values for fits to the I4/*mmm* model seem to better, in general, than fits to the B*bcb* space group but it is not possible to conclusively select one model over the other.

Temperature (°C)	**Temperature ramp direction**	χ^2 **- I4/*mmm* model**	χ^2 **- B*bcb* model**
24	cooling	3.953	3.392
200	heating	3.298	3.571
200	cooling	3.492	3.523
400	heating	3.46	3.615
400	cooling	3.716	4.118
600	heating	3.653	3.976
600	cooling	4.836	4.201
800	heating	3.486	3.888

Table 4.10 *The goodness of fit, χ^2, values from Rietveld refinements of the high temperature x-ray diffraction pattern of $Sr_3Ir_2O_7$ on heating and cooling to both the I4/mmm and Bbcb structural models.*

Looking at the trend in the lattice parameters, the *a* lattice parameter (multiplied by $\sqrt{2}$ when refined in the I4/*mmm* space group for an easier comparison between the models) from the I4/*mmm* model is approximately an average of the *a* and *b* lattice parameters from the B*bcb* structural model (figure 4.22). The *a* and *b* lattice parameters approximately linearly increase with temperature by up to 1.2% from 24°C to 800°C. There is more variation in the *c* lattice parameter at the same temperature on heating and cooling and between the two models however from room temperature up to 600°C the *c* lattice parameter remains more or less constant within the error bars of the refinements. Approaching 800°C the *c* lattice parameter appears to decrease slightly but more data points are needed to confirm this trend. An ESRF report by Blake et al [16] reported that the *c* lattice parameter of $Sr_3Ir_3O_7$ underwent negative thermal expansion from 120 K to 220 K before undergoing positive thermal expansion up to 350 K (or 77°C). From my experimental results it is possible that the *c* lattice parameter of $Sr_3Ir_3O_7$ reverts back to negative thermal expansion beyond 600°C but there is no evidence that this change is linked to a structural transition.

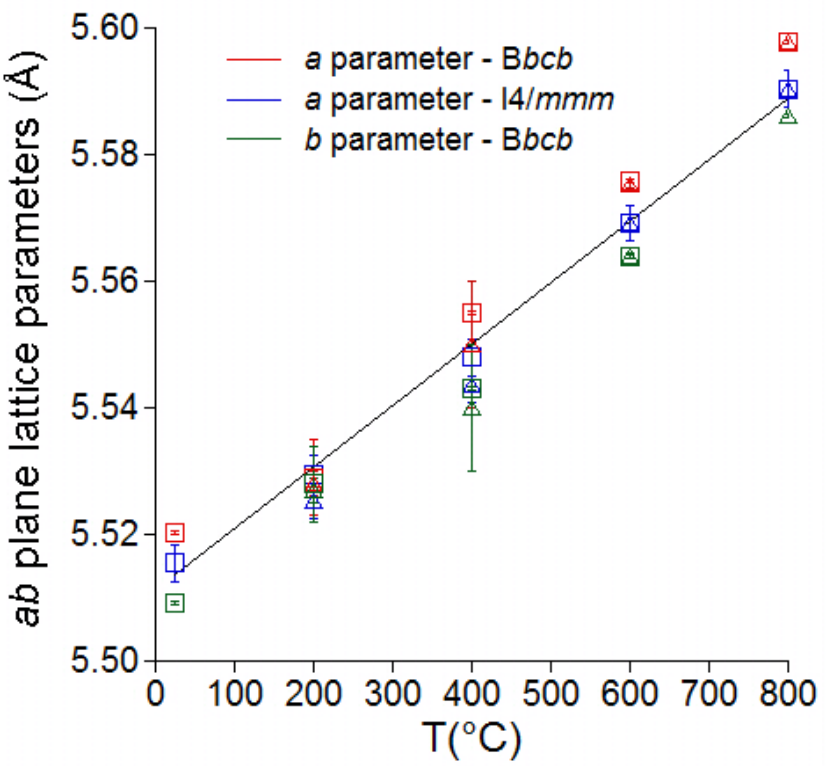

Figure 4.22 *The temperature variation of the a and b lattice parameters on heating (open triangles) and cooling (open squares). Lattice parameters refined from the I4/mmm model are shown in red and those refined from the Bbcb model are shown in blue.*

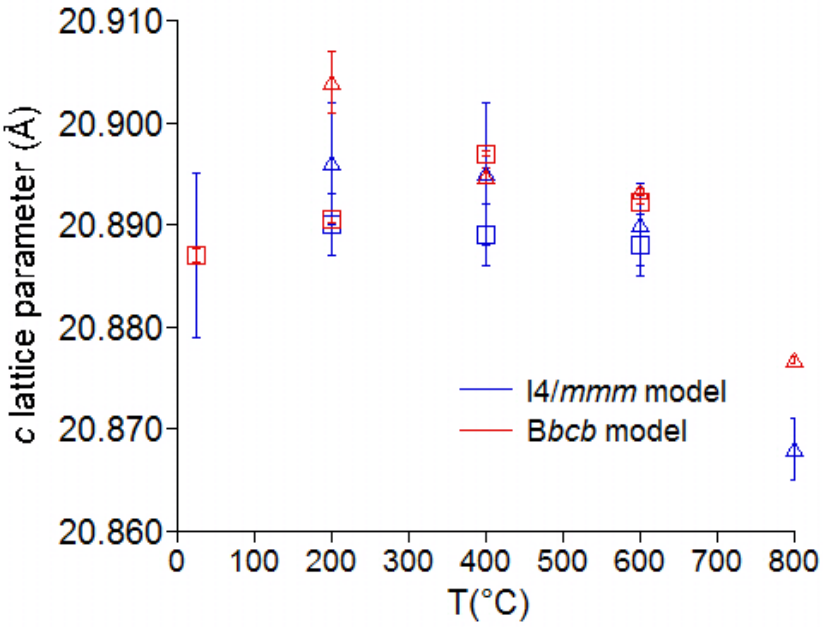

Figure 4.23 *The temperature variation of the c lattice parameters on heating (open triangles) and cooling (open squares). Lattice parameters refined from the I4/mmm model are shown in red and those refined from the Bbcb model are shown in blue. The curved line provides a guide to the eye of the average of all of the refined lattice parameters at each temperature.*

In summary, on heating the *a* lattice parameter linearly increases as expected while the *c* lattice parameter stays constant before decreasing slightly after 600°C. On heating there is no sign of any peak splitting that would differentiate the I4/*mmm* and B*bcb* space group models or any indication of an orthorhombic-tetragonal structural transition. In most cases the I4/*mmm* model gives a slightly better fit to the data than the B*bcb* space group model, however, this does not rule out the B*bcb* structure for $Sr_3Ir_3O_7$ as there is evidence for the B*bcb* space group from electron diffraction and single crystal synchrotron x-ray diffraction experiments [46][87].

4.6 Tuning the electronic properties of $Sr_3Ir_2O_7$ via electron doping

$Sr_3Ir_2O_7$ is isostructural with $Sr_3Ru_2O_7$, which is a metal that has a exhibits nematic order around a field induced quantum critical point below 1 K and between fields of 7.85-8.1 T[17]. It also belongs to the same structural family as La_2CuO_4, which similarly to $Sr_3Ir_2O_7$ is an antiferromagnetic insulator with a high Néel temperature of around 255K[49]. On doping with Sr, La_2CuO_4 becomes metallic and shows unconventional superconducting behaviour below 37.3 K for 7% Sr doped crystals[140]. Superconductivity has also been found in electron-doped cuprates. Thus electron doping $Sr_3Ir_2O_7$ by substituting lanthanum onto the strontium site could potentially induce similar exotic phenomena. Adding electrons to $Sr_3Ir_2O_7$ may also cause a rigid band shift induced metal-insulator transition (MIT).

In section subsec:SIOEPMA it was found that all batches of $Sr_3Ir_2O_7$ grown were slightly strontium and heavily oxygen deficient, giving the iridium ion an oxidation state of +3.4. Thus the $Sr_3Ir_2O_7$ crystals grown are already electron doped. However, from bulk measurements all the crystals are still insulating so either the EPMA determined oxygen content is unreliable or a higher electron doping level is required for the carrier electrons to become delocalised. Regardless, all the crystals grown under slightly different conditions have the same chemical composition so if any strontium can be substituted with lanthanum then additional electrons will be doped into the structure.

The crystal growth conditions for La doped $Sr_3Ir_2O_7$ are currently unpublished so in section 4.6.1 these, along with the saturation limit of La in the structure, are determined. By measuring the bulk properties, including the heat capacity, the effect of La doping on the ground state of $Sr_3Ir_2O_7$ is investigated. check and use powder and single crystal x-ray diffraction data to investigate the structural evolution of $(Sr_{(1-x)}La_x)_3Ir_2O_7$. If there are no-significant changes to the structure, a the (MIT) would be caused by a rigid-band shift from adding electrons to the upper J_{eff}=1/2 Hubbard band. However significant structural distortions may induce metallicity by destroying the J_{eff}=1/2 ground state. In the event of a MIT on electron doping the crystals would be studied by ARPES to investigate the ground state of $Sr_3Ir_2O_7$.

While characterising my own samples of La doped $Sr_3Ir_2O_7$, a paper was published

on $(Sr_{(1-x)}La_x)_3Ir_2O_7$ by Li et al [78] for values of x ranging from 0.01 to 0.05. The bulk measurements from the paper are shown in figure 4.24. They found that a metal-insulator transition occurred between x=0.01 and x=0.02 and that there was a three orders of magnitude drop in the ρ_{300K} across the series. From the molar susceptibility T_N was found to decrease as x increased but was not fully quenched by x=0.05, suggesting an unusual co-existence of long-range antiferromagnetic order with a metallic ground state. Single crystal x-ray diffraction data showed a very slight increase in the in-plane Ir-O-Ir bond angle, θ, of just 0.023° at 295 K upon doping[78]. Such a small increase in θ is not significant as the error on θ is likely to be large due the difficulty in accurately refining the oxygen positions in single crystal x-ray diffraction. In this section dopant levels beyond what was published were studied and the heat capacity of metallic samples of $(Sr_{(1-x)}La_x)_3Ir_2O_7$ was measured for the first time.

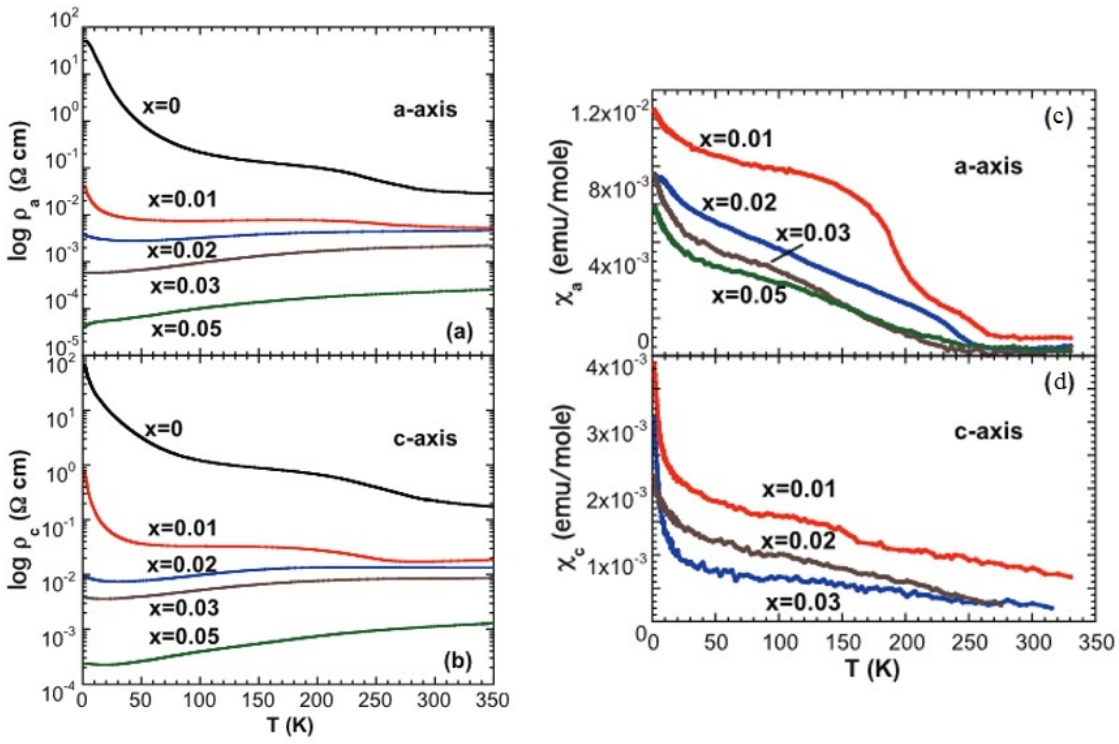

Figure 4.24 *Bulk measurements from L.Li et al's paper [78] of the (a) a axis resistivity ρ_a with temperature, (b) the c axis resistivity ρ_c with temperature, (c) the a axis magnetic susceptibility with temperature X_a and (d) the c axis magnetic susceptibility with temperature X_c.*

4.6.1 The synthesis of $(Sr_{(1-x)}La_x)_3Ir_2O_7$

Table 4.11 gives all of the crystal growth conditions used to grow lanthanum doped $Sr_3Ir_2O_7$. In total eight batches of $(Sr_{(1-x)}La_x)_3Ir_2O_7$ were grown with nominal lanthanum dopant percentages of 1%, 3%, 5%, 10% and 20%. These nominal dopant values will be referred to as x_N. Once known, the actual lanthanum content of the samples will be referred to as x_M. Similar conditions to the best batch of $Sr_3Ir_2O_7$ grown in section 4.2.1 (batch number SIO#F17) were used as a starting point for growing the 5% lanthanum doped $Sr_3Ir_2O_7$ crystals. This resulted in there being a mixture of $Sr_3Ir_2O_7$ and Sr_2IrO_4 crystals in the batch and the yield of crystals was low so the initial dwell temperature of the reaction was lowered from 1200°C to 1175°C to encourage the formation of $Sr_3Ir_2O_7$. This improved the ratio of $Sr_3Ir_2O_7$ formed and generally improved the yield but did not completely eliminate Sr_2IrO_4. From resistivity measurements on the 5% doped samples (see section 4.6.4), batch SLIO#F3 showed the least disorder and thus appeared to be the best quality so the reaction conditions used for this growth were used for further La doping experiments. The exception are the conditions used to grow 1% La doped $Sr_3Ir_2O_7$ which are similar to those of undoped $Sr_3Ir_2O_7$ as there is too small an amount of La_2O_3 present in the starting mixture to largely effect the growth conditions. The nominal 20% doped crystals were grown with the aim of determining the maximum amount of lanthanum that could be doped into the crystals.

Some SEM (scanning electron microscope) photos of the crystals are shown in figure 4.25. All images were collected using an electron energy of 20 keV and a working distance of 15 mm. Prior to the measurements all of the crystals were cleaned in toulene using a hydrosonic bath. The size of the crystals varied depending on the batch but tended to be from 200 μm - 800 μm. From the SEM it was noted that for the nominal 10% doped samples there were some small platelets on the surface of the crystal. From EDX analysis these platelets were determined to be either $SrIrO_3$ or a heavily strontium depleted form of $Sr_3Ir_2O_7$. These platelets were found to be a surface effect as they were not observed in the bulk upon cleaving the sample. However, it meant that all of the samples needed to be cleaved before conducting bulk measurements.

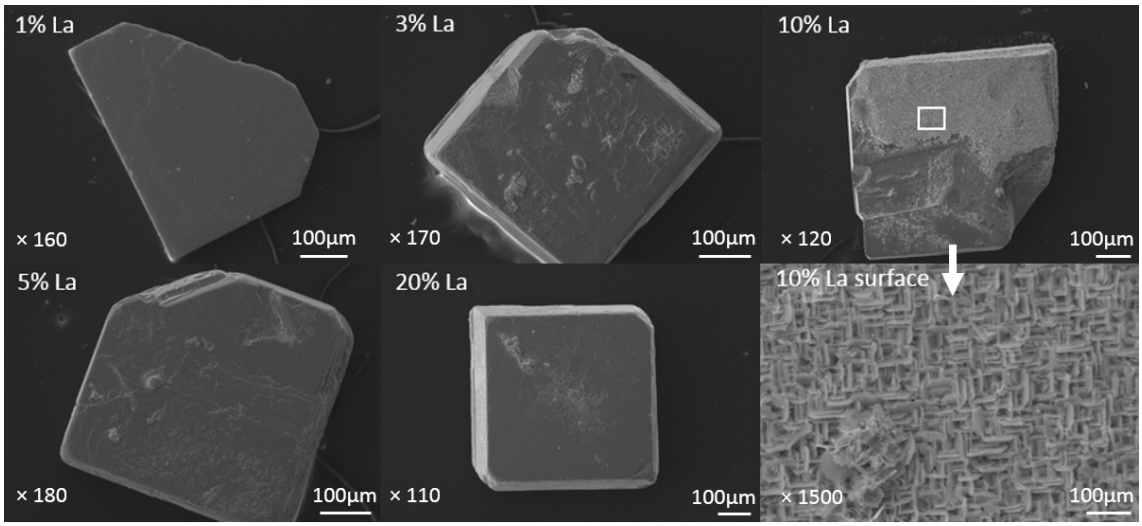

Figure 4.25 *SEM photos of uncleaved as-grown crystals from the five batches of* $(Sr_{(1-x)}La_x)_3Ir_2O_7$*. The nominal La percentage, magnification and scale are shown on each image.*

Table 4.11 *An overview of the crystal growth conditions used to make each batch of* $(Sr_{(1-x)}La_x)_3Ir_2O_7$.

Name	Nominal x	Ratio of starting materials	Reaction conditions	Result
SLIO#F1	0.05	1.30(0.95$SrCO_3$+0.025La_2O_3): IrO_2:7.5$SrCl_2$	1200C for 12 hours. Cool to 1100C over 20 hours then cool to 900C in 1 hour before allowing the sample to furnace cool to room temperature.	Small yield A mixture of approximately 70% Sr_2IrO_4 and 30% $Sr_3Ir_2O_7$. Ir metal present
SLIO#F2	0.05	1.30(0.95$SrCO_3$+0.025La_2O_3): IrO2:8.5$SrCl_2$	1200C for 12 hours. Cool to 1100C over 25 hours then cool to 900C in 1 hour before allowing the sample to furnace cool to room temperature.	Higher yield and no Ir metal detectable. Approximately 50% Sr_2IrO_4 and 50% $Sr_3Ir_2O_7$
SLIO#F3	0.05	1.30(0.95$SrCO_3$+0.025La_2O_3): IrO_2:7.5$SrCl_2$	1175C for 12 hours. Cool to 1100C over 18.75 hours then cool to 900C in 1 hour before allowing the sample to furnace cool to room temperature.	Largest yield yet. A mixture of about 40% Sr_2IrO_4 and 60% $Sr_3Ir_2O_7$. Ir metal at bottom of crucible.
SLIO#F4	0.05	1.30(0.95$SrCO_3$+0.025La_2O_3): IrO_2:8.5$SrCl_2$	1175C for 12 hours. Cool to 1100C over 18.75 hours then cool to 900C in 1 hour before allowing the sample to furnace cool to room temperature.	Low yield and lots of iridium metal present. A mixture of Sr_2IrO_4 and $Sr_3Ir_2O_7$.
SLIO#F5	0.01	1.30(0.99$SrCO_3$+0.005La_2O_3): IrO_2:7.5$SrCl_2$	1200C for 12 hours. Cool to 1100C over 25 hours then cool to 900C in 1 hour before allowing the sample to furnace cool to room temperature.	Large flakes of Sr_2IrO_4, some small crystals of $SrIrO_3$ and some reasonable sized crystals of $Sr_3Ir_2O_7$.
SLIO#F6	0.10	1.30(0.90$SrCO_3$+0.05La_2O_3): IrO_2:7.5$SrCl_2$	1175C for 12 hours. Cool to 1100C over 18.75 hours then cool to 900C in 1 hour before allowing the sample to furnace cool to room temperature.	A mixture of Sr_2IrO_4 and $Sr_3Ir_2O_7$
SLIO#F7	0.03	1.30(0.97$SrCO_3$+0.03La_2O_3): IrO_2:7.5$SrCl_2$	1175C for 12 hours. Cool to 1100C over 18.75 hours then cool to 900C in 1 hour before allowing the sample to furnace cool to room temperature.	Mainly $Sr_3Ir_2O_7$.
SLIO#F8	0.20	1.30(0.80$SrCO_3$+0.20La_2O_3): IrO_2:7.5$SrCl_2$	1175C for 12 hours. Cool to 1100C over 18.75 hours then cool to 900C in 1 hour before allowing the sample to furnace cool to room temperature.	Mainly $Sr_3Ir_2O_7$.

4.6.2 Determination of La content by EPMA and EDX

EPMA and EDX measurements were conducted on crystals from each batch of La doped $Sr_3Ir_2O_7$ in order to determine the amount of La doped into each crystal, how homogenous the doping was across the crystal and whether there was sample variation in the dopant content across a batch. For EPMA measurements, 4-5 crystals were measured from the nominal 1%, 3%, 5%, 10% and 20% La doped sample batches and 5 points on each crystal were measured. Of these five points one was in the centre of the crystal and one point was measured towards each corner of the square-ish crystal to ensure that the points were representative of the whole sample. The small beam size of 1 μm allowed variation in the composition across the crystal to be resolved. The same calibrants and instrument set up was used as for the EPMA measurement on $Sr_3Ir_2O_7$ (described in section 4.4.1) except that an additional rare-earth glass, also provided by the Geosciences department, was used as a calibrant for determining the amount of La in the crystals and the La L_α edge was measured. A plot of the measured La versus the nominal La content of the crystals is shown in figure 4.26. The error bars shown in figure 4.26 take instrumental error, which was incorporated into the automatic analysis by the CAMECA software for each individual point, into account. This was typically around $\pm 0.17\%$ of the atomic percentage of strontium and $\pm 0.07\%$ of the atomic percentage of lanthanum present. This is smaller than variation in the lanthanum content across an individual crystal, which is also incorporated into the error bars.

As can be seen there is a variation in the lanthanum content across a crystal, which can vary from $\pm 0.46\%$ to $\pm 1.83\%$ depending on the crystal. While most crystals cluster around a similar actual lanthanum dopant percentage within a batch there are crystals where the lanthanum content varies significantly. For example the median value of crystals from the nominally doped 3% batch is 4.81% but one of the crystals has a mean lanthanum content of 4.07%. Table 4.12 shows the mean La content of the crystals measured in each batch as well as the median value, which given the outliers is a truer reflection of the La content of a batch.

Taking both figure 4.26 and table 4.12 into account it can been seen that the nominal 1% doped samples typically contain less than the nominally doped amount of lanthanum, then as more lanthanum is added to the flux mixture the amount of lanthanum actually doped into the crystals increases faster than

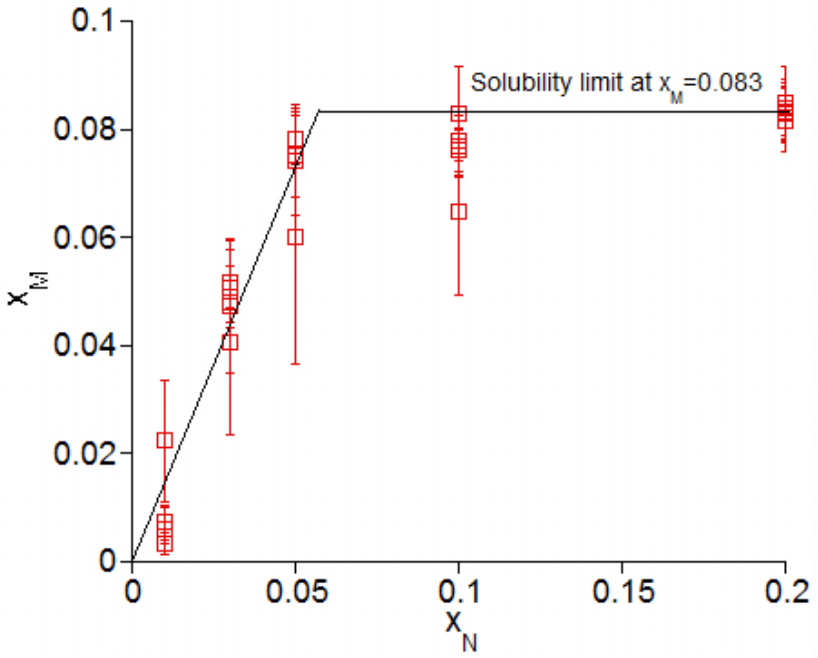

Figure 4.26 *The relationship between the nominal, x_N, and measured, x_M, lanthanum content in $(Sr_{(1-x)}La_x)_3Ir_2O_7$.*

Nominal La content (%)	Mean La content (%)	Standard deviation (%)	Median La content (%)
1	0.97	1.03	0.66
3	4.78	1.09	4.82
5	7.20	1.48	7.47
10	7.57	1.10	7.70
20	8.33	0.66	8.34

Table 4.12 *The mean and median lanthanum content of the crystals for each nominal La percentage as determined by EPMA.*

the nominal rate. There is little change in the actual La content between the nominal 5%, 10% and 20% doped samples with the La content saturating at 8.3%.

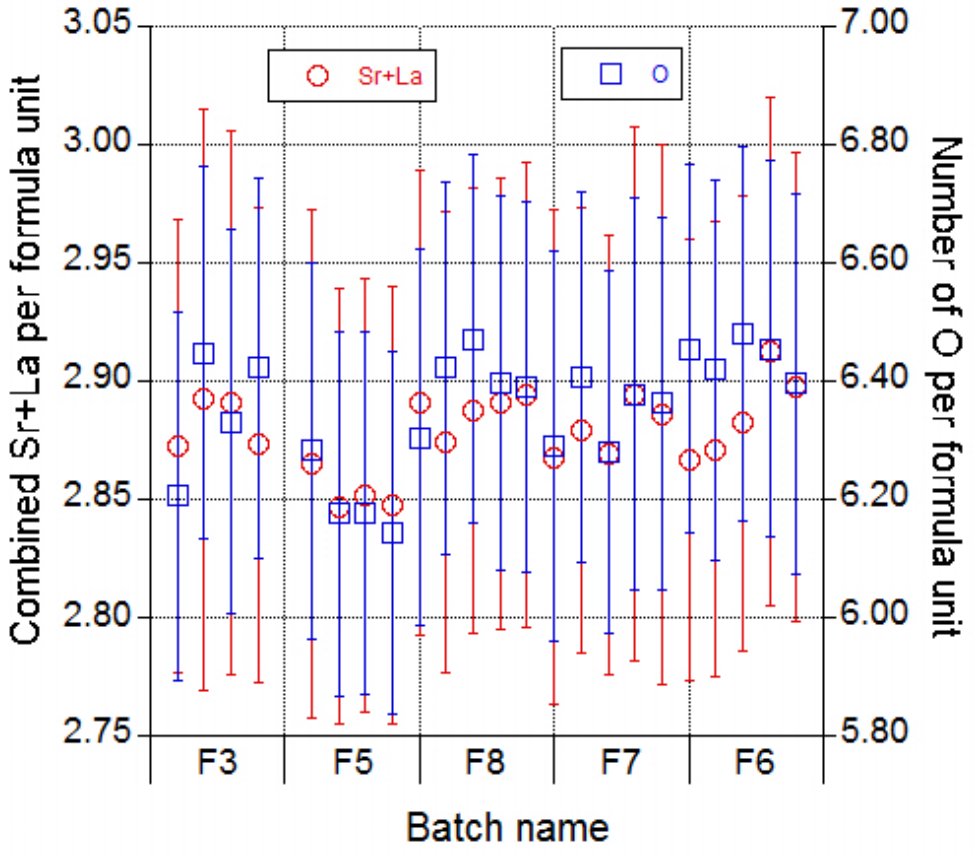

Figure 4.27 *The measured number of strontium and lanthanum ions, y, and oxygen atoms, z, in each crystal of* $(Sr_{(1-x)}La_x)_yIr_2O_z$.

By using the ratio of the atomic percentages of the elements present the number of strontium, lanthanum and oxygen atoms per formula unit could be calculated by assuming that there are two iridium atoms per formula unit. This assumption was made as the (Sr+ La)/Ir ratio was less that the ideal value of 1.5 for stoichiometric $(Sr_{(1-x)}La_x)_3Ir_2O_7$, which implies that the samples are either strontium and lanthanum deficient or iridium rich. Considering the structure it is more likely that there would by strontium and lanthanum vacancies in the (Sr,La)O rock salt layer than extra iridium atoms in the (Sr,La)IrO_3 perovskite layers. The relative amounts of lanthanum, strontium and oxygen in the chemical formula for each crystal measured by EPMA is shown in figure 4.27. From this it can be seen that was little variation in the total amount of strontium and lanthanum and the amount of oxygen in each crystal even between different batches of crystals. The mean formula unit of the La doped crystals is $(Sr_{(1-x)}La_x)_{2.88}Ir_2O_{6.35}$, which

is similar to the result of the EPMA study on undoped $Sr_3Ir_2O_7$ that gave an average composition across all batches of $Sr_{2.87}Ir_2O_{6.27}$. This suggests that $Sr_3Ir_2O_7$ is naturally strontium depleted and the fact that the oxygen content also remains unchanged on doping suggests that adding lanthanum further reduces the oxidation state of the iridium ion. $Sr_{2.87}Ir_2O_{6.27}$ has an oxidation state of +3.4 and when the saturation point of 8.3% is reached the oxidation state of iridium ion has been reduced to +3.35.

The chemical composition of the crystals was also measured by EDX spectroscopy. Table 4.13 shows the nominal La percentage of the batch against actual lanthanum percentage measured by EDX. The measurements were conducted on cleaved crystals to avoid discrepancies in the composition from surface contaminants. The results of the nominal 3% and 5% doped samples are in close agreement with the actual lanthanum content as determined by EPMA. No lanthanum could be detected in the nominal 1% doped samples as it is at levels below the background noise. EPMA has a detection limit for La of 1100 ppm (around 0.1wt%) and so it is much more sensitive to small quantities of La. There also appears to be higher levels of La in the nominal 10% and 20% than detected by EPMA of 8.73% and 9.35% respectively. This may be due to sample variation within the batch as only a couple of samples from each batch were measured or due to differences between the two techniques. EDX is insensitive at measuring the oxygen content but the mean ratio of (Sr+ La): Ir (again setting Ir=2) appears to be similar to the EPMA results at 2.67:2. However, for the remainder of this chapter preference is given to the EPMA results due to the greater sensitivity of the instrument.

Nominal La content (%)	**Mean La content (%) (EDX)**	**Standard deviation (%) (EDX)**	**Median La content (%) (EPMA)**
1	0.00	0.00	0.66
3	5.32	0.64	4.82
5	8.12	1.51	7.47
10	8.73	0.33	7.70
20	9.35	0.99	8.34

Table 4.13 *The mean lanthanum content of crystals from each nominal La percentage as determined by EDX, compared to those determined by EPMA.*

However, EDX is useful for looking at how the lanthanum content varies relatively

across a sample and a map of the concentration of a particular element across a sample surface can be created within half an hour. Figure 4.28 shows the distribution of lanthanum and iridium across a nominal 3% and a nominal 5% doped sample over areas of 16,900 μm^2 and 5250 μm^2 respectively. The brighter the colour, the greater the number of counts per second of a particular element. From the diagrams it can be seen that there is some random variation in the La content across the cleaved surface of the crystal but there is no phase segregation into La rich and La deficient regions. No scale was given but from the EDX measurement the La content varied by 2.1% and 2.5% respectively across the whole crystal. In the map of the iridium distribution across the surface there are a couple of patches where the iridium content is much higher at the expense of lanthanum. These regions are from an intergrowth of a platinum-iridium alloy within the crystal, which was also visible in EPMA measurements conducted on undoped samples (see section 4.4.1). From EPMA the composition of the iridium-platinum alloy was calculated to be $Ir_{0.91}Pt_{0.09}$.

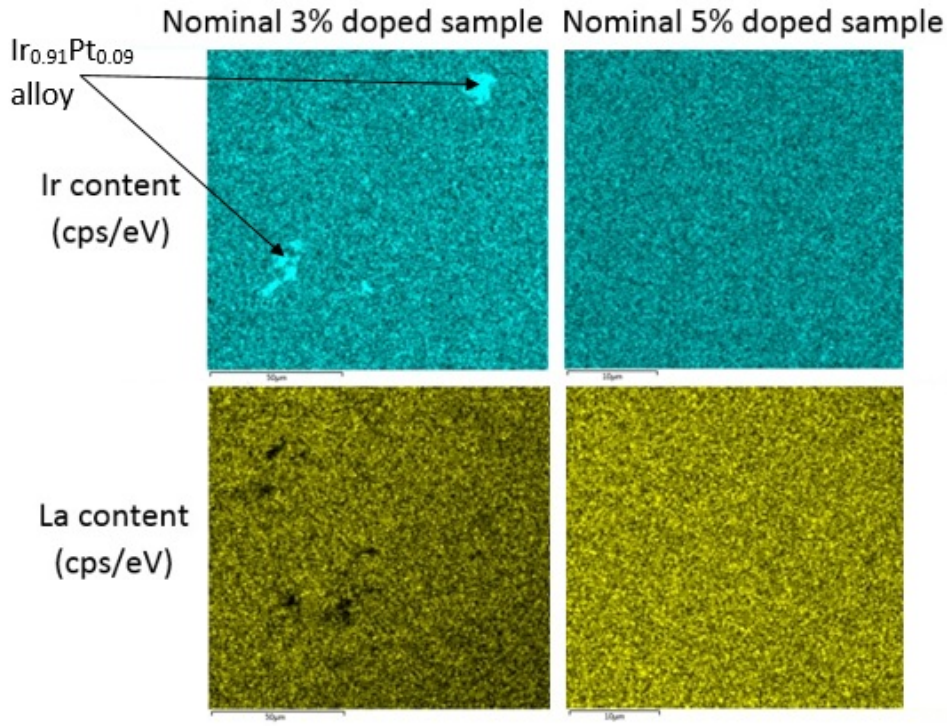

Figure 4.28 *Map of the variation in the lanthanum and iridium content across the surface of a nominally 3% and a nominally 5% La doped sample.*

4.6.3 The structural evolution of $Sr_3Ir_2O_7$ upon La doping

La^{3+} and Sr^{2+} have ionic radii of 1.36$\mathring{A}$ and 1.44$\mathring{A}$ respectively in a 12 coordinate environment so replacing some strontium with lanthanum may alter the unit cell parameters and introduce structural distortions such as changes in the relative rotation and tilts of the IrO_6 octahedra. Given the sensitivity of the Ir-O-Ir angle to oxygen content in Sr_2IrO_4 and the consequent effect of the electronic properties[75] it is important to properly characterise any structural changes to $Sr_3Ir_2O_7$ upon doping. Also there is still a large degree of uncertainty over the correct structure and space group of $Sr_3Ir_2O_7$, which is vital to solve for the electronic ground state of $Sr_3Ir_2O_7$ to be properly understood. For example the current collinear G-type magnetic structure of $Sr_3Ir_2O_7$ does not explain the presence of a weak ferromagnetic-like response in the magnetic susceptibility at 278.5 K.

Around 30 crystals from each batch of $(Sr_{(1-x)}La_x)_3Ir_2O_7$ were ground to a powder in a pestle and mortar for powder x-ray diffraction measurements. The powder was sprinkled evenly onto a low background Si sample holder coated with a small amount of vacuum grease to keep the sample in place. For $(Sr_{(1-x)}La_x)_3Ir_2O_7$ it is preferable to use vacuum grease rather than ethanol to hold the sample in place, despite the higher background, as the preferred orientation of the polycrystalline grains along the (001) direction is reduced. The x-ray powder diffraction data were collected on the Rigaku spectrometer in the material characterisation laboratory at ISIS as detailed in section 3.2.5. X-ray powder diffraction is good for checking the phase purity of samples and for tracking changes in the lattice parameters as phase fractions of different constituents can be calculated by Rietveld refinement. Also lattice parameters can fluctuate from crystal to crystal within a batch so an average of the lattice parameters across many crystals in a powder will give a more accurate impression of general trends on varying x_M.

An example of a Rietveld refinement collected on ground crystals taken from batch x_N=0.05 is shown in figure 4.29. The diffraction pattern shows that the crystals selected are phase pure. Some batches of $(Sr_{(1-x)}La_x)_3Ir_2O_7$ contain a mixture of Sr_2IrO_4 and $Sr_3Ir_2O_7$, which can normally be distinguished by eye, but occasionally a small amount of Sr_2IrO_4 is ground up with $Sr_3Ir_2O_7$ by accident. However there was no evidence for intergrowths of Sr_2IrO_4 in the $Sr_3Ir_2O_7$ crystals in EDX and EPMA measurements so it is believed that the majority of crystals

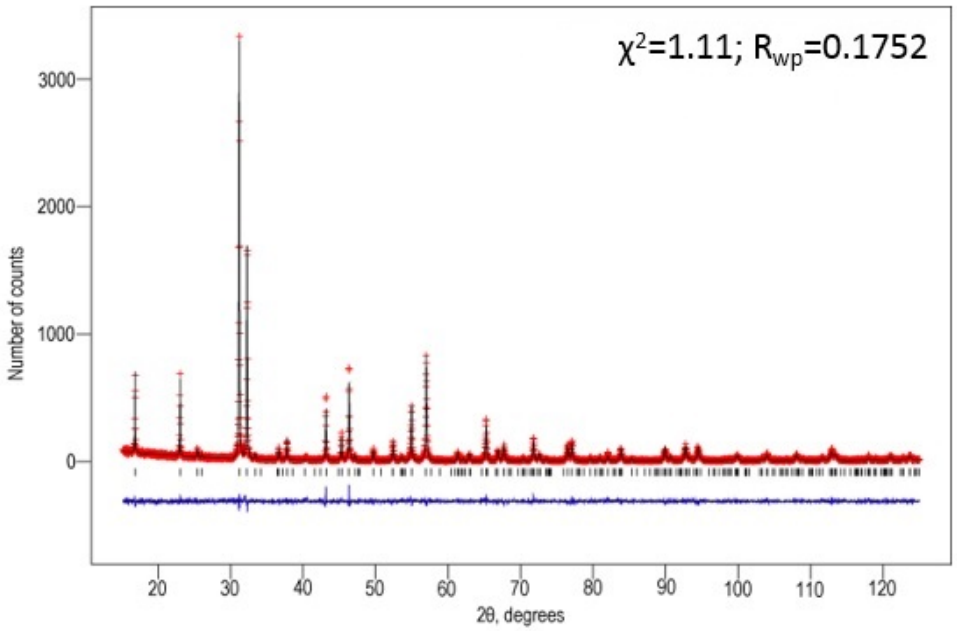

Figure 4.29 *Rietveld refinement using the Bbcb space group model of powder XRD data collected on ground crystals of* $(Sr_{(1-x)}La_x)_3Ir_2O_7$ *from the* x_N*=0.05 batch.*

of $Sr_3Ir_2O_7$ are phase pure. The diffraction pattern in figure 4.29 is fitted to the B*bcb* structural model described earlier but all collected diffraction patterns were fitted to the I4/*mmm* structural model as well to see if the models could be distinguished by a difference in the goodness of fit. However, as can be seen in table 4.14 both models provided a good fit to the data with reduced χ^2 values ranging from 1.11 to 2 with only small inconsistent differences in the fit between the models across the series. There were no additional peaks that the I4/*mmm* model could not fit but the resolution of the data was not sufficient to resolve peak splitting from additional peaks attributed to the B*bcb* space group model . As the *a* and *b* lattice parameters of the pseudo-tetragonal B*bcb* model are near identical it is also not possible to differentiate the two models by observing peak splitting, which would be on a smaller scale than the broadening of the peaks from a variation in the lanthanum content across the crystals in a batch. Thus from this study it is not possible to distinguish between the two models.

x_{M} (%)	B*bcb*				I4/*mmm*			
	a	**b**	**c**	χ^2	**a**	$\sqrt{2}\times$**a**	**c**	χ^2
0	5.5173(2)	5.5147(2)	20.8972(3)	1.291	3.90042(6)	5.51603(8)	20.8972(3)	1.287
0.097	5.5196(1)	5.5151(1)	20.8989(3)	1.912	3.90115(5)	5.51706(7)	20.8982(3)	1.974
4.78	5.5204(4)	5.5178(4)	20.8977(4)	1.366	3.90254(8)	5.5190(1)	20.8975(4)	1.342
7.20	5.5231(5)	5.5215(5)	20.8907(4)	1.128	3.9048(7)	5.522(1)	20.8906(4)	1.131
7.57	5.5241(5)	5.5230(4)	20.8937(3)	1.227	3.90574(7)	5.5236(1)	20.8937(4)	1.212

Table 4.14 *The lattice parameters of each batch of $(Sr_{(1-x)}La_x)_3Ir_2O_7$ as determined by Rietveld refinement using both the I4/mmm and Bbcb structural models.*

Looking at the trend in the lattice parameters as a function of x_M, there is a clear increase in the a and b lattice parameters as x_M increases, irrespective of the model used. The a lattice parameter for the I4/mmm model on the graph has been multiplied by $\sqrt{2}$ to allow for a more direct comparison with the a and b lattice parameters of the Bbcb structural model. As expected the a lattice parameter of the I4/mmm model is approximately an average of the a and b lattice parameters of the Bbcb structural model, which shows that the lattice parameters extracted by Rietveld refinement are reproducible. The c lattice parameters obtained from both structural models generally remain within error of each other. The magnitude of the c lattice parameter remains unchanged up to around x_M=0.05 before sharply decreasing and then recovering slightly, however this c-axis contraction is only small at around 0.03% of the original value. In contrast the a lattice parameter expansion is much larger at 0.16% of the original value, resulting in an overall increase in the unit cell volume upon lanthanum doping. The refined lattice parameters for undoped $Sr_3Ir_2O_7$ are within the range of lattice parameters previously reported in the literature. The overall increase in the unit cell in the ab plane despite the smaller size of the La^{3+} (r=1.36Å) ion in comparison to Sr^{2+} (r=1.44Å) could be explained by the reduction of Ir^{4+} ions (r=0.625Å) to the larger Ir^{3+} ion (r=0.680Å) upon electron doping.

To look for changes in bond angles and bond lengths in the local environment around the iridium ion upon La doping, single crystal x-ray diffraction data was collected on 3 crystals of undoped $Sr_3Ir_2O_7$ and on 3 crystals from the most heavily doped batch of $(Sr_{(1-x)}La_x)_3Ir_2O_7$. Diffraction data was collected on the Agilent Gemini diffractometer in the materials characterisation laboratory at ISIS using a Mo Kα source. The data reduction was automatically carried out in CrysAlis^{Pro}[12] and the refinement was conducted using JANA2006[107]. The structure was refined in the I4/mmm space group as the extra reflections that are associated with the Bbcb structure were undetectable, possibly due to the weaker laboratory x-ray source used rather than synchrotron radiation. Some of the Bragg reflections collected were smeared due to stacking faults between layers, which reduced the quality of the fit, yielding R_1 values ranging between 0.0621 and 0.1062. More details of the data collection parameters and of each individual refinement can be found in Appendix C.

The key bond lengths and angles studied are labelled in figure 4.31. These are the Ir-O bonds from that bridge two IrO_6 octahedra within the bilayer along the c-axis ($O_{bridging}$), the Ir-O bond to the oxygen shared with the (Sr/La)O rock-salt

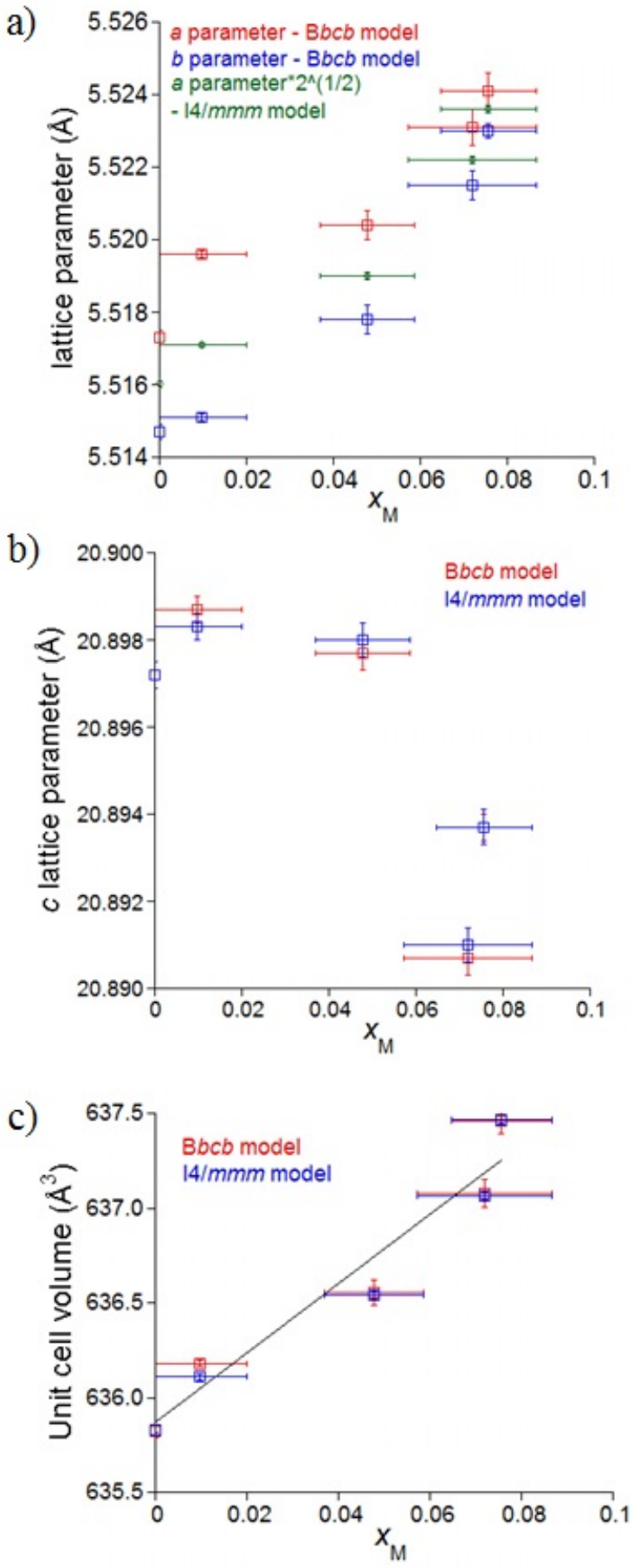

Figure 4.30 *The variation of the a)* a *and* b *lattice parameters, the b)* c *lattice parameter and c) unit cell volume as a function of* x_M *from the refinement of powder x-ray diffraction data to both the Bbcb (red) and I4/mmm (blue) structural models.*

layer (O_{apical}) and the Ir-O bond that join IrO_6 octahedra within the *ab* plane ($O_{in\text{-}plane}$). There is also the in-plane Ir-O-Ir bond angle, θ, the angle of which will affect the hopping rate and bandwidth and thus the metallicity.

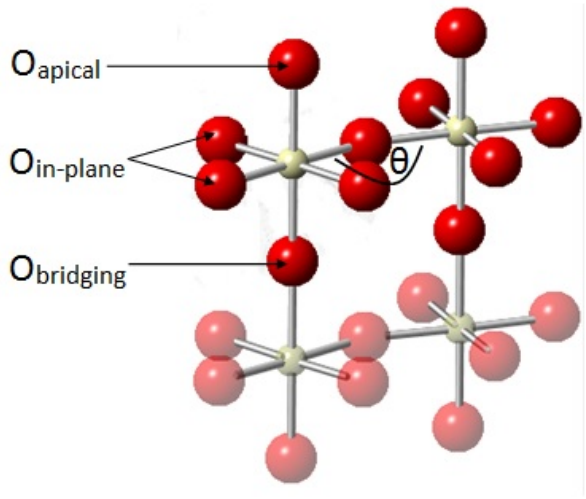

Figure 4.31 *Key Ir-O bond lengths and angles within the $SrIrO_3$ perovskite bilayers in $(Sr_{(1-x)}La_x)_3Ir_2O_7$. The oxygen anions are red spheres and the iridium ions are beige spheres. The strontium ions have been removed for clarity.*

The refined structural parameters for each crystal are shown in table 4.15. The average of each parameter across the three crystals measured from a batch is highlighted in bold. There is some crystal to crystal variation within a batch, however, on average, the *a* lattice parameter increases and the *c* parameter decreases slightly as a function of x_M. This trend is in agreement with the powder x-ray diffraction results. The Ir-O_{apical} bond length increases while the Ir-$O_{bridging}$ bond length remains relatively unchanged, resulting in the two bond lengths becoming near-equal. The Ir-$O_{in\text{-}plane}$ bond length appears to slightly increase and although it is not statistically significant it would explain the increase the unit cell *a* parameter. The angle, θ, appears to decrease on average by 2.5° but again there is a lot of variation in θ value from crystal to crystal and a decrease in θ would cause the *a* lattice parameter to decrease. An increase in the value of θ is also in contrast to the 0.023° increase at 295K observed by L. Li et al[78]. If correct the decrease in the Ir-O-Ir bond angle would push $(Sr_{(1-x)}La_x)_3Ir_2O_7$ towards a more insulating state due to the decreased orbital overlap and bandwidth. To confirm these structural trends it would be good to repeat the study using synchrotron radiation as it may be possible to detect the extra reflections associated with the B*bcb* space group and refine the oxygen positions and hence the Ir-O-Ir bond angle more accurately.

	$(Sr_{0.924}La_{0.076})_3Ir_2O_7$				$Sr_3Ir_2O_7$			
	Crystal 1	Crystal 2	Crystal 3	**Average**	Crystal 1	Crystal 2	Crystal 3	**Average**
a($\AA$)	3.9058(4)	3.9018(10)	3.8990(9)	**3.9022(5)**	3.9021(18)	3.8972(8)	3.8977(5)	**3.8990(7)**
c($\AA$)	20.909(2)	20.884(3)	20.876(5)	**20.8890(2)**	20.919(4)	20.8940(8)	20.876(2)	**20.8963(15)**
$\mathbf{r}_{Ir-O(apical)}$($\AA$)	2.04(3)	2.04(5)	2.073(4)	**2.051(19)**	1.976(8)	1.99(5)	1.99(3)	**1.985(2)**
$\mathbf{r}_{Ir-O(bridging)}$($\AA$)	2.042(2)	2.044(3)	2.033(3)	**2.040(2)**	2.046(8)	2.046(3)	2.0312(13)	**2.041(3)**
$\mathbf{r}_{Ir-O(in-plane)}$($\AA$)	1.994(6)	2.006(12)	1.987(8)	**1.996(5)**	1.97(7)	1.988(7)	1.993(6)	**1.984(24)**
θ(°)	156.65	153.04	157.62	**155.77**	161.6	157.22	155.95	**158.3**

Table 4.15 *The lattice parameters and key bond lengths and angles extracted from single crystal x-ray diffraction data of undoped and 7.6% doped $Sr_3Ir_2O_7$.*

The distortion of the IrO_6 octahedra upon doping

The J_{eff}=1/2 ground state model is only applicable if the IrO_6 octahedra are relatively undistorted. If the tetragonal splitting of the t_{2g} manifold becomes larger than the spin-orbit splitting, λ, then the J_{eff}=1/2 ground state is not realised and the resulting ground state will be metallic. In order to quantitatively determine the relative distortion of the octahedra upon lanthanum doping, I have devised the following model. In an IrO_6 octahedron there are three key bond lengths - $r_{Ir-O(\text{apical})}$, $r_{Ir-O(\text{bridging})}$ and $r_{Ir-O(\text{in-plane})}$, which for simplicity will now be referred to as r_1, r_2 and r_3. In a perfectly symmetrical octahedron the sum of the difference of each bond length, r_i, minus the average bond length, $\bar{r}$, will be zero. The greater the sum of the difference between the actual and mean bond lengths of the octahedron, the more distorted it is. To avoid bond lengths that are smaller than the average bond length from cancelling out bond lengths that are larger than the average bond length these differences will be squared. This value will be divided by the total number of bond lengths, n_i, so that this factor can be used for other polyhedra. Thus this model is given by equation 4.1.

$$D = \frac{\sum_i (r_i - \bar{r})^2}{n_i} \tag{4.1}$$

Using this model undoped $Sr_3Ir_2O_7$ has an average Ir-O bond length of 2.003Å and a distortion value, D, of 0.000710Å^2. In comparison the most heavily doped La doped crystals have an average bond length of 2.029Å and a distortion value of 0.000565Å^2. This shows that the IrO_6 octahedra become less distorted upon doping and that the onset of metallicity cannot be attributed to the J_{eff}=1/2 ground state being lost due to the octahedra becoming too distorted.

4.6.4 The evolution of the bulk properties of $Sr_3Ir_2O_7$ upon La doping

To determine whether the ground state of $Sr_3Ir_2O_7$ is altered by replacing some strontium with lanthanum, the bulk properties of crystals of a nominal La content of x_N=0.01, x_N=0.03, x_N=0.05 and x_N=0.10 were measured. In the case of a rigid band shift electrons would be added to the upper Hubbard band on the addition of lanthanum, which would cause an insulator to metal transition. This was tested by measuring the resistivity of the crystals as a function of temperature for each batch. An insulator to metal transition would also be apparent from changes to the magnetic susceptibility as a function of temperature across the series. The undoped parent compound, $Sr_3Ir_2O_7$, has an antiferromagnetic transition temperature of about 287.5 K while a metal would have a Pauli paramagnetic response.

Resistivity

In section 4.4 it was found that there was some variation in the magnitude of the resistivity depending on sample quality but that the transition temperature of the collinear antiferromagnetic ordering was largely unaltered. In this section the resistivity of the doped samples is compared to that of the best batch of the parent compound - SIO#F17. Figure 4.32 compares the resistivity of the best batch of undoped $Sr_3Ir_2O_7$ to two crystals of 1% doped $Sr_3Ir_2O_7$. From this figure it may initially appear that the resistivity increases slightly on light doping but the variation of the resistivity at 300K of the two 1% doped crystals is greater than the variation between the resistivity of the undoped crystal and the 1% doped sample so it is likely that the increase is from sample-sample variation and from error in the measurement of the sample dimensions. However, if the increase in the resistivity is real it could be from increased electron scattering by impurities with the dopant acting as an impurity. The antiferromagnetic transition is still evident and is clearer when comparing the differential of the resistivity. Going through the transition the gradient of the resistivity becomes noticeably more negative with the onset of this change at the transition temperature. The straight line on the graph shows the Néel temperature of the undoped sample, which coincides with a sharp drop in the gradient. On the substitution of a small amounts of strontium for lanthanum the transition becomes broader, which is characteristic

of the sample becoming more disordered, however due to this broadness it is difficult to pinpoint the exact Néel temperature although it appears to occur at a few degrees lower in temperature.

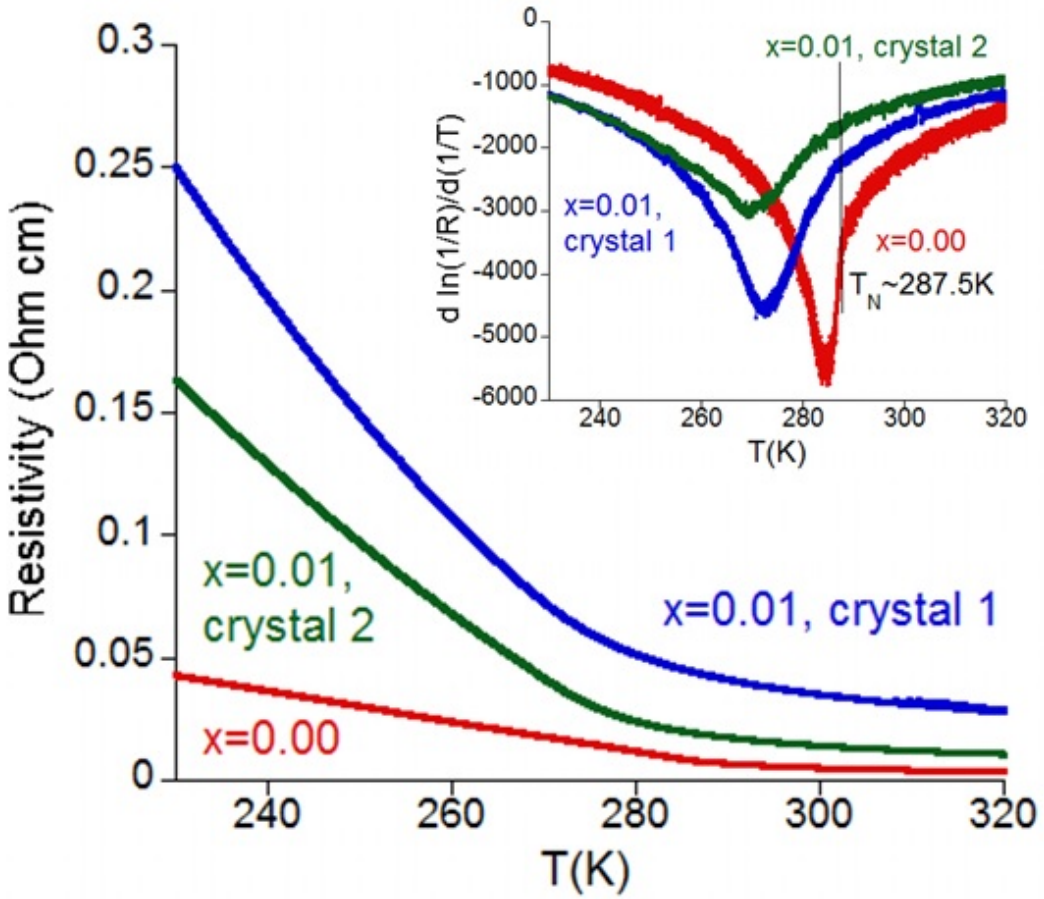

Figure 4.32 *Comparison of the resistivity of an undoped crystal of $Sr_3Ir_2O_7$ from the 'best batch' with two crystals of nominally 1% La doped $Sr_3Ir_2O_7$ from 320 K to 220 K. Inset: The derivative of the conductivity against the inverse of temperature plotted as a function of temperature*

The batch containing nominally 3% La doped crystals were smaller than the other batches and were very difficult to mount for resistivity measurements so only one sample was measured. Within this batch there is also a large variation in the dopant content with a standard deviation of 1.10% on the measured La content of 4.8% (see section 4.6.2). In the literature $(Sr_{(1-x)}La_x)_3Ir_2O_7$ starts to become metallic for values of x above 0.01, although the low temperature upturn did not disappear until x=0.03. However the sample measured appears to be insulating below a metal-insulator transition at 279 K. This metal insulator transition can be clearly seen in figure 4.33 where there is a clear change in the gradient from positive to negative. There appears to be a similar high temperature MIT at

around 260 K in the x=0.01 sample from the data presented in Li et al's paper[78]. The lanthanum content of their samples was determined via EDX, which I have shown to be not as sensitive for detecting small amounts of lanthanum as EPMA, so it is possible that the actual lanthanum content of their samples is higher than published.

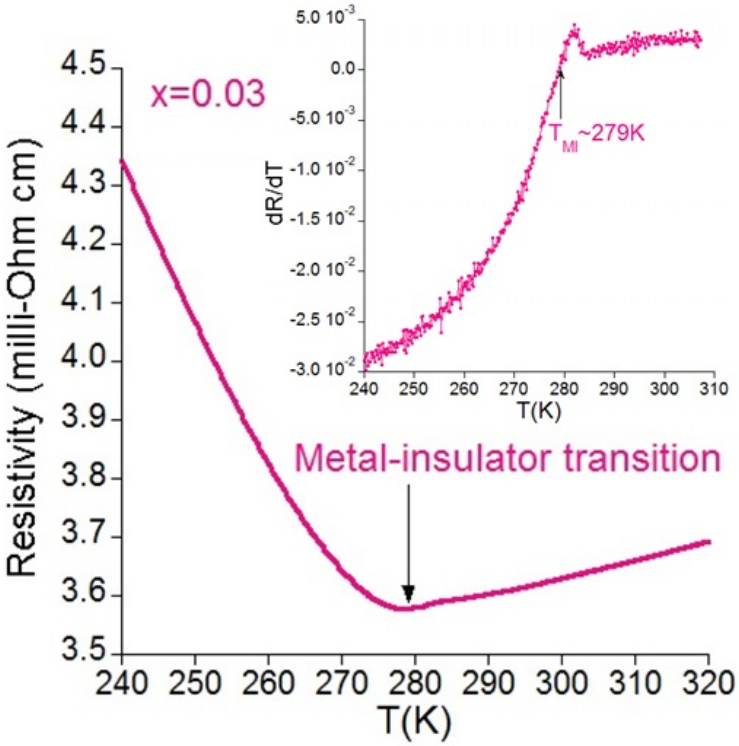

Figure 4.33 *The resistivity of a nominally 3% La doped batch of $Sr_3Ir_2O_7$ from 320 K to 240 K. The metal-insulator transition is clearly visible at just below 280 K. Inset: The derivative of the resistivity of a nominally 3% La doped batch of $Sr_3Ir_2O_7$ as a function of temperature plotted against temperature, showing the metal-transition occurring where dR/dT=0 at 279 K.*

Four different batches of 5% nominally doped $Sr_3Ir_2O_7$ were grown as outlined in table 4.11. Only the resistivity of samples from the first three batches were measured as the crystals from batch name SLIO#F4 were too small and irregularly shaped to mount for resistivity measurements and were consequently excluded from all further bulk characterisation measurements. Figure 4.34 shows the variation of the resistivity with temperature for 2-3 crystals from each of these batches. Noting that the y-axis scale is logarithmic, there is a large variation in the magnitude of the resistivity from crystal to crystal and batch to batch but apart from a low temperature upturn the gradient of the resistivity is positive and thus characteristic of a metal. There is a trend in that as the resistivity decreases

in magnitude this low temperature upturn is pushed to lower temperatures so it may be related to sample homogeneity. In samples that are inhomogeneously doped there is more electron scattering and rather than this just resulting in ρ_0 being higher the conducting electrons can become trapped by a potential well around the impurities at low enough temperatures, causing an increase in the resistivity in a process known as Anderson localisation. In a 2D metal this localisation causes a log T dependence of the conductivity of the sample with temperature. This was plotted in the temperature regions where the upturn occurs for the samples and as shown in figures 4.35 and 4.36 the conductivity does follow a log T dependence. This indicates that $(Sr_{(1-x)}La_x)_3Ir_2O_7$ is a 2D metal for x_M above 0.05, as would be expected as $Sr_3Ir_2O_7$ has a very 2D layered structure with conductivity occurring predominantly in the $SrIrO_3$ bilayers. This upturn is least pronounced in samples from batch SIO#F3, suggesting that the samples are more homogenous, and there is not as much sample to sample variation in crystals from this batch so only crystals from this batch were used for further experiments.

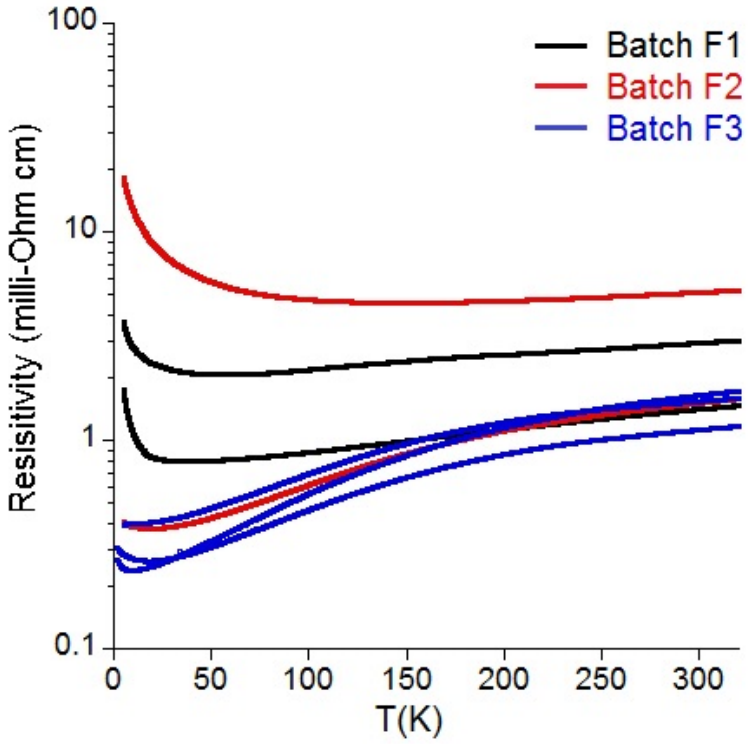

Figure 4.34 *Resistivity as a function of temperature for crystals of nominally 5% La doped $Sr_3Ir_2O_7$ from batches F1, F2 and F3.*

Batch number SIO#F3 of the nominal 5% doped crystals and the single10% doped batch of $Sr_3Ir_2O_7$ crystals that were grown were found to contain very

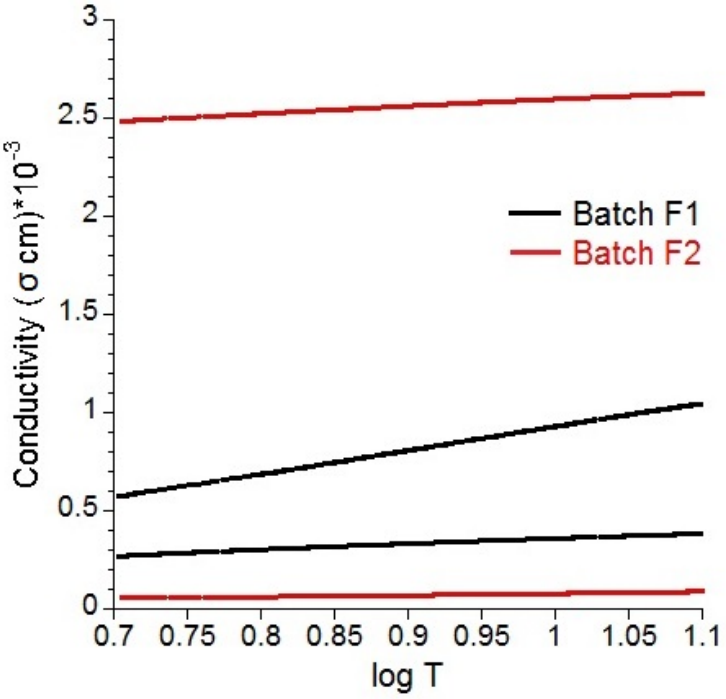

Figure 4.35 *Conductivity against 1/T for the low temperature region where an upturn occurs in the resistivity for nominally 5% La doped $Sr_3Ir_2O_7$ crystals from batches F1 and F2.*

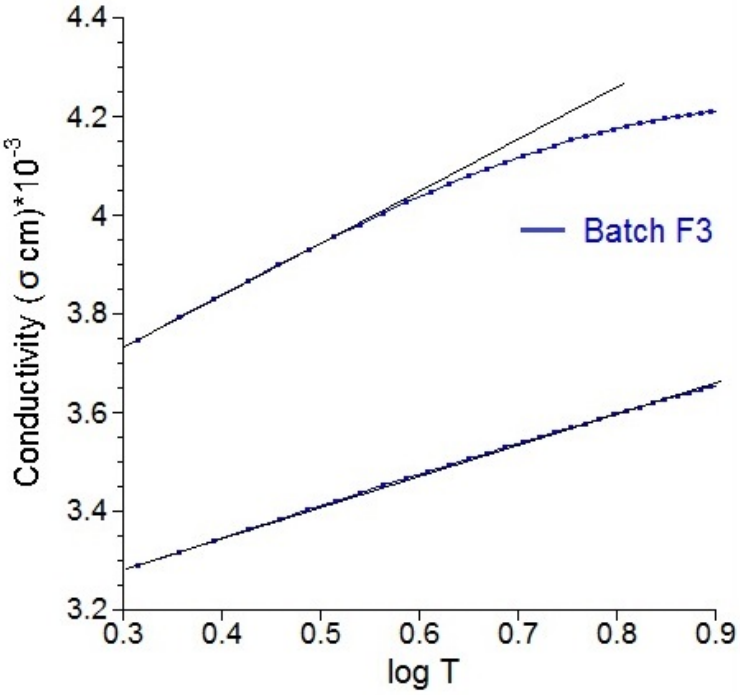

Figure 4.36 *Conductivity against 1/T for the low temperature region where an upturn occurs in the resistivity for nominally 5% La doped $Sr_3Ir_2O_7$ crystals from batch F3.*

similar amounts of La in EPMA and EDX studies (section 4.6.2) at values of x_{M}=0.072±1.48 and x_{M}=0.076±1.1. Thus the magnitude of the resistivity of the nominal 10% La doped crystals is similar to the nominal 5% samples and like the crystals from batch F3 the low temperature upturn of the samples is small. This suggests that the samples are more homogeneous than batches F1 and F2 of the 5% La doped samples. The RRRs of crystals from the nominal 10% batch and batch F3 are around 4, although one of the crystals measured from the F3 batch had an RRR of 7. This low RRR value is reflective of the fact that doped crystals grown by flux growth produce inhomogeneous samples compared to other crystal growth methods such as the floating zone method and that the metallicity of the samples is induced by doping. As a further test of sample homogeneity, 6-point resistivity measurements were conducted on a couple of the nominal 10% doped samples. In a 6-point measurements an extra set of voltage contacts are placed on the opposite side of the crystals (see section 3.2.2), which allows the difference in the resistivity on both sides of the sample to be measured. To take measurement error of the distance between the voltage contacts into account and allow for a more direct comparison to be made, the results were normalised to be at the same magnitude at 300 K. There are some temperatures missing for the second set of contacts for both samples due to the contacts failing either on cooldown (figure 4.37) or warm up (figure 4.38) but the data still shows that the resistivity on both sides of the crystal is remarkably similar. This is additional confirmation to the EDX maps that although there is point to point variation in the distribution of lanthanum in the crystal, the variation is random and there are no significant gradients in the lanthanum content across a crystal.

Figure 4.39 shows the resistivity of the nominal 5% (batch F3) and 10% samples below 80 K. The data has been fitted to a T^2 power law up until the upturn and in most cases the fit is very good. This T^2 dependence is indicative of a Fermi-liquid metal and deviations away from the power law at higher temperatures are due to phononic contributions that become dominant above the Debye temperature of a metal.

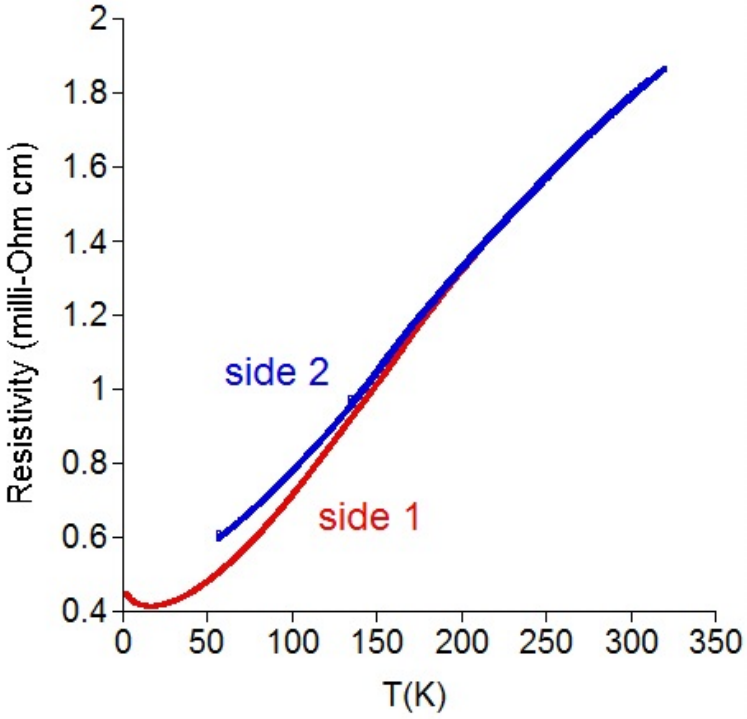

Figure 4.37 *The resistivity of a nominally 10% La doped crystal as a function of temperature measured on both sides of the same crystal simultaneously using a 6 point measurement.*

Magnetic Susceptibility

In the literature $Sr_3Ir_2O_7$ has a very small moment of 0.003 μ_B, and the size of the crystals is are also small at between 200 μm - 800 μm with a mass of typically 0.4 mg which makes measuring the magnetic susceptibility challenging. At a field of 1T, which was used for magnetisation measurements the signal from the sample was in the order of 1×10^{-5} emu while the background from the straw to which the sample was attached was only one order of magnitude lower at around -2×10^{-6} emu thus the sample straw had to be measured separately so that the background could be carefully fitted using a 4th order polynomial, chosen because it provided the best fit to the data, and subtracted from the sample moment. The detection limit of a Quantum design MPMS is in the order of 10^{-6} emu so while the sample was observable, the data contained random noise. Two samples were measured from each of the insulating batches while at least one sample was measured from the nominal 5% and 10% batches to check whether the magnetic susceptibility was characteristic of a metal. All samples were measured with the applied field orientated along the (001) axis of the crystals and the largest crystals of around 1 mg were chosen to increase the signal from the sample.

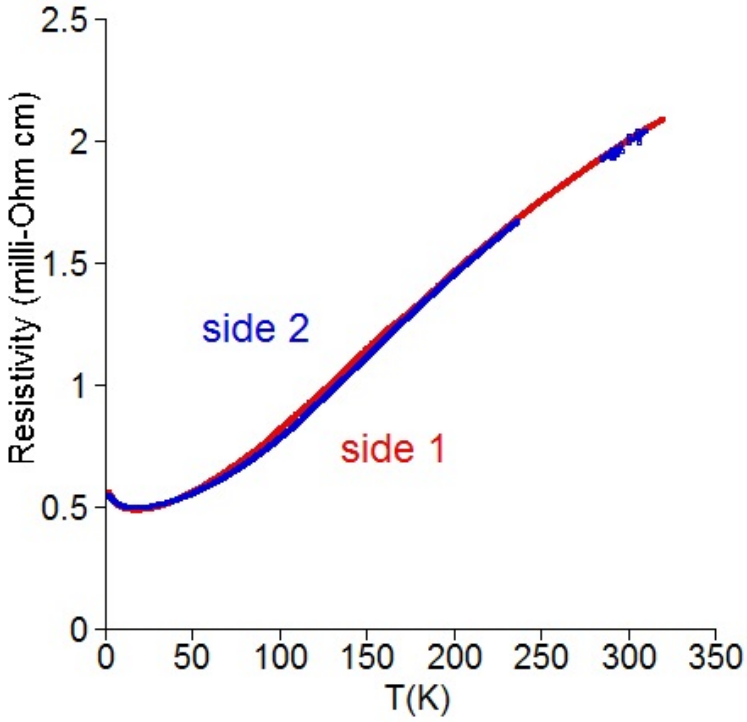

Figure 4.38 *The resistivity of a second nominally 10% La doped crystal as a function of temperature measured on both sides of the same crystal simultaneously using a 6 point measurement.*

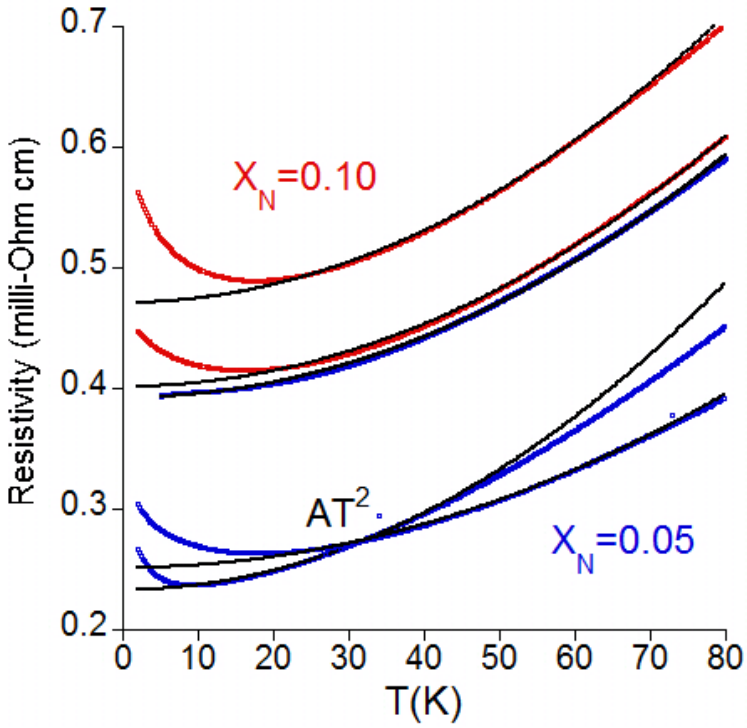

Figure 4.39 *AT^2 fits to the low temperature regime of nominally 10% La doped crystals and nominally 5% La doped crystals from batch F3.*

The magnetic susceptibility of the two lightly doped x_N=0.01 samples is shown in figure 4.40. The magnitude and features of the two samples are similar and are in good agreement with the x_M=0.01 sample measured by L.Li et al. There appear to be two transitions - one at 287 K and one at around 247 K. The origin of this second transition is unclear, although it has been also observed in Li's sample and at temperatures between 230 K and 260 K for undoped $Sr_3Ir_2O_7$ in the literature. One suggestion is that it could be from intergrowths of Sr_2IrO_4 in the crystal although the magnetic transition temperature of Sr_2IrO_4 is slightly lower at 240 K. Another suggestion is that the transition at T* could be due to a reordering of the moments. The transition at 287 K can be more clearly seen in the differential of the magnetic susceptibility with temperature from the onset of a peak in the differential. The differentials of the magnetisation of the two samples are in very good agreement through the transition. When combined with the resistivity data collected in the x_N=0.01 samples it is clear that light doping does not cause a significant decrease in the Néel temperature.

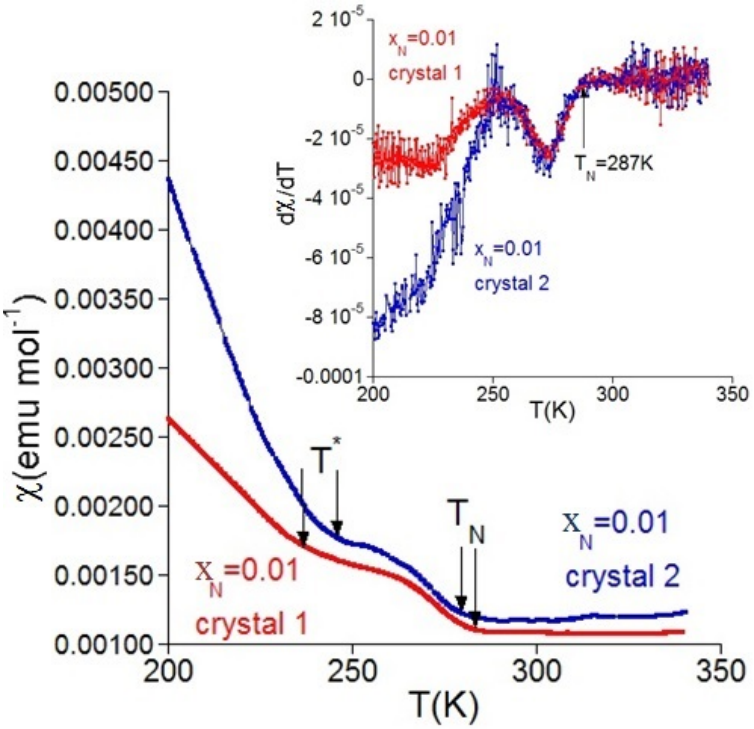

Figure 4.40 *The magnetic susceptibility as a function of temperature of two nominally 1% La doped crystals of $Sr_3Ir_2O_7$. Two magnetic transitions are visible at T_N=287 K and T*=250 K. Inset:The derivative against temperature showing that the onset of T_N is at 287 K.*

The magnetic susceptibility of the two x_N=0.03 samples are also in good agreement with each other as shown in figure 4.41. There is only one magnetic

transition apparent in the susceptibility data at a temperature just below 250 K, which is at a similar temperature to the T* transition observed in the x_N=0.01 crystals so it is unclear whether the Néel temperature has been supressed to a lower temperature on doping or whether the antiferromagnetic transition has been fully quenched while the T* transition has remained unaffected by the doping. There is no feature at the temperature of the metal insulator transition at 279 K so the magnetic transition appears to be decoupled from the metal-insulator transition. From the differential of the magnetic susceptibility with temperature the onset of the transition more clearly appears at around 250 K. The transition also appears to be broader than the transition at 287 K in the x_N=0.01 crystals. This may be due to an increased microscopic variation in the lanthanum content across the crystals and if the antiferromagnetic transition is suppressed by doping, especially if the Néel temperature is very sensitive to the La content of the crystal in this doping range, the transition would appear to occur across a broad range of temperatures.

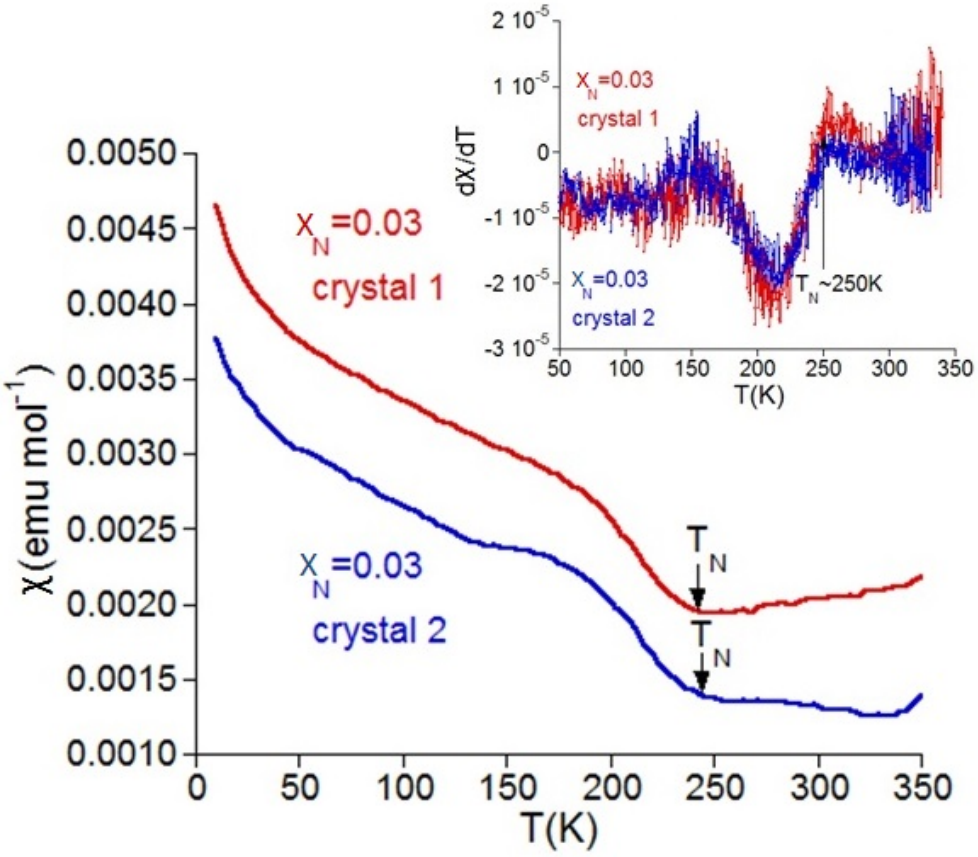

Figure 4.41 *The magnetic susceptibility as a function of temperature of two nominally 3% La doped crystals of $Sr_3Ir_2O_7$. A magnetic transition is visible just below 250 K. Inset is the derivative showing the onset of a broad magnetic transition at 250 K.*

Figures 4.42, 4.43 and 4.44 show the magnetic susceptibility of the nominal 5% and 10% La doped samples. These samples all have a magnetic susceptibility that is characteristic of a Pauli paramagnetic metal with an upturn at lower temperatures. These results add further evidence that by x_{M}=0.072 the samples are fully metallic. There is a slight upturn in the magnetic susceptibility below 200 K but this is less than 8×10^{-5} emu mol^{-1} Ir^{-1}. When the low temperature upturn was fitted as a paramagnetic impurity that obeys the spin-only formula with S=1/2, the impurity was found to makes up approximately 4.2% of the nominal 5% sample and 5.85% and 7.14% of the nominal 10% La doped samples. At these high levels the impurity would show up in the x-ray powder diffraction data collected on the crystals so the upturn cannot be a paramagnetic impurity but a magnetic transition that is intrinsic to the sample. Ir^{4+} has a J_{eff}=1/2 rather than a S=1/2 ground state so the spin-only formula does not apply, however, fitting the upturn to the Curie-Weiss law gives a Ir^{4+} moment of 0.073 BM for the nominal 5% sample and 0.101 BM and 0.124 BM for the nominal 10% La doped samples. It is worth noting that undoped $Sr_3Ir_3O_7$ also has a paramagnetic upturn below 50 K for fields of 1 T in the literature and from a Curie-Weiss fit of this upturn the Ir^{4+} moment was found to be 0.69 BM[32]. Thus the Ir^{4+} moment in these metallic samples is lower than in the insulating parent compound and in both cases the moment does not obey the spin-only formula. When this paramagnetic component is subtracted from the total susceptibility the Pauli paramagnetic term, χ_0, for the nominal 5% doped sample was found to be 9.03Oe$\times10^{-4}$ emu mol^{-1} Ir^{-1} while it was found to be 4.98Oe$\times10^{-4}$ emu mol^{-1} Ir^{-1} and 4.72Oe$\times10^{-4}$ emu mol^{-1} Ir^{-1} for the two crystals from the nominal 10% La doped batch.

Heat Capacity

The heat capacity of the metallic samples of $(Sr_{(1-x)}La_x)_3Ir_2O_7$ was measured in order to obtain additional information about the nature of the electronic correlations. All metals have a phononic and an electronic contribution to the heat capacity with the electronic contribution becoming more dominant at very low temperatures (see section 3.2.3). The Sommerfeld coefficient, γ, gives a measure of how strong the electron-electron correlations are in a metal and can be extracted from a linear fit to C/T against T^2. The heat capacity of a 1 mg crystal from the nominal 5% batch and a 0.9 mg crystal from the nominal 10% batch was measured. It was found that a plot of C/T against T^2 followed a linear fit below

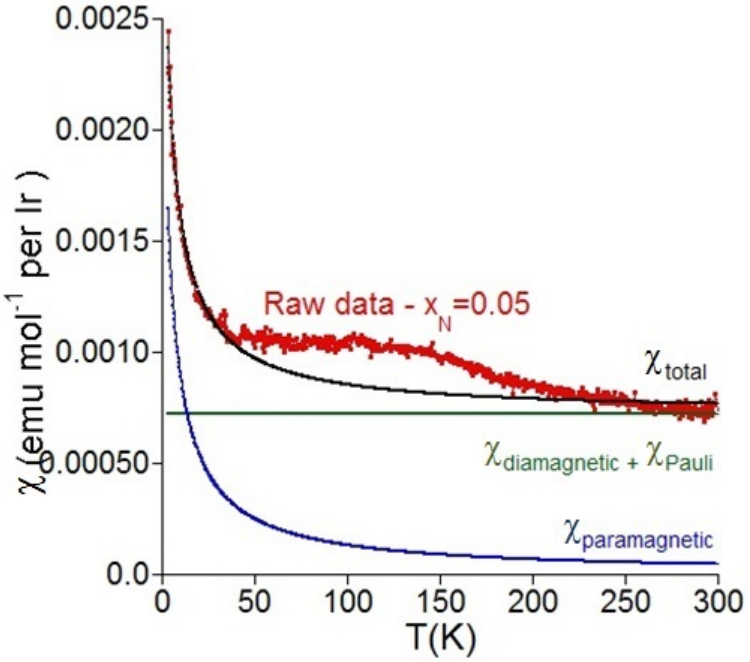

Figure 4.42 *The magnetic susceptibility as a function of temperature of a nominally 5% La doped crystal of $Sr_3Ir_2O_7$ fitted to separate the susceptibility into paramagnetic, Pauli paramagnetic and Landau diamagnetic components.*

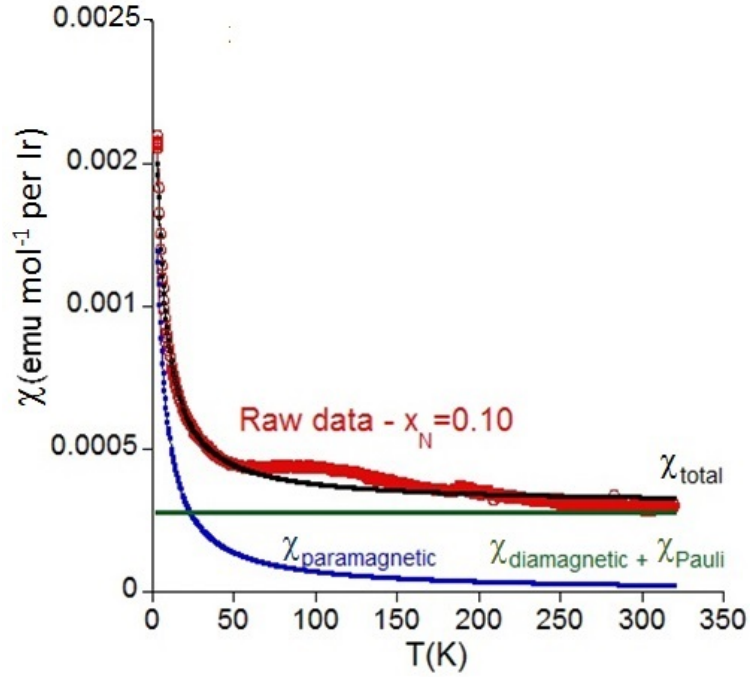

Figure 4.43 *The magnetic susceptibility as a function of temperature of a nominally 10% La doped crystal of $Sr_3Ir_2O_7$ fitted to separate the susceptibility into paramagnetic, Pauli paramagnetic and Landau diamagnetic components.*

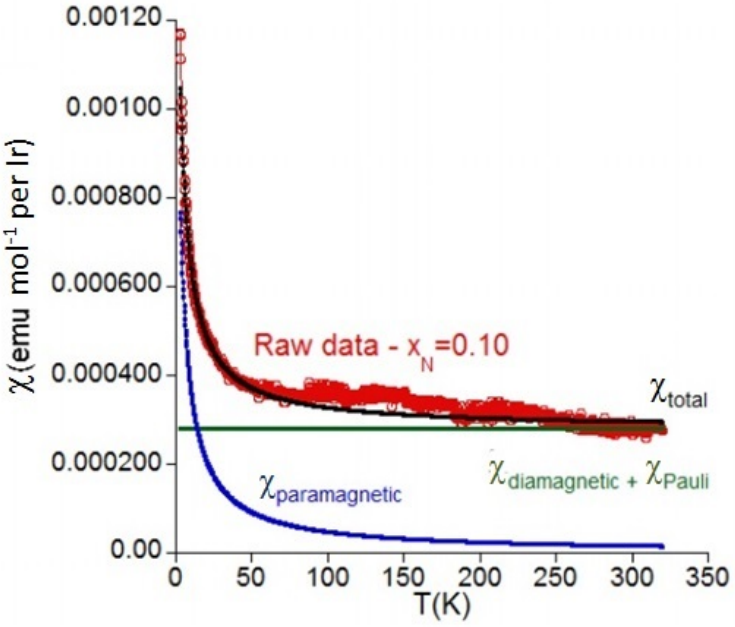

Figure 4.44 *The magnetic susceptibility as a function of temperature of a second nominally 10% La doped crystal of $Sr_3Ir_2O_7$ fitted to separate the susceptibility into paramagnetic, Pauli paramagnetic and Landau diamagnetic components.*

a temperature of 5 K for the nominal 5% crystal and 8 K for the nominal 10% crystal and the values of γ and β were extracted. The measured low temperature heat capacity of the nominal 5% and nominal 10% crystals and the fit of the calculated total heat capacity separated into phononic and electronic components are shown in figures 4.45 and 4.46 respectively. The Sommerfeld coefficient was found to be 11.49 mJ/Ir mol K^2 for the nominal 5% crystal and 8.35 mJ/Ir mol K^2 for the nominal 10% crystal. Given that $Sr_3Ru_2O_7$ has a Sommerfeld coefficient of 70 mJ/Ru mol K^2[113] and Sr_2RuO_4 has a Sommerfeld coefficient of 38.2 mJ/Ru mol K^2[106], which are of the same structural family as $Sr_3Ir_2O_7$, $Sr_3Ir_2O_7$ has a low Sommerfeld coefficient and is thus only weakly correlated in comparison. By combining χ_0 and γ, the Wilson ratio was calculated to be 0.57 for the nominal 5% La doped crystal and on average 0.423 for the nominally 10% La doped crystals. R_W should be above unity so there may be some error in χ_0 especially as my value for γ is in agreement with the value obtained by ARPES. However these low R_W values show that metallic $(Sr_{(1-x)}La_x)_3Ir_2O_7$ is at best a weakly correlated metal.

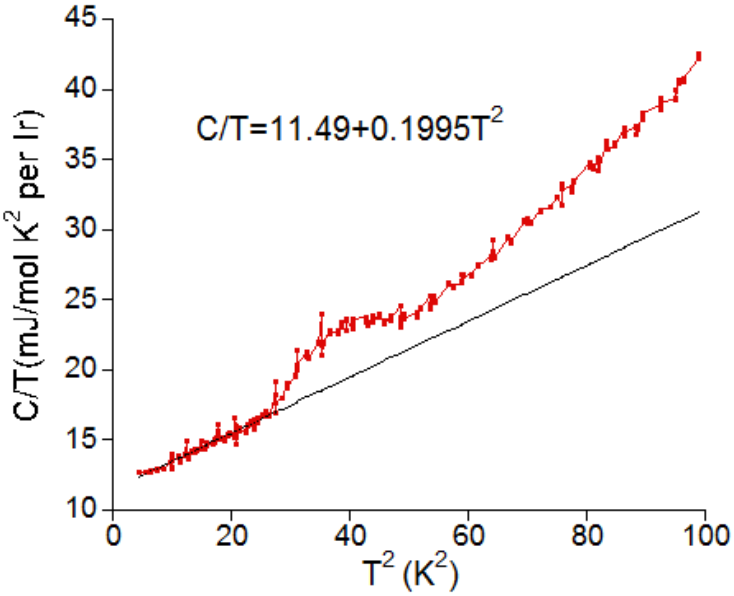

Figure 4.45 *Linear fit of C/T against T^2 of a nominally 5% La doped crystal of $Sr_3Ir_2O_7$ below 4.5 K.*

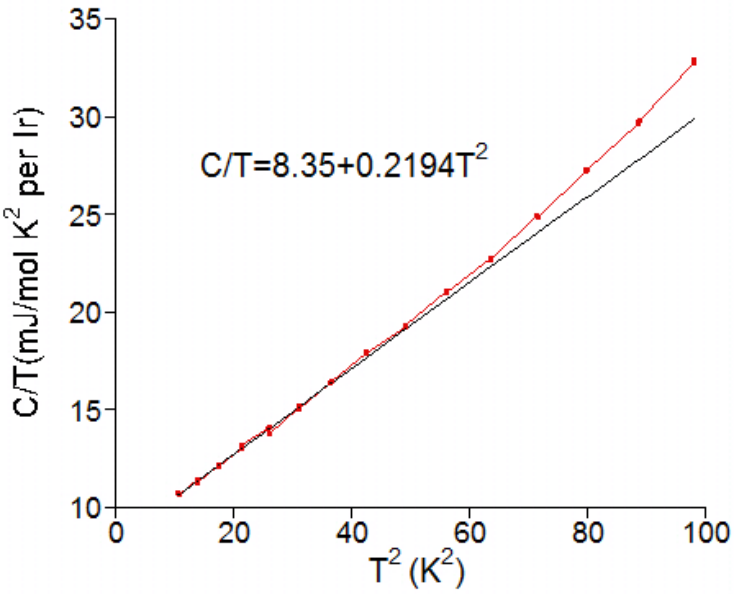

Figure 4.46 *Linear fit of C/T against T^2 of a nominally 10% La doped crystal of $Sr_3Ir_2O_7$ below 6 K.*

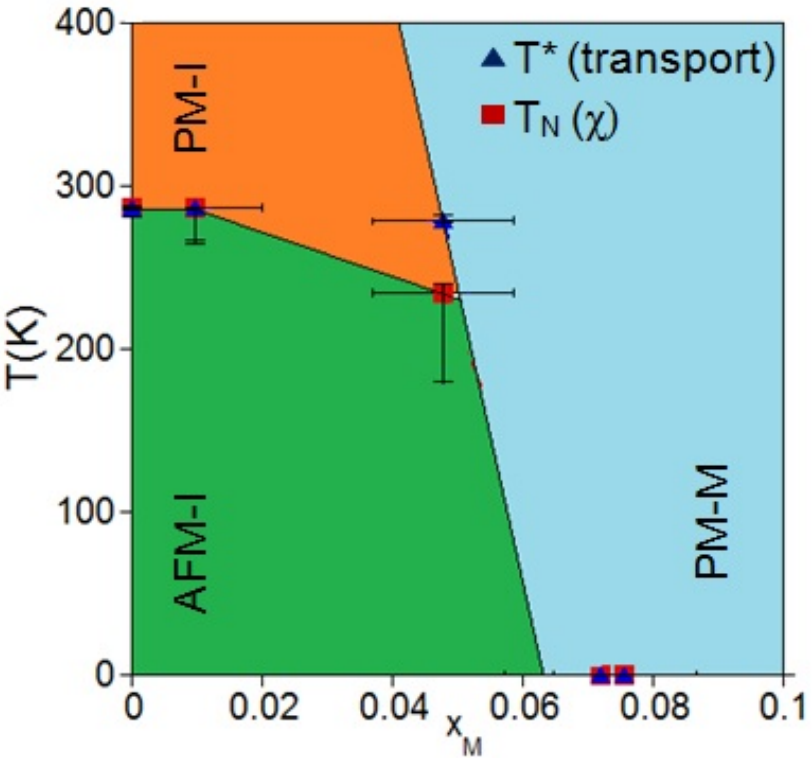

Figure 4.47 *The phase diagram of the different electronic states of $Sr_{(1-x)}La_x)_3Ir_2O_7$ as a function of temperature and measured La content. Blue triangles indicate the temperatures at which transitions were observed in transport (resistivity) measurements while red squares denote the Néel temperature as observed in magnetisation measurements. The orange region indicates where $Sr_{(1-x)}La_x)_3Ir_2O_7$ behaves as a paramagnetic insulator, the green where $Sr_{(1-x)}La_x)_3Ir_2O_7$ behaves as a antiferromagnetic insulator and the blue region indicates where $Sr_{(1-x)}La_x)_3Ir_2O_7$ behaves as a Pauli paramagnetic metal.*

Figure 4.47 gives overview of the bulk properties of $(Sr_{(1-x)}La_x)_3Ir_2O_7$ as a function of temperature and x_M. The plot takes into account the data collected in transport and field cooled magnetic susceptibility measurements in the previous sections. The error bars are large along the x axis to reflect the standard deviation of the measured lanthanum content of the crystals. The error bars along y reflect the uncertainty in the transition temperature due to the transition broadness. The figure reflects that there are three bulk states that $(Sr_{(1-x)}La_x)_3Ir_2O_7$ can adopt - a paramagnetic insulator, a collinear antiferromagnetic insulator and a Pauli-paramagnetic metal. When $(Sr_{(1-x)}La_x)_3Ir_2O_7$ is undoped or lightly doped it is an paramagnetic insulator that orders antiferromagnetically below

287.5 K and the light doping only broadens the transition by introducing some disorder into the crystal. For heavier doping the Néel temperature is suppressed to lower temperatures and by x_{M}=0.072 ±0.015, T_{N} has been fully quenched, which coincides with the onset of full metallic behaviour. For a narrow range of x_{M} there are two separate transitions that are decoupled from each other - a metal to paramagnetic insulator transition followed by a paramagnetic insulator to antiferromagnetic insulator transition.

4.6.5 ARPES study on La doped $Sr_3Ir_2O_7$

Bulk measurements can be an inconclusive probe of the ground state of a material due to sample disorder smearing the data and confusing its interpretation. In order to directly probe the ground state of the electrons the ARPES technique was chosen. ARPES measures the energy of the quasi-particles close to the Fermi energy and is capable of producing maps of the Fermi surface, allowing the unambiguous determination of the ground state. The semi-2D layered nature of the La doped $Sr_3Ir_2O_7$ also means that the samples can be cleaved easily under ulta-high vacuum so that the ground state of the surface measured is representative of the bulk.

Crystals of $(Sr_{(1-x)}La_x)_3Ir_2O_7$ from the undoped and nominal 1%, 3%, 5% and 10% samples were given to the Baumberger group from the University of Geneva. The ARPES experiment was conducted at the brand new I05 beamline at Diamond by Prof. Felix Baumberger and Alberto de la Torres with Dr Moritz Hoesch as the local contact. The I05 beamline was ideal for studying these samples because it delivers a high flux of photons to a spot size of less than 50×50 (h×v) μm^2, which is ideal for the small sample size of the iridate crystals. Also the HR-ARPES branch of I05, on which the data was collected, has an energy resolution of 10meV and an angular resolution of 0.01°. The crystals were cleaved in-situ at 10 K under ultra high vacuum to produce very clean atomically flat surfaces to study that were representative of the bulk properties of the sample. The La content of each crystal measured during the ARPES experiment was determined after the experiment by EDX on the cleaved surface.The electronic structure calculations were performed by A. Subedi using the local density approximation with doping treated within the virtual crystal approximation. More information about the ARPES technique an be found in section 3.2.4.

The band structure calculations were conducted using the B*bcb* space group model. In this model the doubling of the in-plane unit cell due to the ordered rotation of the IrO_6 octahedra about the c-axis and the bilayer nature of $Sr_3Ir_2O_7$ causes there to be an even number of electrons per unit cell. Figure 4.48 shows the calculated band structure of $(Sr_{(1-x)}La_x)_3Ir_2O_7$ for a crystal with a measured lanthanum content, x_M, of 0.065. To investigate the effect of electronic correlations on the band structure the calculations were conducted first with LDA + SO and then with LDA + SO + U. Without electron correlations there is a small hole pocket at Γ (k=0,0,0) and electron pockets at the M points ((0,0,$\frac{\pi}{a}$) and (0,$\frac{\pi}{b}$, 0)) that are caused by the itinerancy of the 5d electrons but the rest of the Brillouin zone is gapped. Adding electronic correlations causes the hole pocket at Γ to be pushed below the chemical potential and increases the filling of the electron pockets at M. In figures 4.49 and 4.50 there is no spectral weight at the chemical potential at Γ and so the LDA + SO + U model is best for describing the ground state of $(Sr_{(1-x)}La_x)_3Ir_2O_7$ and, as demonstrated in figure 4.50, accurately models the size of the electron pockets at the M points. The size of these electron pockets increases as the number of itinerant electrons is increased. As the electronic correlations are weakened upon doping, in the undoped parent compound the hole pocket are further pushed below the chemical potential. Without the electron doping from adding lanthanum the chemical potential is also lower so that the electron pockets are not filled, giving rise to the insulating ground state.

Figure 4.49 shows the doping evolution of the dispersion along the Γ*M* nodal direction of $(Sr_{(1-x)}La_x)_3Ir_2O_7$. The undoped and lightly doped samples have no spectral weight at the chemical potential and are therefore insulators. However, upon light doping, faint spectral weight appears around the M point of the parent compound, which indicates that although some carriers have been added by electron doping, they are localised. At and above x_M=0.05 coherent quasiparticle states appear at the Fermi level that show that at these dopant levels $(Sr_{(1-x)}La_x)_3Ir_2O_7$ is metallic. There are no significant changes to the shape of the dispersion of $(Sr_{(1-x)}La_x)_3Ir_2O_7$ on doping so the onset of metallicity is mainly due to a rigid band shift from electron doping rather than changes to the rotation angle of the IrO_6 octahedra.

From the experimental Fermi surface volume and the calculated quasiparticle velocities the cyclotron mass, m^*, was determined to be 3.1(9) m_e for the x_M sample, which corresponds to a Sommerfeld coefficient of 9(2) mJ/molK^2.

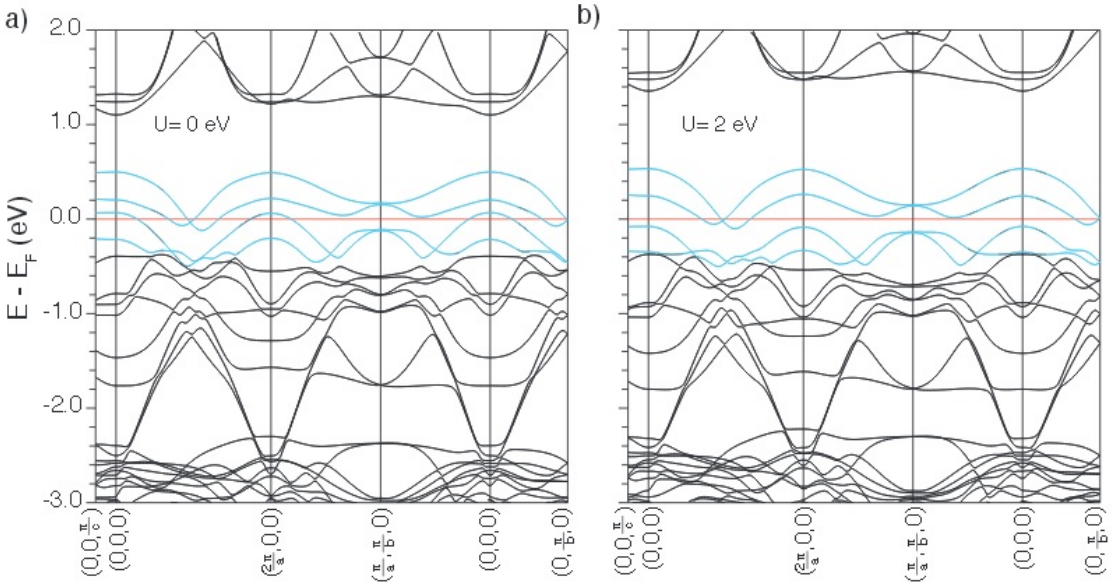

Figure 4.48 *The calculated band structure of $(Sr_{(1-x)}La_x)_3Ir_2O_7$ for x_M = 0.065 using a) LDA + SO and B) LDA + SO + U. Figure taken from the supplementary information of [132]*

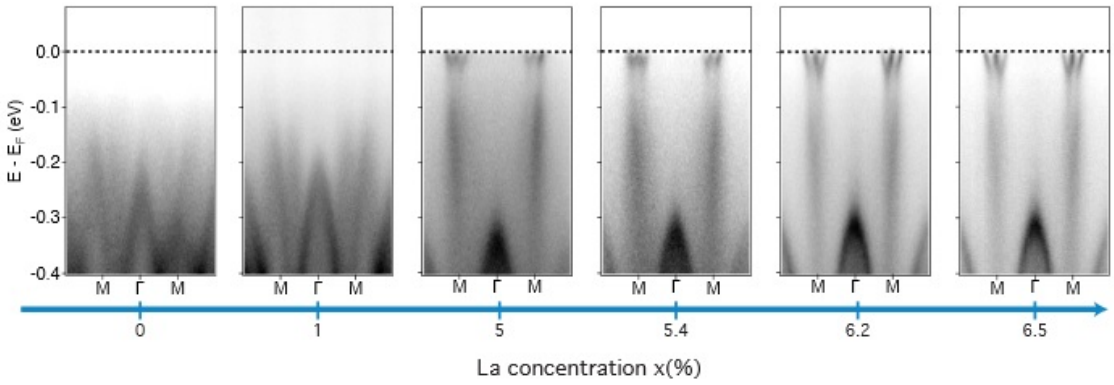

Figure 4.49 *The doping evolution of the dispersion along the nodal direction of $(Sr_{(1-x)}La_x)_3Ir_2O_7$. Figure taken from [132]*

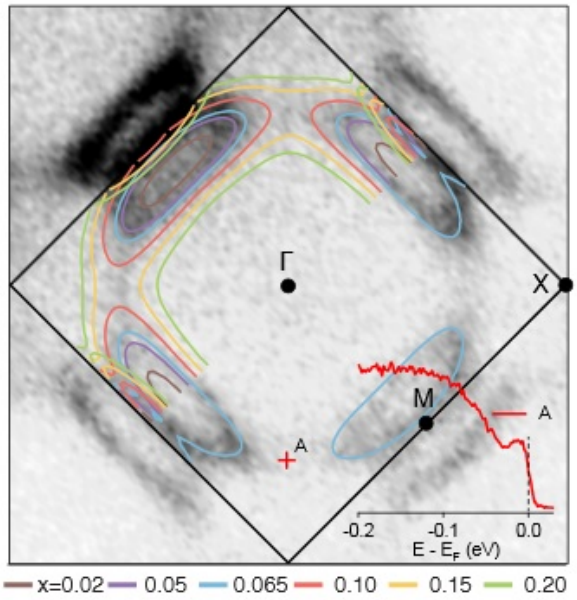

Figure 4.50 *LDA+ SO + U calculations for various different doping levels superimposed on the ARPES measured Fermi surface of the x_M=0.065 sample. The inset, which is an energy distribution curve (EDC) taken at 8 K from around 0 to 0.6π, shows that there is no pseudogap in the antinodal direction at this temperature. Figure taken from [132]*

This is consistent with the Sommerfeld coefficients extracted from heat capacity measurements conducted on metallic $(Sr_{(1-x)}La_x)_3Ir_2O_7$ samples, which were in the region of 8.34 - 11.5 mJ/molK^2. This suggests that the ARPES determined electronic structure is representative of the bulk and that metallic $(Sr_{(1-x)}La_x)_3Ir_2O_7$ is a weakly correlated metal.

In conclusion metallic $(Sr_{(1-x)}La_x)_3Ir_2O_7$ has a small closed Fermi surface with the volume proportional to x_M and has light quasiparticles that are characteristic of a weakly correlated Fermi liquid, in agreement with resistivity measurements that show that the metallic samples exhibit Fermi-liquid behaviour These correlations are stronger in the undoped parent compound and are important in creating the insulating ground state. Spin-orbit coupling is also required to correctly fit the ARPES data. Thus while $Sr_3Ir_2O_7$ has a $J_{\text{eff}} = 1/2$ ground state, no Hubbard bands are required to generate the insulating behaviour.

4.7 Conclusion

From the literature there is no clear distinction in the crystal growth conditions needed to grow different strontium iridate compounds of the series $Sr_{n+1}Ir_nO_{3n+1}$. For all three phases G. Cao simply stated that the crystals were grown "using flux techniques from off-stoichiometric quantities of IrO_2 or Ir, $SrCO_3$, and $SrCl_2$"[28]. The crystal growth conditions for $Sr_3Ir_2O_7$ published by Dhital et al[40], and the crystal growth conditions for Sr_2IrO_4 published by Ishii et al[60] have very similar temperature regimes and differ only by the cooling rate and the IrO_2:$SrCO_3$ molar ratio in the starting materials. Across the literature there is a large variation in the initial starting temperatures used to grow $Sr_3Ir_2O_7$ with the temperatures ranging from 1480°C to 1050°C. Given the lack of clarity in the crystal growth conditions needed to grow each phase, the factors that were important for determining the phase grown were investigated. The investigation was also carried out with the aim of finding the optimal crystal growth conditions for $Sr_3Ir_2O_7$.

36 flux growth attempts were made using a variety of different temperature ranges, cooling rates, ratios of starting materials and different types of crucible. Out of all the variables altered it was found that the molar ratio of IrO_2:$SrCO_3$ in the starting materials was the most important factor in determining the phase formed. Providing that the other reaction conditions remained the same, as the amount of $SrCO_3$ was increased relative to IrO_2 the predominant phase formed changed from $SrIrO_3$ to $Sr_3Ir_2O_7$ to Sr_2IrO_4. The other variables need to be within a certain range for large crystals of a phase to be grown. Crystals of both Sr_2IrO_4 and $Sr_3Ir_2O_7$ could be grown over a range of temperatures from 1200°C to 1300°C, however, reactions below 1150°C generally resulted in the formation of small crystals of $SrIrO_3$ or $SrIrO_3$ powder. Subramanian et al were able to grow $Sr_3Ir_2O_7$ at lower temperatures of 1050°C perhaps due to using a sealed platinum tube rather than a platinum crucible. Varying the cooling rate affected the size and quality of the crystals formed rather than the phase formed with the optimum cooling rate being around 4°C/hr. This is about the same as the cooling rate of 3.4°C/hr used by Dhital et al. Crystals could also be grown from a range of IrO_2:$SrCl_2$ molar ratios of 1:6.5 to 1:20. In summary, it was found that a broad range of reaction conditions could be used to grow all three strontium iridate phases and at a given set of reaction conditions the desired phase could be obtained by simply modifying the IrO_2:$SrCl_2$ ratio.

Six batches of $Sr_3Ir_2O_7$ were grown using different crystal growth conditions to investigate the effect on the crystal quality. Batches SIO#F17, SIO#F18A, SIO#F18B and SIO#F19 had the same reaction conditions apart from a varying IrO_2:$SrCO_3$ ratio while batches SIO#F1 and SIO#F5 were grown using a higher initial firing temperature with a larger amount of flux to compensate for the longer overall cooling time. From EPMA measurements it was found that the crystal growth conditions did not affect the chemical composition of the $Sr_3Ir_2O_7$ crystals formed but the batches that were grown with a smaller proportion of $SrCO_3$ to IrO_2 contained $SrIrO_3$ and IrPt alloy inclusions. This alloy was also more prevalent in samples grown at 1300°C. Batches SIO#F1 and SIO#F17 were found to be of the best quality as they contained no $SrIrO_3$ intergrowths and the least amount of IrPt alloy. From resistivity measurements the crystals from these batches also had the highest and the sharpest change of gradient at the Néel temperature. Batch SIO#F1 had the highest proportion of $SrCO_3$ to IrO_2 in the starting materials of the six batches of $Sr_3Ir_2O_7$ grown but a higher initial firing temperature of1300°C while batch SIO#F17 was grown at a lower temperature of 1200°C and had the second highest proportion of $SrCO_3$ to IrO_2 of the six batches.

Although crystals of $Sr_3Ru_2O_7$ with single layer intergrowths of Sr_2RuO_4 are a problem when trying to grow phase pure $Sr_3Ru_2O_7$ intergrowths[72][1], no Sr_2IrO_4 intergrowths were detected by powder x-ray diffraction in batches SIO#F1 and SIO#F17. There was also no T* transition present in the magnetisation data collected on a crystal from batch SIO#F1. This transition has appeared at temperatures between 230 K and 260 K in the literature and could result from intergrowths of Sr_2IrO_4 as Sr_2IrO_4 has a Néel temperature of around 240 K. For the ruthenates single layer intergrowths appear as additional diamagnetic transitions that can occur at a range or temperatures that differ slightly from the onset of superconductivity in pure Sr_2RuO_4[71]. The fact that no T*transition is evident in my magnetisation data for pure $Sr_3Ir_2O_7$ provides evidence that the T* transition present in the literature is a result of Sr_2IrO_4 intergrowths. Magnetisation, resistivity and heat capacity data consistently found the Néel temperature of the best batches to be around 287.5 K. A Néel temperature lower than this such as Boseggia et al's samples with a Néel temperature of 275 K[19] suggests that the sample is of poorer quality. A good quality sample should also not possess a T* magnetic transition.

The $Sr_3Ir_2O_7$ crystals grown by G. Cao and S. Boseggia et al were grown at much

higher starting temperatures than used in this study at 1480° and 1440°[27][19]. These are temperatures higher than the boiling point of $SrCl_2$ and as it was found that increasing the temperature increased the amount of IrPt alloy formed and both samples were grown using platinum crucibles it is likely that their samples also contain the same amount if not more of this IrPt alloy, especially as it cannot be detected by power x-ray diffraction. It was also found from EPMA that the all the $Sr_3Ir_2O_7$ samples grown were oxygen deficient so the higher temperatures used by G. Cao and S. Boseggia will also likely result in at least the same level of oxygen deficiency. In both cases off-stoichiometric quantities of $SrCO_3$ to IrO_2 were used and as both groups observed a T* transition it is possible that the proportion of $SrCO_3$ to IrO_2 was too high as this would encourage Sr_2IrO_4 intergrowths.

EPMA measurements found all crystals of $Sr_3Ir_2O_7$ to be heavily oxygen deficient giving the iridium ions an average oxidation state of +3.4. EPMA is more accurate for ratios of heavier elements so such a high oxygen deficiency may not be accurate and should be confirmed using another technique such as thermogravimetric analysis. Despite $Sr_3Ir_2O_7$ being already electron doped from the large oxygen deficiency, non of the samples were metallic so the extra carriers were still localised. Given the structural similarities to La_2Cu_4, strontium was substituted with lanthanum to form the series $(Sr_{(1-x)}La_x)_3Ir_2O_7$. As all the batches of $Sr_3Ir_2O_7$ grown had the same chemical composition, replacing some strontium with lanthanum would dope even more electrons into the structure. EPMA measurements confirmed that the oxygen content of $(Sr_{(1-x)}La_x)_3Ir_2O_7$ crystals were similar to that of $Sr_3Ir_2O_7$ and that the saturation limit of La that could be doped into the structure was around 8.3/

Li et al found that T_N of $(Sr_{(1-x)}La_x)_3Ir_2O_7$ decreased as x was increased and that when the system became metallic at x=0.02 the magnetism was not fully quenched[78]. This is surprising as it is unusual to have a co-existence of long range antiferromagnetic order with a metallic ground state. In our samples we similarly found that T_N decreased as x increased but by x=0.072, when the sample was fully metallic, T_N had been fully quenched. A metal-insulator transition (MIT) was also observed at 279 K in the x=0.048 sample that was decoupled from the broad magnetic transition just below 250 K. A similar MIT transition was also seen in L. Li et al's x=0.01 sample at 260 K[78]. Therefore, apart from the complete quenching T_N with the onset of metallicty, our samples appear fully the same trends in bulk properties but at different dopant contents.

Going beyond what was published in Li et al's paper it was found that even at the the maximum dopant level of x=0.083, no superconducting transition was observed. The low temperature power law of the metallic samples was also found to have a T^2 dependence characteristic of a Fermi-liquid metal. Heat capacity measurements were conducted for the first time on metallic samples of $(Sr_{(1-x)}La_x)_3Ir_2O_7$ and it was found from these that the Sommerfeld coefficient was 11.49 mJ/Ir mol K^2 for the x=0.072 crystal and 8.35 mJ/Ir mol K^2 for the x=0.076 crystal. Given that $Sr_3Ru_2O_7$ has a Sommerfeld coefficient of 70 mJ/Ru mol K^2[113] and Sr_2RuO_4 has a Sommerfeld coefficient of 38.2 mJ/Ru mol K^2[106], metallic $(Sr_{(1-x)}La_x)_3Ir_2O_7$ is only weakly correlated in comparison. The electron correlations also appear to decrease as x is increased.

The difference in the La dopant content needed for the metal-insulator transition to occur between our samples and L. Li et al's may be due to from numerous factors. Firstly, the lanthanum content of L. Li samples were determined by EDX rather than EPMA. We used both techniques to measure the La content of our samples and found that the mean La content typically varied by around 1% between the two techniques. EPMA is a more sensitive technique than EDX in determining the La content so the values determined by this technique were deemed to be more accurate. Secondly, there was a large standard deviation of up to 1.5% in the measured La content of a crystal due to a variation in the La content across a sample. EDX maps and 6 point resistivity measurements did not find a concentration gradient of La across the sample or large-scale phase separation so the variation must arise from randomly distributed microscopic domains each containing a different amount of La. As EPMA measures 1 μm sized points the mean La content of a sample could vary depending on the number and exact location of the points measured. There is also a variation in the average La content of each crystal in a batch so the error on the La content when comparing samples is large.

Looking at the structural evolution of $Sr_3Ir_2O_7$ upon La doping, the a and b lattice parameters increase with x but the c lattice parameter does not change significantly. This results in an overall increases in unit cell volume. It is hard to draw conclusive results from the single crystal study due to the difficulty in refining oxygen positions in x-ray diffraction but we found that the IrO_6 octahedra became less distorted on doping and Ir-O-Ir bond angle, θ, decreased by 2.5° on average. A decrease in θ would decrease the orbital overlap to favour a more insulating state while a less distorted octahedron would help stabilise the

J_{eff}=1/2 ground state so it is clear that the MIT is not structurally driven but almost entirely as a result of electron doping. ARPES measurements confirm that the onset of metallicity is largely a result of a rigid band shift as the dispersion of $(Sr_{(1-x)}La_x)_3Ir_2O_7$ remains unchanged apart from spectral weight appearing at the Fermi surface once the metallic phase has been reached. However ARPES found that $(Sr_{(1-x)}La_x)_3Ir_2O_7$ was metallic by x=0.05, with the value of x determined by EDX. Thus the chemically induced MIT must be a sharp transition and occur at around 5% La to fit with the bulk properties data collected.

ARPES measurements conducted by A. de la Torre on the La doped samples grown also revealed that while $Sr_3Ir_2O_7$ has a J_{eff}=1/2 ground state it is not a Mott-Hubbard insulator as no lower and upper Hubbard bands are present in the dispersion[132]. Instead, the insulating ground state is created as a result of the itinerancy of the 5d electrons, which creates an electron pocket and a hole pocket. Electron correlations push the hole pocket below the chemical potential to create an insulating ground state. This is important as the insulating behaviour of $Sr_3Ir_2O_7$ has been previously explained by the narrow half-filled J_{eff}=1/2 band being split by the Mott-Hubbard effect.

The correct space group and hence the structure of $Sr_3Ir_2O_7$ is still under debate as the subtle differences in the oxygen positions that distinguish between the tetragonal and pseudo-tetragonal structural models are hard to distinguish by x-ray diffraction. Throughout this thesis the goodness of fits of two different structural models, namely the I4/*mmm* and B*bcb* space group models, have been compared. However, neither model has been consistently better than the other in terms of goodness of fit. In section 4.5 a high temperature diffraction study was conducted to look for evidence of symmetries lower than I4/*mmm* by following the evolution of any peak splitting with temperature. Another aim of the high temperature study was to look for any high temperature structural phase transitions such as an orthorhombic to tetragonal transition as seen in other Ruddlesden-Popper compounds[50]. However, no structural phase transition or divergence of the a and b lattice parameters were observed to indicate a non-tetragonal space group. The goodness of fit of neither space group to the data was consistently better than the other across all the temperatures measured. Thus no evidence from this study was found to support the B*bcb* space group model of the structure of $Sr_3Ir_2O_7$ and this thesis has found no additional evidence to that provided in the literature of the B*bcb* space group model being correct. As was required to determine the correct structure of $Sr_3Ru_2O_7$, single crystal neutron

diffraction data will be required to unambiguously determine the correct structure of $Sr_3Ir_2O_7$.

Finally the properties of $SrIrO_3$ were re-investigated. From experimenting with the crystal growth conditions to grow all three phases of room pressure strontium iridate, crystals of $SrIrO_3$ were grown with RRR values that were 5 times better than those reported in the literature. $SrIrO_3$ had been described by G. Cao as a non-Fermi liquid close to a quantum critical point with a low temperature mass enhancement of the Wilson ratio[30]. It was also predicted to be a triplet paired superconductor at low temperature due to its proximity to a ferromagnetic instability - as evidenced by an upturn in the magnetic susceptibility below 15 K[30].

With our better quality samples it was found that $SrIrO_3$ followed a T^2 power law below 15 K and that there was no mass enhancement of the Wilson ratio. The R_W value of 1.43 that was calculated is typical of a Fermi liquid metal with some electron-electron correlations. Dilution fridge measurements of the resistivity conducted down to 20 mK also found no evidence of a superconducting transition apart from the onset of a superconducting transition at 78 mK. This was likely caused by the presence of a small amount of IrPt alloy in the crystals. In short no evidence was found for any of the exotic phenomena reported or predicted in the literature and the non T^2 power law originally reported was probably due the crystals being of poor quality.

Chapter 5

Search for novel correlated electronic states in the platinates

5.1 Literature review of the platinates

Platinum, found in group X of the periodic table, is a noble metal and its inert nature makes it an ideal material for crucibles, jewellery and in the production of glass. In 1877 it was found that platinum metal reacted under aggressive conditions to form platinum oxide[64]. Further work uncovered that platinum oxide occurs in five different phases - PtO[91], Pt_3O_4[47], α-PtO_2[11], β-PtO_2[125] and β'-PtO_2[57]. Platinum oxides have a wide range of technological applications from catalysts to nanoelectronics to optics to electrochemistry[82]. Adam's catalyst[11] or α-PtO_2 has multiple uses including, but not limited to, the oxidation of ethanol to acetic acid[148], the hydrosilylation of functionalised alkenes[114] and the oxidation of ammonia to nitric oxide[145]. Thin films of platinum oxides have also been used in nanoelectronics as memory capacitors[76] and in super-resolution near-field structure disks[67].

Although platinate compounds have been studied for catalytic purposes, this section is concerned with searching for novel correlated electronic states in the platinates. As mentioned in section 1.3, platinum most commonly adopts an oxidation state of either +2 or +4 with the +2 cation being in a square planar coordination environment and the +4 cation being in a octahedral coordination environment within the crystal structure. If the compound contains mixed valence

platinum then the crystal structure usually contains a mixture of PtO_2 squares and PtO_6 octahedra, as is the case for APt_3O_6 (A= Cd, Mn, Co, Zn, Mg, Ni[108][118]. This gives the platinum ions a ground state electronic configuration of either t_{2g}^6 (Pt^{4+} Oh) or $d_{yz}^2 d_{xz}^2 d_{xy}^2 d_{z^2}^2$ (Pt^{2+} square planar), both of which have a spin quantum number of zero, which gives rise to diamagnetic band insulators. Mixed valence platinate compounds can be either semiconducting or metallic depending on the activation energy required for electrons to hop between the Pt^{2+} and Pt^{4+} ions and the extent of the orbital overlap. To search for novel correlated electronic states in the platinates one needs to study platinate compounds that contain platinum in an unusual oxidation state such as +1, +3 or +5 so that the spin quantum number is non-zero. There are some known platinate compounds that do contain platinum in unusual oxidation states such $CoPtO_2$[61], $PbPt_2O_4$[130] and $Pb_{1-x}Bi_xPt_2O_4$[98] that are metallic. They provide a good starting point for searching for novel correlated electronic states in the platinates and in section 5.4, the physical properties of one such compound, $CaPt_2O_4$, are re-investigated. $CaPt_2O_4$ is a metal containing platinum in the unusual oxidation state of +3 however its electronic properties had yet to be measured below 77 K.

However, more exploratory work needs to be done to synthesise novel platinum compounds containing platinum in an unusual oxidation state. The lack of platinate compounds in comparison to compounds of other transition metal oxides is due to the difficultly of their synthesis. As mentioned previously platinum is very unreactive but compounds of platinum also tend to have low decomposition temperatures and high melting temperatures, which makes their crystal growth very challenging. However, flux growth, which lowers the temperature at which crystal growth can be conducted, has been previously used to grow crystals of platinate compounds and recently Ln_3NaPtO_7 and La_4PtO_7 (Ln = La, Nd[55]) were discovered by this method. In section 5.2 exploratory flux growths are conducted with the aim of discovering more novel platinate compounds in hope that they may possess exotic correlated electronic phenomena such as superconductivity or spin-orbit facilitated magnetic insulating ground states.

5.2 Discovery and characterisation of Pt^{3+} based $K_2CaPt_{3-\delta}O_6$

It is difficult to grow single crystals of platinum oxides for a variety of reasons. Firstly, platinum is a noble metal and so is by nature unreactive. Secondly, platinum compounds tend to have a low decomposition temperature, such as PtO_2 that has a decomposition temperature of just 450°C, and so will decompose to elemental platinum before high enough temperatures are reached for the compound to melt, especially as platinum metal has a high melting temperature of 1768°C. Flux growth was used to find new platinum compounds as it allows crystals to be grown at lower temperatures than conventional melt growth techniques. Also if the correct flux is used the reactivity of the starting materials can be enhanced.

In the search for crystals of a new platinate compound with an unusual oxidation state a flux was needed that would melt at a reasonably low temperature to prevent the decomposition of any resultant crystals. The flux also should preferably be non-toxic and easy to remove. This narrowed the choice of fluxes down to binary chlorides such as KCl and hydroxide fluxes such as NaOH.

While trying to grow crystals of $CaPt_2O_4$ (section 5.4.2), it was realised that hydroxide fluxes had the added advantage of being strongly alkaline, which stabilises a more reactive PtO_2 anion in solution[96] and had a strongly oxidising effect that would help prevent the reduction of platinum oxide to elemental platinum. Hydroxide ions also have low melting temperature and are highly soluble in water and so can be easily removed. For example NaOH has an optimum crystal growth temperature range from 450°C to 700°C while KOH has an optimum temperature range for crystal growth of 550°C to 750°C[22], although the boiling point of these two fluxes is actually much higher at 1388°C and 1327°C respectively.

Given the oxidising nature of hydroxide fluxes, if PtO_2 was purely used as the source of platinum in the flux growth reaction then the resultant compound would only contain platinum in a +4 oxidation state or higher and while some Pt(V) compounds exist such as $[PtF_5]_4$, they are very rare. To attempt to create novel compounds containing unusual oxidation states of platinum such as +1 or +3, platinum metal or a mixture of platinum metal and platinum oxide were used as starting materials and the oxidising nature of the hydroxide flux

was utilised to oxidise the platinum to a higher, intermediate oxidation state. This method is better than trying to reach an intermediate oxidation state of platinum by reducing a Pt(IV) compound as it would be very easy to over reduce the compound to platinum metal. Given that these high temperature hydroxide solutions attack platinum and that the flux growth reactions occurred at relatively low temperatures, alumina was used as the crucible material. Sealed quartz tubes could not be used for these reactions either as group I metals such as potassium and sodium attack quartz.

5.2.1 Synthesis of $K_2CaPt_{3-\delta}O_6$

Although some small (50 μm) red hexagonal crystals (see figure 5.1) had been observed in attempts to grow crystals of $CaPt_2O_4$ by mixing PtO_2 and $CaCO_3$ in a KOH flux, large amounts of powder and crystals of this unknown material were only synthesised when an excess of elemental platinum was included in the starting materials. Initially the red hexagonal crystals were believed to be KPt_2O_3 as the powder diffraction pattern appeared to be similar to that of KPd_2O_3 on the Eva structural database, however, calcium was clearly an essential component of this new structure as the red crystals and orange powder were not obtained when the reaction was repeated without $CaCO_3$. Therefore the identity of this novel platinate was originally thought to be $CaPt_2O_3$. The initial reaction conditions gave Ca_4PtO_6 and elemental platinum by-products so the reaction conditions were modified to try and synthesise the new compound phase pure. All of the conditions for these flux growth attempts and the reaction outcome are listed in appendix A. Variables that were modified were the ratio of the flux to the starting materials, the ratio of the starting materials, in particular the ratio of Pt to PtO_2, the crucible size and whether a lid was used on crucible and the temperature and dwell time of the reaction. 700°C was found to be the optimum temperature of the reaction as this prevented elemental platinum from forming and resulted in the formation of better quality crystals close to the rim of the crucible. Although there was still some amorphous black material in the powder at the bottom of the crucible there also did not appear to be any Ca_4PtO_6 crystals or powder that could be detected in the x-ray diffraction pattern. The amorphous impurity in the powder could be removed by lowering the temperature to 650°C, however, this reaction temperature was too low for crystals to form. The size of the crystals were largest when a mass ratio of 10:1 of KOH:$K_2CaPt_{3-\delta}O_6$ or an approximately 85:1 molar ratio of KOH:$CaCO_3$ was used, although the largest

crystals were no bigger than 100 μm. A molar ratio of starting materials of 1:1.2:0.8:85 of $CaCO_3$:Pt:PtO_2:KOH and a dwell time of 48 hours were used in the final optimised reaction.

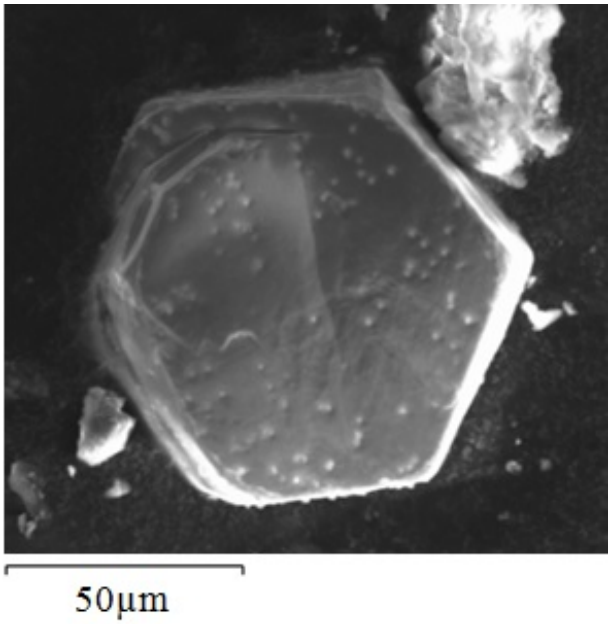

Figure 5.1 *SEM photograph of a hexagonal crystals of $K_2CaPt_{3-\delta}O_6$.*

From a combination of single crystal and powder x-ray diffraction, powder neutron diffraction and EPMA data this phase was identified as $K_2CaPt_{3-\delta}O_6$ (sections 5.2.2, 5.2.3 and 5.3.3). Attempts were made to synthesise polycrystalline powder of $K_2CaPt_{3-\delta}O_6$ via traditional solid state synthesis routes with the aim of making large quantities of pure powder for powder neutron diffraction measurements and to allow the material to be homogeneously doped. Table A.4 shows the conditions that were used in trying to make $K_2CaPt_{3-\delta}O_6$ powder via this route. Although only a few synthesis attempts were conducted, the $CaCO_3$ appears to react preferentially to form $CaPt_2O_4$ rather than $K_2CaPt_{3-\delta}O_6$. It seems that the KOH flux plays an important role in the stabilisation and formation of $K_2CaPt_{3-\delta}O_6$. It should also be noted that when these synthesis attempts were undertaken the Ca:K ratio was believed to be 1:1 so the 3:1 molar ratio of K_2CO_3:$CaCO_3$ used in reaction KCPO#P2 was believed to a large excess of potassium. If further attempts were made to synthesise $K_2CaPt_{3-\delta}O_6$ now, stoichiometric quantities of the starting materials would be used.

Attempt name	Starting materials	Reaction Conditions	Outcome
KCPO#P1	$3PtO_2 + 0.5K_2CO_3 + CaCO_3$	650°C for 12 hours in air	61% Pt, 38%$CaPt_2O_4$ and 1%Ca_4PtO_6 from x-ray powder diffraction
KCPO#P2	$3PtO_2 + 3K_2CO_3 + CaCO_3$	800°C for 12 hours in air	60% Pt and 40%$CaPt_2O_4$ from x-ray powder diffraction
KCPO#P3	$3PtO_2 + KO_2 + CaCO_3$	600°C for 12 hours in air	Mainly amorphous with some unreacted $CaCO_3$ and CaO present

Table 5.1 *The conditions used in attempting to synthesise poycrystalline powder of $K_2CaPt_{3-\delta}O_6$ via traditional solid state routes.*

5.2.2 Single crystal powder and x-ray diffraction

Single crystal x-ray diffraction is the optimum method for determining the crystal structure of novel material and so data were collected via the Edinburgh Crystallography Service on a 62 μm crystal of the novel compound using an Oxford diffraction supernova dual wavelength diffractometer. Mo Kα radiation was selected for the data collection, which was conducted at a temperature of 120 K. When the cell was indexed in the initial refinement it was clear that the crystal structure was different to that of KPd_2O_3 as the a lattice parameter was halved in comparison to give lattice parameters of a=3.1607(4)Å and c=18.7835(12)Å. However, the space group was still R$\bar{3}$m.

The structure was refined and solved using a combination of SHELXS 86 and CRYSTALS. The chemical composition was unknown at the time of the refinement and as potassium and calcium ions possess the same number of electrons they were indistinguishable during the single crystal x-ray refinement process. This meant that the structure was initially refined as being $Ca_{\frac{2}{3}}PtO_2$ with the occupancy of the 6c site being a third. This structure gave an R_1 value of 0.075. EPMA found the crystals to contain an approximately 2:1 ratio of K:Ca and an occupancy of the 6c site of a half. When the data set was re-refined in JANA2006[107] using this new model the R_1 value improved to 0.0719. Powder neutron diffraction data found the 3a site to be slightly platinum deficient, in agreement with the EPMA data, with an occupancy of 0.868 at 4K yielding the formula $K_2CaPt_{3-\delta}O_6$ (δ=0.4), giving the platinum ion an oxidation state of approximately +3.

The structure of $K_2CaPt_{3-\delta}O_6$ is shown in figure 5.2 and the unit cell coordinates and thermal displacement parameters, as refined from the x-ray single crystal data set collected in Edinburgh, are shown in table 5.2. It consists of monolayers of edge-sharing PtO_6 octahedra of which there are 3 full layers per unit cell in a staggered A-B-C formation. The K-Ca 6c site lies above the face of the PtO_6 octahedra, which gives the potassium and calcium ions a coordination number of 6. In section 5.2.4 superstructure peaks in the single crystal data reveal that the potassium and calcium ions are ordered across this site rather than being randomly distributed. However, as the ordering is only correlated within a layer rather than between layers it is not possible to model this ordering using a lower symmetry space group and the positions of the potassium and calcium ions become averaged out over many layers. Refining the single crystal data in

the R$\bar{3}$m space group where the K/Ca ion distribution is averaged equally across all inter-layer sites the six K/Ca-O bond lengths are all equal at 2.725$\mathring{A}$. The Shannon and Prewitt ionic radii of the potassium, calcium and oxygen are 1.38Å, 1.0Å and 1.40Å so from the average bond length the K:Ca ratio is 0.86:0.14. As the K:Ca ratio is 2:1 from EPMA data the larger potassium ion has a greater contribution in setting the K/Ca-O bond length. In this structural model the Pt-O-Pt bond angle was calculated to be 96.56° and the Pt-O bond length of 2.134Å was very similar to the estimated ideal bond length of 2.1325Å for a Pt(III)-O bond.

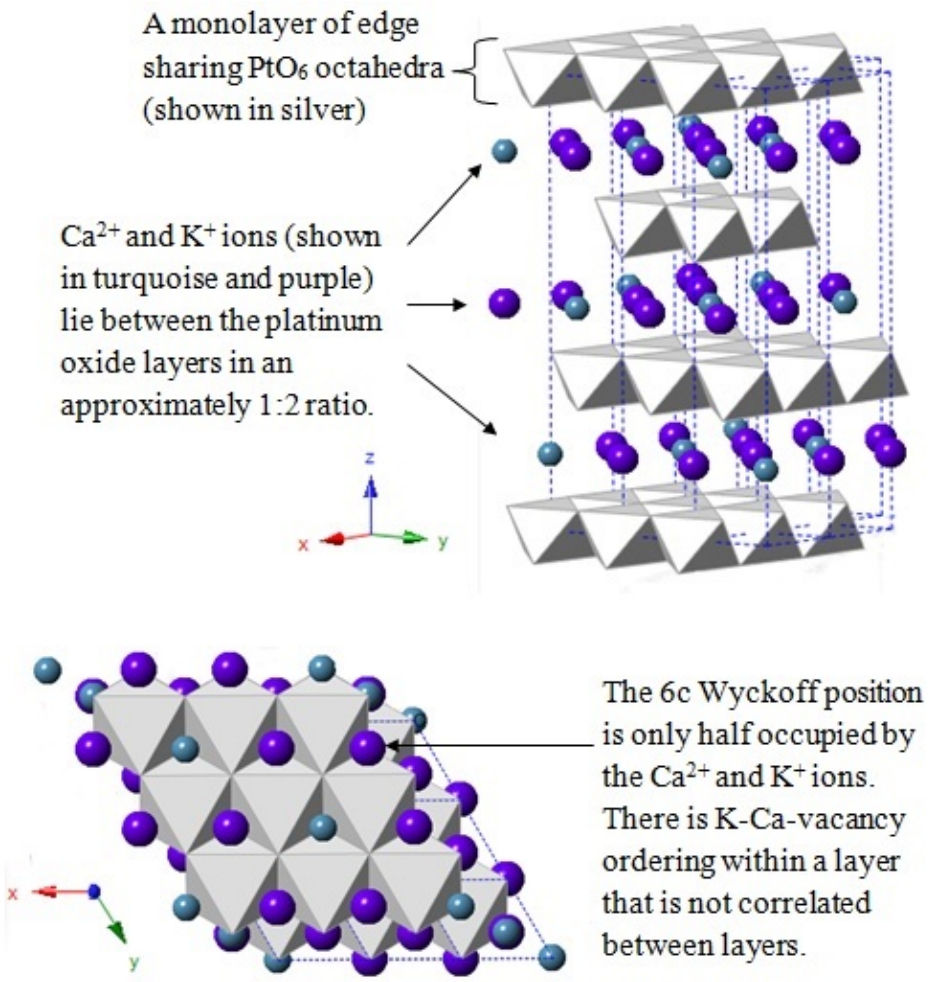

Figure 5.2 *The crystal structure of $K_2CaPt_{3-\delta}O_6$ shown looking down the (001) (bottom) and (111)(top) direction. The unit cell is outlined by the blue dotted lines. The PtO_6 octahedra are shown in grey and the calcium and potassium ions are shown as turquiose and blue spheres respectively. An example of possible K-Ca-vacancy ordering within a layer is shown.*

Atom	Wyckoff Symbol	x	y	z	Occupancy	$U_{iso/eq}$	U_{11}	U_{22}	U_{33}	U_{12}	U_{13}	U_{23}
Pt	3a	2/3	1/3	1/3	1	0.0194(10)	0.0161(13)	0.0161(13)	0.0260(16)	0.0081(7)	0	0
Ca	6c	2/3	1/3	0.5	1/6	0.052(11)	0.062(16)	0.062(16)	0.034(13)	0.031(8)	0	0
K	6c	2/3	1/3	0.5	1/3	0.052(11)	0.062(16)	0.062(16)	0.034(13)	0.031(8)	0	0
O	6c	0	0	0.3922(17)	1	0.0017(9)	0.021(13)	0.021(13)	0.008(13)	0.010(6)	0	0

Table 5.2 *The unit cell of $K_2CaPt_{3-\delta}O_6$ from the refinement of single crystal x-ray diffraction data collected at 120K on an Oxford Diffraction Supernova diffractometer in Edinburgh.*

This structure that was checked against x-ray powder diffraction data, which was collected on some ground up crystals of $K_2CaPt_{3-\delta}O_6$. The results are shown in figure B.34. The structural model appears to be a good fit to the data apart from an additional peak at a 2θ value of 19 degrees. Due to the crystals being so small the powder had to be formed from scrapping crystals from the side of the crucible and grinding them up so it is possible that some impurities were mixed with the crystals. Initially the impurity was thought to be Ca_4PtO_6, as crystals had been grown in previous attempts to grow $K_2CaPt_{3-\delta}O_6$ and the most intense peak of Ca_4PtO_6 was at the correct theta value of the unknown peak. However neutron powder diffraction showed that this impurity phase was not Ca_4PtO_6 and the identity of the impurity phase is still unknown.

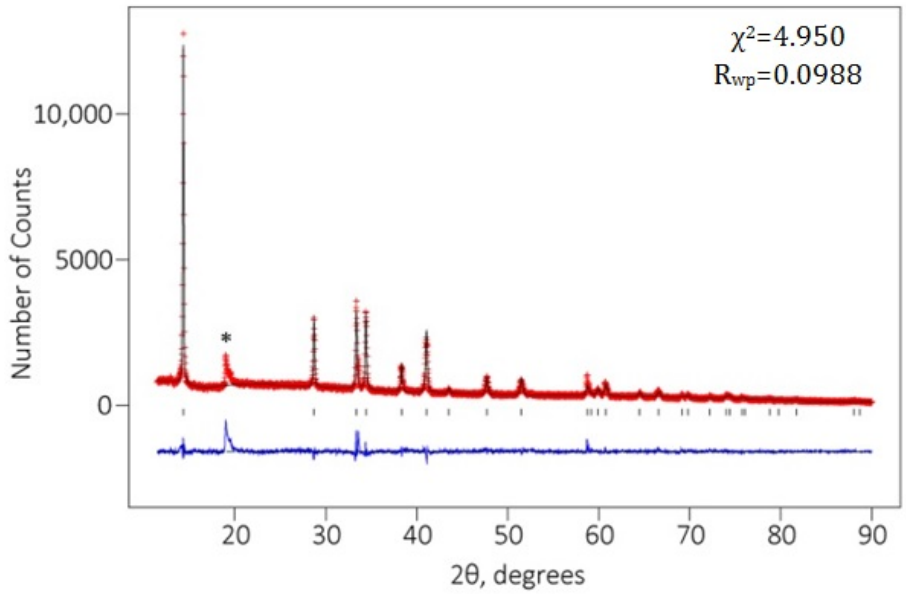

Figure 5.3 *Rietveld refinement of x-ray powder diffraction data collected on $K_2CaPt_{3-\delta}O_6$ to the structural model that was obtained from single crystal x-ray diffraction.*

5.2.3 Powder neutron diffraction on HRPD

From single crystal x-ray diffraction data the structure of $K_2CaPt_{3-\delta}O_6$ has one type of platinum environment and a value of δ=0 giving it an oxidation state of +2.67, which is close to being Pt(III). However, compounds that appear to contain Pt^{3+} often disproportionate to Pt^{2+} and Pt^{4+}. It was possible that the current structural model was too simplistic due to the difficulty in resolving the oxygen positions in contrast to the platinum positions in single crystal x-ray diffraction. To confirm the structural model it was important to conduct powder

neutron diffraction to not only check the oxygen positions, but to also refine the potassium to calcium ratio on the 6c site.

Powder neutron diffraction data were collected using the HRPD beamline at ISIS spallation source with Kevin Knight as local contact. To check for a temperature dependent charge disproportionation of Pt(III) to Pt(II) and Pt(IV) data was collected at 4 K, 100 K, 200 K and 400 K. The powder for the experiment was prepared a week before the experiment to prevent the deterioration of the sample, and was dried at 200°C for 12 hours to remove any absorbed water from the sample. The powder was prepared using the synthetic route at the lower temperature of 650°C as described in section 5.2.1, and appeared pure apart from the anomalous peak at 19° in powder x-ray diffraction. It would have been better to have conducted the study on ground crystals of $K_2CaPt_{3-\delta}O_6$, however, only about a couple of hundred crystals with a diameter of at most 100 μm can be grown at a time so it would have been impractical to obtain the masses required for powder neutron diffraction by this method. For the experiment 1.6332 g of sample was placed in an enclosed flat plate geometry aluminium sample holder with a vanadium window. This sample environment is particular suitable for $K_2CaPt_{3-\delta}O_6$ as platinum has a reasonably large neutron absorption cross-section of 10.3 barn [120] so a thin plate sample geometry minimises the re-absorption of the diffracted neutrons. A preliminary data collection found that there was copper in the initial cryostat used and after the sample was inserted into a new cryostat the background had doubled, which suggested that the sample had absorbed water. The sample was changed with that of another batch, which had a background level that matched the standard background of the cryostat.

Data was initially collected at 4 K, with the data collected over 4 hours to improve the statistics and hence the resolution of the peaks. Further powder neutron diffraction data was collected on warming. The observed neutron diffraction pattern did not change with temperature apart from a slight shift in the Bragg reflections to larger d-spacings on warming due to the thermal expansion of the lattice. Fitting the diffraction pattern to the structural model obtained from single crystal x-ray diffraction showed that this expansion was anisotropic with the expansion of the c axis being about 4 times as large as the expansion of the a lattice parameter (see figure 5.4).

Although Rietveld analysis was conducted on all of the diffraction patterns, figure 5.5 shows data that was collected at a temperature of 4 K as the thermal displacement parameters are smallest at this temperature so the potassium to

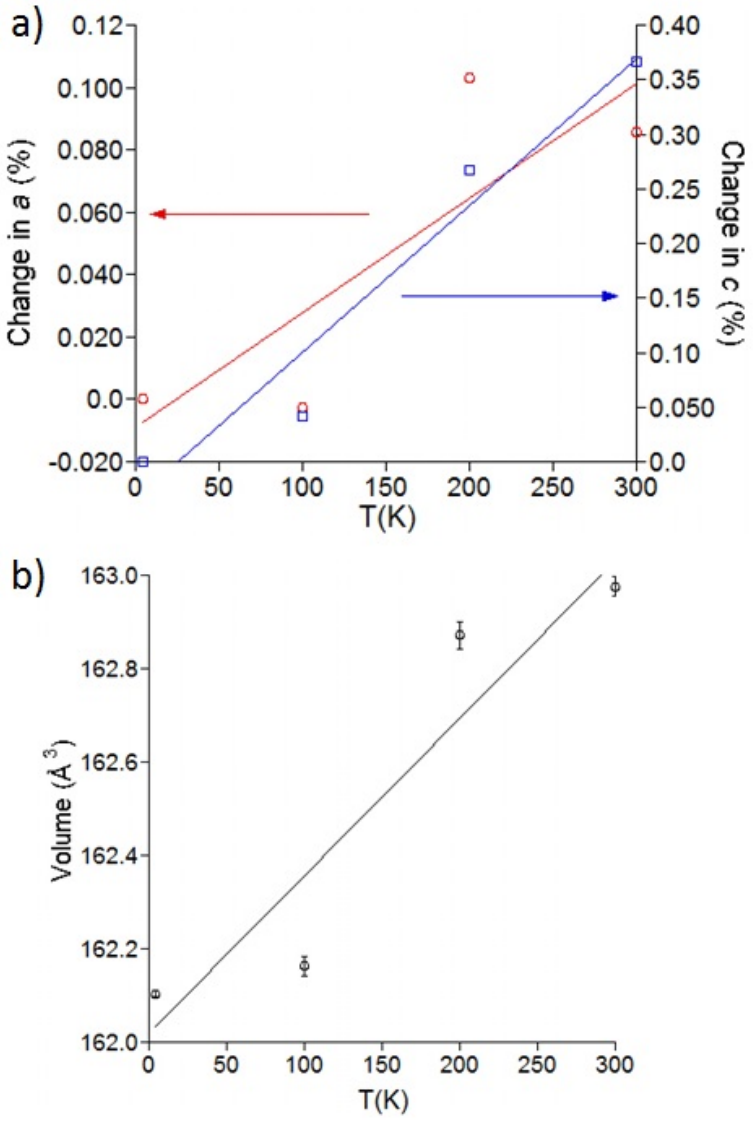

Figure 5.4 *a) The percentage expansion of the* a *and* c *unit cell parameters and b) the increase in the unit cell volume on warming* $K_2CaPt_{3-\delta}O_6$ *from 4 K to 300K.*

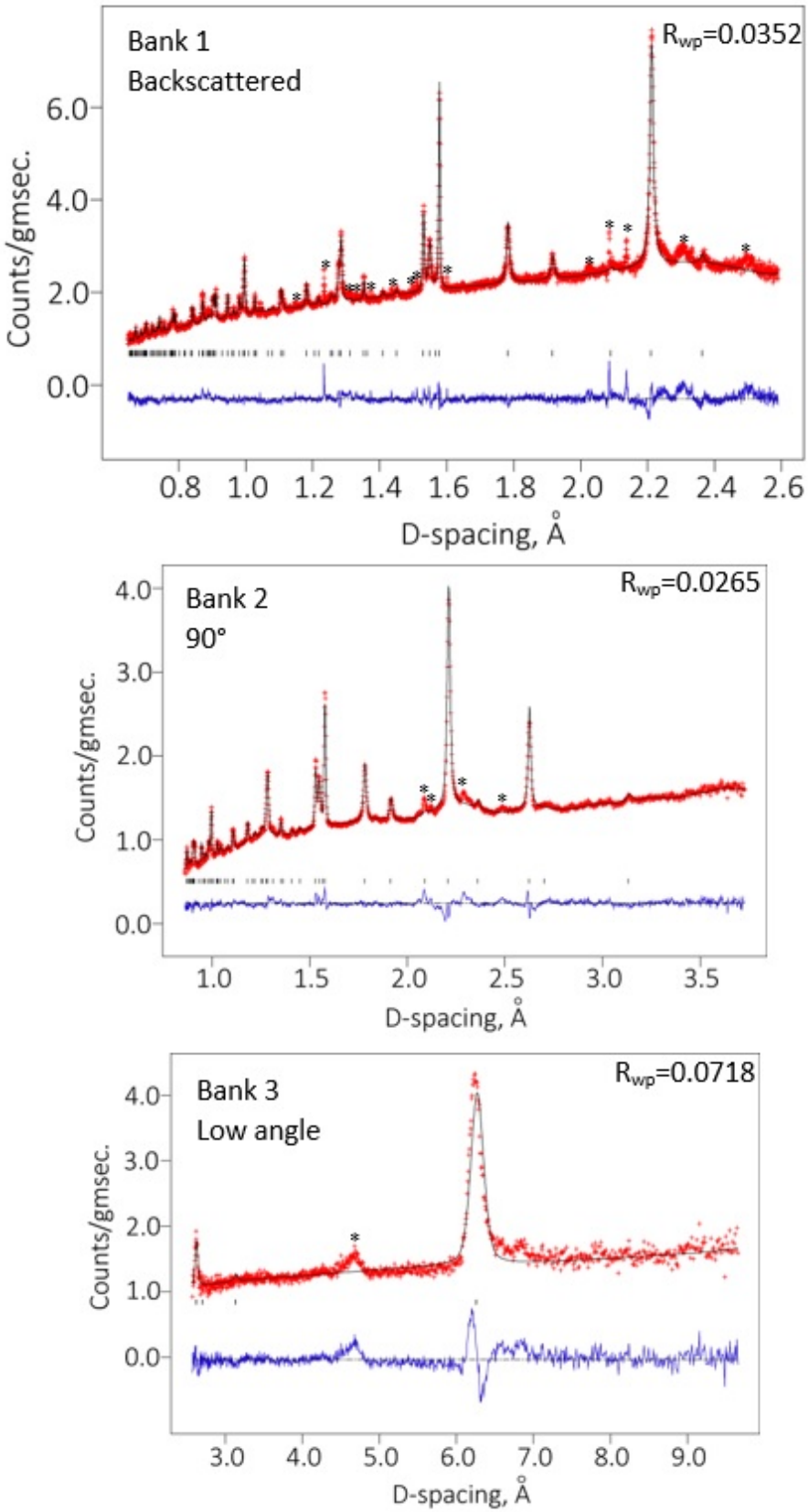

Figure 5.5 *Rietveld refinement of the powder neutron diffraction data collected on $K_2CaPt_{3-\delta}O_6$ at 4K using HRPD at ISIS, using the data from all three detector banks, to the structural model determined by single crystal x-ray diffraction. The starred peaks are those not accounted for by the current structural model.*

calcium ratio can be refined more accurately. The data was refined using all three data banks on HRPD, as outlined in section 3.2.7, and at 4 K the data had a collective χ^2 of 6.528. This higher value of χ^2 is due to the presence of peaks that are unaccounted for by the current structural model, which are starred, and these are thought to correspond to an unknown impurity - perhaps the same impurity responsible for the paramagnetic upturn in the magnetic susceptibility data. Otherwise the intensity and position of the peaks are generally a good fit to the current structural model. At first a K:Ca ratio of 5:1 with a total site occupancy of a half was refined on the 6c site at all measured temperatures. However, setting the K:Ca ratio at 2:1, as indicated by EPMA data, caused the occupancy of the platinum site to decrease to 0.865 while the total occupancy of the K/Ca 6c site remained at a half, causing the total χ^2 value to decrease by typically 0.8. The z position of the oxygen site was refined to be 0.3906(8) and the lattice parameters at 100 K were found to be slightly different to those obtained from single crystal x-ray diffraction with a=3.1549(1)Å and c=18.814(1)Å compared to a=3.1607(3)Å and c=18.786(2)Å. This means that the Ca/K-O bond lengths are longer at 2.749Å, while the Pt-O bond length is shorter at 2.116Å than determined by single crystal x-ray diffraction. It is possible that the powder form of $K_2CaPt_{3-\delta}O_6$ is slightly more potassium rich than the single crystals, which would explain these differences. The U_{iso} values for the Ca/K 6c site are very large at 0.1027, which is nearly double the U_{iso} value derived from the single crystal set, so it may be that as well as being more potassium rich the site is more disordered. The positional parameters refined from the neutron diffraction data collected at 4 K are shown in table 5.3. Tables with parameters from all of the refinements can be found in appendix B

Atom	Wyckoff Symbol	x	y	z	Occupancy	$U_{iso/eq}$
Pt	3a	2/3	1/3	1/3	0.868(11)	0.00518(67)
Ca	6c	2/3	1/3	0.5	1/6	0.1027(26)
K	6c	2/3	1/3	0.5	1/3	0.1027(26)
O	6c	0	0	0.390573(77)	1	0.0906(73)

Table 5.3 *The unit cell of $K_2CaPt_{3-\delta}O_6$ from the refinement of powder neutron diffraction data collected at 4 K on HRPD.*

5.2.4 Superstructure

Due to the appearance of these unaccounted for Bragg peaks in the neutron diffraction patterns, x-ray single crystal data were recollected using the Agilent Supernova diffractometer in the research complex at Harwell campus to double-check the structure. A very small 10 μm crystal that appeared to be of a very high quality from pre-measurement scans was selected and Dr Jeppe Christianson was consulted to optimise the data collection settings. This time Cu Kα radiation was used due to the small size of the crystal and data was collected over 5 runs to cover the entire hemisphere over 12 hours. The high quality of the data is apparent from images of the reciprocal space created in Crysalis^{Pro} that are shown in figure 5.6. The data was still found to be of the space group R$\bar{3}$m but the better quality data resulted in a lower R_1 value of 0.0511. The lattice parameters were also closer to those refined from the powder neutron x-ray diffraction with a=3.1596(4) and c=18.8179(16). When allowed to refine freely while the K:Ca ratio was fixed at 2:1, the occupancy of the platinum site was found to be 0.953, showing only a slight Pt deficiency. The 5:1 K:Ca ratio model was also tested but this increased the R_1 value to 0.0558. Thus the 2:1 K:Ca model seems to be the best fit in agreement with the EPMA data. The smaller Pt deficiency in comparison to the neutron diffraction data and the EPMA data may be due to the insensitivity of x-ray diffraction to light elements in comparison to neutron diffraction or EPMA.

During this second single crystal x-ray diffraction study diffuse scattering was seen along the (hhl) direction, as also shown in figure 5.6, indicating that there is a superstructure within the crystal structure. As the diffuse scattering appears as 1D lines rather than 2D planes in the reciprocal space images it shows that there is ion order within 2D planes rather than 1D lines in the crystal structure, however, the ion ordering within a 2D plane is not correlated between planes. Looking along the (hk0) direction it can be seen that these diffuse scattering lines occur at values of (1/3, 1/3, l) with respect to the unit cell, which implies that the ions are ordered in a 2:1 ratio. These superstructure reflections can be more clearly seen in figure 5.7. The weak nature of the peaks and this 2:1 ordering makes it likely that the superstructure is related to the K-Ca plane. More experimental work will be required to determine the exact nature of the ion ordering but looking at the bond lengths in the Ca-K plane (see figure 5.8) it is apparent that the nearest neighbour bond length is too short at 1.826Å for two ions (r_{K^+}=1.38Å, $r_{Ca^{2+}}$=1.0Å) to be next to each other. Considering that the 6c site has an occupancy of a half the ions will order to be as far apart as possible

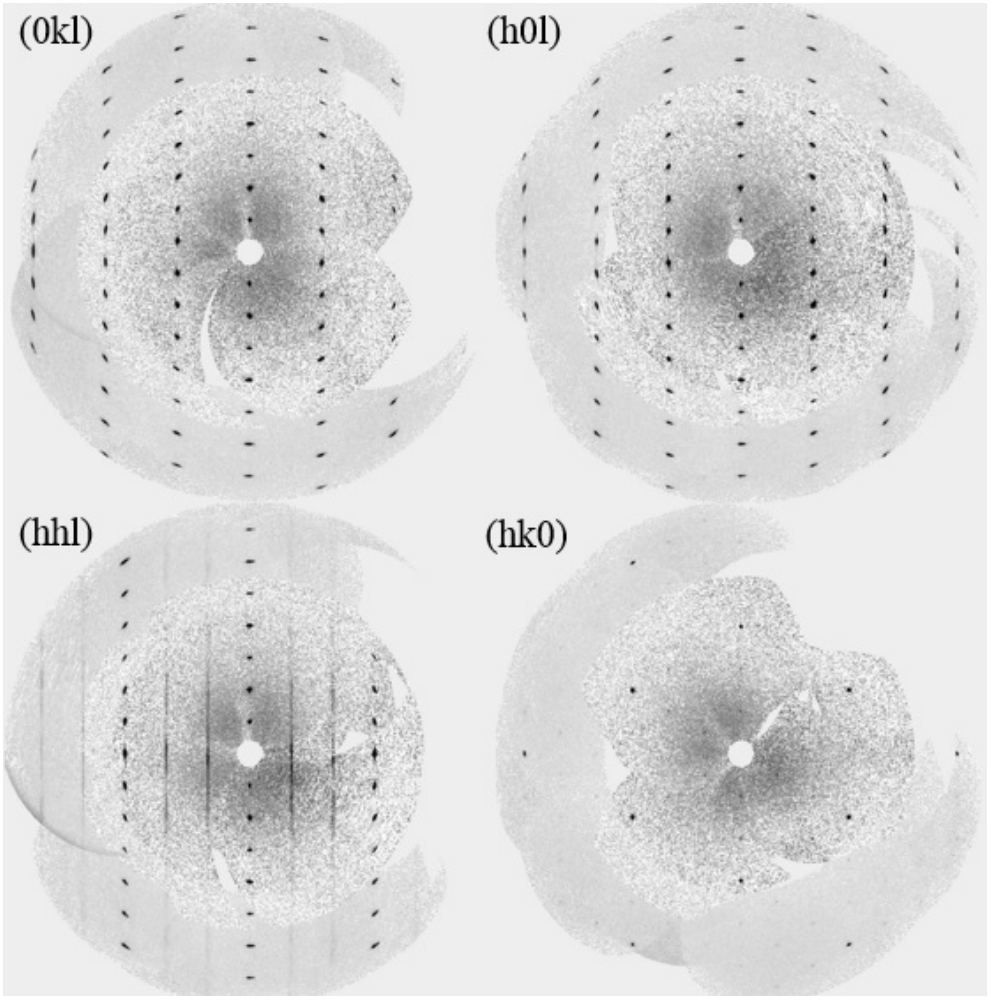

Figure 5.6 *Unwarped images of reciprocal space in the (0kl), (h0l), (hhl) and (hk0) directions constructed from single crystal x-ray diffraction data collected on* $K_2CaPt_{3-\delta}O_6$.

to all be at a distance of 3.160Å apart. A possible arrangement of the potassium and calcium ions across this half occupied site is shown in figure 5.9. This type of 2:1 ion- ordering has been seen in similar compounds to $K_2CaPt_{3-\delta}O_6$ such as $Ca_{0.33}CoO_2$[59], $Li_{0.33}CoO_2$[123] and $Li_{0.33}NiO_2$[37] and would result in a unit cell of the superstructure being $3a \times 3a$ larger than the original unit cell - fitting with the extra reflections observed at (1/3, 1/3, l). This superstructure can be better represented by a smaller unit cell of $\sqrt{3}a \times \sqrt{3}a$.

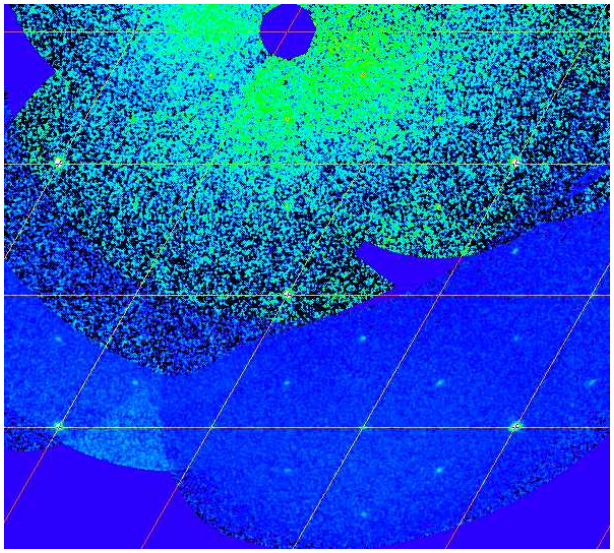

Figure 5.7 *A close up of the unwarped image of reciprocal space in the (hk*0*) direction with the unit cell parameters superimposed on the image. Superstructure peaks are clearly visible at (1/3 1/3 l)*

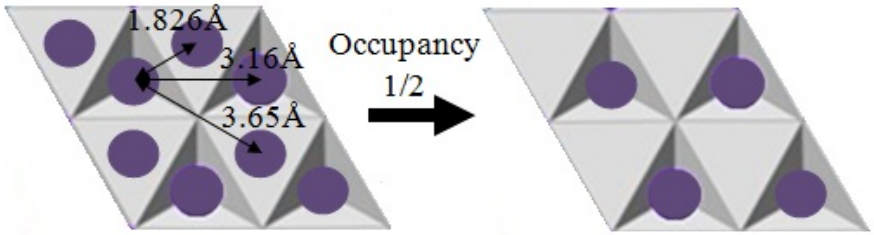

Figure 5.8 *The position and distances between ions on a fully occupied 6c site (purple spheres) and the likely arrangement of ions on the site being half occupied.*

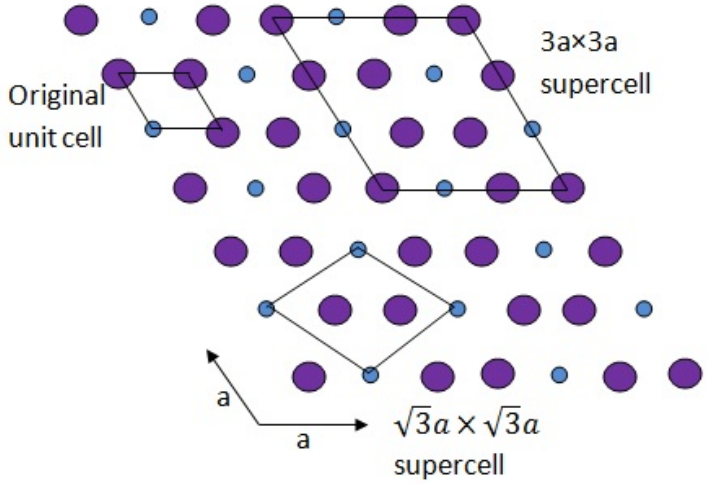

Figure 5.9 *A possible arrangement of 2:1 ordered potassium (purple) and calcium (blue) ions on a hexagonal lattice to produce a* $3a \times 3a$ *supercell.*

5.2.5 Bulk properties

It was not possible to conduct resistivity measurements on $K_2CaPt_{3-\delta}O_6$ as a sintered pressed pellet of the powder could not be produced due to the metastability of the phase. However, a lightly pressed pellet had a large contact resistance of over 1000 ohms and the transparent nature of the crystals and the orange colour of the powder suggest that the compound is an insulator. This insulating behaviour could arise from there being insufficient orbital overlap due to the Pt-O-Pt bond angle being close to 90°. This would create moments that were localised onto the platinum ions. The Pt-Pt bond distance of 3.160Å is also too long for metal-metal bonding to occur.

The magnetisation data, shown in figure 5.10, which was conducted on 30 mg of $K_2CaPt_{3-\delta}O_6$ crystals. The data was collected on the mpms in the materials characterisation laboratory at ISIS using a field of 10,000 Oe. The magnetic susceptibility appears to be largely temperature independent with a paramagnet-like upturn below 50 K. The magnetism is unusual in that even the upturn does not obey the Curie-Weiss law and that TIP is more commonly associated with a metal. The fact the magnetism is not diamagnetic does provide more evidence that $K_2CaPt_{3-\delta}O_6$ contains Pt(III) rather than Pt(IV).

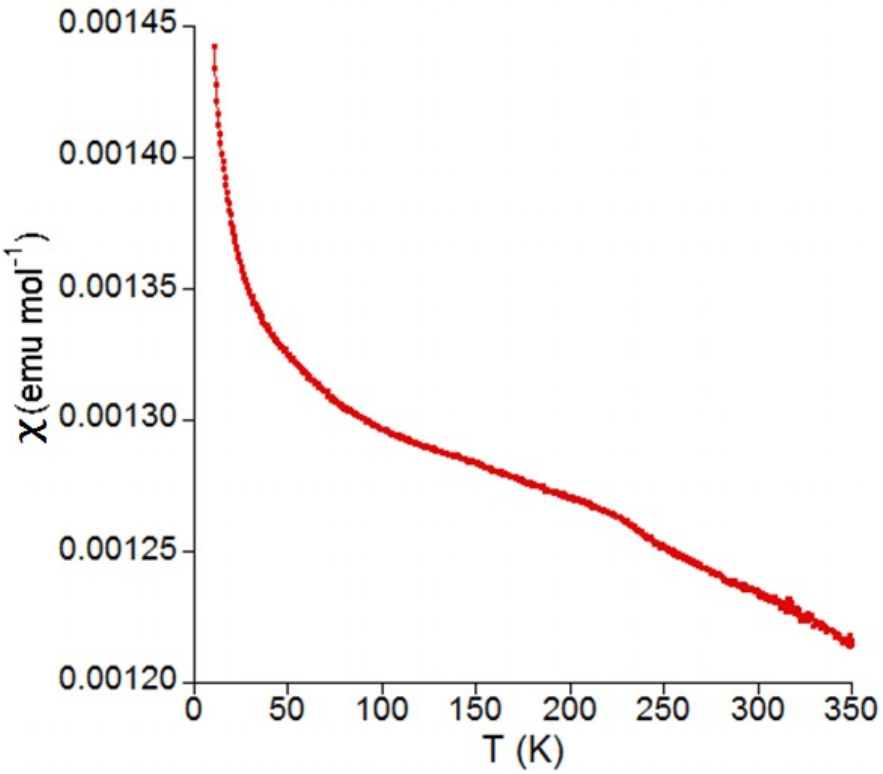

Figure 5.10 *The field cooled magnetic susceptibility of $K_2CaPt_{3-\delta}O_6$ powder as a function of temperature from 10 K to 350 K using an applied field of 10,000 Oe.*

5.3 The results of copper doping experiments on $K_2CaPt_{3-\delta}O_6$

$K_2CaPt_{3-\delta}O_6$ has an interesting structure that is reminiscent of battery materials. For example, $LiCoO_2$, which is commonly used as a cathode material in lithium ion batteries, has a structure consisting of layers of edge-sharing CoO_6 octahedra separated by layers of octahedrally coordinated lithium ions that half fill the 6c site within the $R\bar{3}m$ structure[122]. To test the flexibility of the structure to doping and to see if magnetic order could be introduced into the system, I decided to try doping Cu^{2+} into the system as 3d transition metals are typically more strongly correlated and have larger moments than 5d transition metal ions. Cu^{2+} has a Shannon-Prewitt ionic radius of $0.73\mathring{A}$ in a 6 coordinate environment, which is similar to Pt^{3+} that has an ionic radius of approximately 0.71 in a 6 coordinate environment, so hopefully copper will be doped onto the platinum site rather than the potassium and calcium sites, which have much larger ionic radii of $1.38\mathring{A}$ and $1.00\mathring{A}$ respectively. If the copper remains in an oxidation state of +2 in the structure then replacing some platinum with copper would have the effect of removing electrons from the system, assuming that the ratio of potassium to calcium in the structure remains constant.

5.3.1 Synthesis

The synthesis conditions used to grow crystals of copper doped $K_2CaPt_{3-\delta}O_6$ were similar to the conditions used to grow crystals of undoped $K_2CaPt_{3-\delta}O_6$ in section 5.2.1. As before, a 10:1 KOH:$K_2CaPt_{3-\delta}O_6$ ratio by mass or an approximately 85:1 KOH:$CaCO_3$ molar ratio was used with a molar ratio of $CaCO_3$:Pt:PtO_2 of 1:1.2:0.8. CuO was used as the source of copper and was added to the mixture in place of equimolar amounts of Pt and PtO_2 as demonstrated in equation 5.1.

$$CaCO_3 + (1.2 \times (1 - \frac{x_i}{2}))Pt + (0.8 \times (1 - \frac{x_i}{2}))PtO_2 + x_iCuO \qquad (5.1)$$

Eight flux growths were attempted using values of x_i of 0.05, 0.1, 0.2, 0.3, 0.4, 0.5, 0.6 and 0.8. The reaction conditions were slightly different to those used previously in that a slightly higher dwell temperature of 715°C rather than 700°C was used with a shorter dwell time of 24 hours. These different

conditions produced slightly larger and better formed crystals with the crystals still forming just below the rim of the alumina crucible. As the molar ratio of CuO in the flux was increased the colour of these crystals gradually changed from red to dark brown (figure 5.11), suggesting a change in the composition of the crystals. The colour of the polycrystalline powder produced by grinding up the crystals also changed in colour from orange to yellow. It was later confirmed with EPMA measurements that copper had been successfully doped into the crystals and the amount of copper actually doped into the crystals in each batch, x_M, was determined (see section 5.3.3). The assumption that the K:Ca ratio would remain constant on doping with copper was incorrect although in most copper doped samples the ratio of K:Ca was found to still be approximately 2:1. The occupancy of the K/Ca occupied 6c site is a half at first but decreases once copper is added and given that the ion deficiency of the platinum site fluctuates with the amount of copper added, the chemical formula of this series will be referred to as $(K_{\frac{2}{3}}Ca_{\frac{1}{3}})_{(1-\delta)}Pt_yCu_xO_2$ with the values of δ, y and x being determined by EPMA.

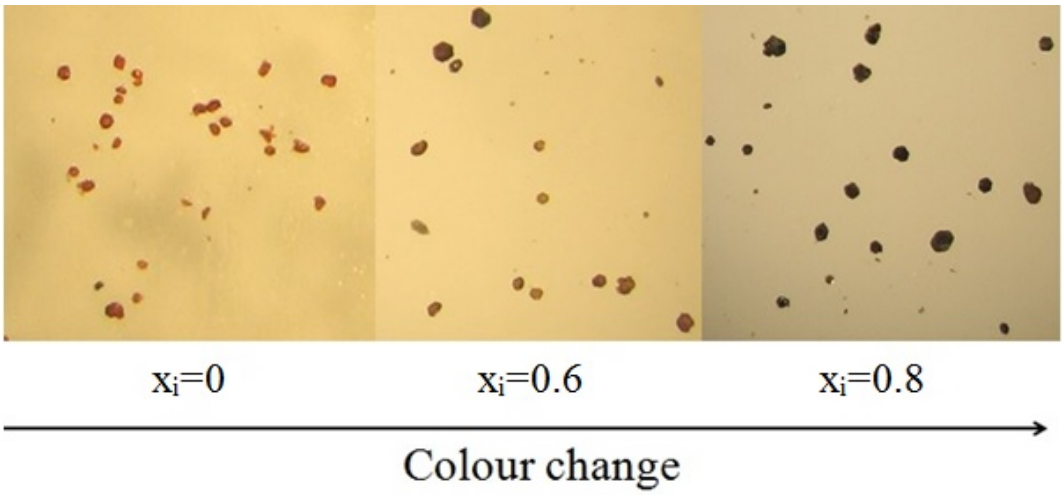

Figure 5.11 *Photos of copper doped crystals of $(K_{\frac{2}{3}}Ca_{\frac{1}{3}})_{(1-\delta)}Pt_yCu_xO_2$ for x_i values of 0.0, 0.6 and 0.8. A clear colour change from red to light brown to dark brown is visible as the nominal amount of copper in the crystals is increased.*

5.3.2 Powder x-ray diffraction

Powder x-ray diffraction data were collected on ground up crystals from each batch of $(K_{\frac{2}{3}}Ca_{\frac{1}{3}})_{(1-\delta)}Pt_xCu_yO_2$ in order to track any changes to the lattice parameters or the crystal structure upon doping. As Cu^{2+} (r=0.73Å) has an

ionic radii that is slightly bigger than Pt^{3+}($r \approx 0.725$) one may initially expect an increase in the lattice parameters upon doping. However as seen in figures 5.12 and 5.13 both the a and c lattice parameters of $(K_{\frac{2}{3}}Ca_{\frac{1}{3}})_{(1-\delta)}Pt_xCu_yO_2$ decrease significantly on doping. This may be due to the decrease in the ionic radii of the platinum ion, as it is oxidised to maintain charge neutrality, offsetting the 0.05Å larger ionic radii of the Cu^{2+} ion.

Up until and including batch CPOC#F6 the structure of $(K_{\frac{2}{3}}Ca_{\frac{1}{3}})_{(1-\delta)}Pt_xCu_yO_2$ does not appear to change on doping apart from a shift in the lattice parameters (as fully shown in appendix B.5). However in the powder diffraction of ground crystals from batch CPOC#F7 there are two phases present - the original phase of $(K_{\frac{2}{3}}Ca_{\frac{1}{3}})_{(1-\delta)}Pt_xCu_yO_2$ and an additional phase with a much larger c lattice parameter of 20.575Å. As shown in figure 5.14 this additional phase can be refined reasonably well using the same structural model as that of $(K_{\frac{2}{3}}Ca_{\frac{1}{3}})_{(1-\delta)}Pt_xCu_yO_2$ but with the larger c lattice parameter. For batch CPOC#F8 the diffraction pattern is dominated by this second phase with only a small phase fraction of $(K_{\frac{2}{3}}Ca_{\frac{1}{3}})_{(1-\delta)}Pt_xCu_yO_2$ remaining. From EPMA measurements the chemical composition of this second phase appears to be $(K_{0.87}Ca_{0.13})_{0.5}Pt_{0.72}Cu_{0.28}O_{1.8}$ (see section 5.3.3) and contains half the number of interlayer potassium and calcium ions and is also oxygen depleted in comparison to the more lightly copper doped batches. The structural model used for $(K_{\frac{2}{3}}Ca_{\frac{1}{3}})_{(1-\delta)}Pt_xCu_yO_2$ is a much poorer fit to the diffraction pattern from batch CPOC#F8 and so a new structural model may be needed. One possibility could be the inclusion of linearly coordinated copper ions in the interlayer region as seen in delafossite compounds such as $CuCrO_2$. Single crystal data should be collected on these crystals in order to correctly modify the structural model.

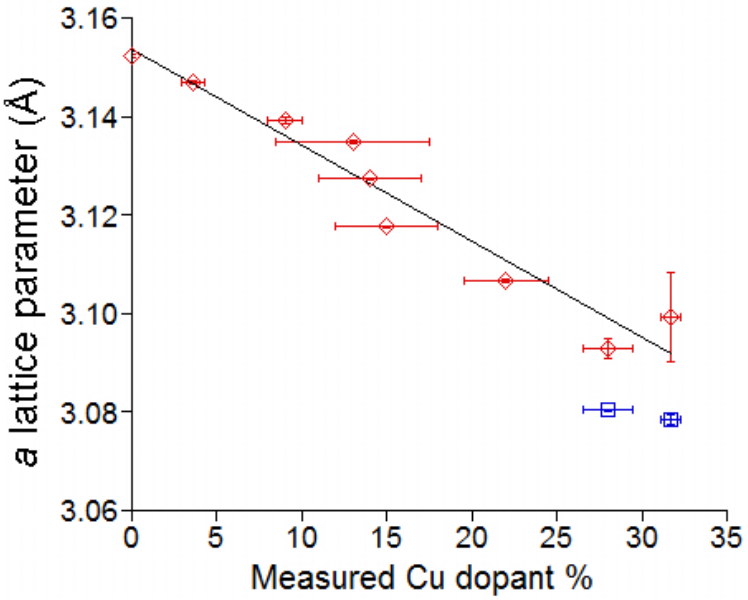

Figure 5.12 *The variation if the* a *lattice parameter of* $(K_{\frac{2}{3}}Ca_{\frac{1}{3}})_{(1-\delta)}Pt_xCu_yO_2$ *with the percentage of copper doped onto the platinum site, as determined from EPMA measurements. The blue squares mark the lattice parameters of an additional phase that appears in the diffraction pattern at dopant levels higher 25%.*

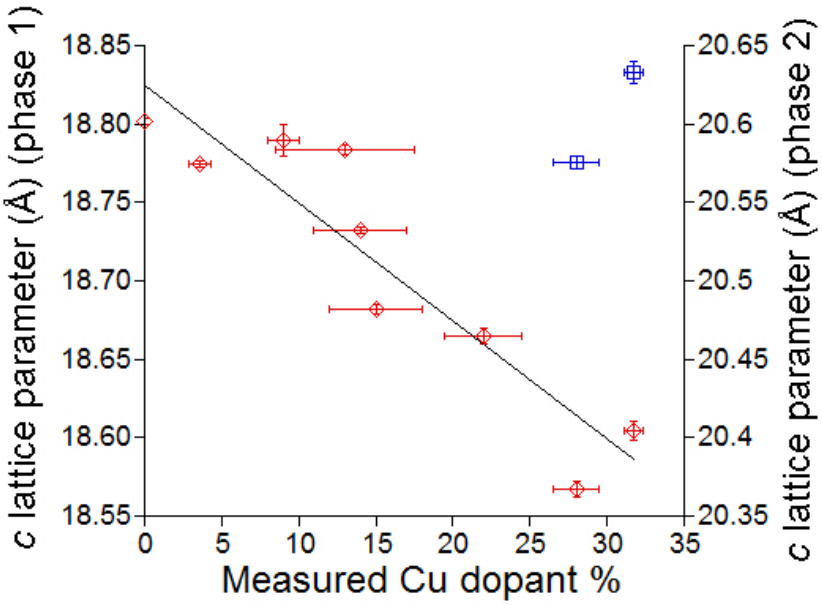

Figure 5.13 *The variation if the* c *lattice parameter of* $(K_{\frac{2}{3}}Ca_{\frac{1}{3}})_{(1-\delta)}Pt_xCu_yO_2$ *with the percentage of copper doped onto the platinum site, as determined from EPMA measurements. The blue squares mark the lattice parameters of an additional phase that appears in the diffraction pattern at dopant levels higher 25%*

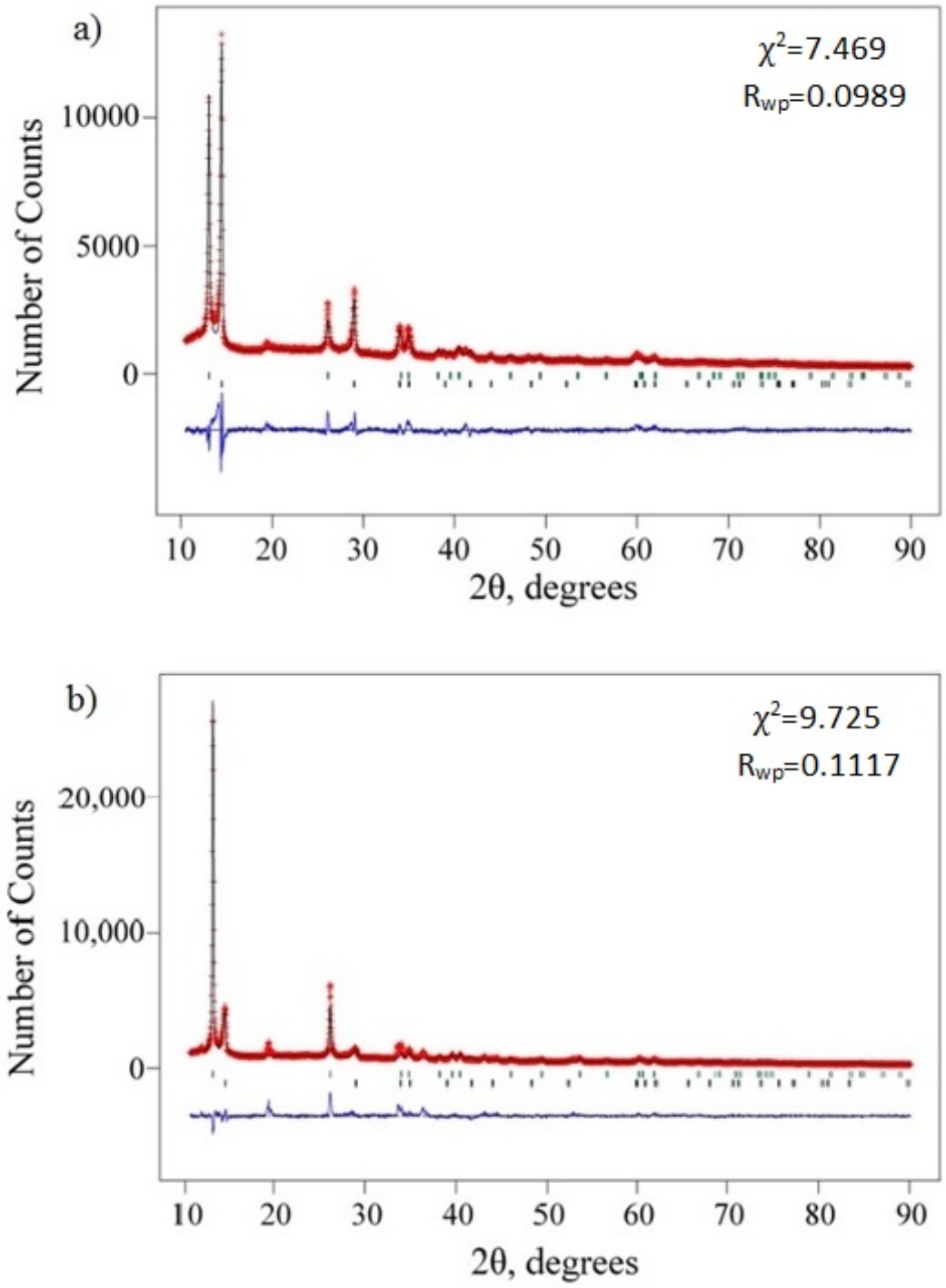

Figure 5.14 *Rietveld refinement of x-ray powder diffraction data collected on ground crystals from batch a) CPOC#F7 and b) CPOC#F8. There are two phases present in both diffraction patterns - the initial* $(K_{\frac{2}{3}}Ca_{\frac{1}{3}})_{(1-\delta)}Pt_xCu_yO_2$ *structure (black tick marks) and a new phase,* $(K_{0.87}Ca_{0.13})_{0.5}Pt_{0.72}Cu_{0.28}O_{1.8}$*, (green tick marks) with a larger* c *parameter.*

5.3.3 EPMA data

To determine how much copper had been doped into each crystal, EPMA measurements were conducted on several crystals from each batch. The composition of at least ten points across three crystals was measured for each batch and a total of 98 points were measured in the day available on the EPMA. Time limitations prevented more points from being measured. The surfaces of a lot of the crystals were fractured from the polishing process (see figure 5.15) so points were selected to be on the smoothest surfaces to improve the quality of the data. Before the measurement the EPMA was calibrated using standards containing a known percentage of each element of interest. These standards were $HfSiO_4$ (known as Hafnon), $KAlSi_3O_8$ (known as Orthoclase) that also contained a known percentage of sodium on the potassium site, $CaSiO_3$ (known as Wollastonite) that also contained known trace amounts of iron, magnesium, manganese and aluminium, and platinum and copper metal. The emission lines selected for measurement were O K_α, K K_α, Ca K_α, Cu K_α and Pt M_α.

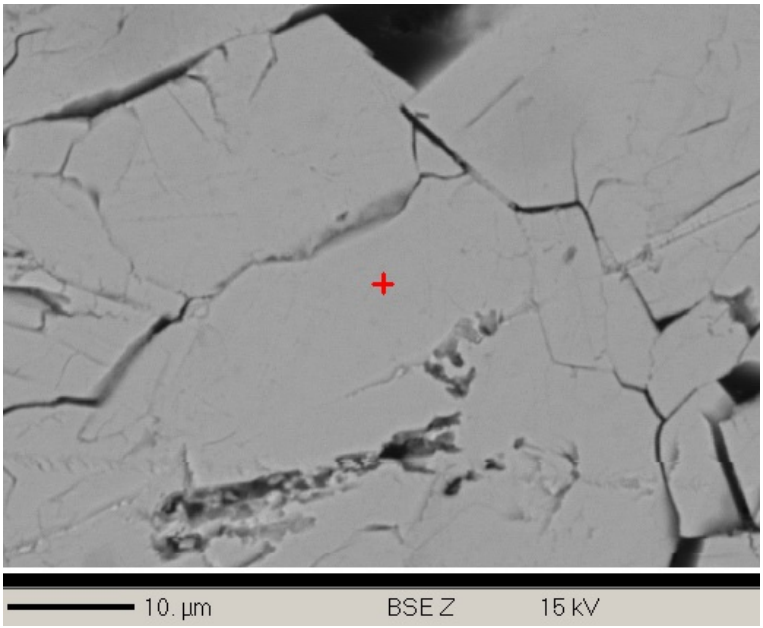

Figure 5.15 *An SEM photograph of the surface of a crystal of* $(K_{\frac{2}{3}}Ca_{\frac{1}{3}})_{(1-\delta)}Pt_xCu_yO_2$ *for* x_M*=0.080. The red cross marks the location of the electron beam.*

The results are summarised in table 5.4. There is a marked difference in composition between the crystals up to batch CPOC#F5 and batches CPOC#F7 and CPOC#F8 with batch CPOC#F6 being of an intermediate composition. This is in agreement with the appearance of a new phase in the power x-ray

diffraction pattern from batch CPO#F7 onwards. Thus the EPMA results from these two batches will be discussed separately.

It should be noted that all of the crystals appear to be either platinum deficient or oxygen rich up to CPOC#F6.There is no room for an extra oxygen site within the current structural model so it is more likely that the compounds are platinum deficient. This deficiency on the platinum site has also been observed in the powder neutron diffraction and single crystal x-ray diffraction. The ratio of potassium to calcium on the 6c wyckoff site does not seem to vary considerably across the first five batches and appears to be of an approximately 2:1 ratio. In lightly doped batches the ratio of (K+Ca):O appears to be 1:2, which confirms that the interlayer 6c site is half occupied. Although EPMA data was not collected on $K_2CaPt_{3-\delta}O_6$, the composition is expected to be similar to the lightly copper doped batches with the ratio of (K+Ca):Pt still being approximately 1:1.

It is not possible to know conclusively onto which site the copper is being doped from the EPMA data. The total amount of potassium and calcium decreases as the amount of copper is increased and the amount of Ca^{2+} decreases slightly so it is possible that Cu^{2+} is going into the K-Ca-vacancy layer and partially replacing Ca^{2+}. However the amount of platinum also appears to be decreasing, despite the fluctuations caused by a large error in the data. The average oxidation state of the platinum ion, calculated from the measured composition of each batch assuming that the oxidation state of copper is +2, also fluctuates a lot as its very sensitive to the large error on the oxygen content. However, the oxidation state of the platinum ion appears to increase to around +4 by a measured dopant percentage of 14.3% (see table5.4). This oxidising effect is more likely to occur with the Cu^{2+} replacing Pt^{3+} rather than Ca^{2+}. The decrease in the total amount of calcium and potassium may occur to partially offset this oxidising effect.

The nominal percentage of copper bears little resemblance to the measured percentage of copper, which is not surprising given that the starting materials were mixed off-stoichiometrically. Although there is variation across the batch, overall trend is that the percentage of copper in the crystals increases as more copper is added to the flux mixture. Initially this increase is rather rapid but slows as it reaches an initial saturation limit of around 15% perhaps due to the platinum ion being fully oxidised up to +4.

Batches CPOC#F7 and CPOC#F8 have markedly different compositions. The amount of copper is larger at around 30%, the amount of calcium in the crystals

has decreased so that the K:Ca ratio is 9:1 rather than 2:1 and the overall (K+Ca):Pt ratio has decreased so that the 6c site has an overall occupancy of 0.25 rather than 0.5. The loss of most of the calcium in between the platinum oxide sheets and some of the potassium coincides with a large increase in the lattice parameters of the unit cell - particularly the c lattice parameter. From this study it is unclear whether the copper is purely going onto the platinum site or whether it is also occupying some of the newly formed vacancies within the K-Ca-vacancy layer. There also appears to be no increased ion deficiency on the 3a platinum site but instead an ion deficiency on the 6c oxygen site. However, given the large change in composition and the change in lattice parameter it is likely that this is a new compound with a different structure. Batch CPOC#F8 has a composition $(K_{0.87}Ca_{0.13})_{0.5(1)}Pt_{0.72}Cu_{0.28}O_{1.8(4)}$, which gives platinum an oxidation state of exactly +4. It should also be noted that a large number of crystals of formula $Ca_{3.5}Cu_{0.5}PtO_6$ were also measured in these batches that are likely to be formed from the excess copper and calcium still left in the flux.

Batch name	Measured Cu %	K %	Ca%	Formula	Pt oxidation state
CPOC#F1	3.6(7)	64(2.4)	36(2.4)	$(K_{0.64}Ca_{0.36})_{0.96(6)}Pt_{0.80}Cu_{0.03}O_{2.0(3)}$	+3.3
CPOC#F2	9.2(1)	67(3.5)	33(3.5)	$(K_{0.67}Ca_{0.33})_{0.96(1)}Pt_{0.79}Cu_{0.08}O_{2.0(3)}$	+3.2
CPOC#F3	14.3(4.5)	70(5)	30(5)	$(K_{0.67}Ca_{0.33})_{0.7(1)}Pt_{0.70}Cu_{0.10}O_{2.0(2)}$	+4.1
CPOC#F4	14(3)	72(4)	28(4)	$(K_{0.72}Ca_{0.28})_{0.8(1)}Pt_{0.75}Cu_{0.12}O_{2.0(3)}$	+3.6
CPOC#F5	15.6(30)	70(2)	30(2)	$(K_{0.70}Ca_{0.30})_{0.7(1)}Pt_{0.65}Cu_{0.12}O_{2.0(2)}$	+4.4
CPOC#F6	22(2.5)	78(2)	22(2)	$(K_{0.78}Ca_{0.22})_{0.64(9)}Pt_{0.71}Cu_{0.20}O_{2.0(4)}$	+4.0
CPOC#F7	31.7(6)	91.7(7)	8.3(7)	$(K_{0.917}Ca_{0.083})_{0.49(4)}Pt_{0.683}Cu_{0.317}O_{1.5(6)}$	+2.7
CPOC#F8	28(1.5)	87(4)	13(4)	$(K_{0.87}Ca_{0.13})_{0.5(1)}Pt_{0.72}Cu_{0.28}O_{1.8(4)}$	+4.0

Table 5.4 *EPMA analysis of the compositions of Cu doped crystals of* $K_{\frac{2}{3}}Ca_{\frac{1}{3}}Pt_{1-x}Cu_xO_2$

5.3.4 The evolution of the magnetic properties of $K_2CaPt_{3-\delta}O_6$ upon copper doping

One of the motivations for doping copper into $K_2CaPt_{3-\delta}O_6$ was to see if magnetic order could be introduced into the system. Thus the magnetic susceptibility as a function of temperature of crystals from batches CPOC#CF2, CPOC#F5 and CPOC#F7 were measured to get an overview of how the magnetic properties evolved as a function of doping. Batch CPOC#F2 is lightly doped and batch CPOC#F5 is the most heavily doped batch before the crystals become mixed phase in powder XRD. I measured crystals from batch CPOC#F7 to measure the magnetic properties of the second phase, although the results are unreliable due to the possibility that the crystals measured contained a mixture of phases.

The results are shown in figures 5.16, 5.17 and 5.18. Unfortunately for batches CPOC#CF2 and CPOC#F5 data was only successfully collected below 100 K due to the limited sample mass making the small moment difficult to measure. However, it is evident that the magnetic susceptibility of the lightly doped $(K_{0.67}Ca_{0.33})_{0.96}Pt_{0.79}Cu_{0.08}O_{2.0}$ is similar to that of $K_2CaPt_{3-\delta}O_6$ in that the Curie-Weiss law is not followed even in the paramagnetic-like upturn. The moment of the largely temperature independent section above 50 K seems slightly lower than for $K_2CaPt_{3-\delta}O_6$ but the difference could be due to a possible variation in the chemical composition compared to that determined by EPMA or a 5% error on the sample mass.

The more heavily copper doped crystals have a larger paramagnetic upturn that obeys the Curie-Weiss law below 20 K. From fitting the inverse susceptibility and approximating that the platinum ions do not contribute to the upturn, since the platinum oxidation state is +4, the moment of the Cu^{2+} is 2.28 BM, which is larger than the spin-only value of 1.73 BM (for s=1/2). For d-orbitals that are more than half-full it is not uncommon for the moment to be larger than the spin-only value and the moment is only slightly outside the range of 1.7-2.2 BM that has been experimentally observed for an octahedrally coordinated Cu^{2+} ion [138]. The slightly larger moment than expected could be due to error introduced from any paramagnetic impurities present in the sample. The Weiss temperature of the crystals was found to be 1.55 K, showing that there are only weak correlations between the copper ions. This is unsurprising as the copper ions are diluted amongst the platinum ions.

The magnetic susceptibility of crystals of the new phase $(K_{0.917}Ca_{0.083})_{0.49}Pt_{0.683}Cu_{0.317}O_{1.5}$ from batch CPOC#F7 were measured up to 300 K due to the increased sample mass available and the larger moment of the samples. The paramagnetic upturn is larger still than crystals from CPOC#F5 and the Curie-Weiss law is followed below 40 K. The upturn was fitted below 20 K to be of a direct comparison to CPOC#F5. Again the platinum ion was assumed not to contribute to the susceptibility. The moment of the copper ion was calculated to be 1.75 BM, which is very close to the spin-only value of 1.73 BM, The Weiss temperature was calculated from the fit to be 1.72 K, showing that the correlations are slightly stronger between the copper ions, correlating to the increase in the number of copper ions in the structure.

From these copper doping experiments it seems that adding copper oxidised the platinum ion to its more common +4 oxidation state. Introducing copper ions does not cause long-range magnetic order to occur but results in the crystals becoming increasingly paramagnetic from the introduced impurity. At the maximum dopant percentage of 31.7% the copper ions are still too dilute within the structure for correlations to occur that will result in long-range magnetic order or spin-glass type behaviour.

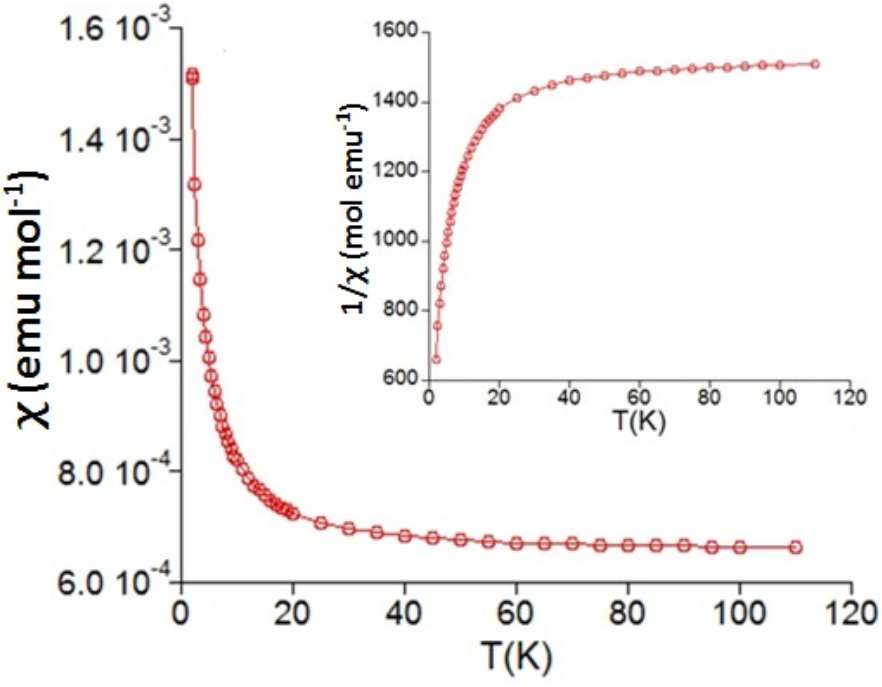

Figure 5.16 *The magnetic susceptibility from 2 K to 100 K of crystals of* $(K_{0.67}Ca_{0.33})_{0.96}Pt_{0.79}Cu_{0.08}O_{2.0}$ *from batch CPOC#F2 using 10 mg of sample and an applied field of 10,000 Oe.*

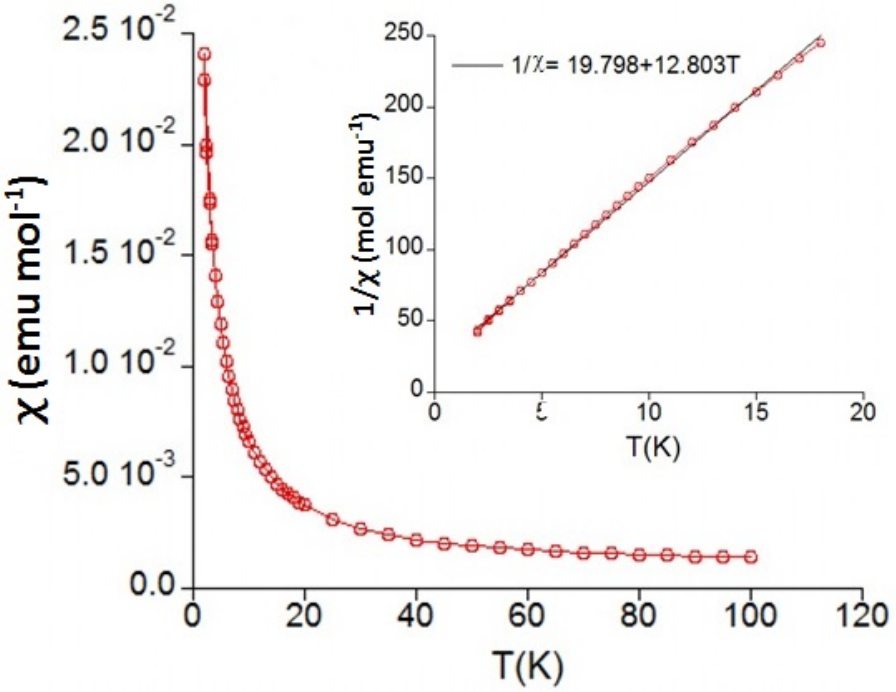

Figure 5.17 *The magnetic susceptibility from 2 K to 100 K of crystals of* $(K_{0.70}Ca_{0.30})_{0.7}Pt_{0.65}Cu_{0.12}O_{2.0}$ *from batch CPOC#F5 using 6.5 mg of sample and an applied field of 10,000 Oe.*

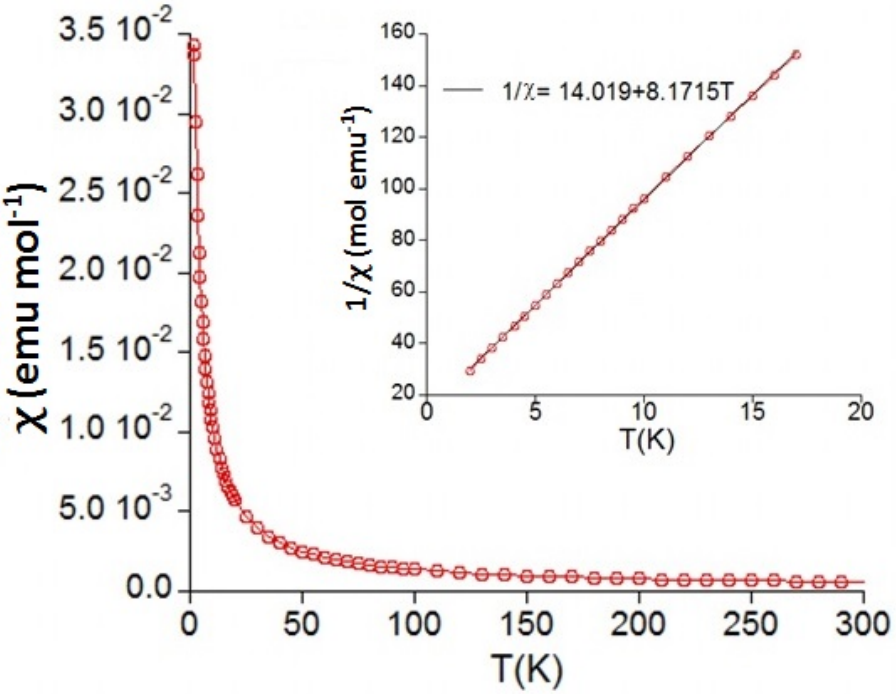

Figure 5.18 *The magnetic susceptibility from 2 K to 100 K of crystals of* $(K_{0.917}Ca_{0.083})_{0.49}Pt_{0.683}Cu_{0.317}O_{1.5}$ *from batch CPOC#F7 using 22.9 mg of sample and an applied field of 10,000 Oe.*

5.4 Investigating the ground state of $CaPt_2O_4$.

5.4.1 Previous work

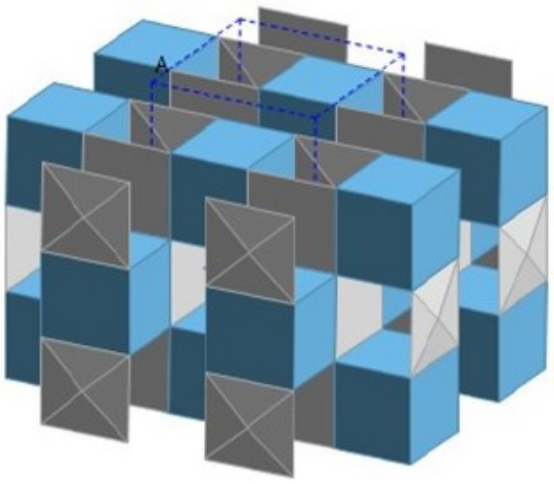

Figure 5.19 *The crystal structure of $CaPt_2O_4$. The unit cell is outlined by the dotted lines. The PtO_2 squares are shown in grey and the cubically coordinated Ca^{2+} cations (C.N. = 8) are shown as blue cubes.*

$CaPt_2O_4$ was discovered by Cahen et al [25] in 1974. From X-ray photoelectron spectra (XPES) data collected by D. Cahen et al[26], there only appeared to be one type of platinum 4f environment in $CaPt_2O_4$ (see figure 5.21), giving the platinum ion a formal oxidation state of +3. Normally Pt^{3+} disproportionates to Pt^{2+} and Pt^{4+}, as is the case for $Cd_xPt_3O_6$, to form $Cd_xPt^{2+}Pt_2^{4+}O_6$. This mixed oxidation state is shown by the presence of two pairs of doublets in the XPES spectrum. These doublet pairs are relatively close in energy and so overlap to form a triplet set of peaks with a 1:2:1 intensity distribution. The XPES spectrum of $CaPt_2O_4$ consists of only one doublet so there is only one type of platinum environment with the ions having the same oxidation state. Bulk measurements on a pressed pellet of polycrystalline $CaPt_2O_4$ suggested that the material may be metallic but only a small number of resistivity points were measured (less than 10 for each frequency) and no points were measured below 77 K. Similarly the magnetic susceptibility was only measured down to 77 K using a gaussmeter.

The structure of $CaPt_2O_4$ was solved using powder x-ray and neutron diffraction and the unit cell, as published, is given in table 5.5. $CaPt_2O_4$ was found to belong to the tetragonal space group of $P4_2/mmc$ with lattice parameters of a=5.7786(5)Å and c=5.5989(7)Å. The structure (as shown in figure 5.19) consists

of chains of square planar PtO_2 along the a and b crystallographic axis that are inter-connected by cubically coordinated calcium ions. Due to the Pt-Pt bond distance between the PtO_2 squares being relatively short at 2.79Å there is the potential for overlap between the Pt d_{z^2} orbitals along the chain. Given the +3 oxidation state of the platinum ion this d_{z^2} orbital is only half filled (see figure 5.20) giving rise to a possible conduction pathway along the overlapping d_{z^2} orbitals.

Atom	Wyckoff Symbol	x	y	z	B	Occupancy
Ca	2c	0	0.5	0	3.9	1
Pt	4j	0.242(4)	0	0	0.7	1
O	8h	0.268(7)	0.268(7)	0.25	0.7	1

Table 5.5 *The structure of $CaPt_2O_4$ as published by D. Cahen et al [25]*

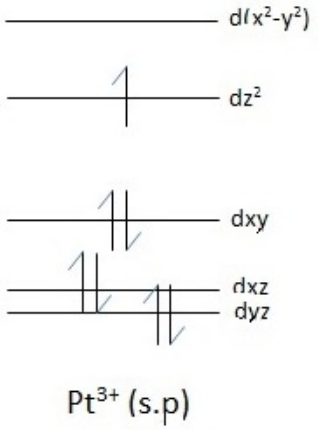

Figure 5.20 *The relative energy levels of the 5d orbitals of the Pt^{3+} in a square planar crystal field. The partially filled d_{z^2} orbital is thought to be responsible for the metallic properties of $CaPt_2O_4$.*

1D chains are prone to undergoing a Peierls distortion as this lowers the energy of the compound by removing the degeneracy of the orbitals. For $CaPt_2O_4$ it is possible that at low temperatures Pt^{3+} ions will pair up to form metal-metal bonds or that the compound will undergo a Peierls distortion as seen for VO_2[65] and $K_2Pt(CN)_4Br_{0.3}.H_2O$[42], which both possess 1D metallic chains. Due to its metallic nature it is also possible that $CaPt_2O_4$, a platinum bronze, will superconduct at low temperatures as seen for some tungsten bronzes such as Na_xWO_3 and K_xWO_3[103]. As the properties of $CaPt_2O_4$ have yet to be measured below 77 K, these exciting phenomena may have potentially been missed. The aim of this section is to grow single crystals of $CaPt_2O_4$ and re-measure the compound's transport and magnetic properties as well as its heat

capacity down to 2K to confirm its metallicity and search for novel correlated electronic phenomena. Single crystals of $CaPt_2O_4$ have never been grown, to my knowledge, by any other research group so, once grown, single crystal x-ray diffraction will be used to check that the structural details still match those calculated from powder samples.

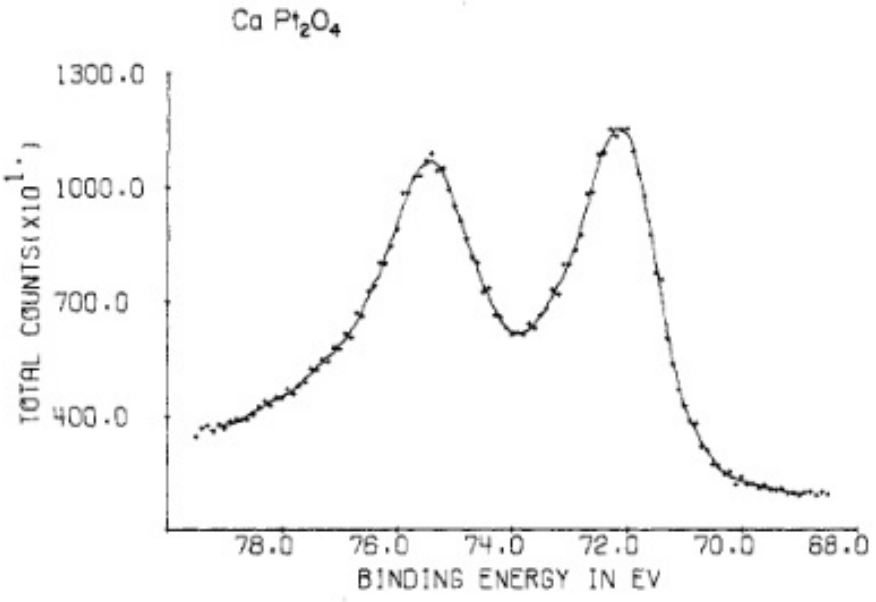

Figure 5.21 *XPES spectra of the Pt 4f core electron levels of $CaPt_2O_4$ that was obtained by using a PDP8/S computer interfaced on an AEI/ES 100B spectrometer as published in [26]*

5.4.2 Synthesis

Before attempting to grow crystals of $CaPt_2O_4$, D. Cahen's work in synthesising powder of $CaPt_2O_4$ was repeated using the conditions outlined in the literature. This powder would be used as a starting material for flux growth reactions. To make the powder, a pellet was formed by mixing $(NH_4)_2PtCl_6$ with stoichiometric amounts of $CaCO_3$, according to equation 5.2.

$$2[(NH_4)_2PtCl_6] + 4CaCO_3 \rightarrow CaPt_2O_4 + 3CaCl_2 + 4NH_4Cl + Cl_2 + 4CO_2 \quad (5.2)$$

D. Cahen wrote that $CaPt_2O_4$ formed when this pellet was heated between 800°C and 900°C in air or O_2. However, when the pellet of starting materials was

heated under 1 atm of O_2 at 800°C for 2 days it was found that another phase, Ca_4PtO_6, was also a major product. The optimum conditions found for forming $CaPt_2O_4$ were heating the pellet for 48 hours under flowing 10% O2/Ar gas mixture in a tube furnace at a temperature of 800°C. The tube furnace was evacuated first to make sure that the atmosphere used for each reaction was identical. Due to $(NH_4)_2PtCl_6$ and Cl_2 being highly toxic the outflowing gas from the tube furnace was bubbled through a water valve into a fume hood. After firing, the pellets were found to contain $CaCl_2$ and a trace of elemental platinum. To purify the powder, $CaCl_2$ was removed by washing the sample with distilled water and the platinum was removed be boiling the sample in aqua regia. According to D. Cahen this does not leach platinum from the platinum bronze but does remove elemental platinum impurities. No changes were detected in the diffraction pattern of the platinum bronze before and after this purification process and the purification process successfully removed all traces of $CaCl_2$ and elemental platinum. A Rietveld refinement of the diffraction data (see figure 5.22) to the structural model proposed by D. Cahen was of a reasonable fit, with a χ^2 of 5.483 and an R_{wp} of 0.14, although it may be possible to improve this model and fit with single crystal data. The lattice parameters were refined to be a=5.777(2)Å and c=5.602(2)Å, which are close to Cahen's values. The peaks of the diffraction pattern are very broad and of low intensity, which suggests that the powder is of poor crystallinity.

Initially a $CaCl_2$ flux mixed with $CaPt_2O_4$ powder was used to attempt to grow $CaPt_2O_4$ single crystals as the flux shares a common cation with the compound so the contamination of any crystals with the flux would be minimal. $CaCl_2$ also melts at 780°C, which is within the temperature range that the powder is normally synthesised in. However, even at the lowest temperatures, $CaPt_2O_4$ decomposed to elemental platinum. $CaPt_2O_4$ powder decomposes at around 825°C so the flux made the compound more thermally unstable. Later it was found that an article by Nakamura et al stated that acidic fluxes stabilise the Pt^{4+} cation while alkali fluxes stabilise the PtO_2 anion[96] so strongly alkali fluxes were used for consequent growth attempts. At first $CaCO_3$ was used as a flux, again, to minimise the incorporation of the flux into any product crystals but the temperature range in which the flux was molten was above the decomposition temperature of $CaPt_2O_4$. Other carbonate fluxes similarly melted at too high a temperature so hydroxide fluxes were investigated. Of these KOH seemed the most suitable as its optimum temperature range for growths is between 550°C and 750°C and La_4PtO_7 had been grown using a K_2CO_3 in the literature without

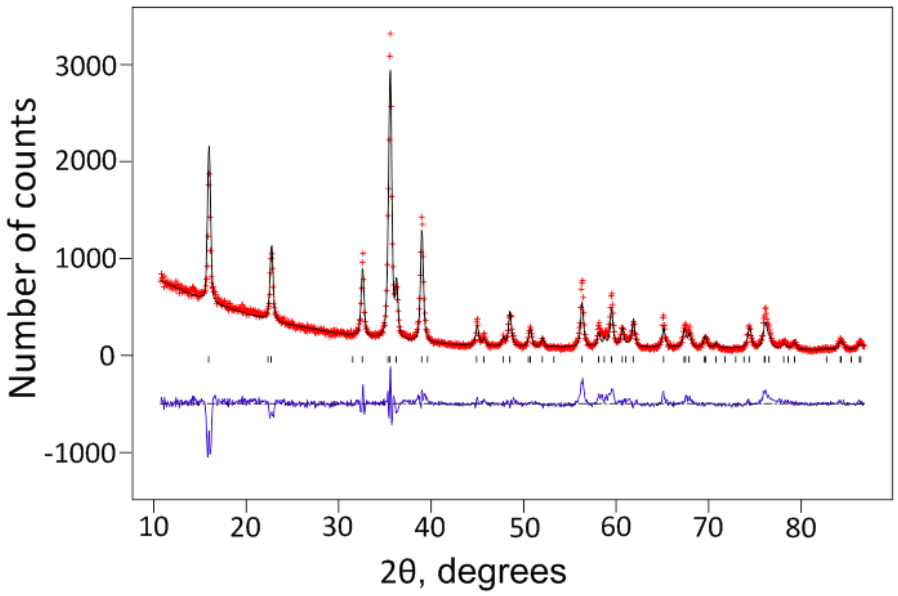

Figure 5.22 *Rietveld refinement of $CaPt_2O_4$ powder using GSAS. The dots mark the observed data, the solid line is the calculated profile and the lowest line is the difference curve. The tick marks indicate the position of the Bragg reflections.*

any potassium being incorporated into the crystals[56]. However, using KOH as a flux resulted crystals of the Pt(IV) compound, Ca_4PtO_6, being grown. These crystals were found to be air sensitive as they underwent a colour change from black/brown to yellow on being left in air. The crystals were also soluble in water. Using a mixture of elemental platinum and PtO_2 as starting materials to try and obtain an intermediate oxidation state of platinum resulted in the formation of $K_2CaPt_{3-\delta}O_6$ rather than the formation of $CaPt_2O_4$. At this point it was decided that powder samples of $CaPt_2O_4$ would be characterised down to 2 K and further attempts would be made to grow crystals depending on the outcome of these measurements.

5.4.3 Bulk characterisation

Given the lack of success in growing single crystals of $CaPt_2O_4$, it was decided that the bulk properties should be measured down to 2 K for the first time using powder samples. The pellet of powder made during synthesis had to be ground up for the purification process so to make pellets for resistivity measurements the powder was initially pressed into a pellet at 200 kbar using a pellet die and sintered in a furnace at 800°C for 12 hours. However, the sintering did not produce a hard

pellet suitable for resistivity measurements so a pellet was made by compressing about 200 mg of $CaPt_2O_4$ in the multi-anvil press in the Department of Chemistry at the University of Edinburgh, with the help of Angel Aravelo Lopez, under a pressure of 3 GPa for 2 hours. No temperature was applied to prevent the reaction or decomposition of the sample. A 4-point resistivity measurement was conducted using the CCR in CSEC from 280 K to 2 K. The results, which are shown in figure 5.23, are similar to those of D. Cahen in that the resistivity has a slight negative gradient and is within the same order of magnitude with ρ_{250K}= 0.0335 Ωcm. There are no transitions visible in the resistivity below the previous temperature limit of 77 K, although there is an upturn below 15 K. This indicates that $CaPt_2O_4$ is a poor metal and the slight negative gradient (only an increase in ρ by 7mΩcm from 280 K to 15 K) and the low temperature upturn are due to grain boundary resistance in the pellet. At low enough temperatures the upturn is caused by the inability of electrons to hop from grain to grain.

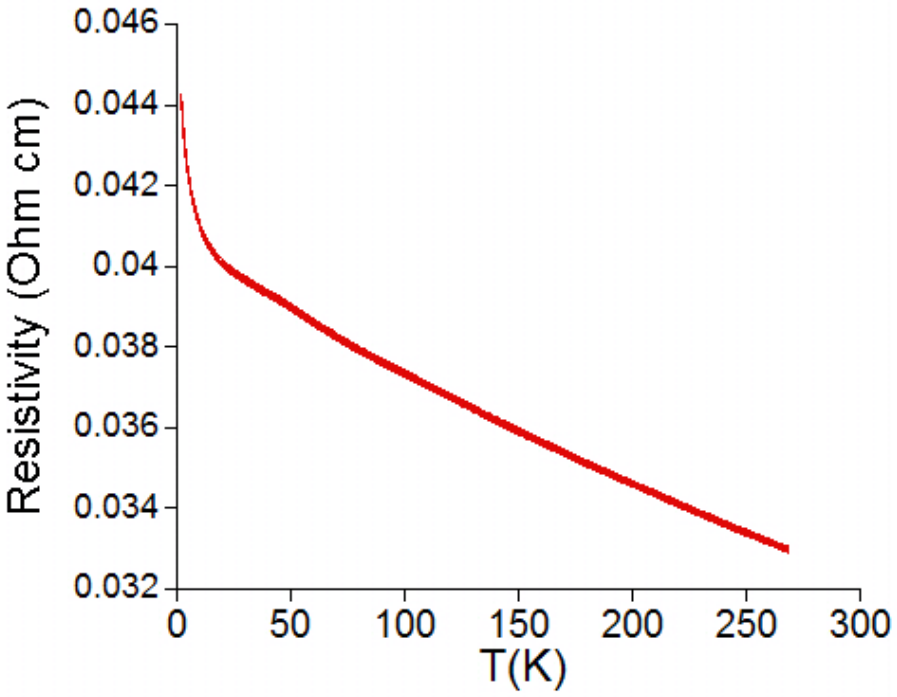

Figure 5.23 *The temperature dependence of the resistivity of a pressed pellet of $CaPt_2O_4$ from 280 K to 2 K.*

Magnetic susceptibility data (see figure 5.24) shows that $CaPt_2O_4$ is Pauli paramagnetic down to 80 K, as expected for a metal, with χ_0 being very small at around 2.21×10^{-4} emu $Oe^{-1}mol^{-1}$. There is a paramagnetic tail below 5 K, which is from an unknown paramagnetic impurity, but by assuming that the impurity is a S=1/2 ion a Curie-Weiss fit shows that it approximately accounts for 0.06% of

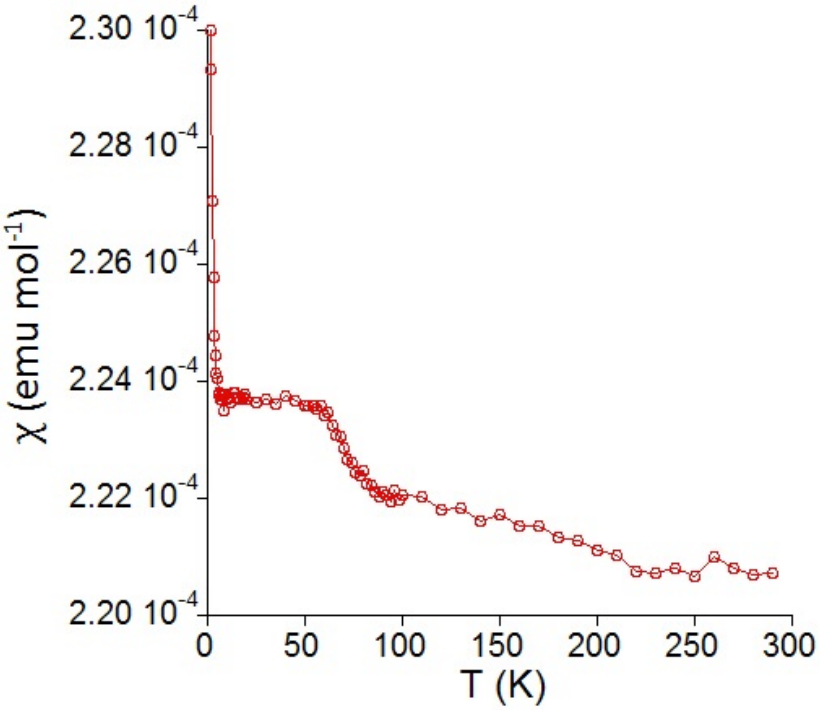

Figure 5.24 *The temperature dependence of the magnetic susceptibility of a 0.1155 g sample of $CaPt_2O_4$ from 300 K to 2 K in a 5 T field.*

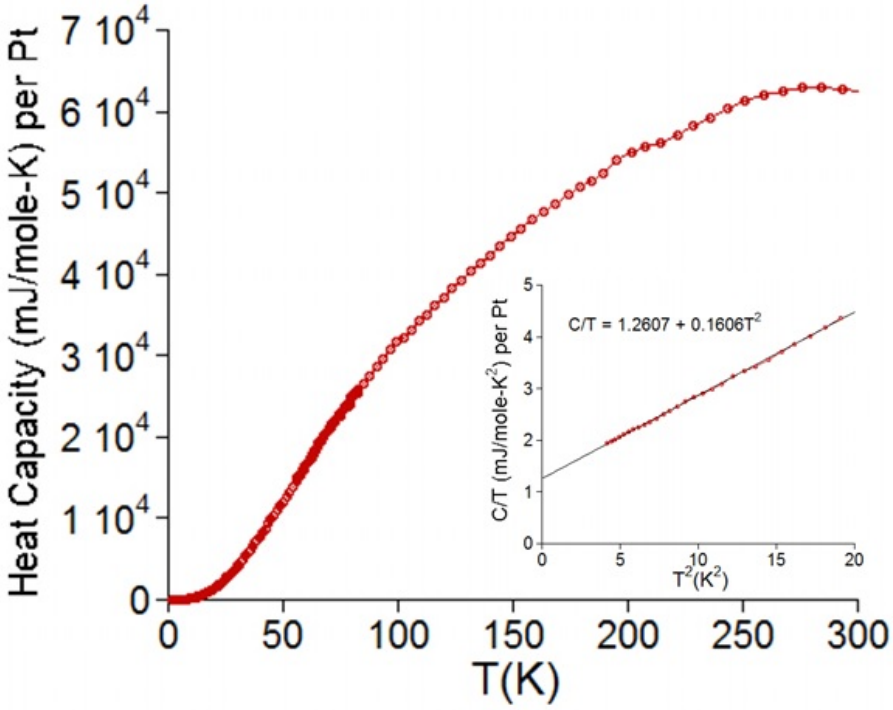

Figure 5.25 *The heat capacity of a pressed pellet of $CaPt_2O_4$ from 300 K to 2 K. Inset is a linear fit to C/T against T^2.*

the sample. There also appears to be a feature below 80 K that is ferromagnetic in nature. The weakness of this ferromagnetic feature indicates that it is from a small amount of a ferromagnetic impurity. This hypothesis is confirmed by heat capacity measurements (see figure 5.25) as no bulk transitions are evident from 300 K to 2 K. From a linear fit to a plot of C/T against T^2, the Sommerfeld coefficient, γ, was found to be only 1.26 mJ/Pt K^2, which suggests that $CaPt_2O_4$ is an uncorrelated metal. The fact that γ is non-zero gives conclusive proof that $CaPt_2O_4$ is a metal despite the slight negative gradient in the resistivity as a function of temperature.

5.5 Conclusion

Following on from exploring the $J_{\text{eff}} = 1/2$ ground state of the strontium iridates, this chapter was concerned with searching for novel correlated electronic behaviour in the platinates. To have a chance of finding novel correlated electronic behaviour the platinum ions needed to have non-zero spin quantum number. Thus platinate compounds needed to be synthesised with oxidation states of +1, +3 or +5.

Flux growth was chosen as the technique for growing crystals of platinate compounds however crystals were only successfully grown when KOH was used as the flux. Depending on the starting materials mixed with the KOH flux and the reaction conditions a range of crystals were grown from Ca_4PtO_6 to $K_2CaPt_{3-\delta}O_6$ to copper doped crystals of $K_2CaPt_{3-\delta}O_6$ with the oxidation state of the platinum ion ranging from around +3 to +4. When $CaCl_2$ and $CaCO_3$ were used as fluxes the source of platinum, whether it is PtO_2 or $CaPt_2O_4$ powder, was reduced to elemental platinum. It is well known that alkaline solutions can stabilise high oxidation states, which may be why highly alkaline KOH was able to prevent the decomposition of PtO_2 to elemental platinum. In the literature other research groups similarly use alkaline fluxes to grow platinate crystals. For example T.J. Hansen grew crystals of La_3NaPtO_7, Nd_3NaPtO_7 and La_4PtO_7[56] from Na_2CO_3 and K_2CO_3 fluxes and H.C zur Loye grew crystals of $K_4[Ln_6Pt_2O_{15}]$ (Ln= La, Pr, Nd, Sm) from molten KOH and $(NaLa_2)NaPtO_6$ from molten NaOH[84]. Due to the oxidising nature of KOH as a flux, the average oxidation state of the platinum starting mixture needed to be lower than +4 to prevent a product forming that contained only Pt^{4+}. To make more platinate compounds that contain either +1 or +3 platinum cations in the future this method of using an oxidising flux to

partially increase the oxidation state of the platinum ion from 0 or +2 is more controlled than achieving these oxidation states by partially reducing a Pt^{4+} ion as it is facile to over-reduce Pt(IV) to elemental platinum.

$K_2CaPt_{3-\delta}O_6$ crystals were grown from KOH and were found to have a structure that consisted of layers of edge-sharing PtO_6 octahedra separated by layers of K and Ca ions. From single crystal x-ray diffraction the presence of superstructure peaks along (1/3 1/3 l) indicate that there is 2:1 K:Ca ordering of the Ca and K ions within a layer and these superstructure peaks are also visible in the powder neutron diffraction data collected on HRPD. However, as the ordering is only with a layer and is not correlated between layers it is not possible to model the ion ordering in a Rietveld refinement using a lower symmetry space group. Thus the structure of $K_2CaPt_{3-\delta}O_6$ is reported using the $R\bar{3}m$ space group where the K or Ca ions are randomly distributed across the 6c sites. This is a novel compound that is similar in structure to battery materials such as $Li_{0.33}CoO_2$[123] and $Li_{0.33}NiO_2$[37] and through de-intercalation of the interlayer Ca and K ions in this flexible structure it may be possible to create a new battery material. The composition as calculated from EPMA measurements gives the platinum ion an oxidation state of around +3. The powder neutron diffraction pattern of $K_2CaPt_{3-\delta}O_6$ does not change on cooling so there is no evidence for a disproportionation of the Pt(III) ions to Pt(II) and Pt(IV) ions and there is only one platinum environment within the structure. The magnetic susceptibility is largely temperature independent paramagnetic (TIP) with a non Curie-Weiss like upturn. However the orange colour of the powder suggests that $K_2CaPt_{3-\delta}O_6$ is an insulator and a Pt(III) compound would be expected to exhibit Curie-Weiss-like paramagnetic behaviour so the TIP nature of the magnetic susceptibility is currently unexplained. The Pt-Pt distance of 3.160Å is too long for metal-metal bonding to occur and the Pt-O-Pt bond angle of 96.56° means that the insulating behaviour could be due to poor orbital overlap.

To my knowledge there are no inorganic compounds with a Pt(III) ion in an octahedral coordination environment. Previous compounds that contain platinum in an oxidation state other than +4 such as $NaPt_3O_4$[119] and $Li_{0.64}Pt_3O_4$[117] and $CaPt_2O_4$ possess platinum only in a square planar coordination environment. In other cases such as for $Ba_8Pt_4Yb_3O_{17.5}$ there are two different platinum environments with Pt(IV) in an octahedral coordination environment and Pt(II) in a square planar environment to give a formula of $Ba_8Pt_3^{2+}Pt^{4+}YbO_{17.5}$[53]. Other coordination environments are possible though as $CoPtO_2$ contains Pt(I)

in a linear coordination environment[61]. $K_2CaPt_{3-\delta}O_6$ presents an opportunity to study the physics of a platinum (III) ion in an octahedra coordination environment and as platinum oxides are used for catalysis it may be interesting to test the catalytic properties of $K_2CaPt_{3-\delta}O_6$.

Although more work needs to be done on determining the structure of copper doped $K_2CaPt_{3-\delta}O_6$, the fact that copper doping is possible shows that the structure is flexible to chemical substitution. Introducing the copper ions did not result in any long-range magnetic order or spin-glass behaviour, even at the maximum dopant percentage of 31.7%. Instead the material followed Curie-Weiss paramagnetic behaviour down to 2 K with the Cu^{2+} ions having a moment 0f 1.75 BM, which is close to the spin-only values of 1.73 BM. This shows that even at this highest dopant percentage the Cu^{2+} ions are too dilute within the platinum oxide layers for electron correlations to occur between the ions.

Finally the bulk properties of a known Pt(III) oxide, $CaPt_2O_4$, were re-investigated. The resistivity, magnetic susceptibility and heat capacity of $CaPt_2O_4$ were measured for the first time below 77 K and showed that $CaPt_2O_4$ was a metal down to 2 K. The low Sommerfeld coefficient of 1.26 mJ/Pt K^2 suggests that $CaPt_2O_4$ behaves as a band metal with only weak electron correlations. No metal-insulator transitions from charge disproportionation are evident, which suggests that the Pt^{3+} oxidation state is surprisingly robust in this compound. No Peierls distortion of the 1D PtO_4 chains at low temperature is evident either so perhaps the system is stabilised by the quasi-2D nature of the interlocking chains.

In comparison to the iridates, the platinate compounds study all seem to be weakly correlated. $CaPt_2O_4$ behaves as a weakly correlated band metal, $K_2CaPt_{3-\delta}O_6$ shows no long range magnetic order and the heavily copper doped $K_2CaPt_{3-\delta}O_6$ compounds exhibit Curie-Weiss behaviour down to 2K with low Weiss temperatures of 1.55 K and 1.72 K. This is the behaviour classically expected of a 5d transition metal oxide as the 5d orbitals are large and diffuse so electronic correlations are weak. The strontium iridates are different as spin-orbit coupling creates a $J_{\text{eff}} = 1/2$ ground state, which has a smaller bandwidth than the s=1/2 ground state of the platinates. Spin-orbit coupling is not possible in the platinate compounds studied as $CaPt_2O_4$ contains Pt(III) in a square planar coordination environment and $K_2CaPt_{3-\delta}O_6$, although containing Pt(III) in an octahedral coordination environment, possesses the unpaired electron in the e_g set. In both of these cases there is no orbital contribution so spin-orbit

coupling is not possible. This study suggests that spin-orbit coupling is necessary for observing correlated electronic behaviour in 5d transition metal oxides. A future avenue of research would be to create Pt(V) compounds as these would be expected to have the same $J_{\text{eff}} = 1/2$ ground state of the iridates.

Chapter 6

Conclusion

In exploring novel correlated electronic behaviour in 5d transition metal oxides two families of compounds were focused on - the $Sr_{n+1}Ir_nO_{3n+1}$ (n=1, 2, ∞) series and platinate compounds. The main findings from the work on each of these families are summarised in two separate sections.

6.1 The $Sr_{n+1}Ir_nO_{3n+1}$ (n=1, 2, ∞) series

It was found that the molar ratio of IrO_2:$SrCO_3$ in the starting materials was the most important factor in determining the phase of strontium iridate formed. Providing that the other reaction conditions remained the same, as the amount of $SrCO_3$ was increased relative to IrO_2 the predominant phase formed changed from $SrIrO_3$ to $Sr_3Ir_2O_7$ to Sr_2IrO_4. To produce crystals of a good size and morphology the cooling rate needed to be around 4°C/hr and to form Sr_2IrO_4 and $Sr_3Ir_2O_7$ crystals and large crystals of $SrIrO_3$ the initial dwell temperature needed to be above 1150°C. From EPMA measurements the reaction conditions used did not affect the chemical composition of the $Sr_3Ir_2O_7$ crystals grown but if the starting mixture had too low a proportion of $SrCO_3$ to IrO_2 then the crystals contained $SrIrO_3$ inclusions. An $Ir_{0.9}Pt_{0.1}$ alloy that was not detectable by powder x-ray diffraction was found in many samples during EPMA measurements and seemed more prevalent in samples that were grown at high temperatures (1300°C) or in samples grown with a low proportion of $SrCO_3$ to IrO_2 in the starting materials. Samples from batches with intergrowths had a slightly lower (by a maximum of

1.5 K) and broader Néel temperature from resistivity measurements but no link between sample quality and the unit cell parameters could be established. The T* transition that appeared at temperatures between 230 K and 260 K in the literature was not present in the magnetisation and resistivity data collected on a phase pure crystal of $Sr_3Ir_2O_7$. The similarity of the T* transition temperature to the Néel temperature of Sr_2IrO_4 suggests that there may have been intergrowths of Sr_2IrO_4 in the literature crystals as single layer intergrowths are known to occur in $Sr_3Ru_2O_7$.

All crystals $Sr_3Ir_2O_7$ grown were found to be heavily oxygen deficient giving the iridium ions an average oxidation state of +3.4. This means that the parent $Sr_3Ir_2O_7$ is already electron doped. However, annealing the crystals under both reducing and oxidising conditions seemed to have at most a small detrimental effect on the bulk properties. More electrons were doped into $Sr_3Ir_2O_7$ by means of partially substituting strontium with lanthanum. The lanthanum content of the crystals was checked using both EDX and EPMA and the saturation limit for substituting lanthanum into the structure was found to be around 8.3%. EDX maps and 6 point resistivity measurements found no concentration gradient of La across a crystal but the large variation in lanthanum content means there must be microscopic domains containing different amounts of lanthanum randomly distributed in the crystal.

Bulk measurements on the crystals found that electron doping induces a metal-insulator transition by a La dopant content of 7.2%. This onset of metallicity coincides with a quenching of the long-range antiferromagnetic order. Below a La dopant content of 5% increased electron doping coincides with a lowering of the Néel temperature and for samples with a La content close to the chemically induced metal-insulator transition there is a de-coupling of a temperature dependent metal-insulator transition and the onset of long-range magnetic order in the insulating state. Heat capacity measurements on the metallic samples prove that the metallicity is a feature of the bulk and demonstrate the $(Sr_{(1-x)}La_x)_3Ir_2O_7$ is only weakly correlated in comparison to $Sr_3Ru_2O_7$ and Sr_2RuO_4.

Given that there were only subtle changes to the structure upon lanthanum substitution and that ARPES measurements showed that a rigid band shift occurred upon electron doping, the onset of metallicity is a result of adding electrons to the band structure rather than structural distortions. LDA + SO + U calculations fitted to the ARPES data revealed that although the ground state

of $Sr_3Ir_2O_7$ still had a J_{eff}=1/2 band the electronic properties of $Sr_3Ir_2O_7$ could be explained without the need of a Mott- Hubbard gap.

No evidence was found from a study of the structure of $Sr_3Ir_2O_7$ at high temperature for the B*bcb* structural model being a more accurate than the I4/*mmm* structural model. No evidence was found either for a high temperature orthorhombic to tetragonal phase transition or any other high temperature structural phase transition.

Crystals of $SrIrO_3$ were grown with RRR values that were 5 times better than those reported in the literature. These better quality crystals were found to obey a T^2 power law below 15 K and had a Wilson ratio of 1.43. No superconducting transition was observed down to 20 mK. This suggests that the $T^{3/2}$ power law at low temperature, the ferromagnetic instability and the mass enhancement of the Wilson ratio reported previously are a result of poor sample quality. Instead $SrIrO_3$ is a Fermi-liquid metal.

6.2 The search for novel correlated electronic states in the platinates

By experimenting with a potassium hydroxide fluxes a novel platinate compound of proposed formula $K_2CaPt_{3-\delta}O_6$ ($\delta \approx 0.4$) was discovered. The chemical composition and structure of this compound was determined through a combination of EPMA, single crystal and powder x-ray diffraction and neutron diffraction. The structure consists of CdI_2 type PtO_2 layers with calcium and potassium ions in between the layers in a 1:2 ratio. The crystallographic site that these ions occupy is only half filled and recent single crystal x-ray diffraction data showed that there is an ordering of these ions and the vacancies within a layer but not between layers. This is evidenced by superstructure peaks at (1/3 1/3 l) in the single crystal data. It is possible that the ions adopt a hexagonal 2:1 ion ordering arrangement that has been seen in other layered hexagonal compounds such as $Ca_{0.33}CoO_2$ but further experimental work is needed to confirm the exact nature of this cation-vacancy ordering. The oxidation state of the platinum ion appears to be around +3, although this is sensitive to the exact chemical composition, which varied from crystal to crystal. The magnetic susceptibility of the crystals is temperature independent paramagnetic, which supports the platinum ion having

an oxidation state other than +4.

$K_2CaPt_{3-\delta}O_6$ was successfully doped with copper to form $(K_{\frac{2}{3}}Ca_{\frac{1}{3}})_{(1-\delta)}Pt_yCu_xO_2$ up to a value of x of around 0.22, after which a further novel phase of formula $(K_{0.87}Ca_{0.13})_{0.5(1)}Pt_{0.72}Cu_{0.28}O_{1.8(4)}$ is formed. The doping changed the magnetic properties of the sample from being largely temperature independent paramagnetic to paramagnetic. At the dopant level reached the copper ions were too dilute in the structure for any magnetic ordering to occur.

The bulk properties of a known Pt(III) oxide, $CaPt_2O_4$, were re-investigated. The resistivity, magnetic susceptibility and heat capacity of $CaPt_2O_4$ were measured for the first time below 77 K and showed that $CaPt_2O_4$ was a metal down to 2 K. The low Sommerfeld coefficient of 1.26 mJ/Pt K^2 suggests that $CaPt_2O_4$ behaves as a band metal with only weak electron correlations, in keeping with the traditional view of 5d transition metal oxides being either band metals or band insulators. No metal-insulator transitions from charge disproportionation are evident, which suggests that the Pt^{3+} oxidation state is surprisingly robust in this compound.

6.3 Implications and further work

One of the points that this thesis illustrates is the importance of sample quality and thoroughly characterising samples using a variety of techniques. For example, the ground state of $SrIrO_3$ had been incorrectly determined in the literature as being a non-Fermi liquid due to poor sample quality. Also EPMA was found to be a much better probe for determining the La content of lightly doped crystals than EDX. Plus multiple probes had to be used to identify and determine the structure of $K_2CaPt_{3-\delta}O_6$. It is also important to understand that there is a variation in the dopant content from crystal to crystal within a batch when flux grown crystals are doped. Thus it is important to characterise individual crystals that are to be measured as a variation in the dopant content can largely effect the properties of the sample.

Secondly the discovery of a platinum (III) ion in an octahedral coordination environment has huge implications within chemistry and physics. To my knowledge there are no known examples of this electronic configuration in a platinum oxide and it may yet be possible to discover novel correlated electronic

behaviour in these type of materials. Flux growth has been shown to be a good synthetic technique for growing crystals of platinate compounds and by using flux growth it may be possible to obtain more platinum compounds that contain platinum in formal oxidation states other than +2 or +4. The superstructure of $K_2CaPt_{3-\delta}O_6$ is reminiscent of sodium cobaltate, which becomes superconducting on hydration and is a candidate thermoelectric material. Thus it is imperative that this compound is studied in more detail. The fact that the compound can be doped with copper shows that the structure is flexible to chemical modification. With further work it may be possible to tune the properties of the compound through deintercalation of the interlayer potassium and calcium ions or through further chemical substitutions. It is also worth investigating whether there are, for example, palladium analogues of this structure.

Further work is also required to fully characterise these new platinum compounds. The nature of the ion-vacancy ordering of $K_2CaPt_{3-\delta}O_6$ has yet to be confirmed and an EXAFS study would be beneficial to confirm the oxidation state/s of the platinum ions. Also the structural transformation that occurs on heavily doping the compound with copper needs to be solved.

Appendix A

Tables of all synthesis attempts carried out

A.1 Flux growth of $Sr_{n+1}Ir_nO_{3n+1}$

Table A.1 *A summary of the key crystal growths in exploring the crystal growth conditions of the strontium iridates.*

Name	Crucible type	Ratio of starting materials	Reaction conditions	Result	Comment
Sr_2IrO_4 - flux 1	Pt with lid	1.8$SrCO_3$, IrO_2,15$SrCl_2$	1300°C for 12 hours. Cooling to 900°C over 50hrs	Mainly $Sr_3Ir_2O_7$ but some $SrIrO_3$	One of the best batches of $Sr_3Ir_2O_7$ grown
SIO - Flux 2	Pt with lid	2.4$SrCO_3$, IrO_2,15$SrCl_2$	1250°C for 12 hours. Cooling to 900°C over 87.5 hours	Very thin platelets of Sr_2IrO_4 About 1 mm square in size	Altering a lot of variables but keeping the amount of flux constant completely changed growth outcome
SIO - Flux 3	Pt with lid	2.2$SrCO_3$, IrO_2,15$SrCl_2$	1300°C for 12 hours. Cooling to 900°C over 50hrs	Thin platelets of Sr_2IrO_4	Identical reaction conditions to F1 except adding more $SrCO_3$ results in Sr_2IrO_4 rather than $Sr_3Ir_2O_7$ forming

Table A.1 – continued from previous page

Name	Crucible type	Ratio of starting materials	Reaction conditions	Result	Comment
SIO#F5	Pt with lid	1.35$SrCO_3$, IrO_2,15$SrCl_2$	1300°C for 12 hours. Cooling to 900°C over 87.5hrs	Thick cuboid crystals of $Sr_3Ir_2O_7$. 0.6mm cubed in size	Lots less $SrCO_3$ compared to F1 and F3 and slightly slower cooling rate results in large crystals of $Sr_3Ir_2O_7$
SIO#F6	Pt with lid	1.35$SrCO_3$, IrO_2, 20$SrCl_2$	1300°C for 12 hours. Cooling to 1100°C over 50hrs	Mainly $SrIrO_3$ with some $Sr_3Ir_2O_7$ crystals. IrO_2 crystals (needle shaped) around rim. Ir residue at bottom of crucible.	Cooling rate halved to F1 with same dwell temperature. More flux and same $Sr_3Ir_2O_7$ as F5 dramatically changes outcome.

Table A.1 – continued from previous page

Name	Crucible type	Ratio of starting materials	Reaction conditions	Result	Comment
SIO#F7	Pt with lid	1.35$SrCO_3$, IrO_2,10$SrCl_2$ with $SrIrO_3$ seed crystals.	1200°C for 12 hours. Cooling to 1000°C over 50hrs.	Large (0.6mm) crystals of $SrIrO_3$.	Experiment using a new lower temperature regime at same cooling rate as F6. Flux quantity halved to compensate for lower flux evaporation rate.
SIO#F8	Pt with lid	1.35$SrCO_3$, IrO_2, 10$SrCl_2$	1200°C for 12 hours. Cooling to 1000°C over 50hrs.	Mixture of $SrIrO_3$ and Sr_2IrO_4. The $SrIrO_3$ crystals grown are smaller.	Identical rection conditions to F7 but without using seed crystals.
SIO#F11	Pt with lid	1.45$SrCO_3$, IrO_2,15$SrCl_2$	1300°C for 12 hours. Cooling to 900°C over 87.5hrs	Large flakes of Sr_2IrO_4 only.	Identical reaction conditions to F5 but slightly more $SrCO_3$ produces Sr_2IrO_4 instead of $Sr_3Ir_2O_7$

Table A.1 – continued from previous page

Name	Crucible type	Ratio of starting materials	Reaction conditions	Result	Comment
SIO#F12	Pt with lid	1.45$SrCO_3$, IrO_2, 15$SrCl_2$	1300°C for 12 hours. Cooling to 1200°C over 87.5hrs	Globular shaped crystals of Sr_2IrO_4. Lots of Ir metal.	Same proportion of starting materials but much slower cooling rate than F11 changes the crystal morphology.
SIO#F13	Pt with lid	1.35$SrCO_3$, IrO_2, 15$SrCl_2$	1300°C for 12 hours. Cooling to 1200°C over 19hrs	Small badly formed plate-like crystals of Sr_2IrO_4 contaminated with lots of Ir metal	Identical to F12 except for a faster cooling rate.
SIO#F14A	Pt without lid (small)	1.35$SrCO_3$, IrO_2, 10$SrCl_2$. In tube furnace under flowing 100% oxygen.	1200°C for 12 hours. Cooling to 1000°C over 50hrs	Mainly Sr_2IrO_4 with very small crystals of $SrIrO_3$ at the bottom of the crucible. Large mass loss of 47.6%.	Same conditions as F8 but in a smaller Pt crucible under flowing O_2 to try to stop Ir metal forming
SIO#15	Pt with lid	1.35$SrCO_3$, IrO_2, 15$SrCl_2$	1245°C for 12 hours. Cooling to 1150°C over 19 hrs	Beautiful large crystals of Sr_2IrO_4. Needle crystals of IrO_2 around rim of crucible.	Same starting materials as F5 but in a lower and narrower temperature range

Table A.1 – continued from previous page

Name	Crucible type	Ratio of starting materials	Reaction conditions	Result	Comment
SIO#F16	Pt with lid	1.35$SrCO_3$, IrO_2, 10$SrCl_2$. Under flowing O_2 in tube furnace with specially designed baffles to reduce heat convection.	1200°C for 12 hours. Cooling to 1000°C over 50hrs	Mass loss much lower at 6.48%. Mainly $SrIrO_3$ powder with some very small crystals of $Sr_3Ir_2O_7$ stuck to the bottom of the crucible. No Ir.	A repeat of F14A but using baffles to reduce flux evaporation rate.
SIO#F17	Pt with lid	1.35$SrCO_3$, IrO_2, 7.5$SrCl_2$	1200°C for 12 hours. Cooling to 1100°C over 25hrs	Large thin crystals of $Sr_3Ir_2O_7$. Very little Ir metal.	Half the amount of flux as F5 with a lower dwell temperature. Best batch of $Sr_3Ir_2O_7$ grown.
SIO#F18A	Pt with lid	1.2$SrCO_3$, IrO_2, 7.5$SrCl_2$	1200°C for 12 hours. Cooling to 1100°C over 25 hrs	Square crystals of $Sr_3Ir_2O_7$ Some crystals of $SrIrO_3$. Ir metal.	Identical conditions to F17 but reducing amount of $SrCO_3$.

Table A.1 – continued from previous page

Name	Crucible type	Ratio of starting materials	Reaction conditions	Result	Comment
SIO#F18B	Pt with lid	1.0$SrCO_3$, IrO_2, 7.5$SrCl_2$	1200C for 12 hours. Cooling to 1100°C over 25 hrs	Square crystals of $Sr_3Ir_2O_7$. Higher mass loss than 18A as crucible not in firebrick and more Ir.	Amount of $SrCO_3$ reduced further to F18A
SIO#F19A	Pt with lid	0.8$SrCO_3$, IrO_2, 7.5$SrCl_2$	1200°C for 12 hours. Cooling to 1100°C over 25 hrs	Mainly $SrIrO_3$ and a lot of Ir metal	Amount of $SrCO_3$ reduced further to F18B.
SIO#F19B	Pt with lid	1.0$SrCO_3$, IrO_2, 12$SrCl_2$	1200°C for 12 hours. Cooling to 1100°C over 25 hrs	Mainly $Sr_3Ir_2O_7$ with some $SrIrO_3$. Still lots of Ir flakes.	Reaction to compare the effect of increasing the amount of flux in comparison to F18B.
SIO#F20	Pt with lid	1.0$SrCO_3$, IrO_2, 12$SrCl_2$	1100°C for 12 hours. Cooling to 900°C over 50hrs	$SrIrO_3$ powder with some microcrystals of $SrIrO_3$ at the bottom of the crucible. A small amount of Ir.	Experiment with lower temperatures to reduce amount of Ir formed.

Table A.1 – continued from previous page

Name	Crucible type	Ratio of starting materials	Reaction conditions	Result	Comment
SIO#F21A	Pt with lid	1.0$SrCO_3$, IrO_2, 12$SrCl_2$	1150°C for 12 hours. Cooling to 1100°C over 12.5hrs	Microcrystals of $SrIrO_3$ and not much Ir metal.	Experiment with a narrower lower temperature range at same cooling rate as F20.
SIO#F21B	Pt with lid	1.0$SrCO_3$, IrO_2, 20$SrCl_2$	1150°C for 12 hours. Cooling to 1100°C over 12.5hrs	Microcrystals of $SrIrO_3$ and not much Ir metal.	Identical to F21A except for a greater propertion of flux.
SIO#F22	Pt with lid	1.0$Sr(OH)_2.8H_2O$, IrO_2, 12$SrCl_2$	1200°C for 12 hours. Cooling to 1100°C over 25 hrs	Small crystals of $SrIrO_3$. Lots of Ir metal.	Experiment with using a different source of Sr in the starting materials.
SIO#F23	Pt with lid	$SrCO_3$, IrO_2, 7.5$SrCl_2$	1150°C for 12 hours. Cooling to 1100°C over 12.5hrs	Medium size $SrIrO_3$ crystals only.	Same conditions as F21A except for a smaller proportion of flux.

Table A.1 – continued from previous page

Name	Crucible type	Ratio of starting materials	Reaction conditions	Result	Comment
SIO#F24A	Pt with lid	$SrCO_3$, IrO_2, $6.5SrCl_2$	1150°C for 12 hours. Cooling to 1100°C over 12.5hrs	Small crystals of $SrIrO_3$ with a few larger crystals. Some small flakes of Sr_2IrO_4. Still some Ir	Same conditions as F23 except for a smaller proportion of flux.
SIO#F24B	Pt with lid	$1.35SrCO_3$, IrO_2, $6.5SrCl_2$	1150°C for 12 hours. Cooling to 1100°C over 12.5hrs	Small flakes of Sr_2IrO_4 and some microcrystals of $SrIrO_3$. Still some Ir and the yield is low	Same conditions as F24A but with a greater proportion of $SrCO_3$ to IrO_2
SIO#F26	Alumina with lid	$1.35SrCO_3$, IrO_2, $7.5SrCl_2$	1200°C for 12 hours. Cooling to 1100°C over 25 hrs	Most of the flux evaporated. Left Ir flakes and needle crystals of IrO_2 behind.	Same conditions as F17, which produced best batch, but in an alumina crucible

Table A.1 – continued from previous page

Name	Crucible type	Ratio of starting materials	Reaction conditions	Result	Comment
SIO#F27	Zirconia with lid	1.35$SrCO_3$, IrO_2, 7.5$SrCl_2$	1200°C for 12 hours. Cooling to 1100°C over 25 hrs	Some large platelets of $Sr_3Ir_2O_7$. $SrIrO_3$ crystals stuck to the bottom of the crucible. Zr crucible sides stained black. No Ir metal.	Same conditions as F17, which produced best batch, but in a zirconia crucible
SIO#F30	Zirconia with lid	1.55$SrCO_3$, IrO_2, 7.5$SrCl_2$	1200°C for 8 hours Cooling to 1100°C over 18 hours	Large square-ish crystals of $Sr_3Ir_2O_7$.	Conditions for the best crystals grown on a zirconia crucible.

A.2 Flux growth of $(Sr_{(1-x)}La_x)_3Ir_2O_7$

Table A.2 *An overview of the crystal growth conditions used to make each batch of* $(Sr_{(1-x)}La_x)_3Ir_2O_7$.

Name	Nominal x	Ratio of starting materials	Reaction conditions	Result
SLIO#F1	0.05	1.30(0.95$SrCO_3$+0.025La_2O_3): IrO_2:7.5$SrCl_2$	1200C for 12 hours. Cool to 1100C over 20 hours then cool to 900C in 1 hour before allowing the sample to furnace cool to room temperature.	Small yield A mixture of approximately 70% Sr_2IrO_4 and 30% $Sr_3Ir_2O_7$. Ir metal present
SLIO#F2	0.05	1.30(0.95$SrCO_3$+0.025La_2O_3): IrO2:8.5$SrCl_2$	1200C for 12 hours. Cool to 1100C over 25 hours then cool to 900C in 1 hour before allowing the sample to furnace cool to room temperature.	Higher yield and no Ir metal detectable. Approximately 50% Sr_2IrO_4 and 50% $Sr_3Ir_2O_7$
SLIO#F3	0.05	1.30(0.95$SrCO_3$+0.025La_2O_3): IrO_2:7.5$SrCl_2$	1175C for 12 hours. Cool to 1100C over 18.75 hours then cool to 900C in 1 hour before allowing the sample to furnace cool to room temperature.	Largest yield yet. A mixture of about 40% Sr_2IrO_4 and 60% $Sr_3Ir_2O_7$. Ir metal at bottom of crucible.
SLIO#F4	0.05	1.30(0.95$SrCO_3$+0.025La_2O_3): IrO_2:8.5$SrCl_2$	1175C for 12 hours. Cool to 1100C over 18.75 hours then cool to 900C in 1 hour before allowing the sample to furnace cool to room temperature.	Low yield and lots of iridium metal present. A mixture of Sr_2IrO_4 and $Sr_3Ir_2O_7$.

Table A.2 – continued from previous page

Name	Nominal x	Ratio of starting materials	Reaction conditions	Result
SLIO#F5	0.01	1.30(0.99$SrCO_3$+0.005La_2O_3): IrO_2:7.5$SrCl_2$	1200C for 12 hours. Cool to 1100C over 25 hours then cool to 900C in 1 hour before allowing the sample to furnace cool to room temperature.	Large flakes of Sr_2IrO_4, some small crystals of $SrIrO_3$ and some reasonable sized crystals of $Sr_3Ir_2O_7$.
SLIO#F6	0.10	1.30(0.90$SrCO_3$+0.05La_2O_3): IrO_2:7.5$SrCl_2$	1175C for 12 hours. Cool to 1100C over 18.75 hours then cool to 900C in 1 hour before allowing the sample to furnace cool to room temperature.	A mixture of Sr_2IrO_4 and $Sr_3Ir_2O_7$
SLIO#F7	0.03	1.30(0.97$SrCO_3$+0.03La_2O_3): IrO_2:7.5$SrCl_2$	1175C for 12 hours. Cool to 1100C over 18.75 hours then cool to 900C in 1 hour before allowing the sample to furnace cool to room temperature.	Mainly $Sr_3Ir_2O_7$.
SLIO#F8	0.20	1.30(0.80$SrCO_3$+0.20La_2O_3): IrO_2:7.5$SrCl_2$	1175C for 12 hours. Cool to 1100C over 18.75 hours then cool to 900C in 1 hour before allowing the sample to furnace cool to room temperature.	Mainly $Sr_3Ir_2O_7$.

A.3 Flux growth of $K_2CaPt_{3-\delta}O_6$

Table A.3 *An overview of attempts to grow crystals of $K_2CaPt_{3-\delta}O_6$.*

Name	Ratio of starting materials	Reaction conditions	Result
KPO#F1a	PtO_2 + 3Pt + 76KOH	Small alumina crucible in tube furnace with baffles. Heat sample at 792°C in air for 24 hours before cooling rapidly to room temperature.	No red/orange powder or microcrystals formed, only green-black amorphous needles.
KPO#F1b	$2.5PtO_2$ + 1.5Pt + 76KOH	Small alumina crucible in tube furnace with baffles. Heat sample at 792°C in air for 24 hours before cooling rapidly to room temperature.	No red/orange powder or microcrystals formed, only some black clusters on the edge of the crucible.
CPO#F18a	$CaCO_3$ + Pt + PtO_2 + 85KOH	Alumina crucible without a lid. Hold at 792°C for 16 hours in air before rapidly cooling to room temperature.	Red and black-purple microcrystals of $K_2CaPt_{3-\delta}O_6$ and Ca_4PtO_6. Some orange powder of $K_2CaPt_{3-\delta}O_6$ at the bottom of the crucible.
CPO#F18b	$CaCO_3$ + Pt + PtO_2 + 256KOH	Alumina crucible without a lid. Hold at 792°C for 16 hours in air before rapidly cooling to room temperature.	The same as CPO#F18a except there were fewer crystals of $K_2CaPt_{3-\delta}O_6$. The size of the crystals was about the same.

Table A.3 – continued from previous page

Name	Ratio of starting materials	Reaction conditions	Result
CPO#F19a	$CaCO_3$ + Pt + PtO_2 + 85KOH	Alumina crucible with lid. Hold at 750°C for 36 hours in air before rapidly cooling to room temperature.	Microcrystals of $K_2CaPt_{3-\delta}O_6$ near the lid and $K_2CaPt_{3-\delta}O_6$ powder at the bottom of the crucuble. Lots of Ca_4PtO_6 crystals also formed.
CPO#F19b	$CaCO_3$ + Pt + PtO_2 + 85KOH	Alumina crucible without a lid. Hold at 750°C for 36 hours in air before rapidly cooling to room temperature.	Microcrystals of $K_2CaPt_{3-\delta}O_6$ near the lid bigger than all previous growths but layer of amorphous green-black material at the bottom of the crucuble. Some Ca_4PtO_6 crystals also formed.
CPO#F20	$CaCO_3$ + 1.2Pt + 0.8PtO_2 + 85KOH	Alumina crucible without a lid. Hold at 700°C for 48 hours in air before rapidly cooling to room temperature.	Microcrystals of $K_2CaPt_{3-\delta}O_6$ near the lid similar size to CPO#F19b but appear to be better quality. Also $K_2CaPt_{3-\delta}O_6$ powder at the bottom of crucible. Some amorphous green-black material on inner side of the crucuble.

Table A.3 – continued from previous page

Name	Ratio of starting materials	Reaction conditions	Result
CPO#F21	$CaCO_3$ + 1.2Pt + 0.8PtO_2 + 85KOH	Alumina crucible without a lid. Hold at 650°C for 48 hours in air before rapidly cooling to room temperature.	Some microcrystals of $K_2CaPt_{3-\delta}O_6$ near the lid similar size and just $K_2CaPt_{3-\delta}O_6$ powder at the bottom of crucible. No amorphous green-black material or other crystals present.
CPO#F22a	$CaCO_3$ + 1.2Pt + 0.8PtO_2 + 26KOH	Alumina crucible without a lid. Hold at 715°C for 32 hours in air before rapidly cooling to room temperature.	$K_2CaPt_{3-\delta}O_6$ powder mixed with amorphous green material at the bottom of the crucible and a few poor quality small crystals of $K_2CaPt_{3-\delta}O_6$ near rim of crucible.
CPO#F22b	$CaCO_3$ + 1.2Pt + 0.8PtO_2 + 426KOH	Alumina crucible without a lid. Hold at 715°C for 32 hours in air before rapidly cooling to room temperature.	Polycrystalline crust of $K_2CaPt_{3-\delta}O_6$ around the rim and outside of the crucible. No $K_2CaPt_{3-\delta}O_6$ powder formed.

Table A.3 – continued from previous page

Name	Ratio of starting materials	Reaction conditions	Result
$Ca_2Pt_3O_6$#F1	$2CaCO_3$ + 1.8Pt + $1.2PtO_2$ + 136KOH	Alumina crucible without a lid. Hold at 715°C for 24 hours in air before rapidly cooling to room temperature.	Microcrystals of $K_2CaPt_{3-\delta}O_6$ near the lid of a similar size to previous growths. Also $K_2CaPt_{3-\delta}O_6$ powder at the bottom of crucible. Some amorphous green-black material on inner side of the crucuble.
$Ca_2Pt_3O_6$#F2	$2CaCO_3$ + 3Pt + 136KOH	Alumina crucible without a lid. Hold at 715°C for 12 hours in air before rapidly cooling to room temperature.	Most of flux had evaporated leaving Ca_4PtO_6 crystals at the bottom of the crucible. Microcrystals of $K_2CaPt_{3-\delta}O_6$ near the lid of a higher yield but poorer quality than previous growths. Some green-black amorphous material.
$Ca_2Pt_3O_6$#F3a	$2CaCO_3$ + 3Pt + 5KOH	Alumina crucible without a lid. Hold at 715°C for 12 hours in air before rapidly cooling to room temperature.	A brown powder formed.

Table A.3 – continued from previous page

Name	Ratio of starting materials	Reaction conditions	Result
$Ca_2Pt_3O_6$#F3b	$2CaCO_3$ + 3.5Pt + 136KOH	Alumina crucible without a lid. Hold at 715°C for 12 hours in air before rapidly cooling to room temperature.	Same as $Ca_2Pt_3O_6$#F2 except there are more amorphous green-black material of the outside of the crucible.
$KCaPt_3O_6$#F1	$CaCO_3$ + 3Pt + 136.KOH	Alumina crucible without a lid. Hold at 715°C for 12 hours in air before rapidly cooling to room temperature.	Microcrystals of $K_2CaPt_{3-\delta}O_6$ near the lid of a similar size to previous growths. $K_2CaPt_{3-\delta}O_6$ powder mixed with amorphous green material at the bottom of the crucible. More amorphous material around the outside of the crucible.
$KCaPt_3O_6$#F2	$CaCO_3$ + 1.5Pt + 1.5PtO_2 + 136.KOH	Alumina crucible without a lid. Hold at 715°C for 12 hours in air before rapidly cooling to room temperature.	Higher yield and larger crystals of $K_2CaPt_{3-\delta}O_6$ than previous growths although still a lot of green-black amorphous substance.
$KCaPt_3O_6$#F3	$CaCO_3$ + 1.5Pt + 1.5PtO_2 + 136.KOH	Alumina crucible without a lid. Hold at 650°C for 24 hours in air before rapidly cooling to room temperature.	Mainly poorly crystalline Ca_4PtO_6 and still a lot of green-black amorphous material.

Table A.3 – continued from previous page

Name	Ratio of starting materials	Reaction conditions	Result
$KCaPt_3O_6$#F4	$0.067CaCO_3$ + 0.20Pt + $0.80PtO_2$ + 45.KOH	Alumina crucible without a lid. Hold at 715°C for 24 hours in air before rapidly cooling to room temperature.	$K_2CaPt_{3-\delta}O_6$ powder formed at bottom of crucible mixed with amorphous grey-green sludge. No crystals formed. Amorphous needles on inside and outside walls of crucible.
KCPO#F5	$0.7CaCO_3$ + 1.2Pt + $0.8PtO_2$ + 85.KOH	Alumina crucible without a lid. Hold at 650°C for 48 hours in air before rapidly cooling to room temperature.	Poor quality $K_2CaPt_{3-\delta}O_6$ microcrystals formed around the rim and $K_2CaPt_{3-\delta}O_6$ powder mixed with amorphous green-black material at the bottom of the crucible.
KCPO#F6	$0.7CaCO_3$ + 1.2Pt + $0.8PtO_2$ + 85.KOH	Alumina crucible without a lid. Hold at 650°C for 48 hours in air before rapidly cooling to room temperature.	Poor quality $K_2CaPt_{3-\delta}O_6$ microcrystals formed around the rim and $K_2CaPt_{3-\delta}O_6$ powder mixed with amorphous green-black material at the bottom of the crucible.

A.4 Power synthesis of $K_2CaPt_{3-\delta}O_6$

Table A.4 *The conditions used in attempting to synthesise poycrystalline powder of $K_2CaPt_{3-\delta}O_6$ via traditional solid state routes.*

Name	Ratio of starting materials	Reaction conditions	Result
KPO#P1	$2PtO_2$:2Pt:$1K_2CO_3$	775°C for 24 hours in air	Mainly Pt in x-ray diffraction pattern but also possible traces of PtO, KO_2 and KO_3
KPO#P2	1.5Pt:2.5PtO_2:2KOH	775°C for 24 hours in air	Powder x-ray diffraction pattern identical to KPO#P1
KPO#P3	$4PtO_2$:2KOH	525°C for 24 hours in air	X-ray powder diffraction pattern consists of 13.5%Pt, 40.3%PtO_2 and 46.1% KO_2.
CPO3#P1	$CaCO_3$ + Pt + PtO_2	650°C for 12 hours in air	5.4% Pt, 93.1%$CaPt_2O_4$ and 1.5%$CaCO_3$ from x-ray powder diffraction
CPO3#P2	$CaCO_3$ + 2Pt	650°C for 12 hours in air	97.3% Pt, 1.8%$CaPt_2O_4$ and 0.9%CaO from x-ray powder diffraction
KCPO#P1	$3PtO_2$:0.5K_2CO_3:1$CaCO_3$	650°C for 12 hours in air	61% Pt, 38%$CaPt_2O_4$ and 1%Ca_4PtO_6 from x-ray powder diffraction
KCPO#P2	$3PtO_2$:3K_2CO_3:1$CaCO_3$	800°C for 12 hours in air	60% Pt and 40%$CaPt_2O_4$ from x-ray powder diffraction
KCPO#P3	$3PtO_2$:1KO_2:1$CaCO_3$	600°C for 12 hours in air	Mainly amorphous with some unreacted $CaCO_3$ and CaO present

A.5 Flux growth of $(K_{\frac{2}{3}}Ca_{\frac{1}{3}})_{(1-\delta)}Pt_xCu_yO_2$

Table A.5 *An overview of attempts to grow crystals of* $(K_{\frac{2}{3}}Ca_{\frac{1}{3}})_{(1-\delta)}Pt_xCu_yO_2$

Name	Ratio of starting materials	Reaction conditions	Result
CPOC#F1	$CaCO_3$ + 1.17Pt + 0.78PtO_2 + 0.05CuO + 84KOH	Alumina crucible without a lid. Hold at 715°C for 24 hours in air before rapidly cooling to room temperature.	Hexagonal red microcrystals of $(K_{\frac{2}{3}}Ca_{\frac{1}{3}})_{(1-\delta)}Pt_xCu_yO_2$ near rim of crucible. Some green-black amorphous material and crystals of Ca_4PtO_6
CPOC#F2	$CaCO_3$ + 1.14Pt + 0.76PtO_2 + 0.10CuO + 83KOH	Alumina crucible without a lid. Hold at 715°C for 24 hours in air before rapidly cooling to room temperature.	Hexagonal red microcrystals of$(K_{\frac{2}{3}}Ca_{\frac{1}{3}})_{(1-\delta)}Pt_xCu_yO_2$ near rim of crucible larger than CPOC#F1. More green-black amorphous material and crystals of Ca_4PtO_6 than CPOC#F1
CPOC#F3	$CaCO_3$ + 1.08Pt + 0.72PtO_2 + 0.20CuO + 81KOH	Alumina crucible without a lid. Hold at 715°C for 24 hours in air before rapidly cooling to room temperature.	Hexagonal red-brown microcrystals of $(K_{\frac{2}{3}}Ca_{\frac{1}{3}})_{(1-\delta)}Pt_xCu_yO_2$ near rim of crucible still larger than CPOC#F1. Green-black amorphous material and crystals of Ca_4PtO_6

Table A.5 – continued from previous page

Name	Ratio of starting materials	Reaction conditions	Result
CPOC#F4	$CaCO_3$ + 1.02Pt + $0.68PtO_2$ + 0.30CuO + 78KOH	Alumina crucible without a lid. Hold at 715°C for 24 hours in air before rapidly cooling to room temperature.	Hexagonal red-brown microcrystals of $(K_{\frac{2}{3}}Ca_{\frac{1}{3}})_{(1-\delta)}Pt_xCu_yO_2$. Orange $(K_{\frac{2}{3}}Ca_{\frac{1}{3}})_{(1-\delta)}Pt_xCu_yO_2$ powder at the bottom of the crucible mixed with a grey powder that can't be identified on structural database.
CPOC#F5	$CaCO_3$ + 0.96Pt + $0.64PtO_2$ + 0.40CuO + 76KOH	Alumina crucible without a lid. Hold at 715°C for 24 hours in air before rapidly cooling to room temperature.	Hexagonal red-brown microcrystals of $(K_{\frac{2}{3}}Ca_{\frac{1}{3}})_{(1-\delta)}Pt_xCu_yO_2$ near rim of crucible still larger than CPOC#F1. Orange-yellow $(K_{\frac{2}{3}}Ca_{\frac{1}{3}})_{(1-\delta)}Pt_xCu_yO_2$ powder at the bottom of the crucible mixed with a grey powder that can't be identified on structural database.
CPOC#F6	$CaCO_3$ + 0.90Pt + $0.60PtO_2$ + 0.50CuO + 73KOH	Alumina crucible without a lid. Hold at 715°C for 24 hours in air before rapidly cooling to room temperature.	Hexagonal red-brown microcrystals of $(K_{\frac{2}{3}}Ca_{\frac{1}{3}})_{(1-\delta)}Pt_xCu_yO_2$ near rim of crucible still larger than CPOC#F1. Yellow $(K_{\frac{2}{3}}Ca_{\frac{1}{3}})_{(1-\delta)}Pt_xCu_yO_2$ powder at the bottom of the crucible mixed with a grey powder that can't be identified on structural database.

Table A.5 – continued from previous page

Name	Ratio of starting materials	Reaction conditions	Result
CPOC#F7	$CaCO_3$ + 0.84Pt + 0.56PtO_2 + 0.60CuO + 71KOH	Alumina crucible without a lid. Hold at 715°C for 24 hours in air before rapidly cooling to room temperature.	Dark-brown microcrystals near rim of crucible of worse quality and smaller yield than previous growths. Some yellow powder mixed with unidentifiable grey powder at the bottom of the crucible. Black square prismatic crystals at bottom of crucible.
CPOC#F8	$CaCO_3$ + 0.72Pt + 0.0.48PtO_2 + 0.80CuO + 67KOH	Alumina crucible without a lid. Hold at 715°C for 24 hours in air before rapidly cooling to room temperature.	A small yield of black hexagonal microcrystals near rim of crucible of worse quality and smaller yield than previous growths. Some specks of yellow powder mixed with unidentifiable grey powder at the bottom of the crucible.

A.6 Powder synthesis of $CaPt_2O_4$

Table A.6 *An overview outcome of synthesis attempts to make $CaPt_2O_4$ powder.*

Name	Ratio of starting materials	Reaction conditions	Result
CPO#P1	$2(NH_4)_2PtCl_6 + 4CaCO_3$	Carried out in mullite tube furnace under 1 atm of flowing O_2. Alumina boat used as crucible. Total pellet mass was 0.4215g. Pellet heated at 825° for 2 days.	Approx 3.1% Ca_4PtO_6 and 66.8% $CaPt_2O_4$ in powder XRD pattern. Some water backflowed into furnace on cooldown. No $CaCl_2$ detectable.
CPO#P2	$2(NH_4)_2PtCl_6 + 4CaCO_3$	Alumina boat used as crucible and reaction carried out in tube furnace with water valves. Total pellet mass was 0.4215g. Pellet heated at 825° in air for 2 days.	Approx 74.4% Ca_4PtO_6, 25.6% $CaPt_2O_4$ and 30.1% $CaCl_2.6H_2O$ in powder XRD pattern.
CPO#P3	$2(NH_4)_2PtCl_6 + 4CaCO_3$	Alumina boat used as crucible and reaction carried out in tube furnace with water valves. Total pellet mass was 0.5028g. Pellet heated at 850° in air for 2 days.	Approx 58% $CaPt_2O_4$, 3.9% $CaCl_2.6H_2O$ and 38.1% Pt metal in powder XRD pattern.
CPO#P4	$2(NH_4)_2PtCl_6 + 4CaCO_3$	Alumina boat used as crucible and reaction carried out in tube furnace with water valves. Total pellet mass was 1.4619g (reaction scaled up). Pellet heated at 850° in air for 2 days.	Very hard silver shiny pellet formed that was soluble in aqua regis. Pellet probably over reduced to platinum metal.

Table A.6 – continued from previous page

Name	Ratio of starting materials	Reaction conditions	Result
CPO#P5	$2(NH_4)_2PtCl_6 + 4CaCO_3$	Carried out in mullite tube furnace under 1 atm of flowing 10%O_2/Ar gas mixture. Alumina boat used as crucible. Total pellet mass was 0.7025g. Pellet heated at 850° for 48 hours.	Grey powder formed that XRD showed contained only Pt metal.
CPO#P6	$2(NH_4)_2PtCl_6 + 4CaCO_3$	Carried out in mullite tube furnace under 1 atm of flowing 10%O_2/Ar gas mixture. Alumina boat used as crucible. Total pellet mass was 0.6336g. Pellet heated at 800° for 48 hours.	Approx 82.1% $CaPt_2O_4$, 10% $CaCl_2.6H_2O$ and 7.9% Pt metal in powder XRD pattern.
CPO#P7	$2(NH_4)_2PtCl_6 + 4CaCO_3$	Carried out in mullite tube furnace under 1 atm of flowing 10%O_2/Ar gas mixture. Alumina boat used as crucible. Total pellet mass was 1.9755g (reaction scaled up). Pellet heated at 800° for 48 hours.	Approx 24.1% $CaPt_2O_4$, 20.7% $CaCl_2.6H_2O$ and 55.2% Pt metal in powder XRD pattern.
CPO#P8	$2(NH_4)_2PtCl_6 + 4CaCO_3$	Carried out in mullite tube furnace under 1 atm of flowing 10%O_2/Ar gas mixture. Alumina boat used as crucible. Total pellet mass was 1.2694g (split into 2 pellets). Pellet heated at 800° for 48 hours.	Sample contained $CaCl_2$ and $CaPt_2O_4$. No Pt detectable.

Table A.6 – continued from previous page

Name	Ratio of starting materials	Reaction conditions	Result
CPO#P9	$2(NH_4)_2PtCl_6 + 4CaCO_3$	Carried out in mullite tube furnace under 1 atm of flowing 10%O_2/Ar gas mixture. Alumina boat used as crucible. Gas ran out part the way through the reaction. Total pellet mass was 1.5003g (split into 2 pellets). Pellet heated at 800° for 48 hours.	Approx 31.4% $CaPt_2O_4$, 26.7% Ca_4PtO_6 3.3% $CaCl_2$ and 38.5% CaClOH in powder XRD pattern.
CPO#P10	$2(NH_4)_2PtCl_6 + 4CaCO_3$	Carried out in mullite tube furnace under 1 atm of flowing 10%O_2/Ar gas mixture. Alumina boat used as crucible. Gas valve became blocked part way through the reaction. Total pellet mass was 1.0958g (split into 2 pellets). Pellet heated at 815° for 48 hours.	Approx 2.7% $CaPt_2O_4$, 72.6% Ca_4PtO_6 and 24.7% Pt in powder XRD pattern.
CPO#P11	$2(NH_4)_2PtCl_6 + 4CaCO_3$	Carried out in mullite tube furnace under 1 atm of flowing 10%O_2/Ar gas mixture. Alumina boat used as crucible. Total pellet mass was 1.3941g (split into 2 pellets). Pellet heated at 805° for 48 hours.	Approx 65.4% $CaPt_2O_4$, 6.4% Ca_4PtO_6 and 28.2% CaClOH in powder XRD pattern.
CPO#P12	$2(NH_4)_2PtCl_6 + 4CaCO_3$	Carried out in mullite tube furnace under 1 atm of flowing 10%O_2/Ar gas mixture. Alumina boat used as crucible. Total pellet mass was 1.4441g (split into 2 pellets). Pellet heated at 810° for 48 hours.	Approx 84.7% $CaPt_2O_4$, 0.4% Ca_4PtO_6 and 14.9% CaClOH in powder XRD pattern.

Table A.6 – continued from previous page

Name	Ratio of starting materials	Reaction conditions	Result
CPO#P13	$2(NH_4)_2PtCl_6 + 4CaCO_3$	Carried out in mullite tube furnace under 1 atm of flowing 10%O_2/Ar gas mixture. Alumina boat used as crucible. Total pellet mass was 0.5504g. Pellet heated at 810° for 48 hours.	Approx 75.7% $CaPt_2O_4$, 12% Ca_4PtO_6 and 12.3% CaClOH in powder XRD pattern. No Pt.
CPO#P15	$1.07PtO_2 + Pt + CaCO_3$	Alumina boat used as crucible. Total pellet mass was 0.2813g. Pellet heated at 650° for 12 hours in air.	Approx 32.2% $CaPt_2O_4$, 67%Pt and 0.7% CaO in powder XRD pattern.
CPO#P16	$1.07PtO_2 + Pt + CaCO_3$	Alumina boat used as crucible. Total pellet mass was 0.2803g. Pellet heated at 650° for 24 hours in air.	Approx 72.5% $CaPt_2O_4$ and 27.5%Pt in powder XRD pattern.
CPO#P17	$2PtO_2 + CaCO_3$	Alumina boat used as crucible. Total pellet mass was 0.2732g. Pellet heated at 625° for 24 hours in air.	Brown pellet that forms a grey-black powder upon grinding. XRD shows that the compound has a regular structure but there is no match for it on the database.
CPO#P18	$2PtO_2 + CaCO_3$	Alumina boat used as crucible. Total pellet mass was 0.2803g. Pellet heated at 650° for 24 hours in air.	Approx 96% $CaPt_2O_4$, 3%Pt and 1% $Ca_2Pt_3O_8$ in powder XRD pattern.
CPO#P19	$2PtO_2 + CaCO_3$	Alumina boat used as crucible. Total pellet mass was 0.2803g. Pellet heated at 675° for 24 hours in air.	XRD very similar to CPO#P18 but $CaPt_2O_4$ peaks appear sharper.

A.7 Crystal growth attempts to make $CaPt_2O_4$

Table A.7 *An overview of attempts to grow crystals of $CaPt_2O_4$.*

Name	Ratio of starting materials	Reaction conditions	Result
CPO#F1	$CaPt_2O_4$ + 30.$CaCl_2$	Alumina crucible used without lid. Heat sample at 825°C in air for 6 hours before cooling to 750° over 12 hours. Sample then quenched to room temperature.	Grey powder containing small white crystals at bottom of crucible. XRD showed that powder composed of Pt and $CaCl_2.6H_2O$.
CPO#F2	$CaPt_2O_4$ + 30.$CaCl_2.2H_2O$	Alumina crucible used without lid. Heat sample at 800°C in air for 6 hours before cooling to room temperature over 48 hours.	Small clumps of $CaPt_2O_4$ powder present (did not dissolve) and Pt peaks dominate XRD pattern.
CPO#F3	$2(NH_4)_2PtCl_6$ + $4CaCO_3$ + 30.$CaCl_2.2H_2O$	Alumina crucible used with lid. Heat sample at 800°C in air for 6 hours before cooling to room temperature over 48 hours.	Only Pt present after washing resultant mixture with water.
CPO#F4	$CaPt_2O_4$ + 100.$CaCl_2.2H_2O$	Alumina crucible used without lid. Heat sample at 790°C in air for 12 hours before cooling to 780°C over 6 hours. Sample then quenched to room temperature.	Flux was still liquid at 780°C when sample quenched. Black powder clusters on side of crucible with leftover flux pale brown in colour. Only elemental Pt detectable by XRD.

Table A.7 – continued from previous page

Name	Ratio of starting materials	Reaction conditions	Result
CPO#F5	$CaPt_2O_4$ + 200.$CaCl_2$.2H_2O	Alumina crucible used without lid. Heat sample at 700°C in air for 8 hours before cooling to 600°C over 7 hours. Sample then quenched to room temperature.	Flux did not melt. Some clumps of shiny purple grains visible under the microscope on the surface of the now grey flux. No $CaPt_2O_4$ detectable by XRD with only $CaCl_2$.6H_2O being detectable.
CPO#F6	$CaPt_2O_4$ + 200.$CaCl_2$.2H_2O	Alumina crucible used without lid. Heat sample at 770°C in air for 144 hours(6 days) before cooling to room temperature over 3 hours.	A lot of $CaCl_2$ had condensed on the outside of the crucible. Only Pt in crucible other than flux.
CPO#F7	$CaPt_2O_4$ + 100.$CaCO_3$	Alumina crucible used without lid. Heat sample at 840°C in air for 24 hours before cooling to room temperature.	$CaCO_3$ flux did not melt despite melting point being 825°C. Some black specs visible on the surface of the flux, which looked like $CaPt_2O_4$ under a microscope.
CPO#H1	0.0961g of $CaPt_2O_4$ + 15ml of H_2O	Hydrothermal synthesis using a 45ml volume hydrothermal cell. Cell heated to 200°C for around 16 hours and then cooled to room temperature overaround 6 hours.	Unreacted $CaPt_2O_4$ powder.

Table A.7 – continued from previous page

Name	Ratio of starting materials	Reaction conditions	Result
CPO#H2	0.0961g of $CaPt_2O_4$ + 5ml of 1 molar KOH solution	Hydrothermal synthesis using a 45ml volume hydrothermal cell. Cell heated to 200°C for around 16 hours and then cooled to room temperature over around 6 hours.	Clusters of powder in hydrothermal cell. X-ray showed the powder to be composed of mainly $CaPt_2O_4$ with KOH and some small hard to identify peaks of other compounds such as $Ca(OH)_2$.
CPO#H3	0.0961g of $CaPt_2O_4$ + 30ml of 5 molar KOH solution	Hydrothermal synthesis using a 45ml volume hydrothermal cell. Cell heated to 200°C for around 16 hours and then cooled to room temperature over around 6 hours.	Product powder appears to be unreacted $CaPt_2O_4$.
CPO#H4	0.2g of $CaPt_2O_4$ + 30ml of 5 molar KOH solution	Hydrothermal synthesis using a 45ml volume hydrothermal cell. Cell heated to around 250°C for 4 days and then cooled to room temperature over around 6 hours.	Product powder appears to be unreacted $CaPt_2O_4$.
CPO#F9	$CaPt_2O_4$ + 530.KOH	Alumina crucible with lid placed inside a larger crucible to slow the rate of flux evaporation. Heat sample at 750°C in air for 24 hours before cooling to room temperature over 48 hours.	$CaCO_3$ Large black/purple crystals of Ca_4PtO_6 mixed with smaller red/orange crystals of $K_2CaPt_{3-\delta}O_6$. Black amorphous fibre-like structures coat the bottom of the crucible that turn yellow on the addition of water.

Table A.7 – continued from previous page

Name	Ratio of starting materials	Reaction conditions	Result
CPO#F10	$CaPt_2O_4$ + 530.KOH	Alumina crucible with lid placed enclosed within firebricks. Heat sample at 900°C in air for 24 hours before cooling to 800°C over 20 hours. Sample then quenched to room temperature.	All of the flux had evaporated leaving behind Pt metal, small crystals of $K_2CaPt_{3-\delta}O_6$, yellow transparent crystals of CaO and clusters of purple-black powder that may be Pt_2O (from x-ray diffraction).
CPO#F11	$CaPt_2O_4$ + 530.KOH	Alumina crucible with lid placed inside a larger crucible. Heat sample at 850°C in air for 24 hours before cooling to 800°C over 25 hours. Sample then quenched to room temperature.	Some yellow crystals in crucible cracks and some small pink/red crystals. XRD reveals that the product composition is approximately 8% Pt, 12.3% Pt_2O and 79.8% KOH plus some unidentifiable peaks.
CPO#F12	$CaPt_2O_4$ + 530.KOH	Alumina crucible with lid placed inside a larger crucible. Heat sample at 800°C in air for 24 hours before cooling rapidly to room temperature.	Most of the flux had evaporated. Small yellow cubic crystals of CaO and also Pt and possibly some $Ca_5Ir_3O_12$ present from x-ray diffraction.
CPO#F13	$CaPt_2O_4$ + 265.KOH	Alumina crucible with lid placed inside a larger crucible. Heat sample at 790°C in air for 18 hours before cooling rapidly to room temperature.	Green-black amorphous needles that turn yellow on the addition of water. Small black crystals of Ca_4PtO_6.

Table A.7 – continued from previous page

Name	Ratio of starting materials	Reaction conditions	Result
CPO#F14	$CaPt_2O_4$ + 88KOH	Small tube-like crucible with lid to match smaller quantity of reagents used imbedded in a firebrick. Heat sample at 795°C in air for 48 hours before cooling rapidly to room temperature.	Flux mostly evaporated leaving behind 50.6% PtO, 8.6% Ca_4PtO_6, 21.5% Al_2O_3, 10.3% KOH and 2% $CaPt_2O_4$ powder (from x-ray diffraction pattern). There were also some large crystals of Ca_4PtO_6.
CPO#F15	$CaPt_2O_4$ + 88KOH	Small tube-like crucible with lid to match smaller quantity of reagents used imbedded in a firebrick. Heat sample at 790°C in air for 48 hours before cooling rapidly to room temperature.	Result similar to CPO#F14 except that Ca_4PtO_6 crystals are cubic rather than prismatic in shape and some red/orange microcrystals were found on the lid (later identified as $K_2CaPt_{3-\delta}O_6$).
CPO#F16	$CaCO_3$ + PtO_2 + 3Pt + 88KOH	Small alumina crucible without lid. Heat sample at 792°C in air for 24 hours before cooling rapidly to room temperature.	Red microcrystals ($K_2CaPt_{3-\delta}O_6$) coating the walls of the crucible and a lot of Pt metal still mixed in with the flux.
CPO#F17	$CaPt_2O_4$ + 88KOH	Small tube-like crucible with lid to match smaller quantity of reagents used imbedded in a firebrick. Heat sample at 780°C in air for 48 hours before cooling rapidly to room temperature.	A mixture of $CaPt_2O_4$ and CaO crystals with Pt powder on the lid.

Appendix B

Additional refinements

This appendix contains all of the powder x-ray refinements used to obtain structural data for this thesis. This appendix is split into several sections to relate the refinements to a particular section of the thesis.

B.1 Powder X-ray diffraction refinements of different batches of $Sr_3Ir_2O_7$

Figures B.1, B.2, B.3, B.4 and B.5 are Rietveld refinements of x-ray diffraction data collected on ground crystals from four different batches of $Sr_3Ir_2O_7$ that were grown under slightly different conditions (see section 4.4). In all of the figures the red crosses mark the observed data, the solid black line is the calculated profile and the solid blue line is the difference curve. The black tick marks show the position of the Bragg reflections of $Sr_3Ir_2O_7$. In some cases an additional set of green tick marks indicate the Bragg reflections of an impurity phase, the percentage weight and identy of which is given in the figure caption. The χ^2 and R_{wp} values of each refinement, which give an indication of the goodness of fit, are also given in the figure caption. The majority of the x-ray diffraction patterns were refined to the Bbcb structural model, however the crystals from batch F17 were also refined in the I4/mmm model for comparison to the lathanum doped $Sr_3Ir_2O_7$ in section 4.6. Key results from each of these refinements are shown in tables B.1, B.2, B.3, B.4 and B.5.

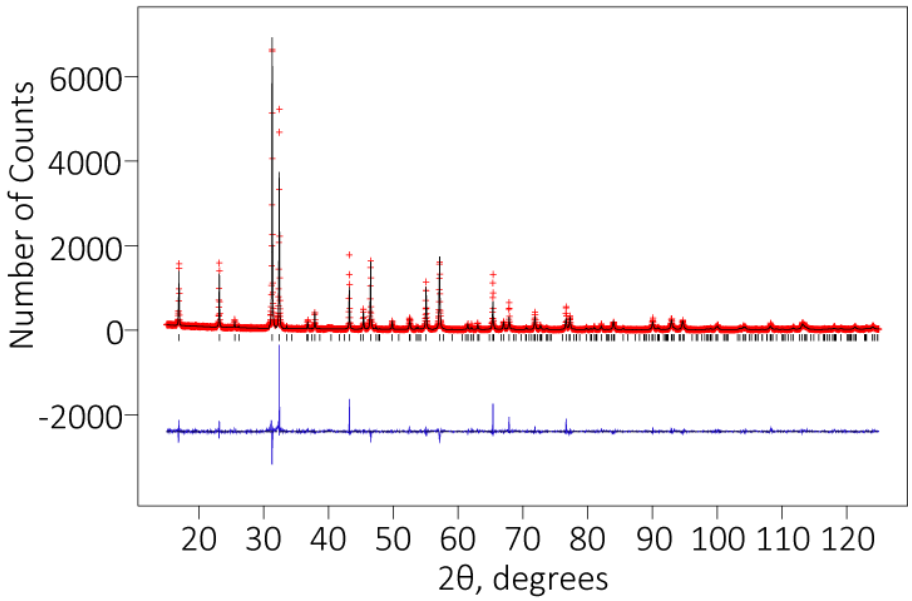

Figure B.1 *X-ray refinement of ground crystals of $Sr_3Ir_2O_7$ from batch number F1 using the Bbcb structural model. χ^2=2.609; R_{wp}=0.1908.*

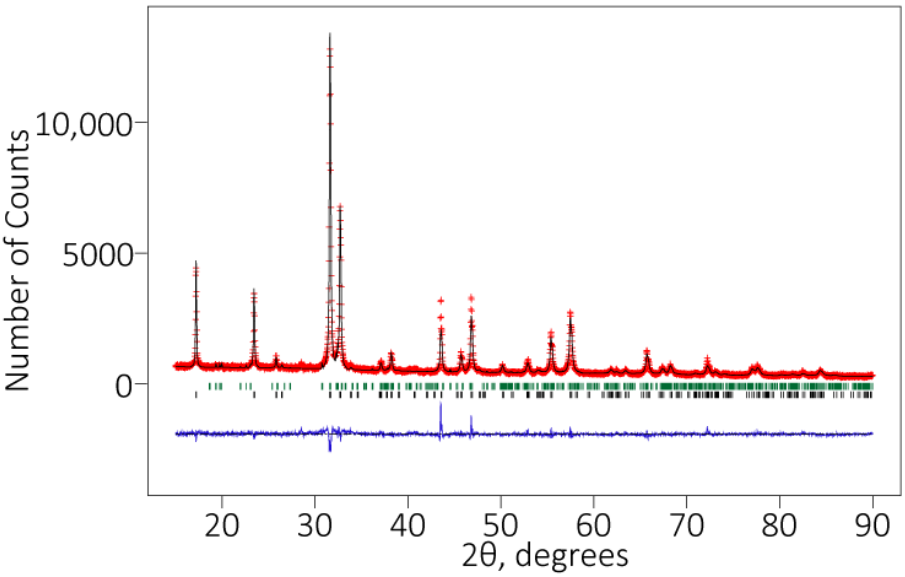

Figure B.2 *X-ray refinement of ground crystals of $Sr_3Ir_2O_7$ from batch number F5 using the Bbcb structural model. There is an additional impurity phase of $SrIrO_3$ in the diffraction pattern that makes up around 3.5% of the sample by weight. χ^2=3.342; R_{wp}=0.0740.*

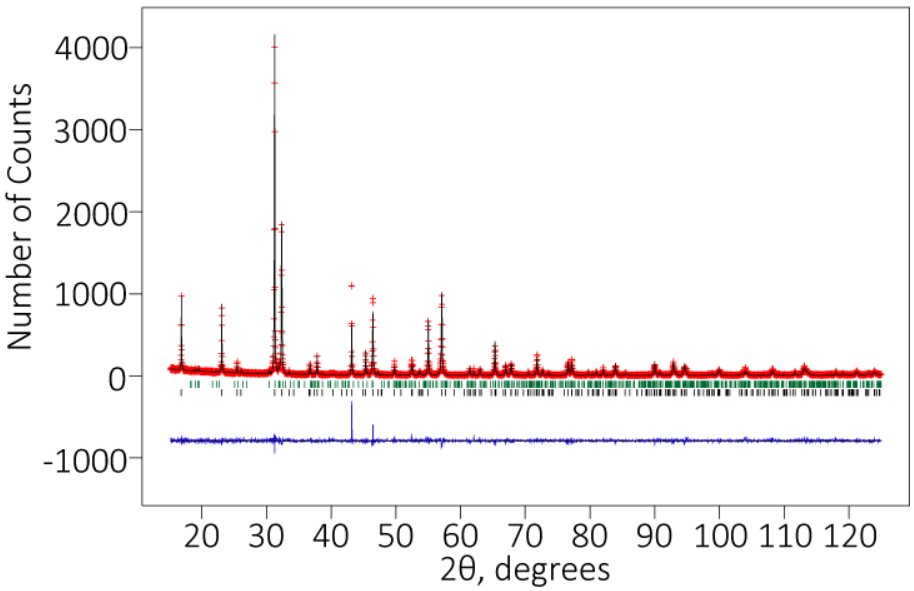

Figure B.3 *X-ray refinement of ground crystals of $Sr_3Ir_2O_7$ from batch number F17 using the Bbcb structural model. There is an additional impurity phase of $SrIrO_3$ in the diffraction pattern that makes up around 4.7% of the sample by weight. χ^2=1.312; R_{wp}=0.1835.*

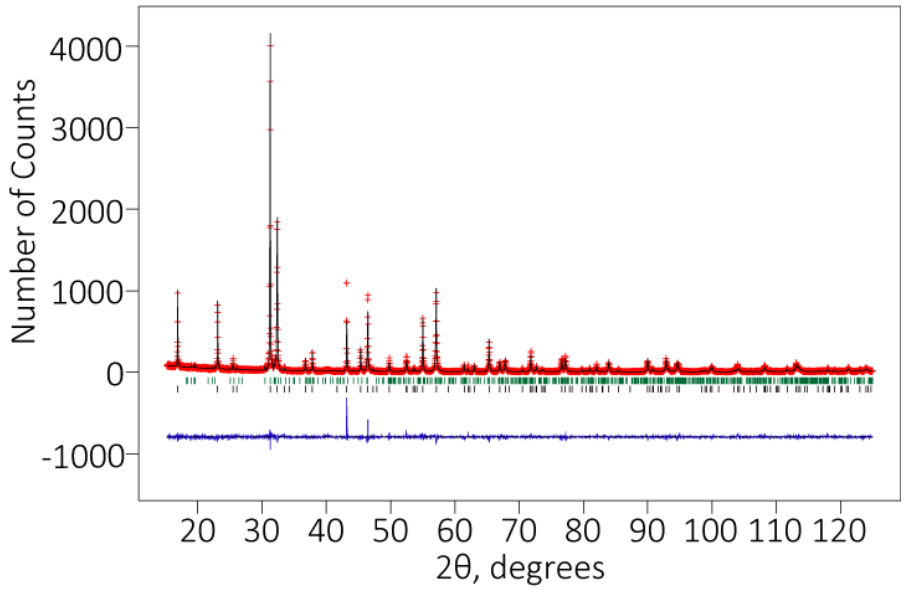

Figure B.4 *X-ray refinement of ground crystals of $Sr_3Ir_2O_7$ from batch number F17 using the I4/mmm structural model. There is an additional impurity phase of $SrIrO_3$ in the diffraction pattern that makes up around 5% of the sample by weight. χ^2=1.310; R_{wp}=0.1833.*

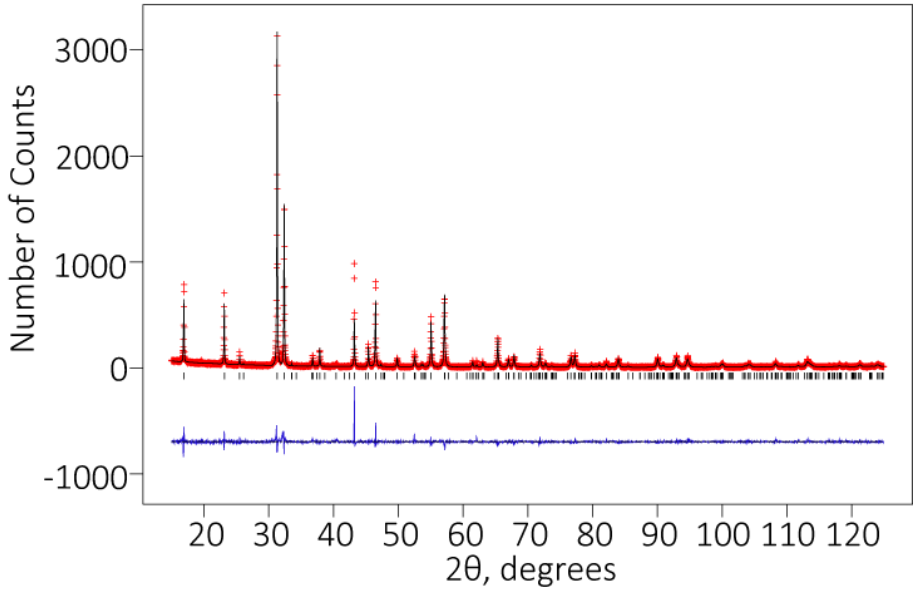

Figure B.5 *X-ray refinement of ground crystals of $Sr_3Ir_2O_7$ from batch number F19B using the Bbcb structural model. χ^2=1.067; R_{wp}=0.1765.*

Atom	Wyckoff Symbol	x	y	z	B	Occupancy
Ir(1)	8e	0.25	0.25	0.40284(7)	0.0149(4)	1
Sr(1)	4a	0.25	0.25	0	0.0012(1)	0.947
Sr(2)	8e	0.25	0.25	0.1876(1)	0.010(8)	0.947
O(1)	4b	0.25	0.25	0.5	0.025	0.886
O(2)	8e	0.25	0.25	0.3048	0.025	0.886
O(3)	16i	0.5308	-0.031	0.096400	0.025	0.886

Table B.1 *Results from the Rietveld refinement on ground crystals of $Sr_3Ir_2O_7$ from batch number F1 using the Bbcb structural model.*

Atom	Wyckoff Symbol	x	y	z	B	Occupancy
Ir(1)	8e	0.25	0.25	0.4026(1)	0.0222(8)	1
Sr(1)	4a	0.25	0.25	0	0.0012(3)	0.947
Sr(2)	8e	0.25	0.25	0.1878(2)	0.014(3)	0.947
O(1)	4b	0.25	0.25	0.5	0.0045(3)	0.889
O(2)	8e	0.25	0.25	0.3048	0.0045(3)	0.889
O(3)	16i	0.5308	-0.031	0.096400	0.0045(3)	0.889

Table B.2 *Results from the Rietveld refinement on ground crystals of $Sr_3Ir_2O_7$ from batch number F5 using the Bbcb structural model.*

Atom	Wyckoff Symbol	x	y	z	B	Occupancy
Ir(1)	8e	0.25	0.25	0.40257(1)	0.0123(3)	1
Sr(1)	4a	0.25	0.25	0	0.0013(1)	0.940
Sr(2)	8e	0.25	0.25	0.1874(1)	0.0126(8)	0.940
O(1)	4b	0.25	0.25	0.5	0.005(2)	0.891
O(2)	8e	0.25	0.25	0.3048	0.005(2)	0.891
O(3)	16i	0.5308	-0.031	0.096400	0.005(2)	0.891

Table B.3 *Results from the Rietveld refinement on ground crystals of $Sr_3Ir_2O_7$ from batch number F17 using the Bbcb structural model.*

Atom	Wyckoff Symbol	x	y	z	B	Occupancy
Ir(1)	4e	0	0	0.09739(7)	0.0123(3)	1
Sr(1)	2b	0.5	0.5	0	0.013(1)	0.940
Sr(2)	4e	0.5	0.5	0.1880(1)	0.013(1)	0.940
O(1)	4a	0	0	0	0.002(2)	0.891
O(2)	2e	0	0	0.1939	0.002(2)	0.891
O(3)	16n	0.1043	0.5	0.0960	0.002(2)	0.891

Table B.4 *Results from the Rietveld refinement on ground crystals of $Sr_3Ir_2O_7$ from batch number F17 using the I4/mmm structural model.*

Atom	Wyckoff Symbol	x	y	z	B	Occupancy
Ir(1)	8e	0.25	0.25	0.40288(6)	0.0171(4)	1
Sr(1)	4a	0.25	0.25	0	0.0018(1)	0.953
Sr(2)	8e	0.25	0.25	0.18800(9)	0.0102(8)	0.953
O(1)	4b	0.25	0.25	0.5	0.015(2)	0.890
O(2)	8e	0.25	0.25	0.3048	0.015(2)	0.890
O(3)	16i	0.5308	-0.031	0.096400	0.015(2)	0.890

Table B.5 *Results from the Rietveld refinement on ground crystals of $Sr_3Ir_2O_7$ from batch number F19B using the Bbcb structural model.*

B.2 Structural evolution of $Sr_3Ir_2O_7$ with temperature

As detailed in section 4.5, to study the structural evolution of $Sr_3Ir_2O_7$ with temperature, x-ray powder diffraction data were collected at 24°C, 200°C, 400°C, 600°C and 800°C using the furnace attachment on the Rigaku x-ray diffractometer in the materials characterisation laboratory at ISIS. Data were collected on the warm up to 800°C and on the cool down back to room temperature and refinemed to both the Bbcb and I4/mmm structural models. The sample consisted of ground up crystals of $Sr_3Ir_2O_7$ from batch F18B. Figures B.8, B.12, B.16 and B.20 are x-ray refinements to the Bbcb structural model from data collected on the warm up, figures B.18, B.14, B.10 and B.6 are x-ray refinements to the Bbcb structural model from data collected on the cool down, figures B.9, B.13, B.17 and B.21 are x-ray refinements to the I4/mmm structural model from data collected on the warm up and figures B.19, B.15, B.11 and B.7 are x-ray refinements to the I4/mmm structural model from data collected on the cool down. For clarity this information is also given in the caption for each figure as well as the χ^2 and R_{wp} values to indicate the goodness of fit. Key results from each of these refinements are shown in tables B.6, B.7, B.8, B.9, B.10, B.11, B.12, B.13, B.14, B.15, B.16, B.17, B.18, B.19, B.20 and B.21.

Atom	Wyckoff Symbol	x	y	z	B	Occupancy
Ir(1)	8e	0.25	0.25	0.40251(8)	0.029(1)	1
Sr(1)	4a	0.25	0.25	0	0.015(1)	1
Sr(2)	8e	0.25	0.25	0.1883(1)	0.015(1)	1
O(1)	4b	0.25	0.25	0.5	0.025	0.9157
O(2)	8e	0.25	0.25	0.3048	0.025	0.9157
O(3)	16i	0.5308	-0.031	0.096400	0.025	0.9157

Table B.6 *Results from the Rietveld refinement on ground crystals of $Sr_3Ir_2O_7$ using the Bbcb structural model with the data collected at a temperature of 24° C on the cool down from 800° C.*

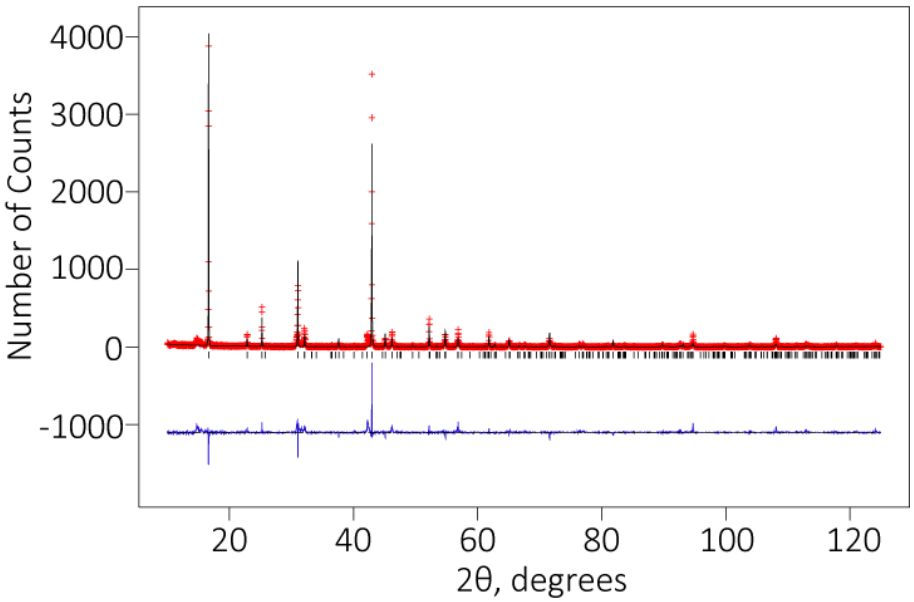

Figure B.6 *X-ray refinement of ground crystals of $Sr_3Ir_2O_7$ using the Bbcb structural model with the data collected at a temperature of 24° C on the cool down from 800° C. χ^2=3.335; R_{wp}=0.4267.*

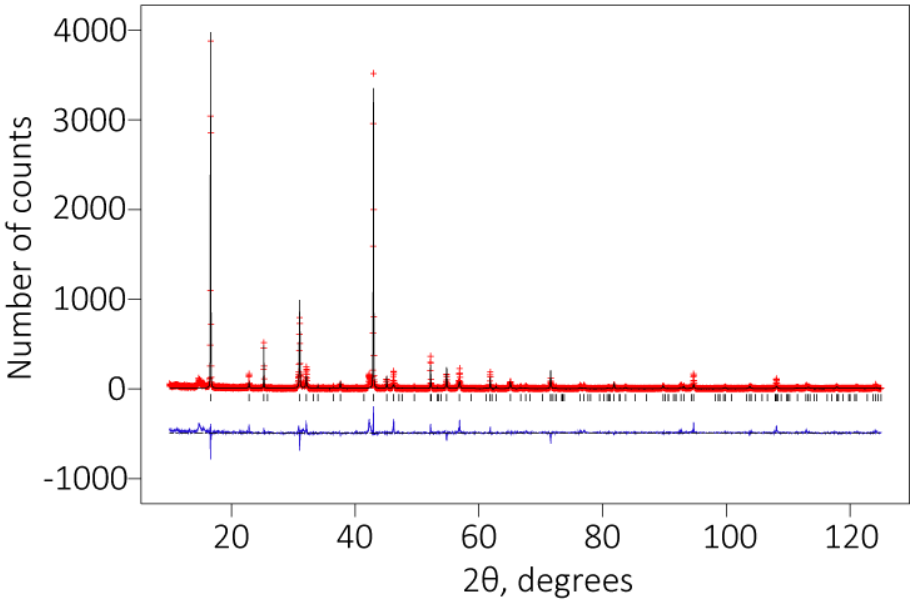

Figure B.7 *X-ray refinement of ground crystals of $Sr_3Ir_2O_7$ using the I4/mmm structural model with the data collected at a temperature of 24° C on the cool down from 800° C. χ^2=3.973; R_{wp}=0.4658.*

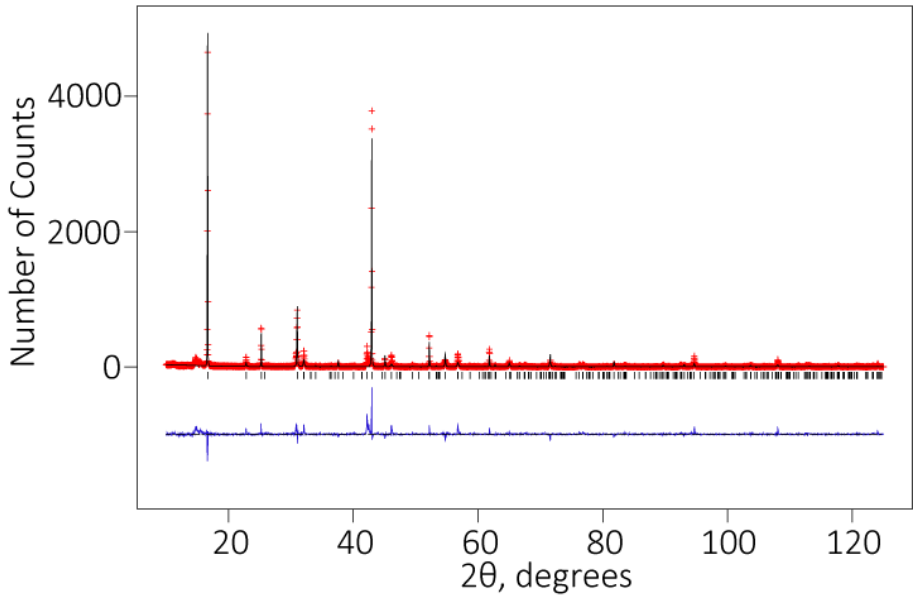

Figure B.8 *X-ray refinement of ground crystals of $Sr_3Ir_2O_7$ using the Bbcb structural model with the data collected at a temperature of 200° C on the warm up from room temperature. χ^2=3.517; R_{wp}=0.4187.*

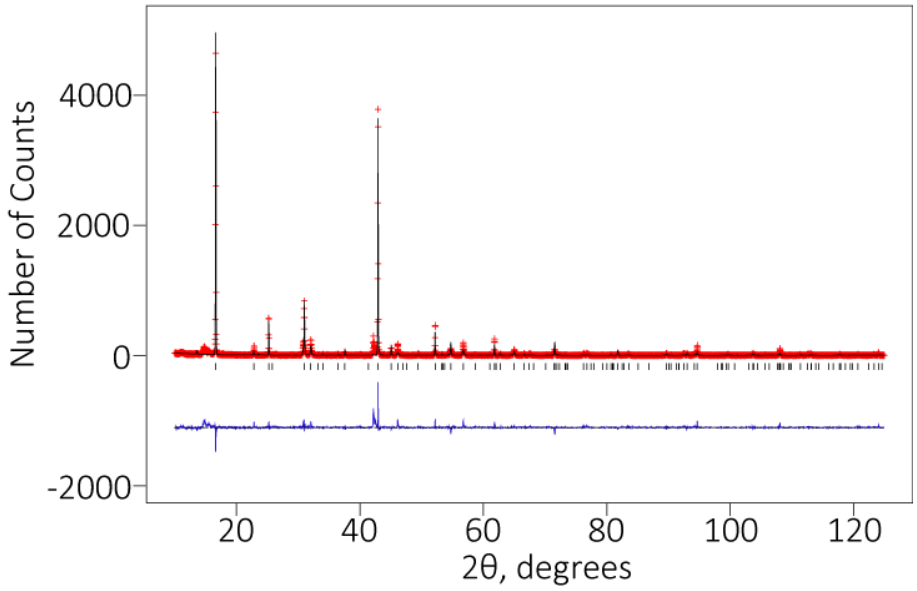

Figure B.9 *X-ray refinement of ground crystals of $Sr_3Ir_2O_7$ using the I4/mmm structural model with the data collected at a temperature of 200° C on the warm up from room temperature. χ^2=3.298; R_{wp}=0.4053.*

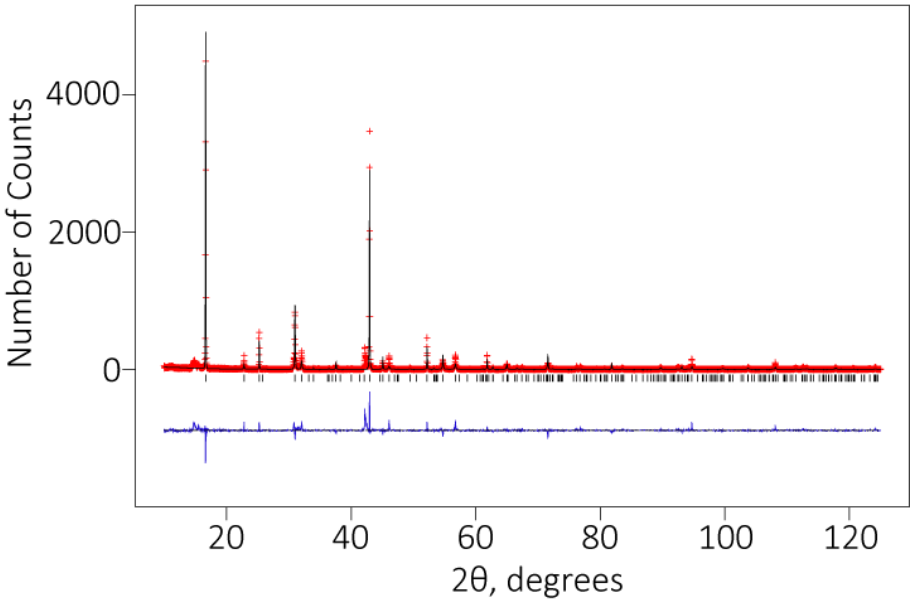

Figure B.10 *X-ray refinement of ground crystals of $Sr_3Ir_2O_7$ using the Bbcb structural model with the data collected at a temperature of 200° C on the cool down from 800° C. χ^2=3.490; R_{wp}=0.4234.*

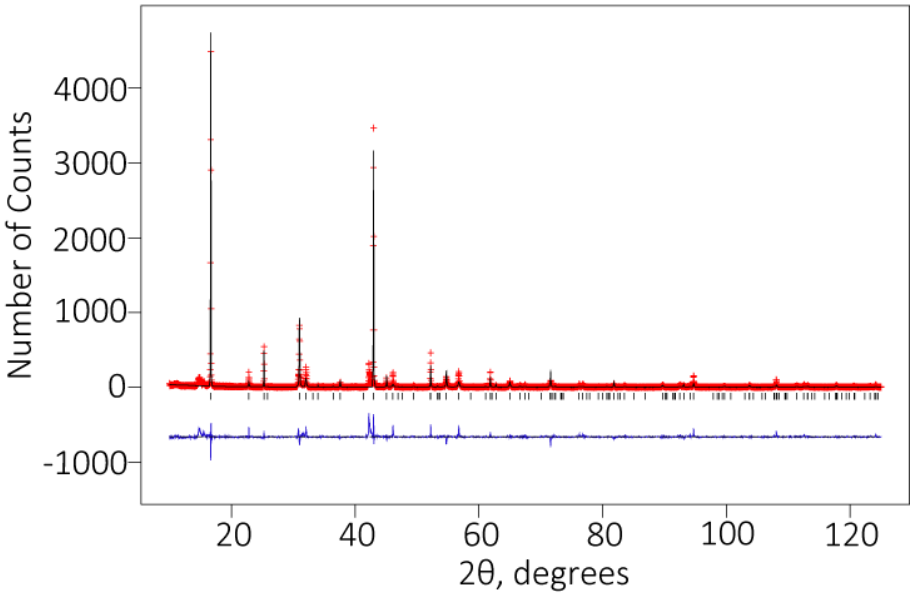

Figure B.11 *X-ray refinement of ground crystals of $Sr_3Ir_2O_7$ using the I4/mmm structural model with the data collected at a temperature of 200° C on the cool down from 800° C. χ^2=3.516; R_{wp}=0.4250.*

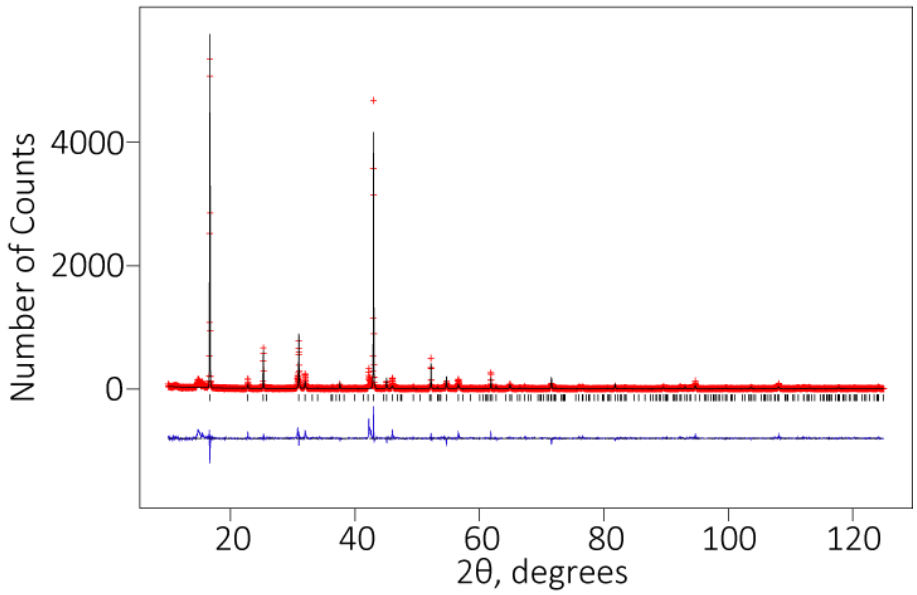

Figure B.12 *X-ray refinement of ground crystals of $Sr_3Ir_2O_7$ using the Bbcb structural model with the data collected at a temperature of 400° C on the warm up from room temperature. χ^2=3.981; R_{wp}=0.4282.*

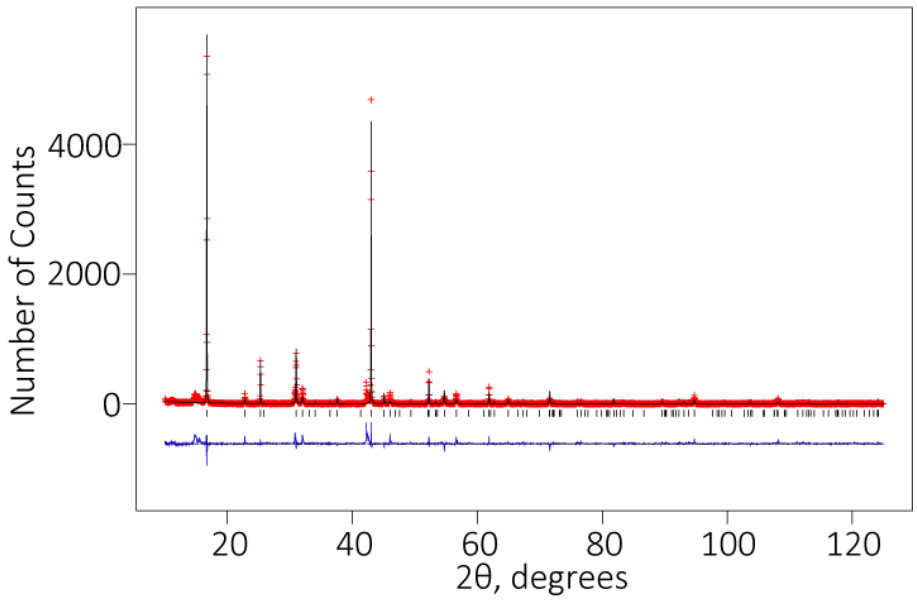

Figure B.13 *X-ray refinement of ground crystals of $Sr_3Ir_2O_7$ using the I4/mmm structural model with the data collected at a temperature of 400° C on the warm up from room temperature. χ^2=3.472; R_{wp}=0.4081.*

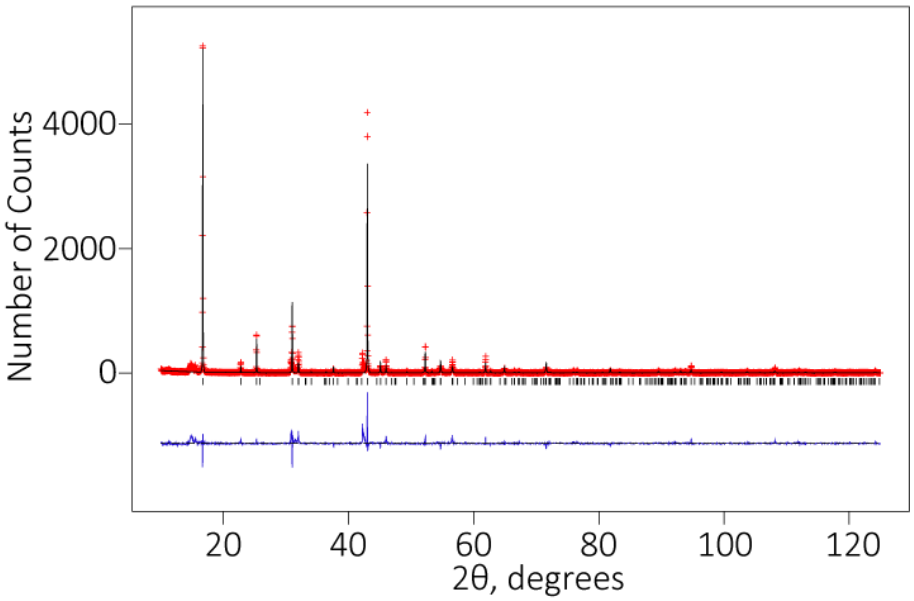

Figure B.14 *X-ray refinement of ground crystals of $Sr_3Ir_2O_7$ using the Bbcb structural model with the data collected at a temperature of 400° C on the cool down from 800° C. χ^2=4.120; R_{wp}=0.4464.*

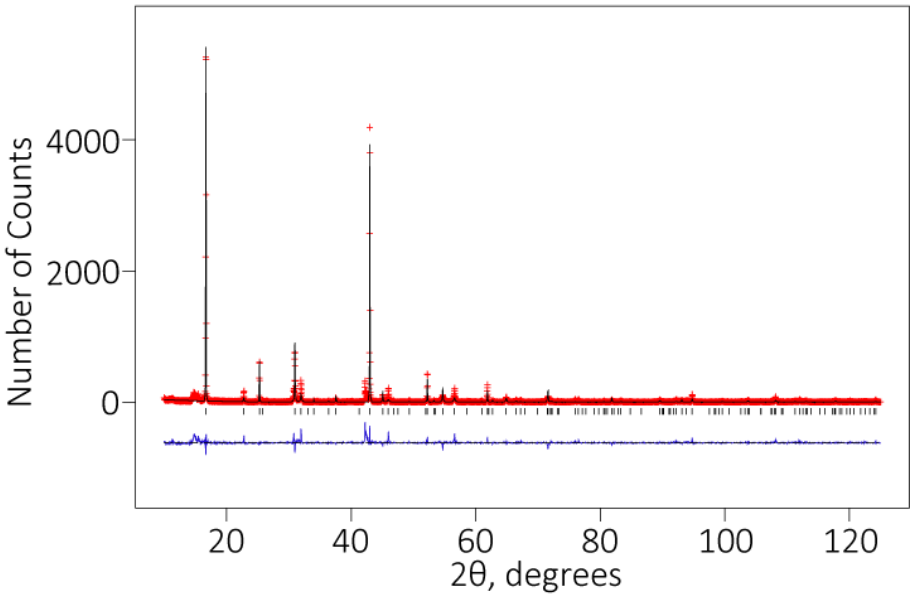

Figure B.15 *X-ray refinement of ground crystals of $Sr_3Ir_2O_7$ using the I4/mmm structural model with the data collected at a temperature of 400° C on the cool down from 800° C. χ^2=3.734; R_{wp}=0.4249.*

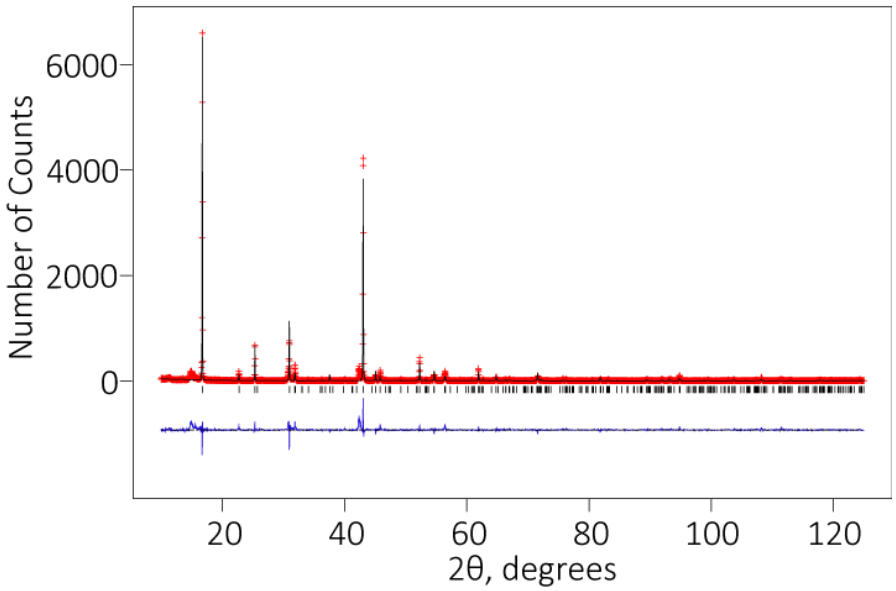

Figure B.16 *X-ray refinement of ground crystals of $Sr_3Ir_2O_7$ using the Bbcb structural model with the data collected at a temperature of 600° C on the warm up from room temperature. χ^2=3.976; R_{wp}=0.4280.*

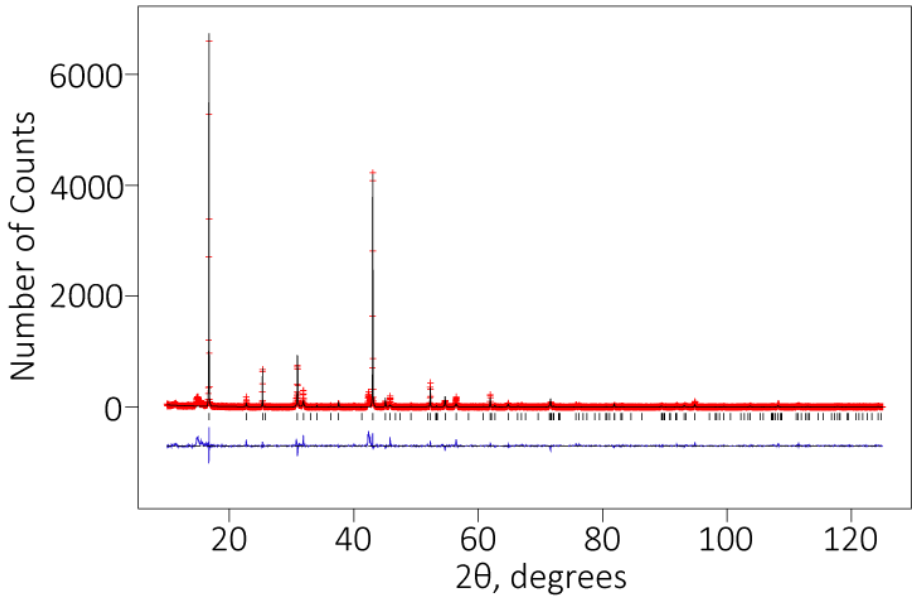

Figure B.17 *X-ray refinement of ground crystals of $Sr_3Ir_2O_7$ using the I4/mmm structural model with the data collected at a temperature of 600° C on the warm up from room temperature. χ^2=3.666; R_{wp}=0.4109.*

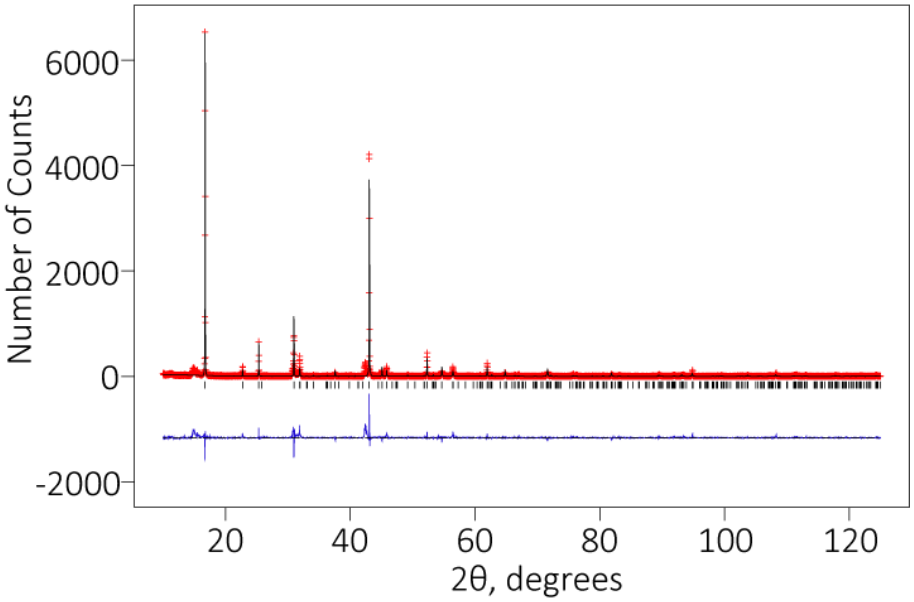

Figure B.18 *X-ray refinement of ground crystals of $Sr_3Ir_2O_7$ using the Bbcb structural model with the data collected at a temperature of 600° C on the cool down from 800° C. χ^2=4.199; R_{wp}=0.4399.*

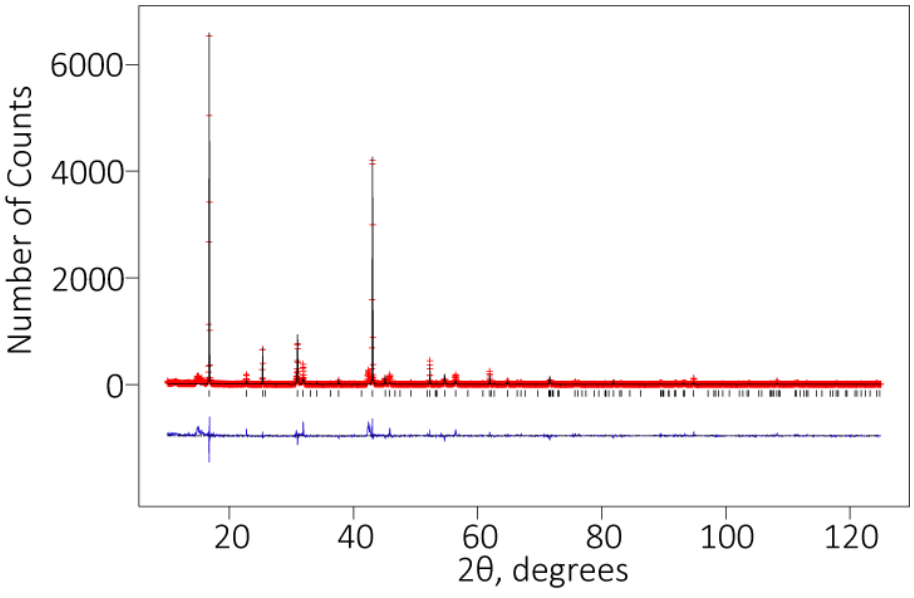

Figure B.19 *X-ray refinement of ground crystals of $Sr_3Ir_2O_7$ using the I4/mmm structural model with the data collected at a temperature of 600° C on the cool down from 800° C. χ^2=4.847; R_{wp}=0.4727.*

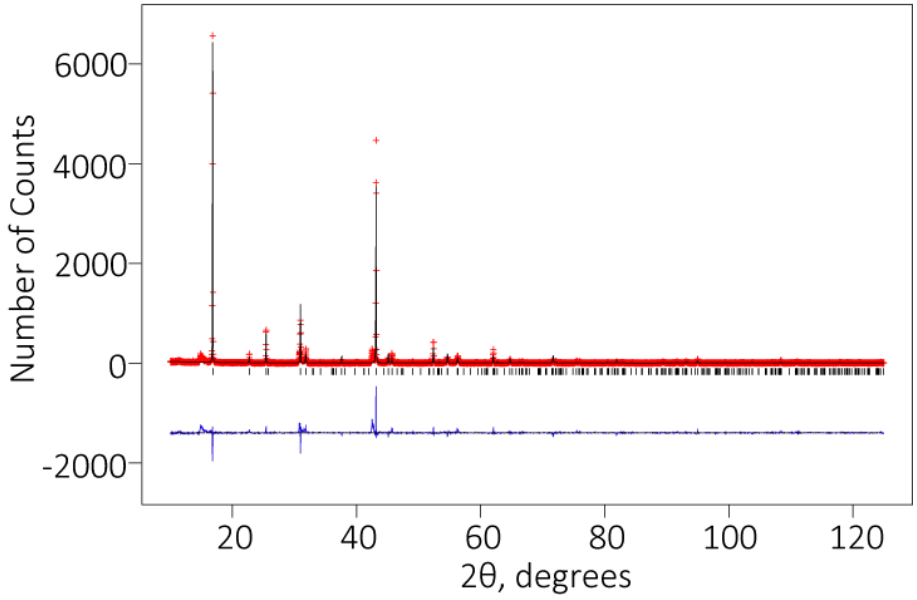

Figure B.20 *X-ray refinement of ground crystals of $Sr_3Ir_2O_7$ using the Bbcb structural model with the data collected at a temperature of 800° C on the warm up from room temperature. χ^2=3.872; R_{wp}=0.4273.*

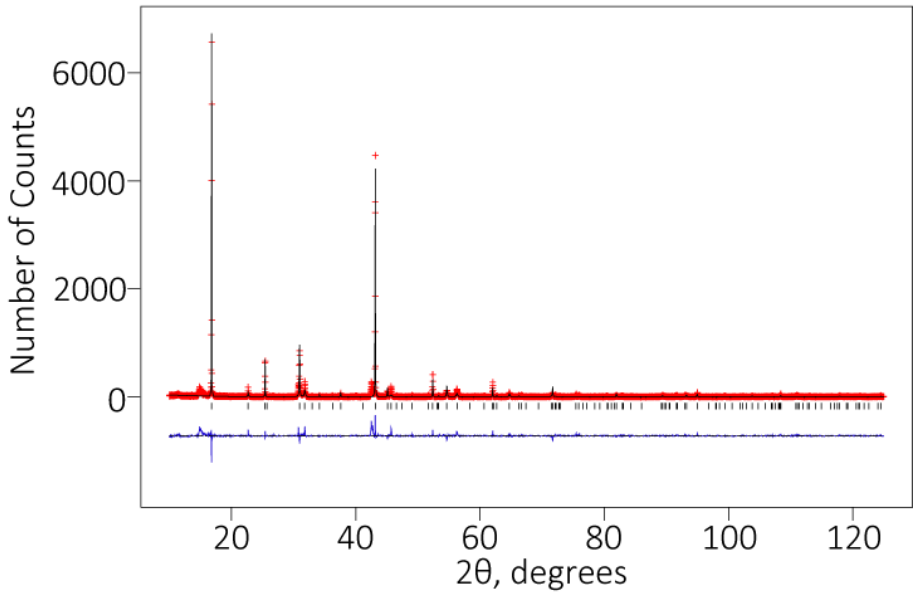

Figure B.21 *X-ray refinement of ground crystals of $Sr_3Ir_2O_7$ using the I4/mmm structural model with the data collected at a temperature of 800° C on the warm up from room temperature. χ^2=3.431; R_{wp}=0.4022.*

Atom	Wyckoff Symbol	x	y	z	B	Occupancy
Ir(1)	4e	0	0	0.09767(9)	0.041(1)	1
Sr(1)	2b	0.5	0.5	0	0.017(2)	1
Sr(2)	4e	0.5	0.5	0.1886(1)	0.011(2)	1
O(1)	4a	0	0	0	0.025	0.9157
O(2)	2e	0	0	0.1939	0.025	0.9157
O(3)	16n	0.1043	0.5	0.0960	0.025	0.4579

Table B.7 *Results from the Rietveld refinement on ground crystals of $Sr_3Ir_2O_7$ using the I4/mmm structural model with the data collected at a temperature of 24° C on the cool down from 800° C.*

Atom	Wyckoff Symbol	x	y	z	B	Occupancy
Ir(1)	8e	0.25	0.25	0.40280(8)	0.036(1)	1
Sr(1)	4a	0.25	0.25	0	0.026(1)	1
Sr(2)	8e	0.25	0.25	0.1881(1)	0.026(1)	1
O(1)	4b	0.25	0.25	0.5	0.025	0.9157
O(2)	8e	0.25	0.25	0.3048	0.025	0.9157
O(3)	16i	0.5308	-0.031	0.096400	0.025	0.9157

Table B.8 *Results from the Rietveld refinement on ground crystals of $Sr_3Ir_2O_7$ using the Bbcb structural model with the data collected at a temperature of 200° C on the warm up from room temperature.*

Atom	Wyckoff Symbol	x	y	z	B	Occupancy
Ir(1)	4e	0	0	0.09715(7)	0.032(1)	1
Sr(1)	2b	0.5	0.5	0	0.034(2)	1
Sr(2)	4e	0.5	0.5	0.1879(1)	0.025(2)	1
O(1)	4a	0	0	0	0.025	0.9157
O(2)	2e	0	0	0.1939	0.025	0.9157
O(3)	16n	0.1043	0.5	0.0960	0.025	0.4579

Table B.9 *Results from the Rietveld refinement on ground crystals of $Sr_3Ir_2O_7$ using the I4/mmm structural model with the data collected at a temperature of 200° C on the warm up from room temperature.*

Atom	Wyckoff Symbol	x	y	z	B	Occupancy
Ir(1)	8e	0.25	0.25	0.40257(8)	0.040(1)	1
Sr(1)	4a	0.25	0.25	0	0.023(1)	1
Sr(2)	8e	0.25	0.25	0.1881(1)	0.023(1)	1
O(1)	4b	0.25	0.25	0.5	0.025	0.9157
O(2)	8e	0.25	0.25	0.3048	0.025	0.9157
O(3)	16i	0.5308	-0.031	0.096400	0.025	0.9157

Table B.10 *Results from the Rietveld refinement on ground crystals of $Sr_3Ir_2O_7$ using the Bbcb structural model with the data collected at a temperature of 200° C on the cool down from 800° C.*

Atom	Wyckoff Symbol	x	y	z	B	Occupancy
Ir(1)	4e	0	0	0.09738(8)	0.041(1)	1
Sr(1)	2b	0.5	0.5	0	0.031(2)	1
Sr(2)	4e	0.5	0.5	0.1881(1)	0.021(2)	1
O(1)	4a	0	0	0	0.025	0.9157
O(2)	2e	0	0	0.1939	0.025	0.9157
O(3)	16n	0.1043	0.5	0.0960	0.025	0.4579

Table B.11 *Results from the Rietveld refinement on ground crystals of $Sr_3Ir_2O_7$ using the I4/mmm structural model with the data collected at a temperature of 200° C on the cool down from 800° C.*

Atom	Wyckoff Symbol	x	y	z	B	Occupancy
Ir(1)	8e	0.25	0.25	0.40265(8)	0.037(1)	1
Sr(1)	4a	0.25	0.25	0	0.036(1)	1
Sr(2)	8e	0.25	0.25	0.1872(1)	0.036(1)	1
O(1)	4b	0.25	0.25	0.5	0.025	0.9157
O(2)	8e	0.25	0.25	0.3048	0.025	0.9157
O(3)	16i	0.5308	-0.031	0.096400	0.025	0.9157

Table B.12 *Results from the Rietveld refinement on ground crystals of $Sr_3Ir_2O_7$ using the Bbcb structural model with the data collected at a temperature of 400° C on the warm up from room temperature.*

Atom	Wyckoff Symbol	x	y	z	B	Occupancy
Ir(1)	4e	0	0	0.09735(7)	0.037(1)	1
Sr(1)	2b	0.5	0.5	0	0.040(2)	1
Sr(2)	4e	0.5	0.5	0.1874(1)	0.036(2)	1
O(1)	4a	0	0	0	0.025	0.9157
O(2)	2e	0	0	0.1939	0.025	0.9157
O(3)	16n	0.1043	0.5	0.0960	0.025	0.4579

Table B.13 *Results from the Rietveld refinement on ground crystals of $Sr_3Ir_2O_7$ using the I4/mmm structural model with the data collected at a temperature of 400° C on the warm up from room temperature.*

Atom	Wyckoff Symbol	x	y	z	B	Occupancy
Ir(1)	8e	0.25	0.25	0.40249(9)	0.033(1)	1
Sr(1)	4a	0.25	0.25	0	0.041(3)	1
Sr(2)	8e	0.25	0.25	0.1870(1)	0.030(2)	1
O(1)	4b	0.25	0.25	0.5	0.025	0.9157
O(2)	8e	0.25	0.25	0.3048	0.025	0.9157
O(3)	16i	0.5308	-0.031	0.096400	0.025	0.9157

Table B.14 *Results from the Rietveld refinement on ground crystals of $Sr_3Ir_2O_7$ using the Bbcb structural model with the data collected at a temperature of 400° C on the cool down from 800° C.*

Atom	Wyckoff Symbol	x	y	z	B	Occupancy
Ir(1)	4e	0	0	0.09748(8)	0.040(1)	1
Sr(1)	2b	0.5	0.5	0	0.047(3)	1
Sr(2)	4e	0.5	0.5	0.1873(1)	0.034(2)	1
O(1)	4a	0	0	0	0.025	0.9157
O(2)	2e	0	0	0.1939	0.025	0.9157
O(3)	16n	0.1043	0.5	0.0960	0.025	0.4579

Table B.15 *Results from the Rietveld refinement on ground crystals of $Sr_3Ir_2O_7$ using the I4/mmm structural model with the data collected at a temperature of 400° C on the cool down from 800° C.*

Atom	Wyckoff Symbol	x	y	z	B	Occupancy
Ir(1)	8e	0.25	0.25	0.40242(8)	0.042(1)	1
Sr(1)	4a	0.25	0.25	0	0.043(2)	1
Sr(2)	8e	0.25	0.25	0.1870(1)	0.043(2)	1
O(1)	4b	0.25	0.25	0.5	0.025	0.9157
O(2)	8e	0.25	0.25	0.3048	0.025	0.9157
O(3)	16i	0.5308	-0.031	0.096400	0.025	0.9157

Table B.16 *Results from the Rietveld refinement on ground crystals of $Sr_3Ir_2O_7$ using the Bbcb structural model with the data collected at a temperature of 600° C on the warm up from room temperature.*

Atom	Wyckoff Symbol	x	y	z	B	Occupancy
Ir(1)	4e	0	0	0.09750(7)	0.047(1)	1
Sr(1)	2b	0.5	0.5	0	0.053(3)	1
Sr(2)	4e	0.5	0.5	0.1873(1)	0.041(2)	1
O(1)	4a	0	0	0	0.025	0.9157
O(2)	2e	0	0	0.1939	0.025	0.9157
O(3)	16n	0.1043	0.5	0.0960	0.025	0.4579

Table B.17 *Results from the Rietveld refinement on ground crystals of $Sr_3Ir_2O_7$ using the I4/mmm structural model with the data collected at a temperature of 600° C on the cool down from 800° C.*

Atom	Wyckoff Symbol	x	y	z	B	Occupancy
Ir(1)	8e	0.25	0.25	0.40227(9)	0.042(1)	1
Sr(1)	4a	0.25	0.25	0	0.043(2)	1
Sr(2)	8e	0.25	0.25	0.1872(1)	0.043(2)	1
O(1)	4b	0.25	0.25	0.5	0.025	0.9157
O(2)	8e	0.25	0.25	0.3048	0.025	0.9157
O(3)	16i	0.5308	-0.031	0.096400	0.025	0.9157

Table B.18 *Results from the Rietveld refinement on ground crystals of $Sr_3Ir_2O_7$ using the Bbcb structural model with the data collected at a temperature of 600° C on the cool down from 800° C.*

Atom	Wyckoff Symbol	x	y	z	B	Occupancy
Ir(1)	4e	0	0	0.09775(9)	0.047(1)	1
Sr(1)	2b	0.5	0.5	0	0.053(3)	1
Sr(2)	4e	0.5	0.5	0.1875(1)	0.041(2)	1
O(1)	4a	0	0	0	0.025	0.9157
O(2)	2e	0	0	0.1939	0.025	0.9157
O(3)	16n	0.1043	0.5	0.0960	0.025	0.4579

Table B.19 *Results from the Rietveld refinement on ground crystals of $Sr_3Ir_2O_7$ using the I4/mmm structural model with the data collected at a temperature of 600° C on the cool down from 800° C.*

Atom	Wyckoff Symbol	x	y	z	B	Occupancy
Ir(1)	8e	0.25	0.25	0.40237(9)	0.044(1)	1
Sr(1)	4a	0.25	0.25	0	0.044(2)	1
Sr(2)	8e	0.25	0.25	0.1876(1)	0.044(2)	1
O(1)	4b	0.25	0.25	0.5	0.025	0.9157
O(2)	8e	0.25	0.25	0.3048	0.025	0.9157
O(3)	16i	0.5308	-0.031	0.096400	0.025	0.9157

Table B.20 *Results from the Rietveld refinement on ground crystals of $Sr_3Ir_2O_7$ using the Bbcb structural model with the data collected at a temperature of 800° C on the warm up from room temperature.*

Atom	Wyckoff Symbol	x	y	z	B	Occupancy
Ir(1)	4e	0	0	0.09749(7)	0.050(1)	1
Sr(1)	2b	0.5	0.5	0	0.060(3)	1
Sr(2)	4e	0.5	0.5	0.1880(1)	0.036(2)	1
O(1)	4a	0	0	0	0.025	0.9157
O(2)	2e	0	0	0.1939	0.025	0.9157
O(3)	16n	0.1043	0.5	0.0960	0.025	0.4579

Table B.21 *Results from the Rietveld refinement on ground crystals of $Sr_3Ir_2O_7$ using the I4/mmm structural model with the data collected at a temperature of 800° C on the warm up from room temperature.*

B.3 Powder x-ray diffraction data of all $(Sr_{(1-x)}La_x)_3Ir_2O_7$ compounds

Figures B.22, B.23, B.24, B.25, B.26, B.27, B.28 and B.29 are Rietveld refinements of x-ray diffraction data collected on ground crystals from batches of $Sr_3Ir_2O_7$ that have been doped with varying amounts of lanthanum (see section 4.6). In all of the figures the red crosses mark the observed data, the solid black line is the calculated profile and the solid blue line is the difference curve. The black tick marks show the position of the Bragg reflections of $(Sr_{(1-x)}La_x)_3Ir_2O_7$. In some cases an additional set of green tick marks indicate the Bragg reflections of an impurity phase, the percentage weight and identy of which is given in the figure caption. The χ^2 and R_{wp} values of each refinement, which give an indication of the goodness of fit, are also given in the figure caption. All the diffraction data in this section have been refined to both the Bbcb and I4/mmm structural models. Key results from each of these refinements are shown in tables B.22, B.23, B.24, B.25, B.26, B.27, B.28 and B.29.

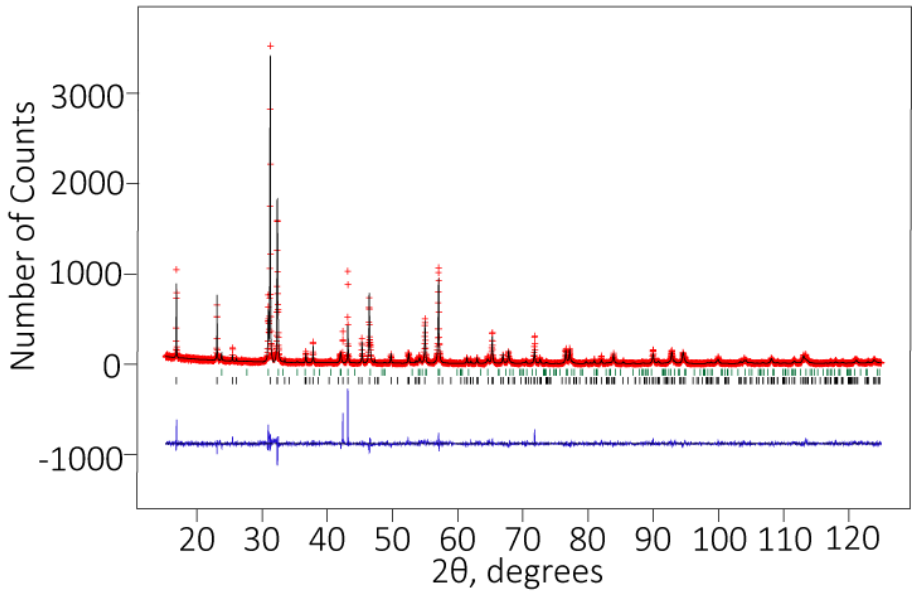

Figure B.22 *X-ray refinement of ground crystals of $(Sr_{(1-x)}La_x)_3Ir_2O_7$ from batch number SLIO#F5 where* x = *0.0097 using the Bbcb structural model. There is an additional impurity phase of Sr_2IrO_4 in the diffraction pattern that makes up around 26% of the sample by weight. χ^2=1.912; R_{wp}=0.2168.*

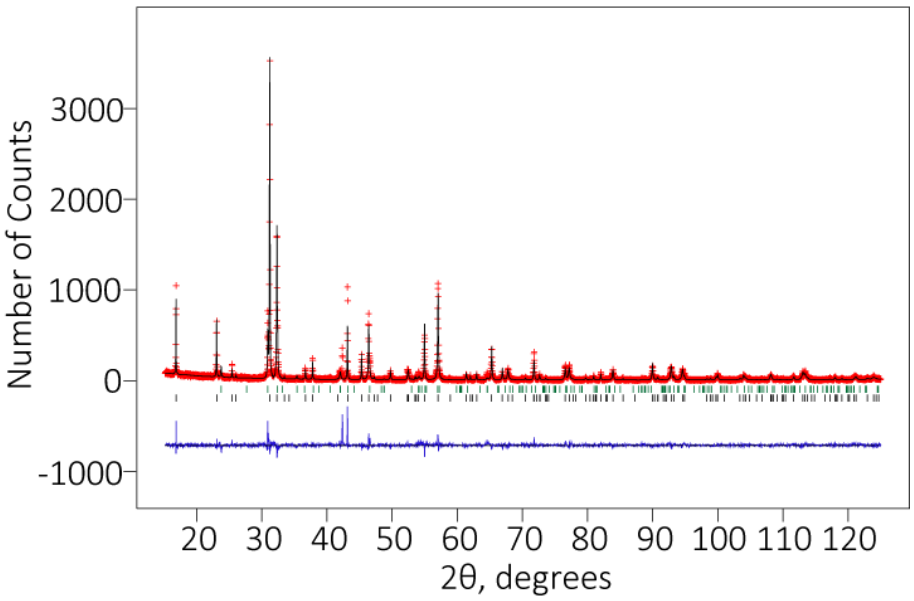

Figure B.23 *X-ray refinement of ground crystals of* $(Sr_{(1-x)}La_x)_3Ir_2O_7$ *from batch number SLIO#F5 where* x = *0.0097 using the I4/mmm structural model. There is an additional impurity phase of* Sr_2IrO_4 *in the diffraction pattern that makes up around 30% of the sample by weight.* χ^2*=1.974;* R_{wp}*=0.2202.*

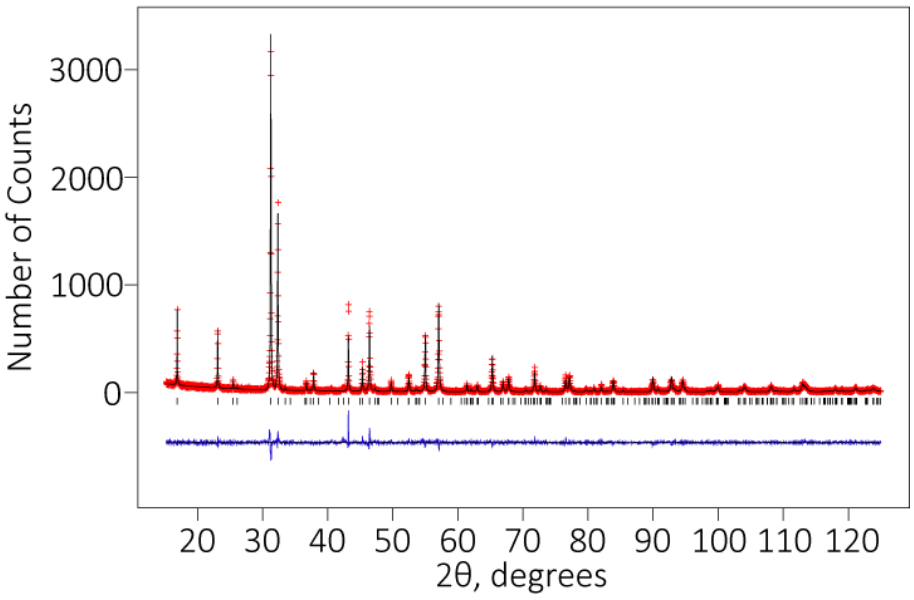

Figure B.24 *X-ray refinement of ground crystals of* $(Sr_{(1-x)}La_x)_3Ir_2O_7$ *from batch number SLIO#F7 where* x = *0.0478 using the Bbcb structural model.* χ^2*=1.366;* R_{wp}*=0.1905*

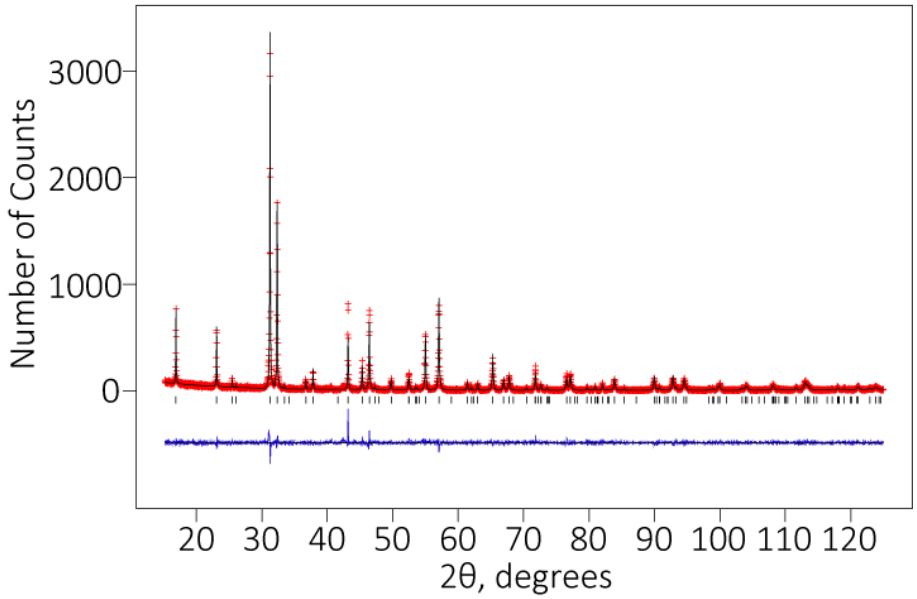

Figure B.25 *X-ray refinement of ground crystals of* $(Sr_{(1-x)}La_x)_3Ir_2O_7$ *from batch number SLIO#F7 where* x = *0.0478 using the I4/mmm structural model.* χ^2*=1.342;* R_{wp}*=0.1888.*

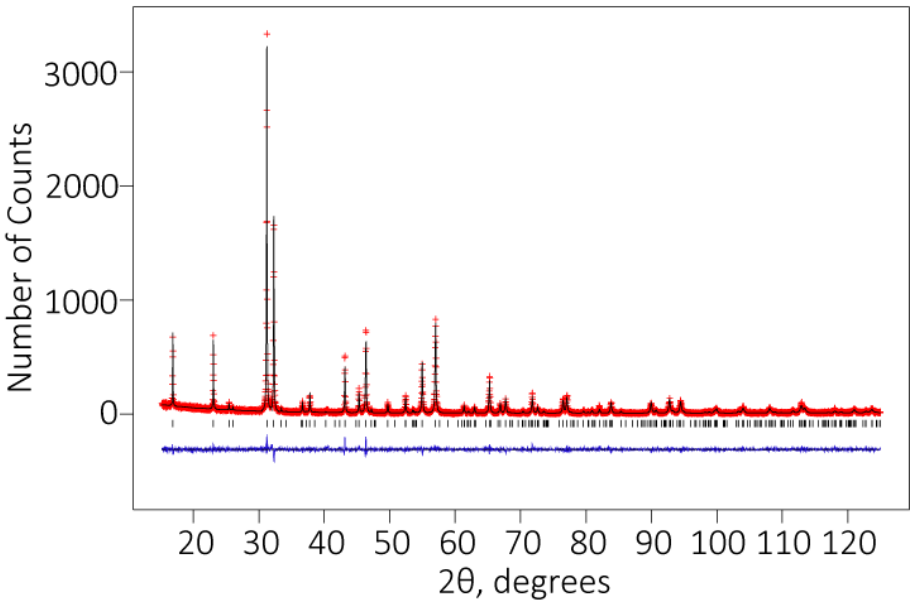

Figure B.26 *X-ray refinement of ground crystals of* $(Sr_{(1-x)}La_x)_3Ir_2O_7$ *from batch number SLIO#F3 where* x = *0.0720 using the Bbcb structural model.* χ^2*=1.128;* R_{wp}*=0.1767.*

Atom	Wyckoff Symbol	x	y	z	B	Occupancy
Ir(1)	8e	0.25	0.25	0.4020(1)	0.0061(4)	1
Sr(1)	4a	0.25	0.25	0	0.0045(13)	0.951
Sr(2)	8e	0.25	0.25	0.1876(1)	0.012(1)	0.951
La(1)	4a	0.25	0.25	0	0.0045(13)	0.009
La(2)	8e	0.25	0.25	0.1876(1)	0.012(1)	0.009
O(1)	4b	0.25	0.25	0.5	0.058(6)	0.907
O(2)	8e	0.25	0.25	0.3048	0.016(7)	0.907
O(3)	16i	0.5308	-0.031	0.096400	0.033(6)	0.907

Table B.22 *Results from the Rietveld refinement on ground crystals of* $(Sr_{(1-x)}La_x)_3Ir_2O_7$ *from batch number SLIO#F5 where* x = *0.0097 using the Bbcb structural model.*

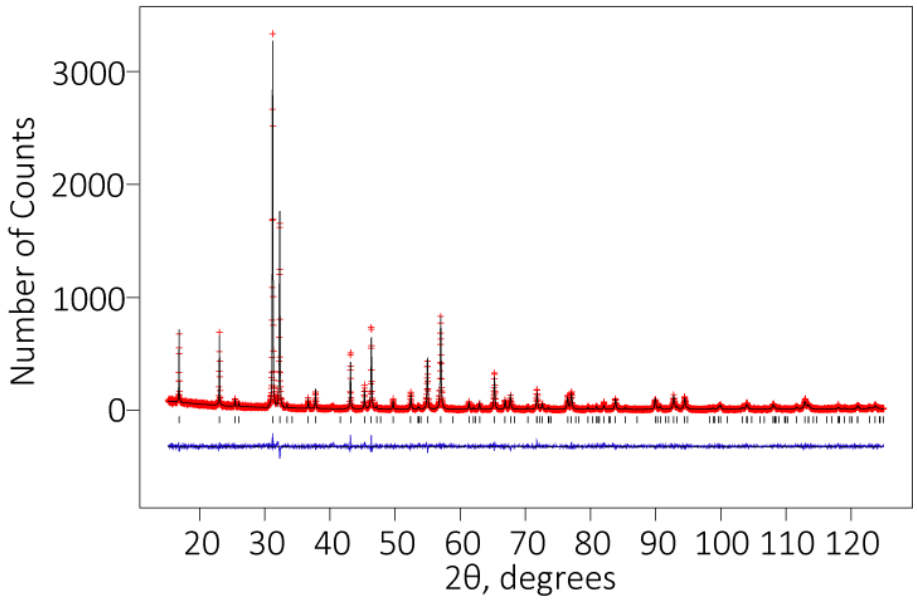

Figure B.27 *X-ray refinement of ground crystals of* $(Sr_{(1-x)}La_x)_3Ir_2O_7$ *from batch number SLIO#F3 where* x = *0.0720 using the I4/mmm structural model.* χ^2*=1.131;* R_{wp}*=0.1769.*

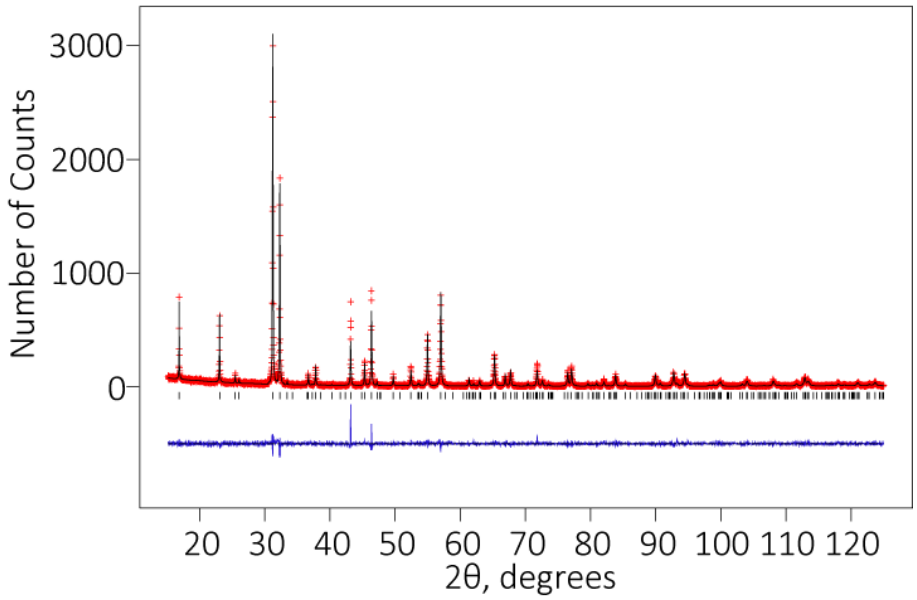

Figure B.28 *X-ray refinement of ground crystals of* $(Sr_{(1-x)}La_x)_3Ir_2O_7$ *from batch number SLIO#F6 where* x = *0.0757 using the Bbcb structural model.* χ^2*=1.227;* R_{wp}*=0.1857.*

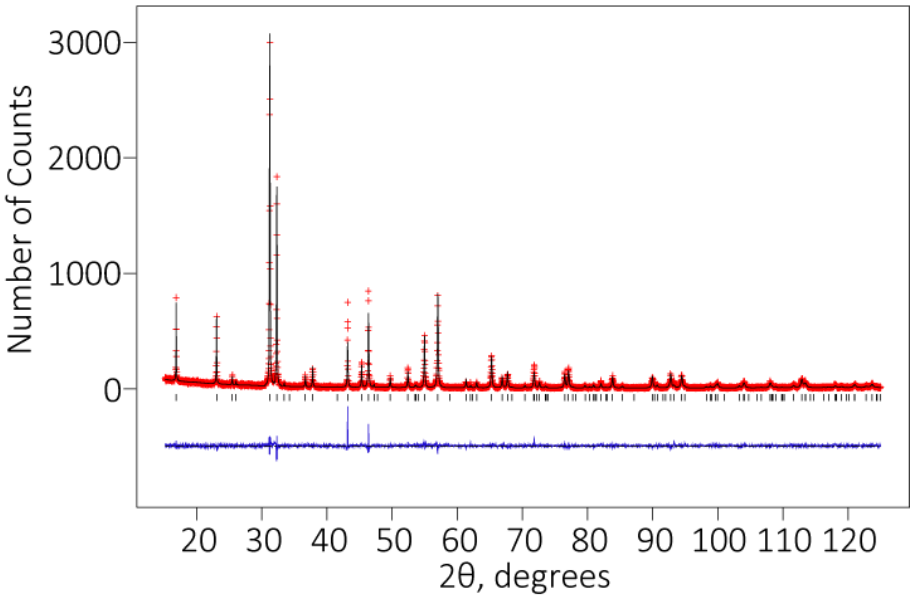

Figure B.29 *X-ray refinement of ground crystals of* $(Sr_{(1-x)}La_x)_3Ir_2O_7$ *from batch number SLIO#F6 where* x = *0.0757 using the I4/mmm structural model.* χ^2*=1.212;* R_{wp}*=0.1845.*

Atom	Wyckoff Symbol	x	y	z	B	Occupancy
Ir(1)	4e	0	0	0.09805(9)	0.0068(4)	1
Sr(1)	2b	0.5	0.5	0	0.0065(12)	0.951
Sr(2)	4e	0.5	0.5	0.1880(1)	0.012(1)	0.951
La(1)	2b	0.5	0.5	0	0.0065(12)	0.009
La(2)	4e	0.5	0.5	0.1880(1)	0.012(1)	0.009
O(1)	4a	0	0	0	0.038(11)	0.907
O(2)	2e	0	0	0.1939	0.027(8)	0.907
O(3)	16n	0.1043	0.5	0.0960	0.0025	0.454

Table B.23 *Results from the Rietveld refinement on ground crystals of* $(Sr_{(1-x)}La_x)_3Ir_2O_7$*from batch number SLIO#F5 where* x = *0.0097 using the I4/mmm structural model.*

Atom	Wyckoff Symbol	x	y	z	B	Occupancy
Ir(1)	8e	0.25	0.25	0.40260(7)	0.0114(4)	1
Sr(1)	4a	0.25	0.25	0	0.0092(11)	0.914
Sr(2)	8e	0.25	0.25	0.1877(1)	0.0103(9)	0.914
La(1)	4a	0.25	0.25	0	0.0092(11)	0.046
La(2)	8e	0.25	0.25	0.1877(1)	0.0103(9)	0.046
O(1)	4b	0.25	0.25	0.5	0.006(6)	0.907
O(2)	8e	0.25	0.25	0.3022(7)	0.015(5)	0.907
O(3)	16i	0.5308	-0.031	0.096400	0.027(4)	0.907

Table B.24 *Results from the Rietveld refinement on ground crystals of* $(Sr_{(1-x)}La_x)_3Ir_2O_7$ *from batch number SLIO#F7 where* x = *0.0478 using the Bbcb structural model.*

Atom	Wyckoff Symbol	x	y	z	B	Occupancy
Ir(1)	4e	0	0	0.09744(7)	0.0114(4)	1
Sr(1)	2b	0.5	0.5	0	0.0098(11)	0.914
Sr(2)	4e	0.5	0.5	0.1876(1)	0.0114(9)	0.914
La(1)	2b	0.5	0.5	0	0.0098(11)	0.046
La(2)	4e	0.5	0.5	0.1876(1)	0.0114(9)	0.046
O(1)	4a	0	0	0	0.012(7)	0.907
O(2)	2e	0	0	0.1939	0.009(5)	0.907
O(3)	16n	0.1043	0.5	0.0960	0.0025	0.454

Table B.25 *Results from the Rietveld refinement on ground crystals of* $(Sr_{(1-x)}La_x)_3Ir_2O_7$*from batch number SLIO#F7 where* x = *0.0478 using the I4/mmm structural model.*

Atom	Wyckoff Symbol	x	y	z	B	Occupancy
Ir(1)	8e	0.25	0.25	0.40245(7)	0.0093(3)	1
Sr(1)	4a	0.25	0.25	0	0.011(1)	0.891
Sr(2)	8e	0.25	0.25	0.187572	0.018(9)	0.891
La(1)	4a	0.25	0.25	0	0.011(1)	0.069
La(2)	8e	0.25	0.25	0.187572(12)	0.018(9)	0.069
O(1)	4a	0.25	0.25	0.5	0.025	0.907
O(2)	8e	0.25	0.25	0.3021(8)	0.025	0.907
O(3)	16i	0.5308	-0.031	0.096400	0.037(4)	0.907

Table B.26 *Results from the Rietveld refinement on ground crystals of* $(Sr_{(1-x)}La_x)_3Ir_2O_7$ *from batch number SLIO#F3 where* x = *0.0720 using the Bbcb structural model.*

Atom	Wyckoff Symbol	x	y	z	B	Occupancy
Ir(1)	4e	0	0	0.09731(7)	0.01305(3)	1
Sr(1)	2b	0.5	0.5	0	0.013(8)	0.891
Sr(2)	4e	0.5	0.5	0.18764(9)	0.015(8)	0.891
La(1)	2b	0.5	0.5	0	0.013(8)	0.069
La(2)	4e	0.5	0.5	0.18764(9)	0.015(8)	0.069
O(1)	4a	0	0	0	0.025	0.907
O(2)	2e	0	0	0.1939	0.025	0.907
O(3)	16n	0.1043	0.5	0.0960	0.0024(32)	0.454

Table B.27 *Results from the Rietveld refinement on ground crystals of $(Sr_{(1-x)}La_x)_3Ir_2O_7$ from batch number SLIO#F3 where* x *= 0.0720 using the I4/mmm structural model.*

Atom	Wyckoff Symbol	x	y	z	B	Occupancy
Ir(1)	8e	0.25	0.25	0.40224(8)	0.0105(3)	1
Sr(1)	4a	0.25	0.25	0	0.0091(11)	0.887
Sr(2)	8e	0.25	0.25	0.1869(1)	0.014(1)	0.887
La(1)	4a	0.25	0.25	0	0.0091(11)	0.073
La(2)	8e	0.25	0.25	0.1869(1)	0.014(1)	0.073
O(1)	4b	0.25	0.25	0.5	0.020(7)	0.907
O(2)	8e	0.25	0.25	0.3017(8)	0.025	0.907
O(3)	16i	0.5308	-0.031	0.0964	0.025	0.907

Table B.28 *Results from the Rietveld refinement on ground crystals of $(Sr_{(1-x)}La_x)_3Ir_2O_7$ from batch number SLIO#F6 where* x *= 0.0757 using the Bbcb structural model.*

Atom	Wyckoff Symbol	x	y	z	B	Occupancy
Ir(1)	4e	0	0	0.09770(8)	0.0108(4)	1
Sr(1)	2b	0.5	0.5	0	0.010(1)	0.887
Sr(2)	4e	0.5	0.5	0.18770(1)	0.008(6)	0.887
La(1)	2b	0.5	0.5	0	0.010(1)	0.073
La(2)	4e	0.5	0.5	0.18770(1)	0.008(6)	0.073
O(1)	4a	0	0	0	0.0078(62)	0.907
O(2)	2e	0	0	0.1983(9)	0.044(7)	0.907
O(3)	16n	0.1043	0.5	0.0960	0.016(4)	0.454

Table B.29 *Results from the Rietveld refinement on ground crystals of $(Sr_{(1-x)}La_x)_3Ir_2O_7$ from batch number SLIO#F6 where* x *= 0.0757 using the I4/mmm structural model.*

B.4 Neutron diffraction refinements from the HRPD experiment on the structure of $K_2CaPt_{3-\delta}O_6$

Figures B.30, B.31, B.32 and B.33 show all the refinements of the powder neutron diffraction data collected on $K_2CaPt_{3-\delta}O_6$ using HRPD at ISIS at 4K, 100K, 200K and 300K. HRPD has three detector banks as detailed in section 3.2.7 so each figure shows the data collected from each data bank seperately, as labelled. There are numerous peaks that do not fit the current structural model, which are starred. As the data was collected on powder from the bottom of the flux reaction it was thought that these peaks were from an unknown impurity, however it is possible that some of these peaks may arise from the superstructure. Key results from each of these refinements are shown in tables B.30, B.31, B.32 and B.33 and the unit cell parameters as a function of temperature are shown in table B.34.

Atom	Wyckoff Symbol	x	y	z	B	Occupancy
Pt(1)	3a	2/3	1/3	1/3	0.00659(75)	0.868(11)
Ca(1)	6c	2/3	1/3	0.5	0.1018(28)	1/6
K(1)	6c	2/3	1/3	0.5	0.1018(28)	1/3
O(1)	6c	0	0	0.390642(84)	0.0967(79)	1

Table B.30 *Results from the Rietveld refinement of the HRPD data collected at 4K.*

Atom	Wyckoff Symbol	x	y	z	B	Occupancy
Pt(1)	3a	2/3	1/3	1/3	0.00518(67)	0.879(11)
Ca(1)	6c	2/3	1/3	0.5	0.1027(26)	1/6
K(1)	6c	2/3	1/3	0.5	0.1027(26)	1/3
O(1)	6c	0	0	0.390573(77)	0.0906(73)	1

Table B.31 *Results from the Rietveld refinement of the HRPD data collected at 100K.*

Atom	Wyckoff Symbol	x	y	z	B	Occupancy
Pt(1)	3a	2/3	1/3	1/3	0.00646(69)	0.869(11)
Ca(1)	6c	2/3	1/3	0.5	0.1181(30)	1/6
K(1)	6c	2/3	1/3	0.5	0.1181(30)	1/3
O(1)	6c	0	0	0.390616(80)	0.01111(79)	1

Table B.32 *Results from the Rietveld refinement of the HRPD data collected at 200K.*

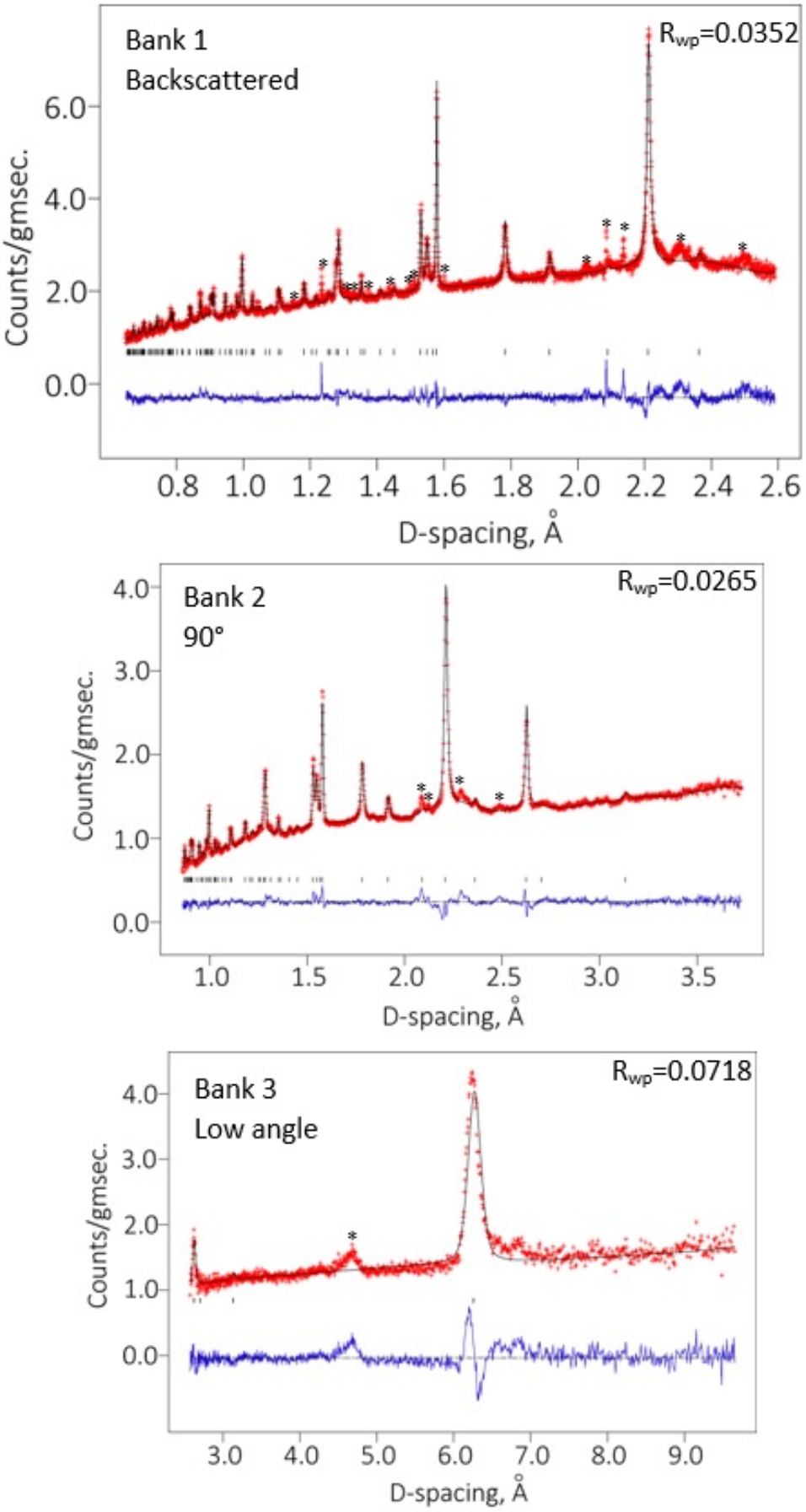

Figure B.30 *Rietveld refinement of the powder neutron diffraction data collected on $K_2CaPt_3O_6$ at 4K using HRPD at ISIS, using the data from all three detector banks, to the structural model determined by single crystal x-ray diffraction. The starred peaks are those not accounted for by the current structural model. For this set of refinements the total χ^2 value is 6.528.*

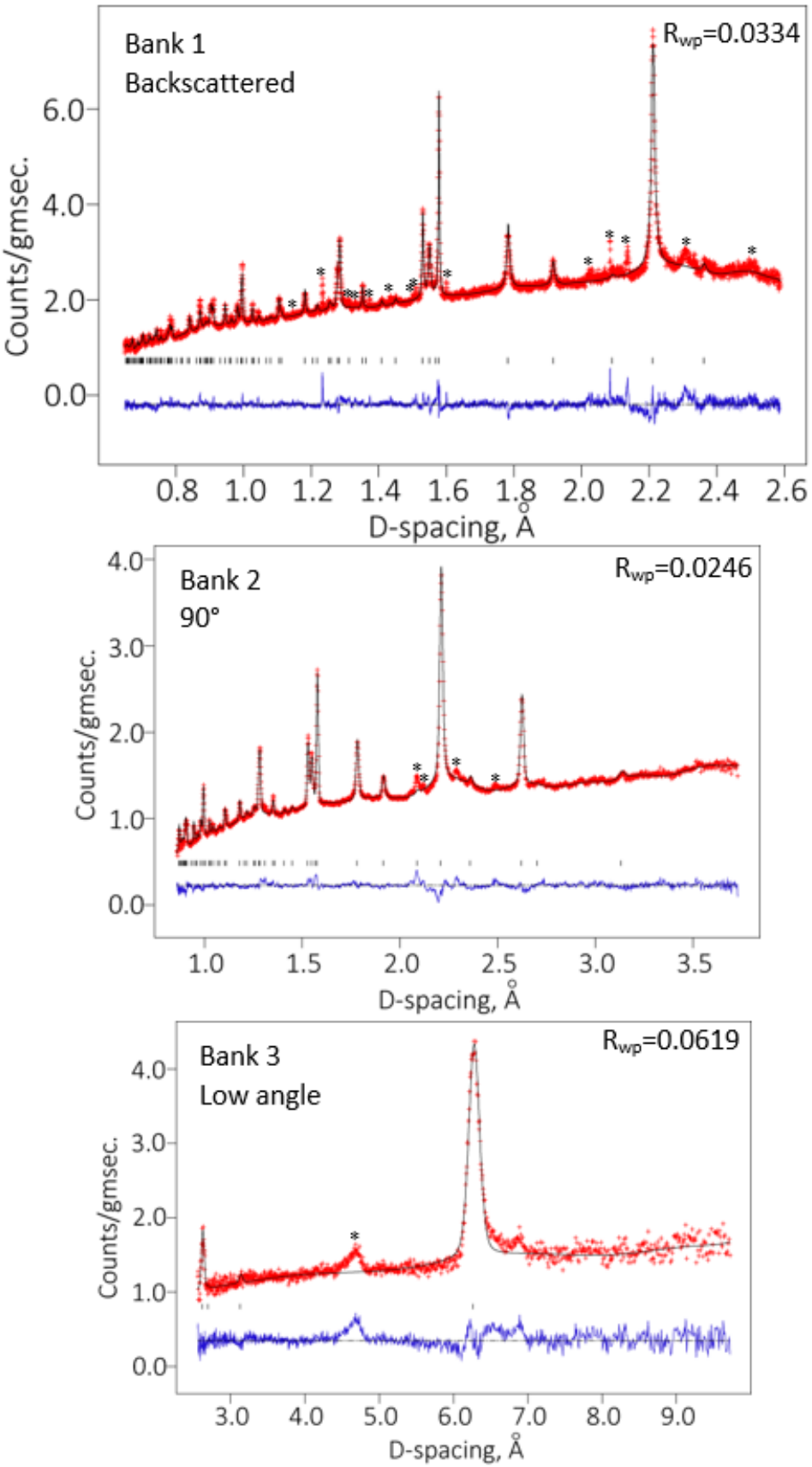

Figure B.31 *Rietveld refinement of the powder neutron diffraction data collected on $K_2CaPt_3O_6$ at 100K using HRPD at ISIS, using the data from all three detector banks, to the structural model determined by single crystal x-ray diffraction. The starred peaks are those not accounted for by the current structural model. For this set of refinements the total χ^2 value is 5.659.*

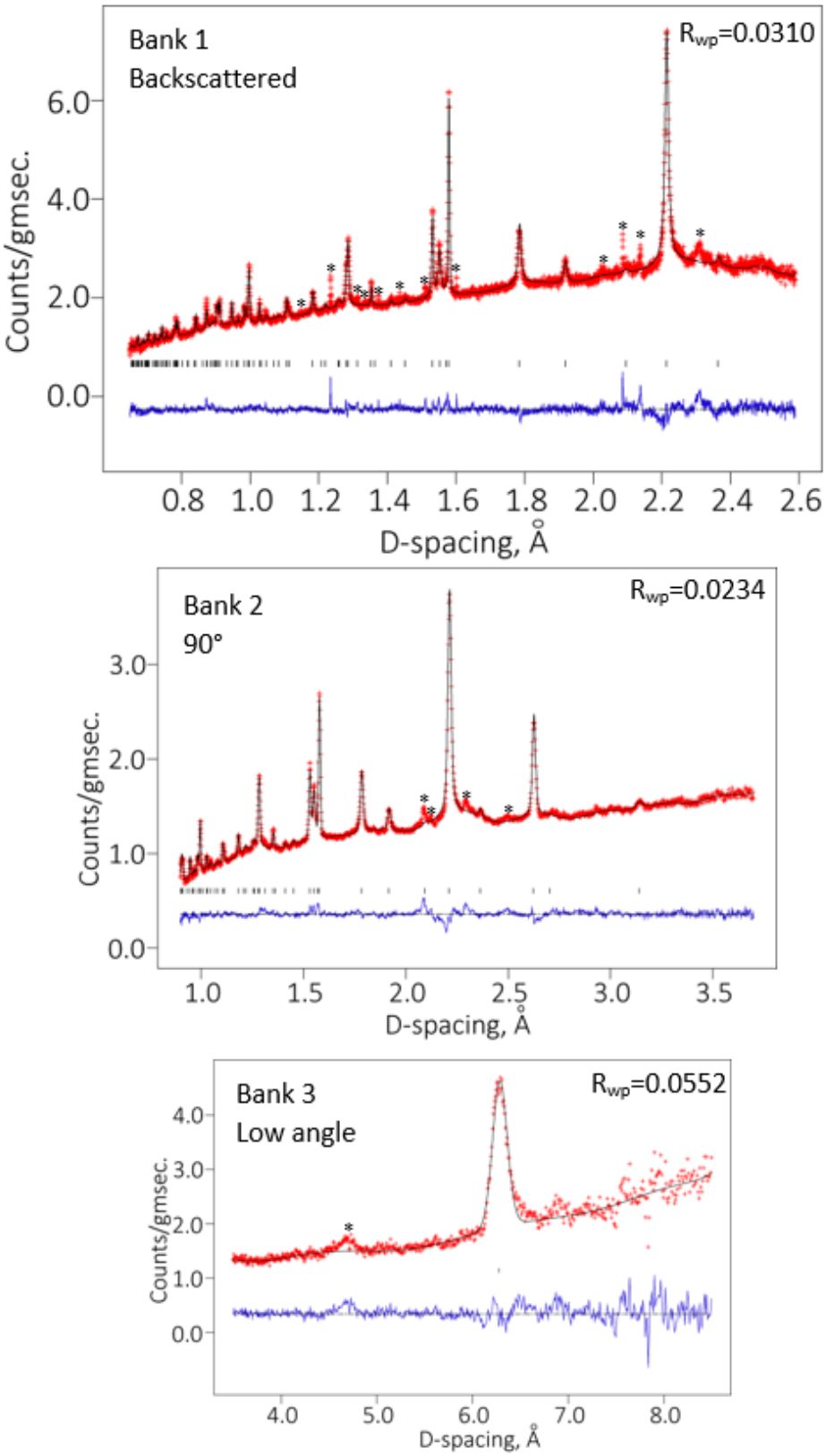

Figure B.32 *Rietveld refinement of the powder neutron diffraction data collected on $K_2CaPt_3O_6$ at 200K using HRPD at ISIS, using the data from all three detector banks, to the structural model determined by single crystal x-ray diffraction. The starred peaks are those not accounted for by the current structural model. For this set of refinements the total χ^2 value is 5.188.*

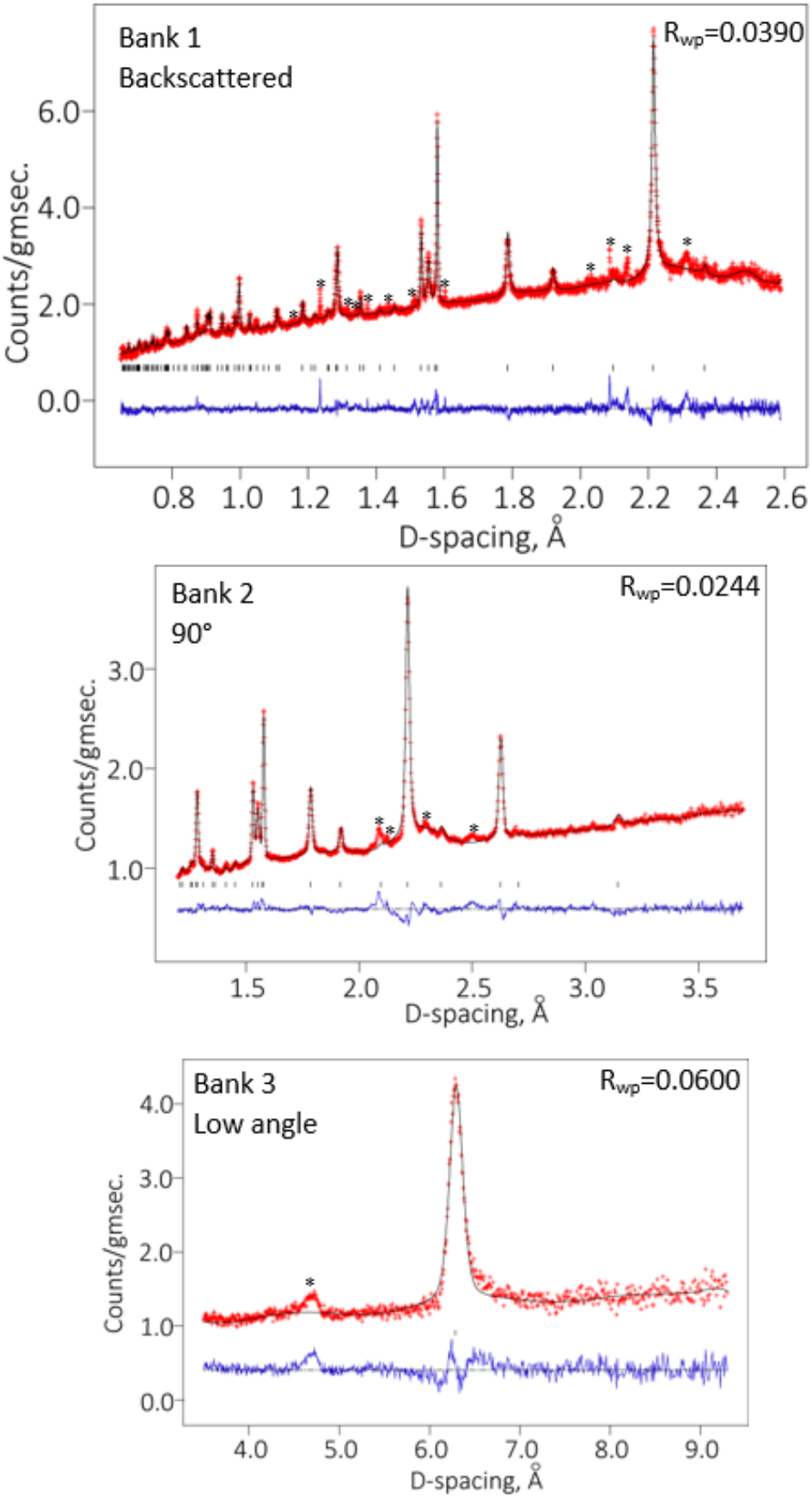

Figure B.33 *Rietveld refinement of the powder neutron diffraction data collected on $K_2CaPt_3O_6$ at 300K using HRPD at ISIS, using the data from all three detector banks, to the structural model determined by single crystal x-ray diffraction. The starred peaks are those not accounted for by the current structural model. For this set of refinements the total χ^2 value is 4.658.*

Atom	Wyckoff Symbol	x	y	z	B	Occupancy
Pt(1)	3a	2/3	1/3	1/3	0.00605(72)	0.909(11)
Ca(1)	6c	2/3	1/3	0.5	0.1142(28)	1/6
K(1)	6c	2/3	1/3	0.5	0.1142(28)	1/3
O(1)	6c	0	0	0.390267(85)	0.01074(84)	1

Table B.33 *Results from the Rietveld refinement of the HRPD data collected at 300K.*

Temperature (K)	a ($\mathring{A}$)	c ($\mathring{A}$)	V ($\mathring{A}^3$)
4	3.154891(53)	18.80578(80)	162.103(7)
100	3.15481(15)	18.8137(12)	162.163(21)
200	3.15814(20)	18.8561(15)	162.871(28)
300	3.15760(14)	18.8747(12)	162.976(20)

Table B.34 *The refined lattice parameters and unit cell volume of $K_2CaPt_{3-\delta}O_6$ as a function of temperature.*

B.5 Powder x-ray diffraction data of all $(K_{\frac{2}{3}}Ca_{\frac{1}{3}})_{(1-\delta)}Pt_yCu_xO_2$ compounds

Figure B.34 is the Rietveld refinement of the powder x-ray diffraction data collected on ground up crystals of $K_{\frac{2}{3}}Ca_{\frac{1}{3}}Pt_{3-\delta}O_6$ and key parameters from this refinement are shown in table B.35. Figures B.35, B.36, B.37, B.38, B.39 and B.40 are x-ray powder diffraction refinements of data collected on ground up crystals of $(K_{\frac{2}{3}}Ca_{\frac{1}{3}})_{(1-\delta)}Pt_yCu_xO_2$ with the values of x and y and δ, determined by EPMA (see section 5.3). Key results from each of these refinements are shown in tables B.36, B.37, B.38, B.39, B.40 and B.41. The crystals from batches B.41 and B.42 contain a second phase, which is denoted by the green tick marks, the structure of which is still unknown but has been fitted to the same structural model as the original phase but with an expanded c lattice parameter. During the refinement of these two batches the composition of the first phase was refined to be identical to the crystals of CPOC#F6 but the second phase was given the composition of the new phase. The refined parameters of this second phase are given in tables B.42 and B.43.

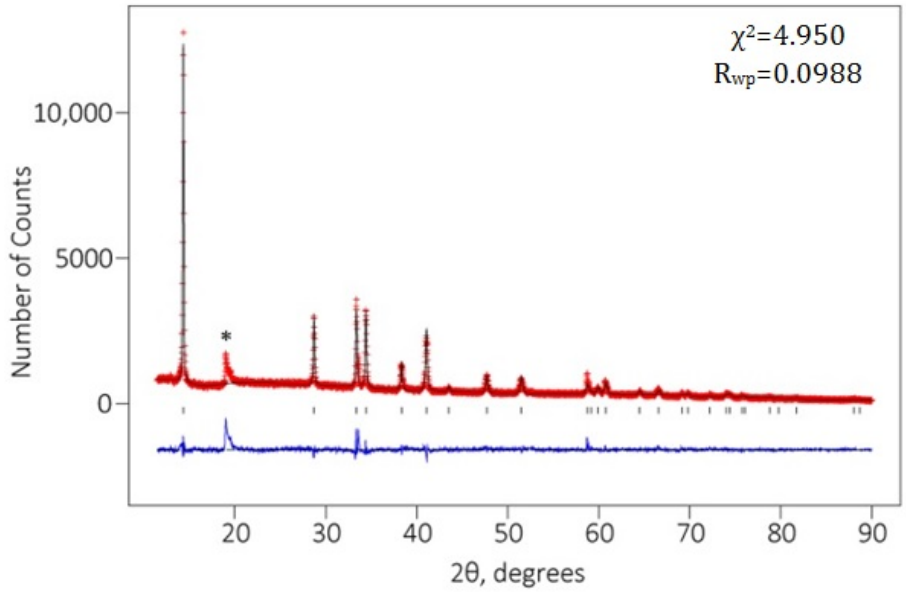

Figure B.34 *X-ray diffraction data collected on ground crystals of* $K_{\frac{2}{3}}Ca_{\frac{1}{3}}Pt_{3-\delta}O_6$ *from batch number CPO#F19* χ^2*=4.950;* R_{wp}*=0.0988.*

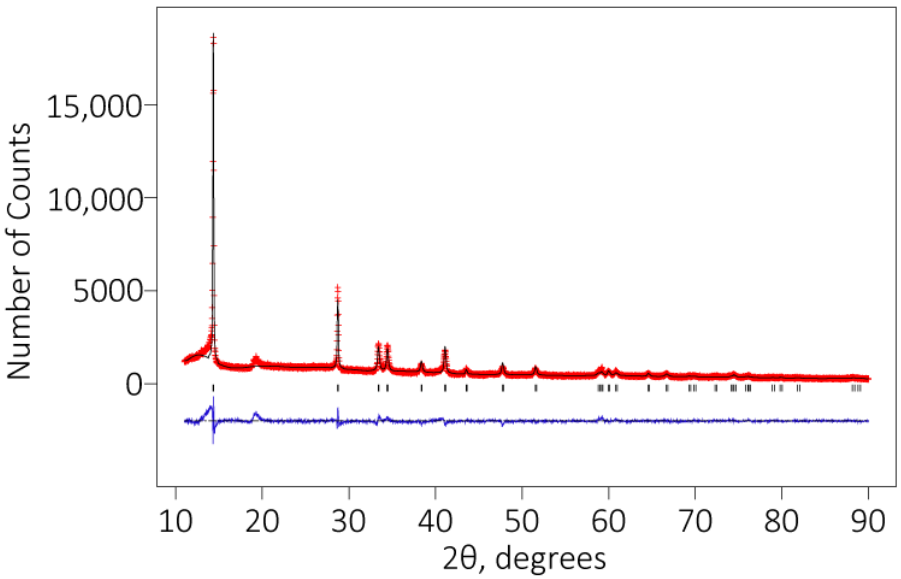

Figure B.35 *X-ray refinement of ground crystals of* $(K_{\frac{2}{3}}Ca_{\frac{1}{3}})_{(1-\delta)}Pt_yCu_xO_2$ *from batch number CPOC#F1 where* x = *0.036.* χ^2=*5.699;* R_{wp}=*0.1215.*

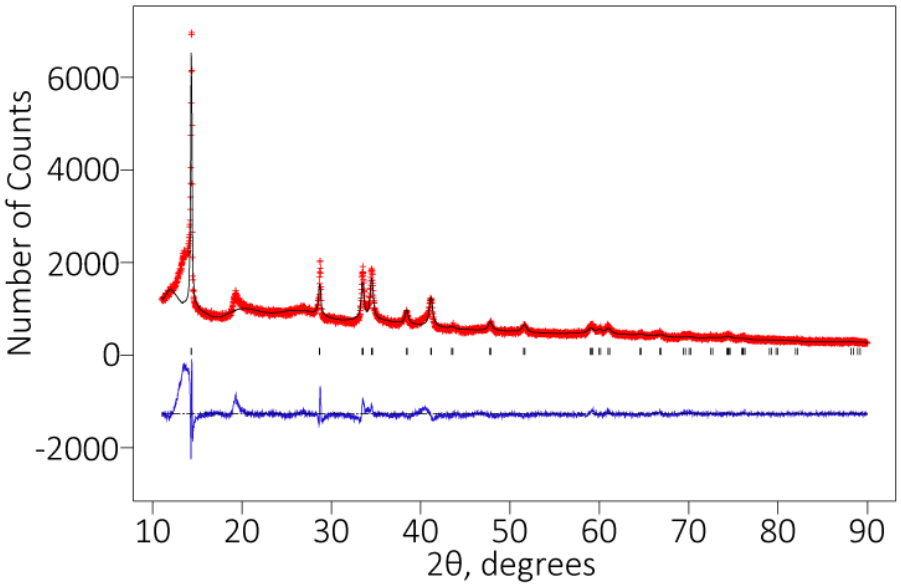

Figure B.36 *X-ray refinement of ground crystals of* $(K_{\frac{2}{3}}Ca_{\frac{1}{3}})_{(1-\delta)}Pt_yCu_xO_2$ *from batch number CPOC#F2 where* x = *0.09.* χ^2=*9.795;* R_{wp}=*0.1215.*

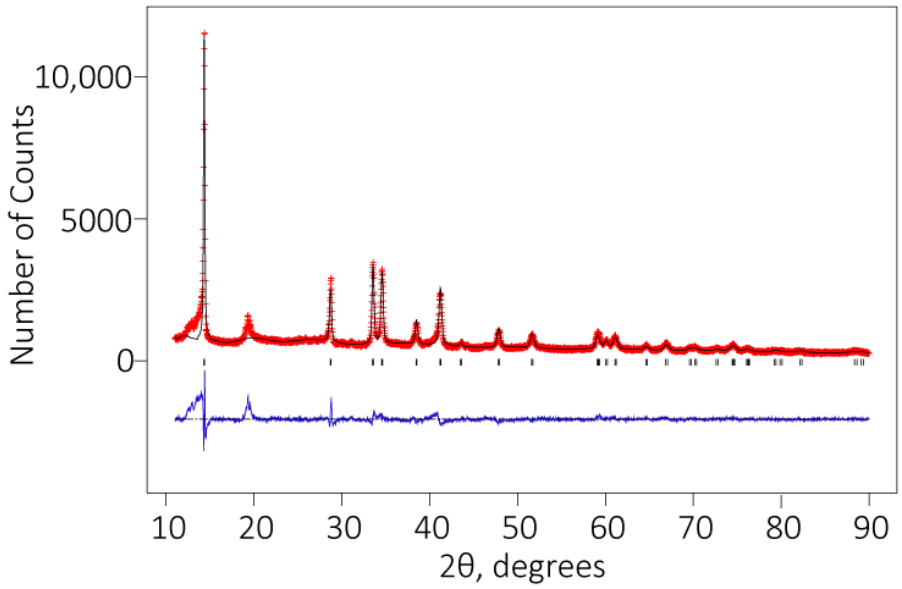

Figure B.37 *X-ray refinement of ground crystals of* $(K_{\frac{2}{3}}Ca_{\frac{1}{3}})_{(1-\delta)}Pt_yCu_xO_2$ *from batch number CPOC#F3 where* x = *0.13.* χ^2=*10.61;* R_{wp}=*0.1298.*

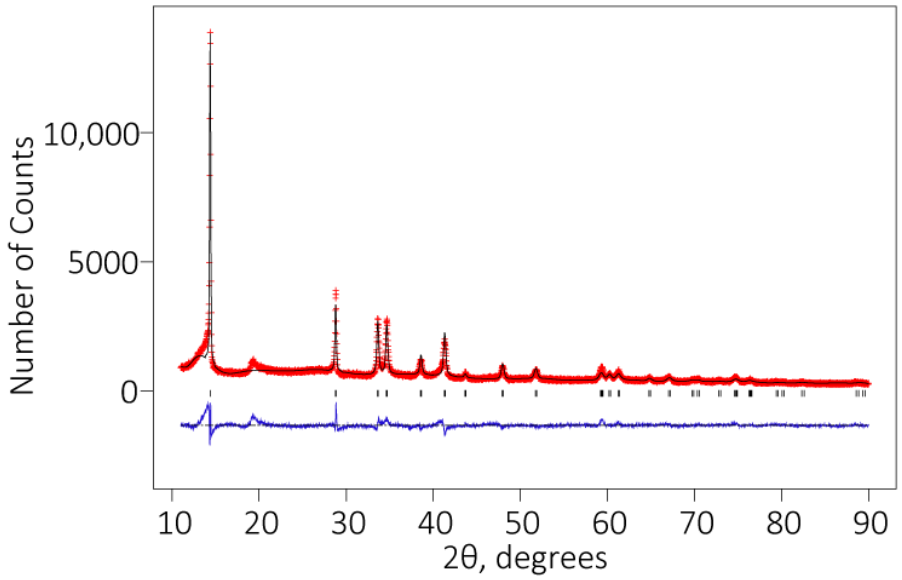

Figure B.38 *X-ray refinement of ground crystals of* $(K_{\frac{2}{3}}Ca_{\frac{1}{3}})_{(1-\delta)}Pt_yCu_xO_2$ *from batch number CPOC#F4 where* x = *0.14.* χ^2=*6.434;* R_{wp}=*0.1005.*

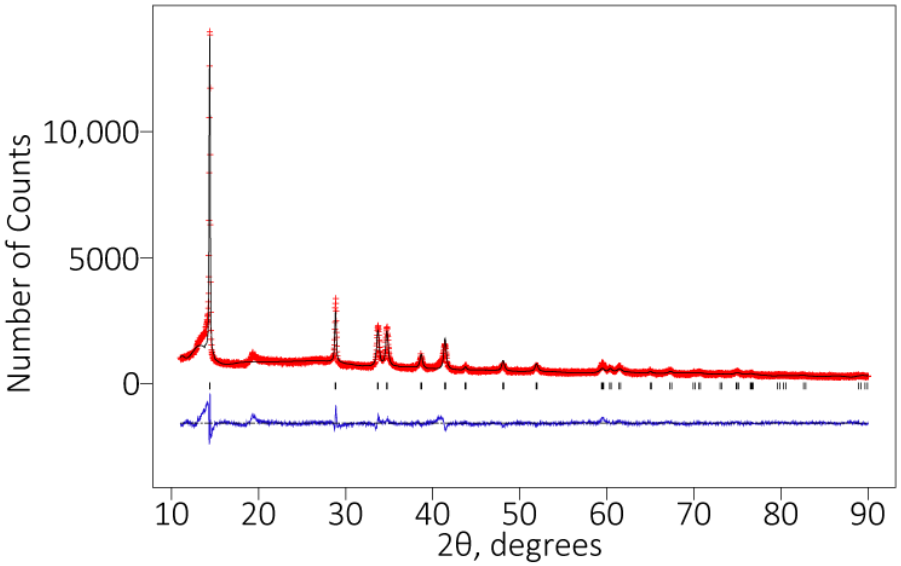

Figure B.39 *X-ray refinement of ground crystals of* $(K_{\frac{2}{3}}Ca_{\frac{1}{3}})_{(1-\delta)}Pt_yCu_xO_2$ *from batch number CPOC#F5 where* x = *0.15.* χ^2=*6.202;* R_{wp}=*0.0969.*

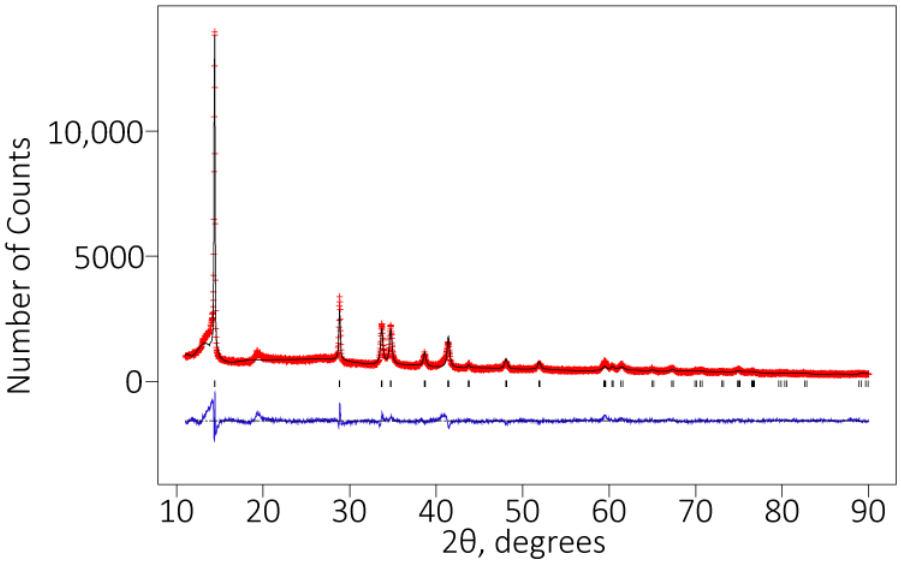

Figure B.40 *X-ray refinement of ground crystals of* $(K_{\frac{2}{3}}Ca_{\frac{1}{3}})_{(1-\delta)}Pt_yCu_xO_2$ *from batch number CPOC#F6 where* x = *0.22.* χ^2=*12.32;* R_{wp}=*0.1335.*

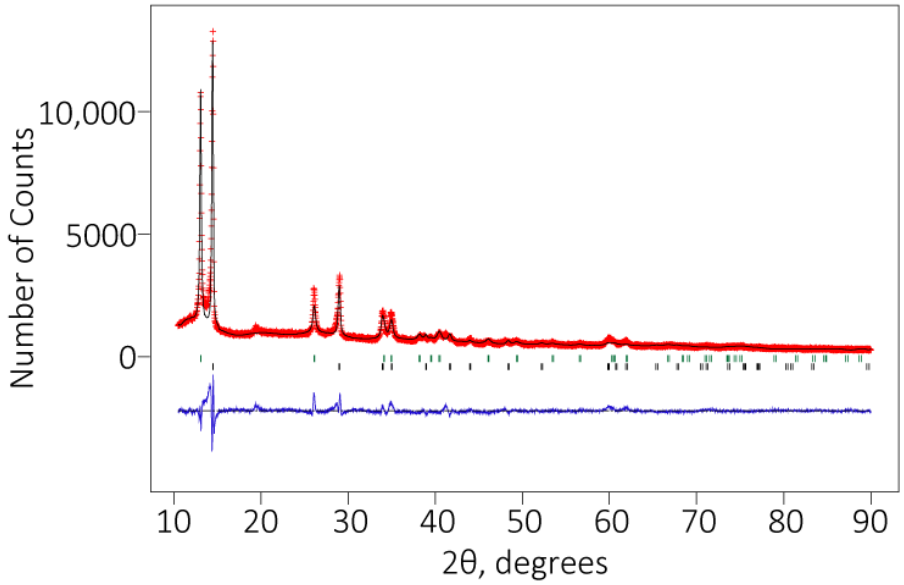

Figure B.41 *X-ray refinement of ground crystals of* $(K_{0.917}Ca_{0.083})_{0.49(4)}Pt_{0.683}Cu_{0.317}O_{1.5(6)}$ *from batch number CPOC#F7 where* x = *0.32.* χ^2=*7.469;* R_{wp}=*0.0989.*

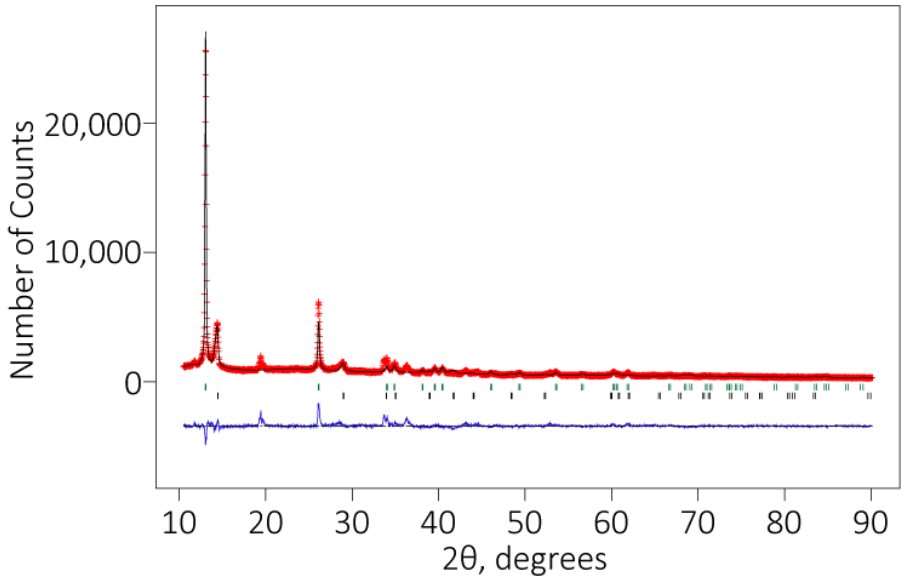

Figure B.42 *X-ray refinement of ground crystals of* $(K_{0.87}Ca_{0.13})_{0.5(1)}Pt_{0.72}Cu_{0.28}O_{1.8(4)}$ *from batch number CPOC#F8 where* x = *0.28.* χ^2=*9.725;* R_{wp}=*0.1117.*

Atom	Wyckoff Symbol	x	y	z	B	Occupancy
Pt(1)	3a	2/3	1/3	1/3	0.054(2)	0.868
Ca(1)	6c	2/3	1/3	0.5	0.28(1)	1/6
K(1)	6c	2/3	1/3	0.5	0.28(1)	1/3
O(1)	6c	0	0	0.3853(9)	0.021(5)	1

Table B.35 *Results from the Rietveld refinement of ambient temperature x-ray diffraction data collected on ground crystals of* $K_{\frac{2}{3}}Ca_{\frac{1}{3}}Pt_{3-\delta}O_6$ *from batch number CPO#F19. a=3.1522(2); c=18.802(2); V=161.797(28).*

Atom	Wyckoff Symbol	x	y	z	B	Occupancy
Pt(1)	3a	2/3	1/3	1/3	0.00515(21)	0.80
Cu(1)	3a	2/3	1/3	1/3	0.00515(21)	0.03
Ca(1)	6c	2/3	1/3	0.5	0.204(12)	1/6
K(1)	6c	2/3	1/3	0.5	0.204(12)	1/3
O(1)	6c	0	0	0.3803(16)	0.0817(97)	1

Table B.36 *Results from the Rietveld refinement of ambient temperature x-ray diffraction data collected on ground crystals of* $(K_{\frac{2}{3}}Ca_{\frac{1}{3}})_{(1-\delta)}Pt_yCu_xO_2$ *from batch number CPOC#F1 where* x = *0.036. a=3.14687(20); c=18.7742(15); V=161.009(24).*

Atom	Wyckoff Symbol	x	y	z	B	Occupancy
Pt(1)	3a	2/3	1/3	1/3	0.00672(46)	0.79
Cu(1)	3a	2/3	1/3	1/3	0.00672(46)	0.08
Ca(1)	6c	2/3	1/3	0.5	0.418(46)	1/6
K(1)	6c	2/3	1/3	0.5	0.418(46)	1/3
O(1)	6c	0	0	0.3901(20)	0.044(15)	1

Table B.37 *Results from the Rietveld refinement of ambient temperature x-ray diffraction data collected on ground crystals of* $(K_{\frac{2}{3}}Ca_{\frac{1}{3}})_{(1-\delta)}Pt_yCu_xO_2$ *from batch number CPOC#F2 where* x = *0.09. a=3.13907(71); c=18.791(10); V=160.35(14).*

Atom	Wyckoff Symbol	x	y	z	B	Occupancy
Pt(1)	3a	2/3	1/3	1/3	0.0284(16)	0.70
Cu(1)	3a	2/3	1/3	1/3	0.0284(16)	0.10
Ca(1)	6c	2/3	1/3	0.5	0.087(10)	0.1167
K(1)	6c	2/3	1/3	0.5	0.087(10)	0.2333
O(1)	6c	0	0	0.3888(10)	0.0529(76)	1

Table B.38 *Results from the Rietveld refinement of ambient temperature x-ray diffraction data collected on ground crystals of* $(K_{\frac{2}{3}}Ca_{\frac{1}{3}})_{(1-\delta)}Pt_yCu_xO_2$ *from batch number CPOC#F3 where* x = *0.13. a=3.13484(26); c=18.7843(35); V=159.866(46).*

Atom	Wyckoff Symbol	x	y	z	B	Occupancy
Pt(1)	3a	2/3	1/3	1/3	0.0430(17)	0.75
Cu(1)	3a	2/3	1/3	1/3	0.0430(17)	0.12
Ca(1)	6c	2/3	1/3	0.5	0.1147(99)	0.112
K(1)	6c	2/3	1/3	0.5	0.1147(99)	0.288
O(1)	6c	0	0	0.3744(12)	0.0521(79)	1

Table B.39 *Results from the Rietveld refinement of ambient temperature x-ray diffraction data collected on ground crystals of ground crystals of* $(K_{\frac{2}{3}}Ca_{\frac{1}{3}})_{(1-\delta)}Pt_yCu_xO_2$ *from batch number CPOC#F4 where* x = *0.14. a=3.12725(20); c=18.7320(22); V=158.650(31).*

Atom	Wyckoff Symbol	x	y	z	B	Occupancy
Pt(1)	3a	2/3	1/3	1/3	0.0684(25)	0.65
Cu(1)	3a	2/3	1/3	1/3	0.0684(25)	0.12
Ca(1)	6c	2/3	1/3	0.5	0.179(15)	0.105
K(1)	6c	2/3	1/3	0.5	0.179(15)	0.245
O(1)	6c	0	0	0.3663(11)	0.0548(83)	1

Table B.40 *Results from the Rietveld refinement of ambient temperature x-ray diffraction data collected on ground crystals of* $(K_{\frac{2}{3}}Ca_{\frac{1}{3}})_{(1-\delta)}Pt_yCu_xO_2$ *from batch number CPOC#F5 where* x = *0.15. a=3.11710(27); c=18.6802(29); V=157.186(40).*

Atom	Wyckoff Symbol	x	y	z	B	Occupancy
Pt(1)	3a	2/3	1/3	1/3	0.0341(20)	0.71
Cu(1)	3a	2/3	1/3	1/3	0.0341(20)	0.20
Ca(1)	6c	2/3	1/3	0.5	0.054(11)	0.070
K(1)	6c	2/3	1/3	0.5	0.054(11)	0.250
O(1)	6c	0	0	0.3708(14)	0.0289(88)	1

Table B.41 *Results from the Rietveld refinement of ambient temperature x-ray diffraction data collected on ground crystals of* $(K_{\frac{2}{3}}Ca_{\frac{1}{3}})_{(1-\delta)}Pt_yCu_xO_2$ *from batch number CPOC#F6 where* x = *0.22. a=3.10534(39); c=18.6488(48); V=155.740(67).*

Atom	Wyckoff Symbol	x	y	z	B	Occupancy
Pt(1)	3a	2/3	1/3	1/3	0.083(57)	0.683
Cu(1)	3a	2/3	1/3	1/3	0.083(57)	0.317
Ca(1)	6c	2/3	1/3	0.5	0.030(25)	0.0203
K(1)	6c	2/3	1/3	0.5	0.030(25)	0.2247
O(1)	6c	0	0	0.39180	0.1732(34)	0.75

Table B.42 *Results from the Rietveld refinement of ambient temperature x-ray diffraction data collected on ground crystals of* $(K_{0.917}Ca_{0.083})_{0.49(4)}Pt_{0.683}Cu_{0.317}O_{1.5(6)}$ *from batch number CPOC#F7 where* x = *0.317. a=3.0795(9); c=20.631(7); V=169.432(96).*

Atom	Wyckoff Symbol	x	y	z	B	Occupancy
Pt(1)	3a	2/3	1/3	1/3	0.088	0.72
Cu(1)	3a	2/3	1/3	1/3	0.088	0.28
Ca(1)	6c	2/3	1/3	0.5	0.026	0.0325
K(1)	6c	2/3	1/3	0.5	0.026	0.2175
O(1)	6c	0	0	0.39180	0.0098	0.90

Table B.43 *Results from the Rietveld refinement of ambient temperature x-ray diffraction data collected on ground crystals of* $(K_{0.87}Ca_{0.13})_{0.5(1)}Pt_{0.72}Cu_{0.28}O_{1.8(4)}$ *from batch number CPOC#F8 where* x *= 0.28. a=3.0804(8); c=20.575(3); V=169.084(82).*

Appendix C

Single crystal refinements

C.1 $(Sr_{(1-x)}La_x)_3Ir_2O_7$

To map the structural evolution of $Sr_3Ir_2O_7$ upon lanthanum doping, single crystal x-ray diffraction data was collected on three crystals of undoped $Sr_3Ir_2O_7$ and three crystals of La doped $Sr_3Ir_2O_7$ from the most heavily doped batch. Data was collected on the Agilent Gemini diffractometer in the Materials Characterisation Laboratory at ISIS spallation source using Mo K_α radiation. The data reduction was carried out in CrysAlis and all refinements were conducted using JANA2006. The structure was refined in the I4/mmm space group as the extra peaks associated with the Bbcb space group were not detectable. 20 parameters were refined in each refinement and there were no constraints applied. The fractional occupancies of the Sr/La sites were fixed to give the average La content as determined by EPMA. The following tables give the positional and harmonic ADP parameters for each of the six crystals. Some of the ADP parameters are negative, which may be due to the absence of an absorption correction. Table C.1 compares key data collection and refinement parameters of each data set. One data set from batch covers the whole hemisphere to allow for space group determination. Once the I4/mmm space group was established, only reflections associated with the I4/mmm space group were measured in the other data sets. Table C.2 compare the refined lattice parameters, Ir-O bond lenghts and Ir-O-Ir bond angle of each of the crystals, the results of which are discussed in section 4.6.3.

Positional parameters for $(Sr_{0.924}La_{0.076})_3Ir_2O_7$ - crystal 1					
Atom	**Occupancy**	**x**	**y**	**z**	U_{iso}
Ir1	1	0	0	0.09764(8)	-0.0028(5)
Sr1	0.924	0.5	0.5	0	0.0002(12)
La1	0.076	0.5	0.5	0	0.0002(12)
Sr2	0.924	0.5	0.5	0.1869(2)	0.0058(10)
La2	0.076	0.5	0.5	0.1869(2)	0.0058(10)
O1	1	0	0	0.1951(13)	0.000(7)
O2	1	0	0	0	0.021(12)
O3	0.5	0.103(7)	0.5	0.0964(14)	0.003(10)

Harmonic ADP parameters for $(Sr_{0.924}La_{0.076})_3Ir_2O_7$ - crystal 1						
Atom	U_{11}	U_{22}	U_{33}	U_{12}	U_{13}	U_{23}
Ir1	0.0021(8)	0.0021(8)	-0.0125(10)	0	0	0
Sr1	0.0043(18)	0.0043(18)	-0.008(3)	0	0	0
La1	0.0043(18)	0.0043(18)	-0.008(3)	0	0	0
Sr2	0.0135(16)	0.0135(16)	-0.0096(19)	0	0	0
La2	0.0135(16)	0.0135(16)	-0.0096(19)	0	0	0
O1	0.012(11)	0.012(11)	-0.022(12)	0	0	0
O2	0.04(2)	0.04(2)	-0.02(2)	0	0	0
O3	0.00(2)	-0.006(15)	0.011(18)	0	0.010(12)	0

Positional parameters for $(Sr_{0.924}La_{0.076})_3Ir_2O_7$ - crystal 2					
Atom	**Occupancy**	**x**	**y**	**z**	U_{iso}
Ir1	1	0	0	0.09789(14)	0.0000(8)
Sr1	0.924	0.5	0.5	0	0.004(2)
La1	0.076	0.5	0.5	0	0.004(2)
Sr2	0.924	0.5	0.5	0.1861(4)	0.0096(17)
La2	0.076	0.5	0.5	0.1861(4)	0.0096(17)
O1	1	0	0	0.196(2)	-0.006(10)
O2	1	0	0	0	0.001(14)
O3	0.5	0.120(13)	0.5	0.097(2)	0.002(15)

Harmonic ADP parameters for $(Sr_{0.924}La_{0.076})_3Ir_2O_7$ - crystal 2						
Atom	U_{11}	U_{22}	U_{33}	U_{12}	U_{13}	U_{23}
Ir	0.0113(14)	0.0113(14)	-0.0227(14)	0	0	0
Sr1	0.016(3)	0.016(3)	-0.021(4)	0	0	0
La1	0.016(3)	0.016(3)	-0.021(4)	0	0	0
Sr2	0.023(3)	0.023(3)	-0.018(3)	0	0	0
La2	0.023(3)	0.023(3)	-0.018(3)	0	0	0
O1	0.004(15)	0.004(15)	-0.03(2)	0	0	0
O2	0.03(3)	0.03(3)	-0.055(19)	0	0	0
O3	0.02(3)	0.01(2)	-0.028(18)	0	-0.01(2)	0

Positional parameters for $(Sr_{0.924}La_{0.076})_3Ir_2O_7$ - crystal 3					
Atom	**Occupancy**	**x**	**y**	**z**	U_{iso}
Ir1	1	0	0	0.09740(13)	-0.0014(7)
Sr1	0.924	0.5	0.5	0	0.0040(19)
La1	0.076	0.5	0.5	0	0.0040(19)
Sr2	0.924	0.5	0.5	0.1873(3)	0.0056(14)
La2	0.076	0.5	0.5	0.1873(3)	0.0056(14)
O1	0.5	0.099(10)	0.5	0.0975(14)	-0.007(14)
O2	1	0	0	0.197(2)	0.007(11)
O3	1	0	0	0	0.10(4)

Harmonic ADP parameters for $(Sr_{0.924}La_{0.076})_3Ir_2O_7$ - crystal 3						
Atom	U_{11}	U_{22}	U_{33}	U_{12}	U_{13}	U_{23}
Ir1	0.0072(12)	0.0072(12)	-0.0185(12)	0	0	0
Sr1	0.012(3)	0.012(3)	-0.012(4)	0	0	0
La1	0.012(3)	0.012(3)	-0.012(4)	0	0	0
Sr2	0.016(2)	0.016(2)	-0.015(3)	0	0	0
La2	0.016(2)	0.016(2)	-0.015(3)	0	0	0
O1	0.01(3)	0.00(2)	-0.034(12)	0	0.013(16)	0
O2	0.022(19)	0.022(19)	-0.023(19)	0	0	0
O3	0.18(9)	0.18(9)	-0.066(15)	0	0	0

Positional parameters for $Sr_3Ir_2O_7$ - crystal 1					
Atom	**Occupancy**	**x**	**y**	**z**	U_{iso}
Ir1	1	0	0	0.09781(13)	-0.0107(9)
Sr1	1	0.5	0.5	0	-0.009(2)
Sr2	1	0.5	0.5	0.1860(4)	-0.0013(19)
O1	1	0	0	0	-0.016(15)
O2	1	0	0	0.192(3)	0.003(15)
O3	0.5	0.103	0.5	0.0966	0.00(2)

Harmonic ADP parameters for $Sr_3Ir_2O_7$ - crystal 1						
Atom	U_{11}	U_{22}	U_{33}	U_{12}	U_{13}	U_{23}
Ir1	-0.0043(15)	-0.0043(15)	-0.0235(15)	0	0	0
Sr1	0.000(4)	0.000(4)	-0.027(4)	0	0	0
Sr2	0.008(3)	0.008(3)	-0.020(3)	0	0	0
O1	-0.01(2)	-0.01(2)	-0.03(3)	0	0	0
O2	0.01(2)	0.01(2)	0.00(3)	0	0	0
O3	0.00(4)	0.03(5)	-0.02(2)	0	-0.03(2)	0

Positional parameters for $Sr_3Ir_2O_7$ - crystal 2					
Atom	**Occupancy**	**x**	**y**	**z**	U_{iso}
Ir1	1	0	0	0.09791(10)	-0.0043(6)
Sr1	1	0.5	0.5	0	-0.0007(17)
Sr2	1	0.5	0.5	0.1861(3)	0.0064(14)
O1	1	0	0	0	0.009(14)
O2	0.5	0.100(9)	0.5	0.0966(13)	-0.006(12)
O3	1	0	0	0.193(2)	0.013(11)

Harmonic ADP parameters for $Sr_3Ir_2O_7$ - crystal 2						
Atom	textbfU_{11}	U_{22}	U_{33}	U_{12}	U_{13}	U_{23}
Ir1	-0.0032(10)	-0.0032(10)	-0.0065(13)	0	0	0
Sr1	0.003(2)	0.003(2)	-0.008(4)	0	0	0
Sr2	0.010(2)	0.010(2)	-0.001(3)	0	0	0
O1	0.02(2)	0.02(2)	-0.02(2)	0	0	0
O2	-0.01(2)	0.00(2)	-0.013(14)	0	-0.011(13)	0
O3	0.017(17)	0.017(17)	0.01(2)	0	0	0

Positional parameters for $Sr_3Ir_2O_7$ - crystal 3					
Atom	**Occupancy**	**x**	**y**	**z**	U_{iso}
Ir1	1	0	0	0.09730(6)	-0.0037(5)
Sr1	1	0.5	0.5	0	0.0032(12)
Sr2	1	0.5	0.5	0.18719(19)	0.0017(8)
O1	1	0	0	0	0.016(11)
O2	1	0	0	0.1925(15)	0.008(7)
O3	0.5	0.106(7)	0.5	0.0963(10)	0.004(9)

Harmonic ADP parameters for $Sr_3Ir_2O_7$ - crystal 3						
Atom	$\mathbf{U}_{11}$	$\mathbf{U}_{22}$	$\mathbf{U}_{33}$	$\mathbf{U}_{12}$	$\mathbf{U}_{13}$	$\mathbf{U}_{23}$
Ir1	0.0003(7)	0.0003(7)	-0.0116(9)	0	0	0
Sr1	0.0064(18)	0.0064(18)	-0.003(3)	0	0	0
Sr2	0.0075(13)	0.0075(13)	-0.0098(16)	0	0	0
O1	0.026(17)	0.026(17)	0.00(2)	0	0	0
O2	0.010(10)	0.010(10)	0.003(14)	0	0	0
O3	0.02(2)	0.011(15)	-0.021(11)	0	-0.003(8)	0

	$(Sr_{0.924}La_{0.076})_3Ir_2O_7$			$Sr_3Ir_2O_7$		
	Crystal 1	Crystal 2	Crystal 3	Crystal 1	Crystal 2	Crystal 3
Measured reflections	1040	296	270	280	290	951
Independent reflections	146	139	135	136	138	145
θ_{min}	1.95	1.95	1.95	1.95	1.96	1.95
θ_{max}	27.64	27.75	27.77	26.98	27.45	27.63
R_{int}	10.91	10.97	7.09	7.44	6.89	7.34
Index ranges	-4 < h < 4; -5 < k < 5; -26 < l < 23	-3 < h < 3; -5 < k < 4; -26 < l <11	-5 < h < 4; -3 < k < 1; -16 < l < 26	-3 < h < 5; -2 < k < 4; -20 < l < 26	-4 < h < 4; -4 < k < 3; -15 < l < 26	-5 < h < 4; -5 < k < 3; -26 < l < 20
R_1	0.0646	0.0954	0.0791	0.1062	0.0757	0.0621
wR_2	0.0670	0.1007	0.0817	0.1116	0.0772	0.0594

Table C.1 *Key data collection parameters and the R_1 and R_{wp} values for x-ray single crystal data set.*

	$(Sr_{0.924}La_{0.076})_3Ir_2O_7$				$Sr_3Ir_2O_7$			
	Crystal 1	Crystal 2	Crystal 3	**Average**	Crystal 1	Crystal 2	Crystal 3	**Average**
a($\AA$)	3.9058(4)	3.9018(10)	3.8990(9)	**3.9022(5)**	3.9021(18)	3.8972(8)	3.8977(5)	**3.8990(7)**
c($\AA$)	20.909(2)	20.884(3)	20.876(5)	**20.8890(2)**	20.919(4)	20.8940(8)	20.876(2)	**20.8963(15)**
$\mathbf{r}_{Ir-O(apical)}(\AA)$	2.04(3)	2.04(5)	2.073(4)	**2.051(19)**	1.976(8)	1.99(5)	1.99(3)	**1.985(2)**
$\mathbf{r}_{Ir-O(bridging)}(\AA)$	2.042(2)	2.044(3)	2.033(3)	**2.040(2)**	2.046(8)	2.046(3)	2.0312(13)	**2.041(3)**
$\mathbf{r}_{Ir-O(in-plane)}(\AA)$	1.994(6)	2.006(12)	1.987(8)	**1.996(5)**	1.97(7)	1.988(7)	1.993(6)	**1.984(24)**
$\theta(^\circ)$	156.65	153.04	157.62	**155.77**	161.6	157.22	155.95	**158.3**

Table C.2 *The lattice parameters and key bond lengths and angles extracted from single crystal x-ray diffraction data of undoped and 7.6% doped $Sr_3Ir_2O_7$.*

C.2 $K_2CaPt_{3-x}O_6$

Two x-ray single crystal data sets were collected on $K_2CaPt_{3-x}O_6$. The first was collected on an Oxford diffraction supernova dual wavelength diffractometer in the Department of Chemistry at the University of Edinburgh on a 62μm crystal using a Mo K_α source. Gary Nichol applied Gaussian and Spherical Harmonic based absorption corrections to the data and on refinement the Gaussian absorption correction produced the best fit. The second set of data was collected on the Agilent Supernova diffractometer in the Research Complex at Harwell using Cu K_α radiation. The crystal measured was so small (around 10μm) that an absorption correction was not required. Originally the data set from Edinburgh was refined with the assistance of Stephen Moggach using a combination of SHELXS 86 and CRYSTALS. However, this original refinement gave the composition to be $Ca_2Pt_3O_6$. In the light of the EPMA data I re-refined the data using JANA2006 with a 2:1 ratio of Ca and Pt on the 6c site with a total site occupancy of a half, which improved the R_1 value from 0.075 to 0.0719. The partial occupancy of the Pt 3a site was not detectable when the occupancy of the platinum site was freely refined and so the value was fixed at 1.

The data set at Harwell was collected on a better quality, smaller crystal, which resulted in an improved R_1 value of 0.0511. The atomic positions, bond lengths and Pt-O-Pt angle refined from this data are in close agreement with those refined from the data set collected in Edinburgh. Details of the data collection in Edinburgh and Harwell and key parameters derived from the refinements can be found in the tables in this section.

Data set	Edinburgh	Harwell
Radiation type	Mo K_α	Cu K_α
Space group	R$\bar{3}$m	R$\bar{3}$m
a	3.1607(4)	3.1596(4)
c	18.7835(12)	18.8179(16)
Measured reflections	788	920
Independent reflections	74	59
θ_{min}	3.25	7.06
θ_{max}	28.46	73.93
R_{int}	14.49	10.04
Index ranges	-4 < h < 4; -4 < k < 4; -23 < l < 24	-3 < h < 3; -3 < k < 3; -22 < l < 22
R_1	0.0719	0.0511
wR_2	0.0851	0.0588
Number of parameters refined	8	8
Absorption Correction type	Gaussian	None

Key Bond lengths and angles		
	Edinburgh	**Harwell**
Pt-O	2.134$\mathring{A}$	2.138$\mathring{A}$
Ca/K-O	2.725$\mathring{A}$	2.722$\mathring{A}$
Pt-Pt	3.161$\mathring{A}$	3.160$\mathring{A}$
Pt-O-Pt	95.56°	95.26°

Positional parameters for $K_2CaPt_{3-x}O_6$ - Edinburgh data set					
Atom	**Occupancy**	**x**	**y**	**z**	**U_{iso}**
Pt1	1	0.6667	0.3333	0.3333	0.0194(10)
O1	1	0	0	0.3922(17)	0.017(9)
K1	0.3333	0.6667	0.3333	0.5	0.052(11)
Ca1	0.1667	0.6667	0.3333	0.5	0.052(11)

Harmonic ADP parameters for $K_2CaPt_{3-x}O_6$ - Edinburgh data set						
Atom	**U_{11}**	**U_{22}**	**U_{33}**	**U_{12}**	**U_{13}**	**U_{23}**
Pt1	0.0161(13)	0.0161(13)	0.0260(16)	0.0081(7)	0	0
O1	0.021(13)	0.021(13)	0.008(13)	0.010(6)	0	0
K1	0.062(16)	0.062(16)	0.034(13)	0.031(8)	0	0
Ca1	0.062(16)	0.062(16)	0.034(13)	0.031(8)	0	0

Positional parameters for $K_2CaPt_{3-x}O_6$ - Harwell data set					
Atom	**Occupancy**	**x**	**y**	**z**	**U_{iso}**
Pt1	1	0.6667	0.3333	0.3333	0.0094(9)
O	1	0	0	0.3926(13)	0.002(6)
K1	0.3333	0.6667	0.3333	0.5	0.045(8)
Ca1	0.1667	0.6667	0.3333	0.5	0.045(8)

Harmonic ADP parameters for $K_2CaPt_{3-x}O_6$ - Harwell data set						
Atom	**U_{11}**	**U_{22}**	**U_{33}**	**U_{12}**	**U_{13}**	**U_{23}**
Pt1	0.0096(12)	0.0096(12)	0.0091(13)	0.0048(6)	0	0
O1	0.003(8)	0.003(8)	0.002(11)	0.001(4)	0	0
K1	0.054(11)	0.054(11)	0.027(11)	0.027(6)	0	0
Ca1	0.054(11)	0.054(11)	0.027(11)	0.027(6)	0	0

Appendix D

Novel pressure-induced phase transition in $Sr_3Ir_2O_7$

As well as crystal quality, temperature and electron doping, another tuning parameter that can be used to alter the ground state of a material is pressure. For materials such as $Sr_3Ir_2O_7$ where there are many competing interactions of a similar energy scale, changing the inte-ratomic distances between ions can induce novel phenomena such as structural phase transitions to a more energetically favourable state and superconductivity, particularly when pressure is used as a tuning mechanism around a quantum critical point.

A previous paper by Z.Zhao et al found a second-order structural transition in $Sr_3Ir_2O_7$ at about 14 GPa[147]. This is evidenced by a deviation from the previously linear increase in the d-spacing of particular peaks above 14 GPa as shown in figure D.1, which is attributed to a change in the compressibility of the sample. This deviation from linearity can also be seen in the variation of c/c_0, a/a_0 and c/a with pressure. Also resistivity measurements conducted by L. Li et al[78] found that there is an order of magnitude decrease in the resistivity between 12.6 GPa and 13.2 GPa, which roughly corresponds to the pressure where the deviation from linearity in the lattice parameters occurred. However, the variation of lattice parameter with pressure should be modelled by an equation of state, which is curved, rather than a linear fit and although the authors found the error on performing two equation of state fits above and below 14 GPa to be less than performing one equation of state across all of the experimental data, the evidence for a second-order transition from the structural measurements is

not particularly convincing. We performed high pressure powder x-ray diffraction experiments on Beamline ID09 at the ESRF firstly to see if the evidence for the second-order transition was repeatable and to secondly extend the experiment to higher pressures to look for a first-order structural phase transition. I provided the samples and attended and helped collect the data on two high pressure x-ray powder diffraction experiments along with Christian Donnerer, James Vale and Dr Zhuo Feng from UCL, Prof Malcolm McMahon from the University of Edinburgh and Prof Henrik Ronnow from the EPFL, Geneva. The data from the experiments was analysed by Christian Donnerer, from whom I obtained the diagrams that are shown in this section of my thesis. The first experiment was conducted on beamline I15 at Diamond with Heribert Wilhelm as local contact. In this experiment we went up to 30 GPa at room temperature using a diamond anvil cell provided by Malcolm McMahon, but no evidence of a first-order or the second-order transition was observed.

At ID09 our local contact was Michael Hanfland, who provided the diamond anvil cells and loaded the samples. The samples were loaded with a He pressure medium and the pressure was adjusted using gas membranes. The gasket of the Diamond anvil cells was made of steel and the culet size was 30 μm. A sample of $Sr_3Ir_2O_7$ was initially measured at 20 K up to 50 GPa and then remeasured up to 60 GPa at room temperature to allow higher pressures to be reached. The pressure of the sample was determined by measuring the previously calibrated florescence wavelength of a small amount of W power that was also in the Diamond anvil cell. Due to the strong x-ray scattering ability of Iridium, the exposure time of each measurement was only between 1 and 3 seconds, depending on the pressure used, and data was collected over a 6 degree angular range. The resulting Laue image was integrated using fit2D to create a 2D powder diffraction pattern with the number of counts as a function of 2θ. High intensity peaks from the diamonds in the cell were excluded before integration.

Figure D.2 compares our data collected from 5 GPa to 30 GPa at room temperature with the data collected by Z. Zhuo et al from about 3 GPa to 23.1 GPa that was collected at 25 K using a Neon pressure medium. The deviation from linearity of the c/c_0, a/a_0 and c/a ratios are visible just below 15 GPa in Z.Zhuo et al's data (figures D.2(a) and D.2(b)), however such a trend is not visible in our data (figures D.2(c) and D.2(d)), which contain more data points. No evidence for the second-order structural transition was found in either of our data that was collected at 20 K or room temperature. A Vinet equation of state

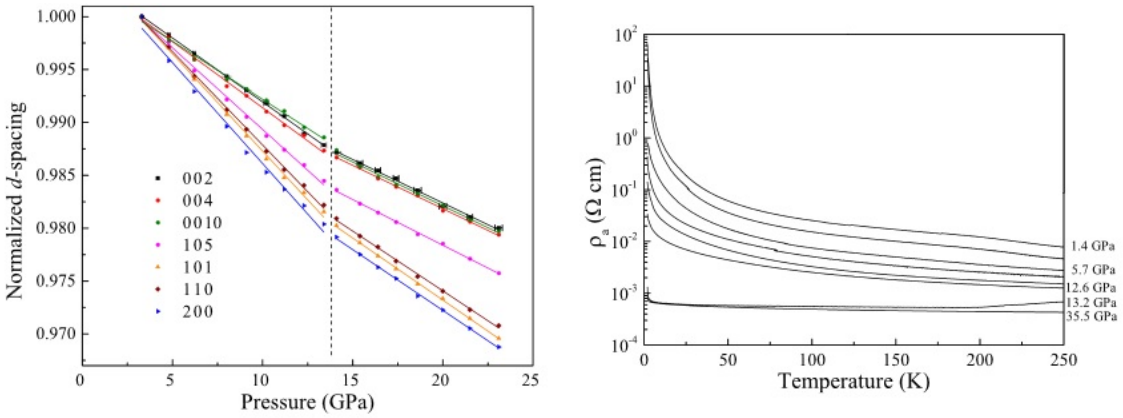

Figure D.1 *Previously published data showing a second order phase transition at around 14 GPa [147]*

fit to our data at 20 K yielded a zero pressure volume of V_0=317.5 Å^3 (fixed) and a bulk modulus of K_0=168(2) GPa. At ambient pressure the zero pressure volume was V_0=318.04 Å^3 and the bulk modulus was K_0=157(4) GPa, which means that at pressures above about 10 GPa $Sr_3Ir_2O_7$ undergoes negative thermal expansion.

At ambient temperature powder x-ray diffraction data was collected up to 60 GPa. As shown in figure D.3 there is a large discontinuity in the unit cell volume above 50 GPa, which occurs simultaneously to a change in the powder diffraction pattern, corresponding to a first-order structural phase transition. The structural transition was found to be reversible when the x-ray diffraction data was collected on the reduction of pressure, with the ambient pressure structure becoming phase pure by 48 GPa. Malcolm McMahon determined the space group of this new phase to be of the monoclinic space group C2. Christian Donnerer was able to use Jana to find the coordinates of the Ir and Sr atoms within this new structure. There is still uncertainty in the oxygen positions of the structure as currently the Ir-O bond lengths along c are too short at 1.75 Å compared to a more reasonable 1.9 Å in the a direction. This is due to the a lattice parameter being shorter than the c lattice parameter in the high pressure phase with the b-axis changing to become the long axis. However due to the poor quality of the data at high pressure and the dominance of the iridium ions in the Bragg peak intensities it was not possible to refine the oxygen positions. Preliminary coordinates of the unit cell of the high pressure phase are given in table D.1. At 60 GPa the lattice parameters were refined in GSAS to be a=3.8310(9) Å, b=17.802(5) Å and c=3.5147(8) Å and the angle, β was refined to be 92.44(1)°. This refinement is shown in figure D.5. As shown in figure D.4 it is thought that there is a 0.5 Å shift in the rock salt layers in comparison to the $SrIrO_3$ layers at about 53 GPa, which

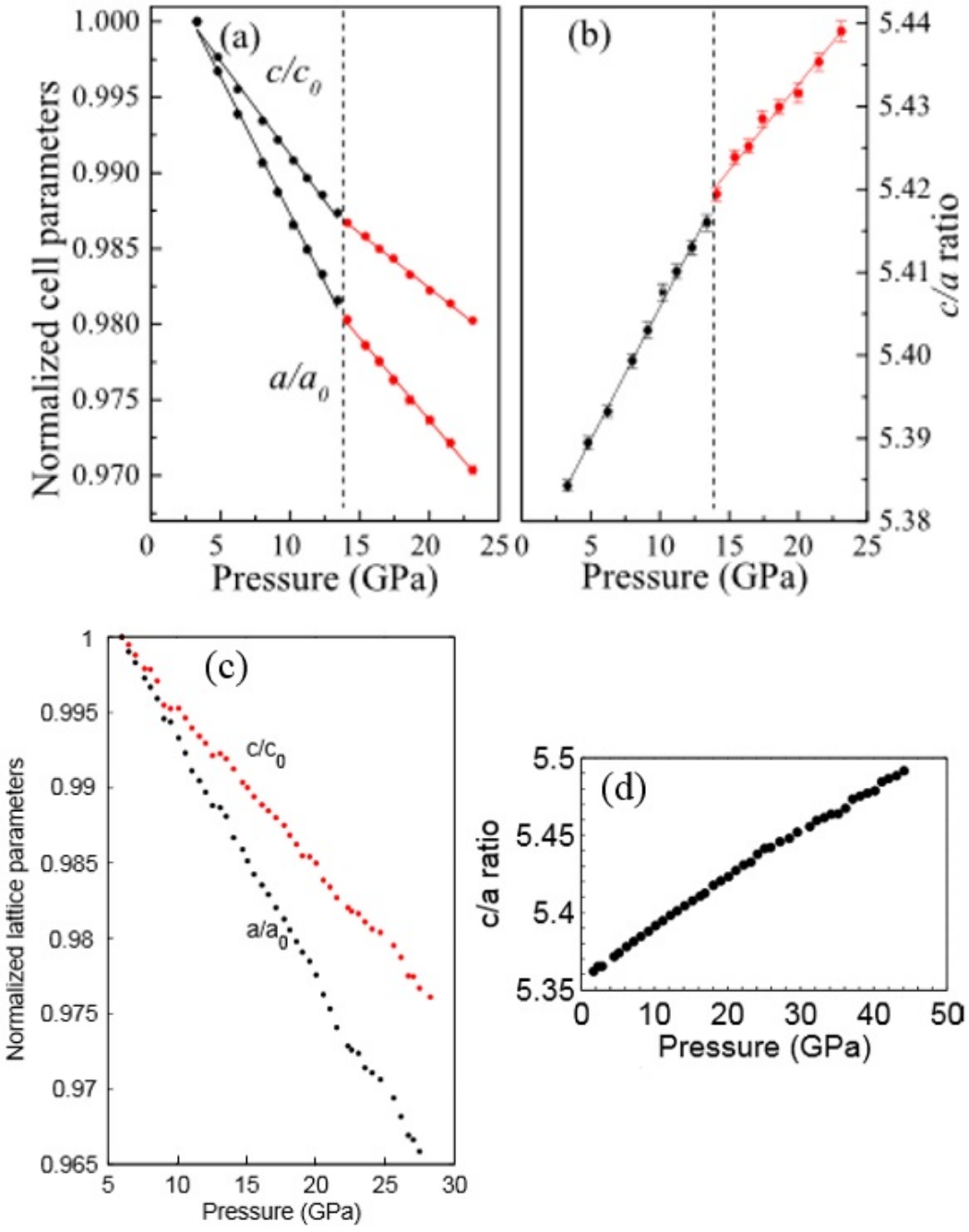

Figure D.2 *The trend of the lattice parameters of $Sr_3Ir_2O_7$ with pressure. a) and b) show previously published work [147] while c) and d) show the data that we collected on ID09. These figures were prepared by Christian Donnerer from UCL*

causes a sharp reduction in the c-lattice parameter and the unit cell volume.

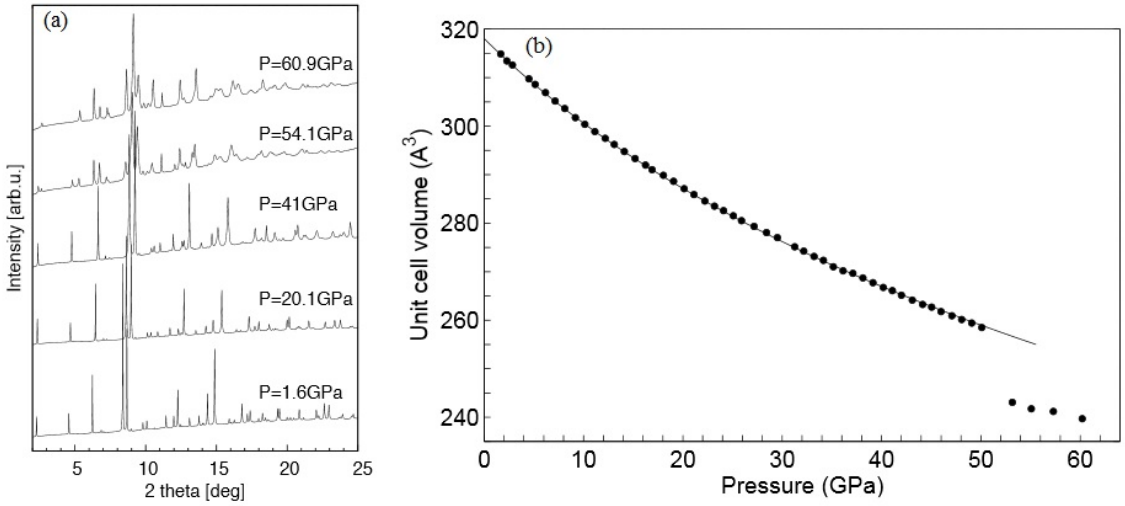

Figure D.3 *a) Diffraction patterns to show the change in the crystal structure on going through the structural phase transition and b) the discontinuity in the unit cell volume as a function of pressure going through the structural phase transition. These figures were prepared by Christian Donnerer from UCL.*

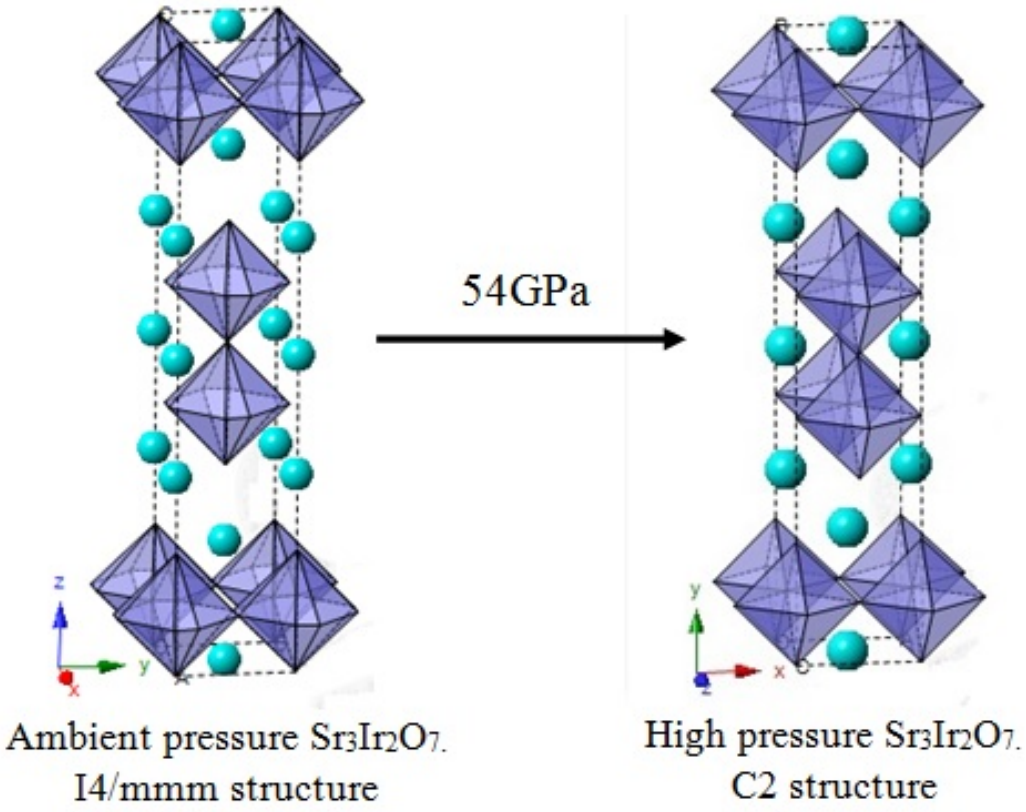

Figure D.4 *The preliminary model of the high pressure structural phase transition that $Sr_3Ir_2O_7$ undergoes.*

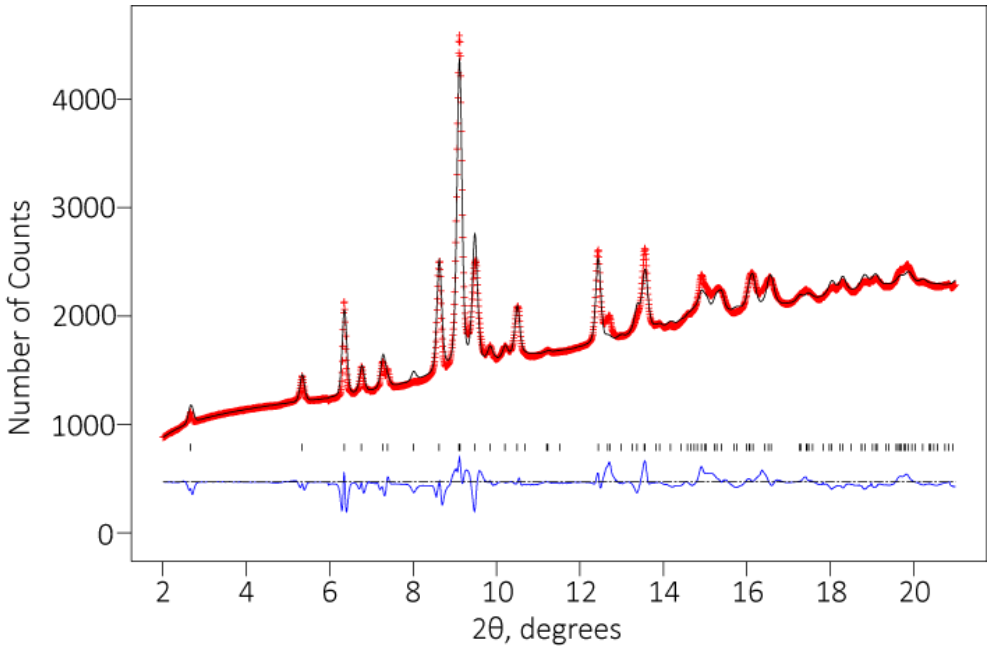

Figure D.5 *Rietveld refinement of the high pressure phase of $Sr_3Ir_2O_7$ using data collected at 60GPa. χ^2 =4.955; R_{wp}=0.0212*

Atom	**Wyckoff Symbol**	**x**	**y**	**z**	B_{iso}	Occupancy
Ir(1)	2a	0.0	0.9	0.0	0.025	1
Ir(2)	2a	0.0	0.1	0.0	0.025	1
Sr(1)	2a	0.5	0.0	0.5	0.025	1
Sr(2)	2a	0.5	0.2	0.5	0.025	1
Sr(3)	2a	0.5	0.8	0.5	0.025	1
O(1)	2b	0.5	0.5	0.0	0.025	1
O(2)	2a	0.0	0.2	0.0	0.025	1
O(3)	2b	0.5	0.9	0.0	0.025	1
O(4)	2b	0.0	0.9	0.5	0.025	1
O(5)	2a	0.0	0.8	0.0	0.025	1
O(6)	2b	0.5	0.1	0.0	0.025	1
O(7)	2b	0.0	0.1	0.5	0.025	1

Table D.1 *The proposed unit cell for the high pressure phase of* $Sr_3Ir_2O_7$.

Appendix E

Preparation of a multicrystal mount for neutron scattering experiments on $Sr_3Ir_2O_7$

To solve the uncertainty surrounding the correct space group and hence structure of $Sr_3Ir_3O_7$ I would have ideally conducted a single crystal neutron diffraction experiment. In fact I attempted such an experiment on I11 at the ILL but the crystals used were too small (around 500μm) and the absorption cross section of iridium too large to observe many reflections. For future neutron diffraction experiments to be successful a larger mass of sample would be required however the largest crystals I ever grew were only around 1mm in size.

A group of collaborators were also interested in conducting single crystal neutron and inelastic neutron scattering measurements on $Sr_3Ir_2O_7$ so they could solve the magnetic structure and look for evidence of a low energy acoustic phonon mode. These were Christian Ruegg, Henrik Ronnow, Des McMorrow and Paul Freeman Gregory. With the input of these collaborators I designed and made a multicrystal mount containing approximately 140 crystals of co-aligned $Sr_3Ir_2O_7$, which amounted to 50mg of sample. A picture of this multicrystal mount is shown in figure E.2. It was designed so that the crystals would cover a large area but be of a narrow depth to minimise the absorption of the neutrons by the sample. A 0.5mm thick piece of high purity aluminium was used as the material to make the sample mount as aluminium has a very low neutron absorption cross section. The mount was made by the mechanical workshop at the University of

Edinburgh to our design. There was much discussion over the best way to attach the crystals to the mount. In the end CYTOP glue was used as it is hydrogen free and sets upon annealing at 150°C for 20 minutes to provide a more durable hold than would have been provided by using a highly viscous oil such as Fomblin Y. This was an important factor given that the multicrystal mount would need to be used for multiple neutron scattering experiments over several years - possibly even using high fields of up to 15T. This also meant that the size and design of the holder had to be compatible with several different instruments and I was given a maximum diameter for the holder of 20mm. The final design had dimensions of 18.35mm × 17.68mm × 0.5mm and the crystals were aligned along eight 0.2mm deep groves of 1mm in diameter. There were also 3mm diameter holes to allow the sample to be firmly attached to the beamline mount using aluminium screws.

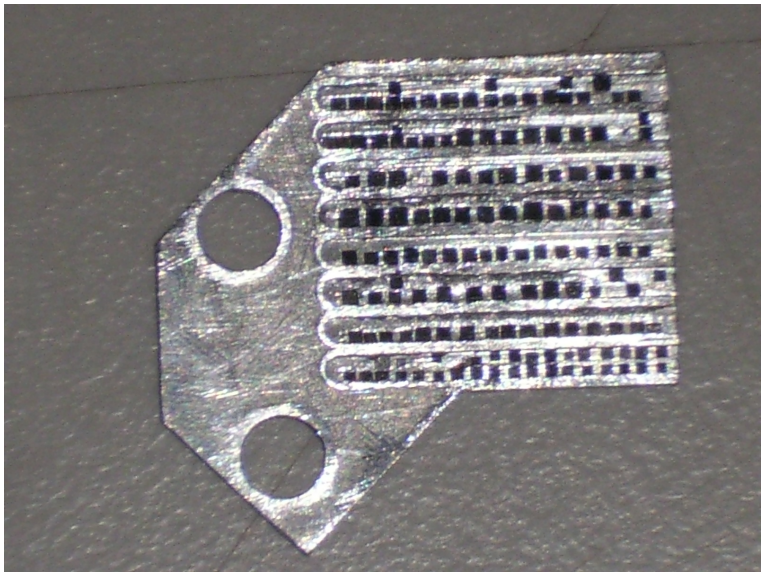

Figure E.1 *Multicrystal mount containing co-aligned crystals of* $Sr_3Ir_2O_7$

To get 50mg of sample I had to use crystals from several different batches of $Sr_3Ir_2O_7$. Due to the square shape of the crystals the alignment was largely done by eye but I used an automated program designed by William Whitley on a four circle single crystal diffractometer in CSEC to construct an interactive map of the crystals of the mount so that I could check that the crystals were roughly aligned and remove any poor quality crystals.

A neutron scattering experiment on EIGER at PSI carried out be Paul Freeman Gregory found that the mosaicity of the multicrystal mount was approximately 3°. Magnetic reflections were found at (0.5 0.5 l) for l=2,3, which were tracked as a function of temperature from 1.5K to 300K (see figure X). The magnetic

reflection at (0.5 0.5 2) disappears above 280K but the (0.5 0.5 3) reflection is still present above 280K. We have successfully applied for time on IN20 at the ILL to carry out polarised neutron scattering experiments on the sample to determine whether the peak at (0.5 0.5 3) is also magnetic in origin. The presence of these peaks at (0.5 0.5 l) show that the magnetic structure is either Bbcb and Acaa and polarised neutron scattering will be able to differentiate between these structures and determine whether there is a canted spin structure below 280K. The flux on EIGER was insufficient for the size of the sample to measure the acoustic phonon mode, although there was a small excess of counts between 2-3meV at (0.5 0.5 3). We have also successfully applied for time on IN8 at the ILL, which has a higher flux, to see whether this weak signal arises from acoustic magnons and to investigate whether a acoustic phonon mode exists at (0.5 0.5 2).

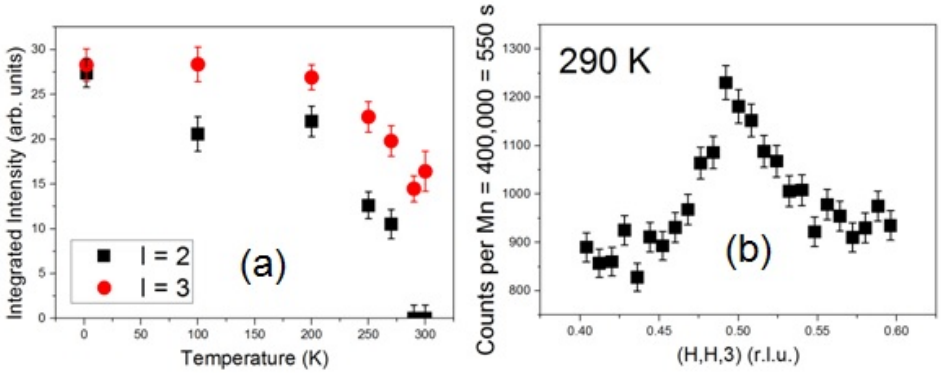

Figure E.2 *Data from the EIGER experiment at PSI on the multicrystal mount, collected and analysed by Paul Freeman Gregory. a) The temperature dependence of the (0.5 0.5 2) and (0.5 0.5 3) magnetic Bragg reflections. b) The (0.5 0.5 3) reflection is still present at 290K, which is above the antiferromagnetic transition temperature of* $Sr_3Ir_2O_7$.

In summary, I was able to grow and co-align enough crystals of $Sr_3Ir_2O_7$ on a specially designed mount to allow single crystal neutron scattering measurements to be conducted. Experiments are still being carried out using this multicrystal mount which will hopefully allow the magnetic structure of $Sr_3Ir_2O_7$ to be unambiguously resolved within the next couple of years and it may be possible to probe the electronic structure of $Sr_3Ir_2O_7$ using single crystal inelastic neutron scattering for the first time.

Appendix F

Crystal field splitting in $Sr_{n+1}Ir_nO_{3n+1}$ (n=1, 2) iridates probed by x-ray Raman spectroscopy

Samples of Sr_2Ir_4 and $Sr_3Ir_2O_7$ that were grown as a product of this thesis were provided for an x-ray Raman spectroscopy study conducted principally by Marco Moretti Sala. The outcome of the study is briefly discussed here as the results provide some experimental evidence for the J_{eff}=1/2 ground state in the strontium iridates, which is the model used in this thesis.

As discussed in section 2.4, the J_{eff}=1/2 ground state is only theoretically feasible for an iridium ion in perfect cubic symmetry. However, in reality this state can still occur if the tetragonal splitting is much smaller than the spin-orbit splitting of the t_{2g} manifold and if the cubic crystal field splitting is much larger than the spin-orbit splitting so that the e_g states do not contribute to the ground state wavefunction. Given that Sr_2IrO_4 and $Sr_3Ir_2O_7$ possess IrO_6 octahedra that undergo a small tetragonal distortion, it was important to test the validaity of the J_{eff}=1/2 ground state model by measuring the magnitude of the cubic and tetragonal components of the crystal field. Given the difficulty of conducting inelastic neutron scattering experiments on iridate samples due to the large absorption cross section of iridium, x-ray scattering is the technique of choice. Resonant x-ray magnetic scattering (RXMS) and resonant inelastic

x-ray scattering (RIXS) have previously been used to estimate the strength of the cubic crystal field. Our study used x-ray raman spectroscopy (XRS), which is a type of nonresonant inelastic x-ray scattering (NIXS). The advantage of XRS over RIXS and RXMS is that the energy of the incoming and scattered photons is far from the Ir $L_{2,3}$ absorption edges of the material and so does not suffer from self-absorption effects and is more representative of the bulk of the sample.

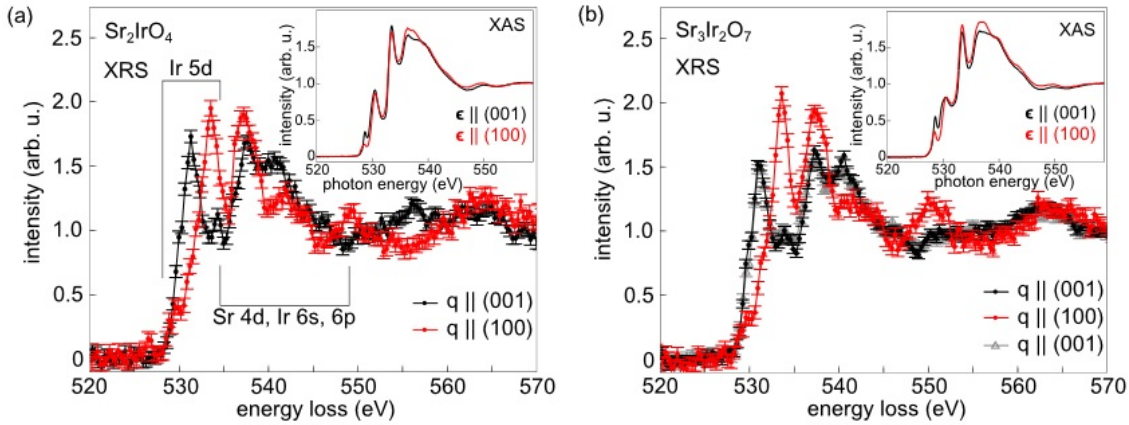

Figure F.1 *XRS spectra of (a) Sr_2IrO_4 and (b) $Sr_3Ir_2O_7$ for transferred moment along q||(001) (black) and q||(100) (red). Inset are the corresponding XAS spectra for the same samples for incoming polarization ϵ||(001) (black) and ϵ||(100) (red). Figure taken from [92]*

Figure F.1 shows XRS spectra of Sr_2IrO_4 and $Sr_3Ir_2O_7$ that was collected on ID20 at the ESRF, Grenoble. The inset shows XAS data, another technique that suffers from self absorption effects, that was collected on beamline ID08 at the ESRF on the same samples. While the overall shapes of the spectra are similar, the XRS spectra is of a higher resolution and is more sensitive to sample orientation. This is because XAS is dominated by dipole-dipole transitions, making it difficult to resolve anisotropic charge distribution in high symmetry systems, while XRS is more sensitive to non-dipole features such as low energy valence-valence excitations that are affected more by the anisotrpic crystal field [51]. By fitting several peaks in the XRS spectra (shown in figure F.2) that correspond to the dipolar transitions from the O 1s to hybridised O 2p-Ir 5d states and by giving careful consideration to the hybridation strength and the cross-sections of different transistions associated with each orbital, the cubic component (known as Δ or 10Dq) of the crystal field was extracted. This is given by the energy difference between the centres of mass of the e_g and t_{2g} orbitals and was calculated to be 3.80±0.82eV for Sr_2IrO_4 and 3.55±0.13eV for $Sr_3Ir_2O_7$, assuming that the spin-orbit splitting is about 0.4eV as calculated by B.J. Kim et al. The tetragonal component, Δ_{t1}, of the crystal field was calculated

from the splitting of the e_g states to be 1.60±0.82eV for Sr_2IrO_4 and 1.90±0.13eV for $Sr_3Ir_2O_7$. The x^2-y^2 orbital was found to be the highest energy suggesting an elongation of the IrO_6 octahedra along z, which is consistent with the results of single crystal x-ray diffraction. However, the splitting of the t_{2g} set by the tetragonal crystal field, Δ_{t2} was found to be negligible. For clarity, the ground state of $Sr_3Ir_2O_7$, as determined from this study is illustrated in figure F.3.

From the extracted values, the cubic crystal field is the largest energy scale and sufficiently larger than the tetragonal field to prevent mixing of the e_g set into the ground state wavefunction. The splitting of the t_{2g} states by the tetragonal crystal is also much smaller than the spin-orbit splitting, λ, of around 0.4eV. Both of these findings are consistent with Sr_2IrO_4 and $Sr_3Ir_2O_7$ having a spin-orbit assisted J_{eff}=1/2 Mott insulating ground state.

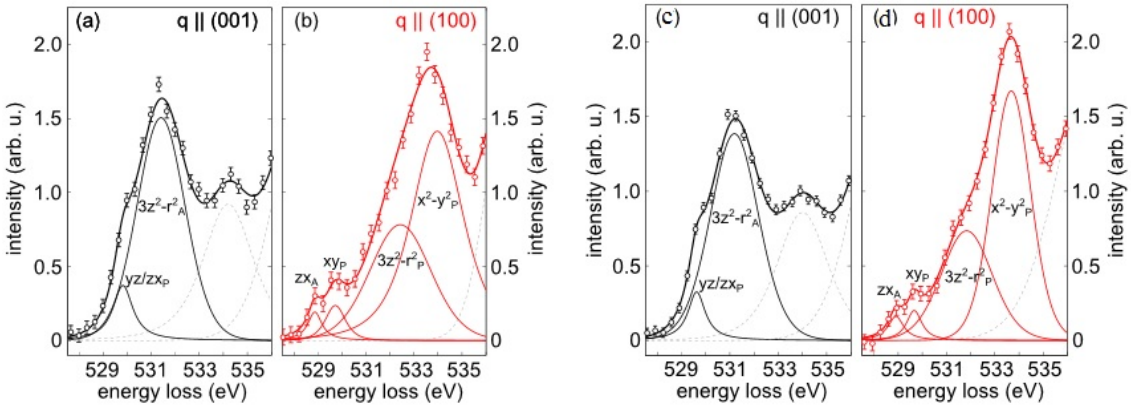

Figure F.2 *Constrained fits (solid thick line) to the raw XRS spectra (open dots) for (a) q||(001) and (b) q||(100)for Sr_2IrO_4 and for (c) q||(001) and (d) q||(100) for $Sr_3Ir_2O_7$. The peak fits associated with a particular transition are shown as solid lines with dashed lines for higher energy transitions. Figure taken from [92].*

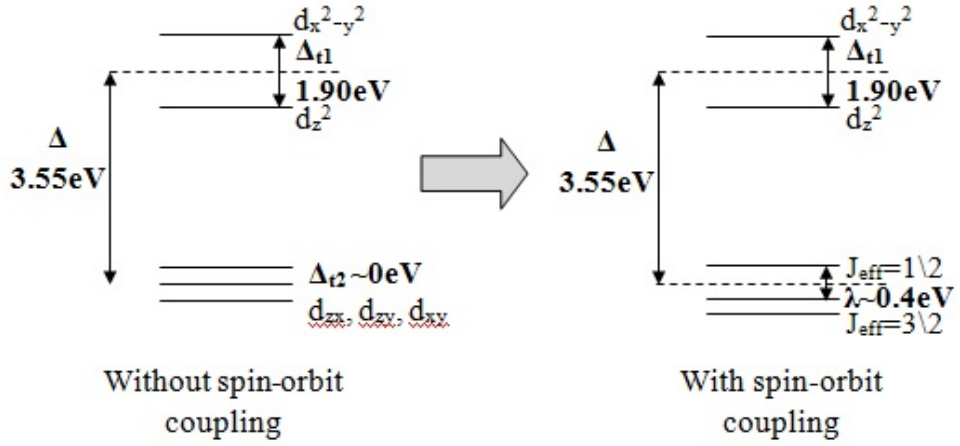

Figure F.3 *Illustration of the ground state of $Sr_3Ir_2O_7$ with and without applying spin-orbit coupling using the values obtained from M. Moretti Sala et al's paper [92]. Any Mott-Hubbard splitting of the J_{eff}=1/2 state is not shown.*

Appendix G

Diamagnetic correction factors

Table G.1 contains all of the diamagnetic correction factors (also known as Pascals's constants) that were used in this thesis to calculate the magnetic susceptibilty of a compound from the measured magnetisation as outlined in section 2.5. The values for the diamagnetic correction factors were taken from the Journal of Chemical Education [15].

Ion	χ_D (10^{-6} emu mol^{-1})
Ca^{2+}	-10.4
Cu^{2+}	-11
Ir^{3+}	-35
Ir^{4+}	-29
K^{+}	-14.9
La^{3+}	-20
Na^{+}	-6.8
Pt^{2+}	-40
Pt^{3+}	-33
Pt^{4+}	-28
Sr^{2+}	-19
O^{2-}	-12

Table G.1 *Diamagnetic correction factors for all of the ions in the compounds in this thesis*

Bibliography

[1] .

[2] "Centronast." http://centronast.it/wp-content/uploads/2007/08/figura_1_bis1.jpg, . Accessed: 2015-05-27.

[3] "hrpd-manual6735." http://www.isis.stfc.ac.uk/instruments/hrpd/documents/hrpd-manual6735.pdf, . Accessed: 2015-05-27.

[4] "Quantum Design - China." http://www.qd-china.com/products2.aspx?id=53, . Accessed: 2015-05-27.

[5] "Refinement of time-of-flight Profile Parameters in GSAS." http://www.isis.stfc.ac.uk/instruments/polaris/data-analysis/refinement-of-profile-parameters-with-polaris-data11478.pdf, . Accessed: 2015-05-27.

[6] "Scattering of X-rays by a Collection of Electrons as in an Atom." http://pd.chem.ucl.ac.uk/pdnn/diff1/scaten.htm, . Accessed: 2014-08-26.

[7] "UMR6508 - D8 Advance Vario1 Bruker diffractometer." http://www-crismat.ensicaen.fr/spip.php?article478&lang=en, . Accessed: 2015-05-27.

[8] "Crystal growth of Ba2MOsO6 (M=Li, Na) from reactive hydroxide fluxes." *Solid State Sciences* 4, 3: (2002) 311 – 316.

[9] *Ultrathin Metal Films: Magnetic And Structural Properties*. Springer, 2004.

[10] A.C. Larson, R. v.-D. "Los Alamos National Laboratories." *Report LAUR* .

[11] Adams, R., and R. L. Shriner. "Platinum oxide as a catalyst in the reduction of organic compounds. III. Preparation and properties of the oxide of platinum obtaine by the fusion of chloroplatinic acid with sodium nitrate1." *Journal of the American Chemical Society* 45, 9: (1923) 2171–2179.

[12] Agilent Technologies, X. P. *CrysAlis^{Pro} User Manual*. Agilent Technologies, 2013.

[13] Anisimov, V. I., M. A. Korotin, and E. Z. Kurmaev. "Band-structure description of Mott insulators (NiO, MnO, FeO, CoO)." *Journal of Physics: Condensed Matter* 2, 17: (1990) 3973.

[14] Bachmann, K. J., and T. Wakiyama. "Czochralski pulling of cobalt and of cobalt-rich cobalt/iron alloy crystals." *Journal of Crystal Growth* 30, 3: (1975) 327 – 334.

[15] Bain, G. A., and J. F. Berry. *Journal of Chemical Education* 85: (2008) 532.

[16] Blake, G. R., G. Cao, and P. G. Radaelli. "Low temperature crystal structure of the ferromagnetic insulator $Sr_3Ir_2O_7$." `http://ftp.esrf.eu/pub/UserReports/28617_A.pdf`, . Accessed: 2014-09-09.

[17] Borzi, R. A., S. A. Grigera, J. Farrell, R. S. Perry, J. S. Lister, S. L. Lee, D. A. Tennant, Y. Maeno, and A. P. Mackenzie. "Formation of a Nematic Fluid at High Fields in $Sr_3Ru_2O_7$." *Science* 315, 5809: (2007) 214.

[18] Boseggia, S., R. Springell, H. C. Walker, A. T. Boothroyd, D. Prabhakaran, S. P. Collins, and D. F. McMorrow. "On the magnetic structure of $Sr_3Ir_2O_7$: an x-ray resonant scattering study." *Journal of Physics Condensed Matter* 24.

[19] Boseggia, S., R. Springell, H. C. Walker, A. T. Boothroyd, D. Prabhakaran, D. Wermeille, L. Bouchenoire, S. P. Collins, and D. F. McMorrow. "Antiferromagnetic order and domains in $Sr_3Ir_2O_7$ probed by x-ray resonant scattering." *Physical Review B* 85.

[20] Boseggia, S., R. Springell, H. C. Walker, H. M. Rønnow, C. Rüegg, H. Okabe, M. Isobe, R. S. Perry, S. P. Collins, and D. F. McMorrow. "Robustness of Basal-Plane Antiferromagnetic Order and the $J_{eff} = 1/2$ State in Single-Layer Iridate Spin-Orbit Mott Insulators." *Phys. Rev. Lett.* 110: (2013) 117,207.

[21] Bramnik, K. G., G. Miehe, H. Ehrenberg, H. Fuess, A. M. Abakumov, R. V. Shpanchenko, V. Y. Pomjakushin, and A. M. Balagurov. "Preparation, Structure, and Magnetic Studies of a New $Sr_11Re_4O_24$ Double Oxide." *Journal of Solid State Chemistry* 149, 1: (2000) 49 – 55.

[22] Bugaris, D. E., and H. C. zur Loye. *Angewandte Chemie* 51: (2012) 3780–3811.

[23] Bugaris, D. E., and H. zurLoye. "Materials Discovery by Flux Crystal Growth: Quaternary and Higher Order Oxides." *Angewandte Chemie International Edition* 51, 16: (2012) 3780–3811.

[24] Buras, B., and L. Gerward. *Acta Crystallographica* 31: (1975) 372.

[25] Cahen, D., J. A. Ibers, and M. H. Mueller. "Platinum bronzes. II. Crystal structures of calcium platinum oxide ($CaPt_2O_4$) and cadmium platinum oxide ($Cd_{0.3}Pt_3O_4$)." *Inorganic Chemistry* 13, 1: (1974) 110–115.

[26] Cahen, D., J. A. Ibers, and J. B. Wagner. "Platinum Bronzes. IV. Preparation, Crystal Chemistry, and Physical Properties." .

[27] Cao, G., J. Bolivar, S. McCall, J. E. Crow, and R. P. Guertin. "Weak ferromagnetism, metal-to-nonmetal transition, and negative differential resistivity in single-crystal Sr_2IrO_4." *Physical Review B* 57, 18: (1998) 11,039–11,042.

[28] ———. "Weak ferromagnetism, metal-to-nonmetal transition, and negative differential resistivity in single-crystal Sr_2IrO_4." *Phys. Rev. B* 57: (1998) R11,039–R11,042.

[29] Cao, G., J. E. Crow, R. P. Guertin, P. F. Henning, C. C. Homes, M. Strongin, D. N. Basov, and E. Lochner. "Charge density wave formation accompanying ferromagnetic ordering in quasi-one-dimensional $BaIrO_3$." *Solid State Communications* 113, 11: (2000) 657–662.

[30] Cao, G., S. Durairaj, S. Chikara, L. E. DeLong, S. Parkin, and P. Schlottmann. "Non-Fermi-liquid behaviour in nearly ferromagnetic $SrIrO_3$ single crystals." *Physical Review B* 76: () 100,402(R).

[31] Cao, G., V. Durairaj, S. Chikara, L. E. DeLong, S. Parkin, and P. Schlottmann. "Non-Fermi-liquid behavior in nearly ferromagnetic $SrIrO_3$ single crystals." *Physical Review B* 76, 10.

[32] Cao, G., Y. Xin, C. S. Alexander, J. E. Crow, P. Schlottmann, M. K. Crawford, R. L. Harlow, and W. Marshall. "Anomalous magnetic and transport behavior in the magnetic insulator $Sr_3Ir_2O_7$." *Phys. Rev. B* 66: (2002) 214,412.

[33] Chaloupka, J., G. Jackeli, and G. Khaliullin. "Kitaev-Heisenberg Model on a Honeycomb Lattice: Possible Exotic Phases in Iridium Oxides A_2IrO_3." *Physical Review Letters* 105, 2.

[34] Choi, S. K., R. Coldea, A. N. Kolmogorov, T. Lancaster, I. I. Mazin, S. J. Blundell, P. G. Radaelli, Y. Singh, P. Gegenwart, K. R. Choi, S. W. Cheong, P. J. Baker, C. Stock, and J. Taylor. "Spin Waves and Revised Crystal Structure of Honeycomb Iridate Na_2IrO_3." *Phys. Rev. Lett.* 108: (2012) 127,204.

[35] Clarke, J. *Scientific American* 271: (1994) 46.

[36] Crawford, M. K., M. A. Subramanian, R. L. Harlow, J. A. Fernandez-Baca, Z. R. Wang, and D. C. Johnston. "Structural and magnetic studies of Sr_2IrO_4." *Phys. Rev. B* 49: (1994) 9198.

[37] Delmas, C., M. Ménétrier, L. Croguennec, S. Levasseur, J. P. Pérés, C. Pouiller, G. Prado, L. Fournés, and F. Weill. *International Journal of Inorganic Materials* 1: (1999) 11.

[38] Design, Q. *Heat Capacity Option User's Manual*. Quantum Design, 2000.

[39] Dhital, C., T. Hogan, W. Zhou, X. Chen, Z. Ren, M. Pokharel, Y. Okad, M. Heine, W. Tian, Z. Yamani, C. Opeil, J. Helton, J. Lynn, Z. Wang, V. Madhavan, and S. Wilson. "Carrier localization and electronic phase separation in a doped spin-orbit driven Mott phase in $Sr_3(Ir_{1-x}Ru_x)_2O_7$." *Nature Communications* 5.

[40] Dhital, C., S. Khadka, Z. Yamani, C. de la Cruz, T. C. Hogan, S. M. Disseler, M. Pokharel, K. C. Lukas, W. Tian, C. P. Opeil, Z. Wang, and S. D. Wilson. "Spin ordering and electronic texture in the bilayer iridate $Sr_3Ir_2O_7$." *Phys. Rev. B* 86: (2012) 100,401.

[41] Donnerer, C., Z. Feng, J. G. Vale, S. N. Andreev, I. V. Solovyev, E. C. Hunter, M. Hanfland, R. S. Perry, H. M. Rønnow, M. I. McMahon, V. V. Mazurenko, and D. F. McMorrow. "Pressure-induced metallization of the spin-orbit Mott insulator $Sr_3Ir_2O_7$." *ArXiv e-prints* .

[42] Dressel, M. "Charge-Ordering Phenomena in One-Dimensional Solids." *ArXiv:0705.1940* .

[43] (Editor), T. H. *International Tables for Crystallography Volume A: Space-group symmetry*. Springer, 2002, fifth edition.

[44] Elwell, D., and H. Scheel. *Crystal Growth from High-Temperature Solutions*. Academic Press, 1975.

[45] Erickson, A. S., S. Misra, G. J. Miller, R. R. Gupta, Z. Schlesinger, W. A. Harrison, J. M. Kim, and I. R. Fisher. "Ferromagnetism in the Mott Insulator Ba_2NaOsO_6." *Phys. Rev. Lett.* 99: (2007) 016,404.

[46] Fujiyama, S., K. Ohashi, H. Ohsumi, K. Sugimoto, T. Takayama, T. Komesu, M. Takata, T. Arima, and H. Takagi. "Weak antiferromagnetism of J_{eff}=1/2 band in bilayer iridate $Sr_3Ir_2O_7$." *Physical Review B* 86, 17.

[47] Galloni, E. E., and J. Angel E. Roffo. "The Crystalline Structure of Pt_3O_4." *The Journal of Chemical Physics* 9, 12: (1941) 875–877.

[48] Gardner, J. S., M. J. P. Gingras, and J. E. Greedan. "Magnetic pyrochlore oxides." *Reviews of Modern Physics* 82.

[49] Ginsberg, D. M. *Physical Properties of High Temperature Superconductors*. World Scientific, 1992.

[50] Goodenough, J. B., and S. L. Cooper. *Localized to Itinerant Electronic Transition in Perovskite Oxides.* Springer Science and Business Media, 2001.

[51] Gordon, R. A., M. W. Haverkort, S. S. Gupta, and G. A. Sawatzky. "Orientation-dependent x-ray Raman scattering from cubic crystals: natural linear dichroism in MnO and CeO_2." *Journal of Physics: Conference Series* 190, 1: (2009) 012,047.

[52] Guo, H. M., and M. Franz. "Three-Dimensional Topological Insulators on the Pyrochlore Lattice." *Phys. Rev. Lett.* 103: (2009) 206,805.

[53] Gutau, W., and H. Mueller Buschbaum. "Neue Verbindungen zum $Ba_8Pt_4Y_3O_{17.5}$-Typ. $Ba_8Pt_4Ln_3O_{17.5}$ (Ln= Er, Yb, Tm)." *Zeitschrift fuer Anorganische und Allgemeine Chemie* 584: (1990) 7–11.

[54] Hanawa, M., Y. Muraoka, T. Tayama, T. Sakakibara, J. Yamaura, and Z. Hiroi. "Superconductivity at 1 K in $Cd_2Re_2O_7$." *Phys. Rev. Lett.* 87: (2001) 187,001.

[55] Hansen, T. J., R. B. Macquart, M. B. Smith, and H. C. zur Loye. "Crystal growth and structures of three new platinates: Ln_3NaPtO_7 (Ln =La, Nd) and La_4PtO_7." *Solid State Sciences* 9, 9: (2007) 785 – 791.

[56] Hansen, T. J., R. B. Macquart, M. D. Smith, and H. C. zur Loye. *Solid State Sciences* 9: (2007) 785.

[57] Herrero-Fernandez, M. P., and B. L. Chamberland. "A new high pressure form of PtO_2." *Journal of the Less Common Metals* 99, 1: (1984) 99 – 105.

[58] Huang, Q., J. W. Lynn, R. W. Erwin, J. Jarupatrakorn, and R. J. Cava. "Oxygen displacements and search for magnetic order in $Sr_3Ru_2O_7$." *Phys. Rev. B* 58: (1998) 8515–8521.

[59] Huang, R., T. Mizoguchi, K. Sugiura, H. Ohta, K. Koumoto, T. Hirayama, and Y. Ikuhara. *Applied Physics Letters* 93: (2008) 181,907.

[60] Ishii, K., I. Jarrige, M. Yoshida, K. Ikeuchi, J. Mizuki, K. Ohashi, T. Takayama, J. Matsuno, and H. Takagi. "Momentum-resolved electronic excitations in the Mott insulator Sr_2IrO_4 studied by resonant inelastic x-ray scattering." *Phys. Rev. B* 83: (2011) 115,121.

[61] Itoh, M., M. Mori, M. Tanaka, and H. Takei. "NMR study of two-dimensional itinerant magnets $PtCoO_2$ and $PdCoO_2$ with a triangular lattice." *Physica B-Condensed Matter* 259-61: (1999) 999–1000.

[62] Jacko, A., J. Fjaerestad, and B. Powell. "A unified explanation of the Kadowaki-Woods ratio in strongly correlated metals." *Nature Physics* 5.

[63] J.Clarke. *Nature* 372: (1994) 501.

[64] Jorgenson, M. *J. Prakt. Chem.* 16.

[65] Kawakubo, Tatsuyuki, Nakagawa, and Takenhiko. "Phase transition in VO_2." *Journal of the Physical Society of Japan* 1964.

[66] Keimer, B., N. Belk, R. J. Birgeneau, A. Cassanho, C. Y. Chen, M. Greven, and M. A. Kastner. "Magnetic excitations in pure, lightly doped, and weakly metallic La_2CuO_4." *Physical Review B* 46, 21: (1992) 14,034.

[67] Kikukawa, T., T. Nakano, T. Shima, and J. Tominaga. *Appl. Phys. Lett.* 81.

[68] Kim, B. J., H. Jin, S. J. Moon, J. Y. Kim, B. G. Park, C. S. Leem, J. Yu, T. W. Noh, C. Kim, S. J. Oh, J. H. Park, V. Durairaj, G. Cao, and E. Rotenberg. "Novel J_{eff}=1/2 Mott State Induced by Relativistic Spin-Orbit Coupling in Sr_2IrO_4." *Phys. Rev. Lett.* 101: (2008) 076,402.

[69] ———. "Novel J_{eff}=1/2 Mott State Induced by Relativistic Spin-Orbit Coupling in Sr_2IrO_4." *Physical Review Letters* 101, 7: (2008) 076,402.

[70] Kim, C. H., H. S. Kim, H. Jeong, H. Jin, and J. Yu. "Topological Quantum Phase Transition in 5d Transition Metal Oxide Na_2IrO_3." *Phys. Rev. Lett.* 108: (2012) 106,401.

[71] Kittaka, S., S. Fusanobori, S. Yonezawa, H. Yaguchi, Y. Maeno, R. Fittipaldi, and A. Vecchione. "Multiple superconducting transitions in the $Sr_3Ru_2O_7$ region of $Sr_3Ru_2O_7$-Sr_2RuO_4 eutectic crystals." *Phys. Rev. B* 77: (2008) 214,511.

[72] Kittaka, S., S. Yonezawa, H. Yaguchi, Y. Maeno, R. Fittipaldi, A. Vecchione, J. F. Mercure, A. Gibbs, R. S. Perry, and A. P. Mackenzie. "Evidence for the Sr_2RuO_4 intercalations in the $Sr_3Ru_2O_7$ region of the $Sr_3Ru_2O_7$ - Sr_2RuO_4 eutectic system." *Journal of Physics Conference Series* 150: (2009) 052,113.

[73] Kiyanagi, R., K. Tsuda, N. Aso, H. Kimura, Y. Noda, Y. Yoshida, S. Ikeda, and Y. Uwatoko. "Investigation of the Structure of Single Crystal $Sr_3Ru_2O_7$ by Neutron and Convergent Beam Electron Diffractions." *Journal of the Physical Society of Japan* 73: (2004) 639–642.

[74] König, M., S. Wiedmann, C. Brüne, A. Roth, H. Buhmann, L. W. Molenkamp, X. L. Qi, and S. C. Zhang. "Quantum Spin Hall Insulator State in HgTe Quantum Wells." *Science* 318, 5851: (2007) 766–770.

[75] Korneta, O. B., Q. Tongfei, S. Chikara, S. Parkin, L. E. De Long, P. Schlottmann, and G. Cao. "Electron-doped $Sr_2IrO_{4-\delta}$ ($0 \leq \delta \leq 0.04$): Evolution of a disordered J_{eff}=1/2 Mott insulator into an exotic metallic state." *Physical Review B* 82, 11: (2010) 115,117.

[76] Kuribayashi, K., and S. Kitamura. *Thin Solid Films* 400.

[77] Laguna-Marco, M. A., D. Haskel, N. Souza-Neto, J. C. Lang, V. V. Krishnamurthy, S. Chikara, G. Cao, and M. van Veenendaal. "Orbital Magnetism and Spin-Orbit Effects in the Electronic Structure of $BaIrO_3$." *Physical Review Letters* 105, 21.

[78] Li, L., P. P. Kong, T. F. Qi, C. Q. Jin, S. J. Yuan, L. E. DeLong, P. Schlottmann, and G. Cao. "Tuning the J_{eff}=1/2 Insulating State via Electron Doping and Pressure in Double-Layered Iridate $Sr_3Ir_2O_7$." *Physical Review B* 87, 23: (2013) 235,127.

[79] Lindell, R., J. Penttila, M. Sillanpaa, and P. Hakonen. *Physical Review B* 68: (2003) 052,506.

[80] Ling, C. D., J. E. Millburn, J. F. Mitchell, D. N. Argyriou, J. Linton, and H. N. Bordallo. "Interplay of spin and orbital ordering in the layered colossal magnetoresistance manganite $La_{2-2x}Sr_{1+2x}Mn_2O_7$(0.5<x<1.0)." *Phys. Rev. B* 62: (2000) 15,096–15,111.

[81] Liu, X., T. Berlijn, W. G. Yin, W. Ku, A. Tsvelik, Y.-J. Kim, H. Gretarsson, Y. Singh, P. Gegenwart, and J. P. Hill. "Long-range magnetic ordering in Na_2IrO_3." *Physical Review B* 83, 22.

[82] L.Maya, T. T.-C. Y., L.Riester. *J, Appl. Phys.* 84.

[83] Longo, J. M., J. A. Kafalas, and R. Arnott. "Structure and properties of the high and low pressure forms of $SrIrO_3$." *Journal of Solid State Chemistry* 3: (1971) 174.

[84] zur Loye, H. C., T. J. Hansen, Q. Zhao, S. J. Mugavero III, R. L. Withers, and M. D. Smith. "Crystal Growth of Novel Lanthanide-Containing Platinates $K_4[Ln_6Pt_2O_{15}]$ (Ln = La, Pr, Nd, Sm) with a Unique Framework Structure." *Inorganic Chemistry* 48, 2: (2009) 414–416.

[85] Luke, G., Y. Fudamoto, K. Kojima, M. Larkin, J. Merrin, B. Nachumi, Y. Uemura, Y. Maeno, Z. Mao, Y. Mori, H. Nakamura, and M. Sigrist. "Time-reversal symmetry-breaking superconductivity in Sr_2RuO_4." *Nature* 394: (1998) 558–561.

[86] Mandrus, D., J. R. Thompson, R. Gaal, L. Forro, J. C. Bryan, B. C. Chakoumakos, L. M. Woods, B. C. Sales, R. S. Fishman, and V. Keppens. "Continuous metal-insulator transition in the pyrochlore $Cd_2Os_2O_7$." *Phys. Rev. B* 63: (2001) 195,104.

[87] Matsuhata, H., I. Nagai, Y. Yoshiyuki, S. Hara, S. Ikeda, and N. Shirakawa. "Crystal structure of $Sr_3Ir_2O_7$ investigated by transmission electron microscopy." *Journal of Solid State Chemistry* 177.

[88] Matsuhira, K., M. Wakeshima, R. Nakanishi, T. Yamada, A. Nakamura, W. Kawano, S. Takagi, and Y. Hinatsu. "Metal-insulator transition in pyrochlore iridates $Ln_2Ir_2O_7$ (Ln = Nd, Sm, and Eu)." *Journal of the Physical Society of Japan* 76, 4.

[89] Mller-Buschbaum, H., and J. Wilkens. "Ein Beitrag ber Sr_2RuO_4 und $Sr_3Ru_2O_7$ Zur Oktaederstreckung von M^{4+} in K_2NiF^{4-} und $Sr_3Ti_2O_7$-Typ-Verbindungen." *Zeitschrift fr anorganische und allgemeine Chemie* 591: (1990) 161–166.

[90] Moon, S. J., M. W. Kim, K. W. Kim, Y. S. Lee, J. Y. Kim, J. H. Park, B. J. Kim, S. J. Oh, S. Nakatsuji, Y. Maeno, I. Nagai, S. I. Ikeda, G. Cao, and T. W. Noh. "Electronic structures of layered perovskite Sr_2MO_4 (M=Ru, Rh, and Ir)." *Phys. Rev. B* 74: (2006) 113,104.

[91] Moore, W. J., and L. Pauling. "The Crystal Structures of the Tetragonal Monoxides of Lead, Tin, Palladium, and Platinum." *Journal of the American Chemical Society* 63, 5: (1941) 1392–1394.

[92] Moretti Sala, M., M. Rossi, S. Boseggia, E. C. Hunter, R. S. Perry, D. Prabhakaran, and A. T. Boothroyd. "Crystal field splitting in $Sr_{n+1}Ir_nO_{3n+1}$ (n=1,2) iridates probed by x-ray Raman spectroscopy." *Physical Review B* 90, 8: (2014) 085,126.

[93] Morris, D. J. P., D. A. Tennant, S. A. Grigera, B. Klemke, C. Castelnovo, R. Moessner, C. Czternasty, M. Meissner, K. C. Rule, J. U. Hoffmann, K. Kiefer, S. Gerischer, D. Slobinsky, and R. S. Perry. "Dirac Strings and Magnetic Monopoles in the Spin Ice $Dy_2Ti_2O_7$." *Science* 326, 5951: (2009) 411–414.

[94] Murakami, Y., J. P. Hill, D. Gibbs, M. Blume, I. Koyama, M. Tanaka, H. Kawata, T. Arima, Y. Tokura, K. Hirota, and Y. Endoh. "Resonant X-Ray Scattering from Orbital Ordering in $LaMnO_3$." *Phys. Rev. Lett.* 81: (1998) 582–585.

[95] Nagai, I., Y. Yoshida, S. I. Ikeda, H. Matsuhata, H. Kito, and M. Kosaka. "Canted antiferromagnetic ground state in $Sr_3Ir_2O_7$." *Journal of Physics: Condensed Matter* 19, 13: (2007) 136,214.

[96] Nakamura, S., K. Iwasawa, K. Morita, and N. Sano. "The influence of basicity on the solubility of platinum in oxide melts." *Metallurgical and Materials Transactions B* 29: (1998) 411–414.

[97] Nakamura, S., and N. Sano. "Solubility of platinum in molten fluxes as a measure of basicity." *Metallurgical and Materials Transactions B* 28: (1997) 103–108.

[98] Obbade, S., N. Tancret, F. Abraham, and E. Suard. "Synthesis, Electrical Properties, and Powder Neutron Crystal Structure Refinement of $Pb_{1x}Bi_xPt_2O_4$ Compounds ($0 \leq x \leq 0.3$)." *Journal of Solid State Chemistry* 166, 1: (2002) 58 – 66.

[99] Okabe, H., M. Isobe, E. Takayama-Muromachi, A. Koda, S. Takeshita, M. Hiraishi, M. Miyazaki, R. Kadono, Y. Miyake, and J. Akimitsu.

"Ba_2IrO_4: A spin-orbit Mott insulating quasi-two-dimensional antiferromagnet." *Physical Review B* 83, 15.

[100] Okamoto, Y., M. Nohara, H. Aruga-Katori, and H. Takagi. "Spin-liquid state in the S=1/2 hyperkagome antiferromagnet $Na_4Ir_3O_8$." *Physical Review Letters* 99, 13.

[101] Ong, K. P., D. J. Singh, and P. Wu. "Unusual Transport and Strongly Anisotropic Thermopower in $PtCoO_2$ and $PdCoO_2$." *Physical Review Letters* 104, 17.

[102] Opagiste, C., C. Paulsen, E. Lhotel, P. Rodire, R. M. Galera, P. Bordet, and P. Lejay. "Crystal growth, structure and ferromagnetic properties of a $Ce_3Pt_23Si_11$ single crystal." *Journal of Magnetism and Magnetic Materials* 321, 6: (2009) 613 – 618.

[103] Ostenson, J., H. Shanks, and D. Finnemore. "Superconductivity in the tungsten bronzes." *Journal of the Less Common Metals* 62, 0: (1978) 149 – 153.

[104] Park, H. J., C. H. Sohn, D. W. Jeong, G. Cao, K. W. Kim, S. J. Moon, H. Jin, D. Y. Cho, and T. W. Noh. "Phonon-assisted optical excitation in the narrow bandgap Mott insulator $Sr_3Ir_2O_7$." *Phys. Rev. B* 89: (2014) 155,115.

[105] Perry, R., and Y. Maeno. "Systematic approach to the growth of high-quality single crystals of SrRuO." *Journal of Crystal Growth* 271: (2004) 134–141.

[106] Perry, R. S., F. Baumberger, L. Balicas, N. Kikugawa, N. J. C. Ingle, A. Rost, J. F. Mercure, Y. Maen, Z. X. Shen, and A. P. Mackenzie. "Sr_2RhO_4:a new, clean correlated electron metal." *New Journal of Physics* 8: (2006) 175.

[107] Petricek, V., M. Dusek, and L. Palatinus. *Z. Kristallographie* 229: (2014) 345.

[108] Prewitt, C. T., K. B. Schwartz, and R. D. Shannon. "Synthesis and structure of orthorhombic cadmium platinum oxide, $CdPt_3O_6$." *Acta Crystallographica Section C* 39, 5: (1983) 519–521.

[109] Qasim, I., B. J. Kennedy, and M. Avdeev. "Synthesis, structure and properties of transition metal doped $SrIrO_3$." *Journal of Materials Chemistry A* 1: (2013) 3127–3132.

[110] Qi, T. F., O. B. Korneta, X. Wan, L. E. DeLong, P. Schlottmann, and G. Cao. "Strong magnetic instability in correlated metal $Bi_2Ir_2O_7$." *arXiv:1201.0538* .

[111] Radwanski, R. J., and Z. Ropka. "Relativistic effects in the electronic structure for the 3d paramagnetic ions." *arXiv:cond-mat/9907140* .

[112] Raub, C. J., A. R. Sweedler, M. A. Jensen, S. Broadston, and B. T. Matthias. "Superconductivity of Sodium Tungsten Bronzes." *Phys. Rev. Lett.* 13: (1964) 746–747.

[113] Rost, A. W., S. A. Grigera, J. A. N. Bruin, R. S. Perry, D. Tian, S. Raghu, S. A. Kivelson, and A. P. Mackenzie. "Thermodynamics of phase formation in the quantum critical metal $Sr_3Ru_2O_7$." *PNAS* 108: (2011) 16,549.

[114] Sabourault, N., G. Mignani, A. Wagner, and C. Mioskowski. *Org. Lett* 4.

[115] Saito, M., R. Higashinaka, and Y. Maeno. "Magnetodielectric response of the spin-ice $Dy_2Ti_2O_7$." *Phys. Rev. B* 72: (2005) 144,422.

[116] Scheel, H. J. "Crystal growth problems of $YBa_2Cu_3O_{7x}$." *Physica C: Superconductivity* 153155, Part 1, 0: (1988) 44 – 49.

[117] Schwartz, K. B., J. B. Parise, C. T. Prewitt, and R. D. Shannon. "Analysis of structural distortions in non-stoichiometric ternary platinum oxides: $Li_{0.64}Pt_3O_4$ and $Co_{0.37}Na_{0.14}Pt_3O_4$." *Acta Crystallographica B* 38: (1982) 2109–2116.

[118] ———. "Structure and crystal chemistry of mixed-valence ternary platinum oxides: $MnPt_3O_6$, $CoPt_3O_6$, $ZnPt_3O_6$, $MgPt_3O_6$, and $NiPt_3O_6$." *Acta Crystallographica Section B* 39, 2: (1983) 217–226.

[119] Schwartz, K. B., and C. T. Prewitt. "Neutron Powder Diffraction Study of Two Sodium Platinum Oxides: $Na_{1.0}Pt_3O_4$ and $Na_{0.73}Pt_3O_4$." *Acta Crystallographica B* 38: (1982) 363–368.

[120] Sears, V. F. "Neutron scattering lengths and cross sections." *Neutron News* 3: (1992) 29.

[121] Shaked, H., J. Jorgensen, O. Chmaissem, S. Ikeda, and Y. Maeno. "Neutron Diffraction Study of the Structural Distortions in $Sr_3Ru_2O_7$." *Journal of Solid State Chemistry* 154: (2000) 361–367.

[122] Shao-Horn, Y., L. Croguennec, C. Delmas, E. C. Nelson, and M. A. O'Keefe. *Nature Materials* 2: (2003) 464.

[123] Shao-Horn, Y., S. Levasseur, F. Weill, and C. Delmas. *Journal of the electrochemical society* 150: (2003) A366.

[124] Shull, C. G., and J. S. Smart. *Physical Review* 76: (1949) 1256.

[125] Siegel, S., H. R. Hoekstra, and B. S. Tani. "The crystal structure of beta-platinum dioxide." *Journal of Inorganic and Nuclear Chemistry* 31, 12: (1969) 3803 – 3807.

[126] Singleton, J. *Band Theory and Electronic Properties of Solids.* Oxford Univeristy Press, 2003.

[127] Slater, J. C. "Magnetic Effects and the Hartree-Fock Equation." *Phys. Rev.* 82: (1951) 538–541.

[128] Subedi, A. "First-principles study of the electronic structure and magnetism of $CaIrO_3$." *Phys. Rev. B* 85: (2012) 020,408.

[129] Subramanian, M. A., M. K. Crawford, and R. L. Harlow. "Single crystal structure determination of double layered strontium iridium oxide $Sr_3Ir_2O_7$." *Materials Research Bulletin* 29, 6: (1994) 645 – 650.

[130] Tancret, N., S. Obbade, N. Bettahar, and F. Abraham. "Synthesis and ab initio Structure Determination from Powder X-Ray Diffraction Data of a New Metallic Mixed-Valence PlatinumLead Oxide $PbPt_2O_4$." *Journal of Solid State Chemistry* 124, 2: (1996) 309 – 318.

[131] Terashima, T., N. Kurita, A. Kiswandhi, E. S. Choi, J. S. Brooks, K. Sato, J. I. Yamaura, Z. Hiroi, H. Harima, and S. Uji. "Large and homogeneous mass enhancement in the rattling-induced superconductor KOs_2O_6." *ArXiv e-prints* .

[132] Torre, A. d. l., E. C. Hunter, A. Subedi, S. McKeown Walker, A. Tamai, T. K. Kim, M. Hoesch, R. S. Perry, A. Georges, and F. Baumberger. *Physical Review Letters* 113: (2014) 256,402.

[133] Urland, W., and R. Hoppe. "Zur Kenntnis der Oxoplatinate Na_2PtO_2, Na_2PtO_3, K_2PtO_3 and Rb_2PtO_3." *Zeitschrift für anorganische und allgemeine Chemie* 392, 1: (1972) 23–36.

[134] Vivas, P., M. Chacon, M. Gomez, and P. Prieto. *Physica status solidi (b)* 220: (2000) 503.

[135] Wakeshima, M., and Y. Hinatsu. "Crystal structure and magnetic ordering of novel perovskite-related barium osmate $Ba_{11}Os_4O_{24}$." *Solid State Communications* 136, 9-10: (2005) 499–503.

[136] Waser, J., and E. McClanahan. "The structure of $NaPt_3O_4$." *Cellular and Molecular Life Sciences* 6: (1950) 379–380.

[137] Wojek, B. M., M. H. Berntsen, S. Boseggia, A. T. Boothroyd, D. Prabhakaran, D. F. , H. M. Rønnow, J. Chang, and O. Tjernberg. "The $J_{eff} = \frac{1}{2}$ insulator Sr_3 Ir_2O_7 studied by means of angle-resolved photoemission spectroscopy." *Journal of Physics: Condensed Matter* 24, 41: (2012) 415,602.

[138] Wulfsberg, G. *Inorganic Chemistry.* University Science Books, 2000.

[139] Xiao, D., Y. Yao, W. Feng, J. Wen, W. Zhu, X. Q. Chen, G. M. Stocks, and Z. Zhang. "Half-Heusler Compounds as a New Class of Three-Dimensional Topological Insulators." *Phys. Rev. Lett.* 105: (2010) 096,404.

[140] Yamada, K., S. Wakimoto, G. Shirane, C. H. Lee, M. A. Kastner, S. Hosoya, M. Greven, Y. Endoh, and R. J. Birgeneau. "Direct Observation of a Magnetic Gap in Superconducting $La_{1.85}Sr_{0.15}CuO_4$ (T_C=37.3K)." *Physical Review Letters* 75, 8: (1995) 1626.

[141] Ye, F., S. Chi, B. C. Chakoumakos, J. A. Fernandez-Baca, T. Qi, and G. Cao. "Magnetic and crystal structures of Sr_2IrO_4: A neutron diffraction study." *Phys. Rev. B* 87: (2013) 140,406.

[142] Yonezawa, S., Y. Muraoka, and Z. Hiroi. "New β-Pyrochlore Oxide Superconductor $CsOs_2O_6$." *Journal of the Physics Society Japan* 73, 7: (2004) 1655–1656.

[143] Yonezawa, S., Y. Muraoka, Y. Matsushita, and Z. Hiroi. "New Pyrochlore Oxide Superconductor $RbOs_2O_6$." *Journal of the Physical Society of Japan* 73, 4: () 819–821.

[144] ———. "Superconductivity in a pyrochlore-related oxide KOs_2O_6." *Journal of Physics: Condensed Matter* 16, 3: () L9.

[145] Zakharchenko, N. *Russ. J. Appl. Chem* 74.

[146] Zhao, S., J. M. Mackie, D. E. MacLaughlin, O. O. Bernal, J. J. Ishikawa, Y. Ohta, and S. Nakatsuji. "Magnetic transition, long-range order, and moment fluctuations in the pyrochlore iridate $Eu_2Ir_2O_7$." *Physical Review B* 83, 18.

[147] Zhao, Z., S. Wang, T. F. Qi, W. Zeng, S. Hirai, P. P. Kong, L. Li, C. Park, C. Q. Jin, G. Cao, and W. L. Mao. *Journal of Physics: Condensed Matter* 26: (2014) 215,402.

[148] Zhensheng, J., X. Chanjuan, Z. Qingmei, Y. Feng, Z. Jiazheng, and X. Jinzhen. "Catalytic behavior of nanoparticle α-PtO_2 for ethanol oxidation." *Journal of Molecular Catalysis A: Chemical* 191, 1: (2003) 61 – 66.